



National Library  
of Canada

Bibliothèque nationale  
du Canada

Acquisitions and  
Bibliographic Services Branch

Direction des acquisitions et  
des services bibliographiques

395 Wellington Street  
Ottawa, Ontario  
K1A 0N4

395, rue Wellington  
Ottawa (Ontario)  
K1A 0N4

*Your file* *Vostra referenca*

*Our file* *Notre référence*

## NOTICE

The quality of this microform is heavily dependent upon the quality of the original thesis submitted for microfilming. Every effort has been made to ensure the highest quality of reproduction possible.

If pages are missing, contact the university which granted the degree.

Some pages may have indistinct print especially if the original pages were typed with a poor typewriter ribbon or if the university sent us an inferior photocopy.

Reproduction in full or in part of this microform is governed by the Canadian Copyright Act, R.S.C. 1970, c. C-30, and subsequent amendments.

## AVIS

La qualité de cette microforme dépend grandement de la qualité de la thèse soumise au microfilmage. Nous avons tout fait pour assurer une qualité supérieure de reproduction.

S'il manque des pages, veuillez communiquer avec l'université qui a conféré le grade.

La qualité d'impression de certaines pages peut laisser à désirer, surtout si les pages originales ont été dactylographiées à l'aide d'un ruban usé ou si l'université nous a fait parvenir une photocopie de qualité inférieure.

La reproduction, même partielle, de cette microforme est soumise à la Loi canadienne sur le droit d'auteur, SRC 1970, c. C-30, et ses amendements subséquents.

Canada

**Crustal Structure of the Extinct Spreading Centre  
in the Labrador Sea: Implications for Dynamic  
Models of Flow Beneath Mid-Ocean Ridges**

by

John Collamer Osler

Submitted in partial fulfilment of the requirements for the degree

of Doctor of Philosophy

at

Dalhousie University

Halifax, Nova Scotia

April, 1993

© Copyright by John Collamer Osler, 1993



National Library  
of Canada

Acquisitions and  
Bibliographic Services Branch

395 Wellington Street  
Ottawa, Ontario  
K1A 0N4

Bibliothèque nationale  
du Canada

Direction des acquisitions et  
des services bibliographiques

395, rue Wellington  
Ottawa (Ontario)  
K1A 0N4

*Your title - Votre référence*

*Our title - Notre référence*

**The author has granted an irrevocable non-exclusive licence allowing the National Library of Canada to reproduce, loan, distribute or sell copies of his/her thesis by any means and in any form or format, making this thesis available to interested persons.**

**L'auteur a accordé une licence irrévocable et non exclusive permettant à la Bibliothèque nationale du Canada de reproduire, prêter, distribuer ou vendre des copies de sa thèse de quelque manière et sous quelque forme que ce soit pour mettre des exemplaires de cette thèse à la disposition des personnes intéressées.**

**The author retains ownership of the copyright in his/her thesis. Neither the thesis nor substantial extracts from it may be printed or otherwise reproduced without his/her permission.**

**L'auteur conserve la propriété du droit d'auteur qui protège sa thèse. Ni la thèse ni des extraits substantiels de celle-ci ne doivent être imprimés ou autrement reproduits sans son autorisation.**

ISBN 0-315-87487-2

**Canada**

Name John Collamer Osler

Dissertation Abstracts International is arranged by broad, general subject categories. Please select the one subject which most nearly describes the content of your dissertation. Enter the corresponding four digit code in the spaces provided.

Geophysics

**0373 U.M.I.**

SUBJECT TERM

SUBJECT CODE

**Subject Categories**

**THE HUMANITIES AND SOCIAL SCIENCES**

**COMMUNICATIONS AND THE ARTS**

Architecture 0729  
 Art History 0777  
 Cinema 0900  
 Dance 0378  
 Fine Arts 0357  
 Information Science 0723  
 Journalism 0391  
 Library Science 0399  
 Mass Communications 0708  
 Music 0413  
 Speech Communication 0459  
 Theater 0465

**EDUCATION**

General 0515  
 Administration 0514  
 Adult and Continuing 0516  
 Agricultural 0517  
 Art 0273  
 Bilingual and Multicultural 0282  
 Business 0688  
 Community College 0275  
 Curriculum and Instruction 0727  
 Early Childhood 0518  
 Elementary 0524  
 Finance 0277  
 Guidance and Counseling 0519  
 Health 0680  
 Higher 0745  
 History of 0520  
 Home Economics 0273  
 Industrial 0521  
 Language and Literature 0279  
 Mathematics 0280  
 Music 0522  
 Philosophy of 0998  
 Physical 0523

Psychology 025  
 Reading 0535  
 Religion 0527  
 Sciences 0714  
 Secondary 0533  
 Social Sciences 0534  
 Sociology of 0340  
 Special 0529  
 Teacher Training 0530  
 Technology 0710  
 Tests and Measurements 0288  
 Vocational 0747

**LANGUAGE, LITERATURE AND LINGUISTICS**

Language  
 General 0679  
 Ancient 0289  
 Linguistics 0290  
 Modern 0291  
 Literature  
 General 0401  
 Classical 0294  
 Comparative 0295  
 Medieval 0297  
 Modern 0298  
 African 0316  
 American 0591  
 Asian 0305  
 Canadian (English) 0352  
 Canadian (French) 0355  
 English 0593  
 Germanic 0311  
 Latin American 0312  
 Middle Eastern 0315  
 Romance 0313  
 Slavic and East European 0314

**PHILOSOPHY, RELIGION AND THEOLOGY**

Philosophy 0422  
 Religion  
 General 0318  
 Biblical Studies 0321  
 Clergy 0319  
 History of 0320  
 Philosophy of 0322  
 Theology 0469

**SOCIAL SCIENCES**

American Studies 0323  
 Anthropology  
 Archaeology 0324  
 Cultural 0326  
 Physical 0327  
 Business Administration  
 General 0310  
 Accounting 0272  
 Banking 0770  
 Management 0454  
 Marketing 0338  
 Canadian Studies 0385  
 Economics  
 General 0501  
 Agricultural 0503  
 Commerce Business 0505  
 Finance 0508  
 History 0509  
 Labor 0510  
 Theory 0511  
 Folklore 0358  
 Geography 0366  
 Gerontology 0351  
 History  
 General 0578

Ancient 0579  
 Medieval 0581  
 Modern 0582  
 Black 0328  
 African 0331  
 Asia Australia and Oceania 0332  
 Canadian 0334  
 European 0335  
 Latin American 0336  
 Middle Eastern 0333  
 United States 0337  
 History of Science 0585  
 Law 0398  
 Political Science  
 General 0615  
 International Law and Relations 0616  
 Public Administration 0617  
 Recreation 0814  
 Social Work 0452  
 Sociology  
 General 0626  
 Criminology and Penology 0627  
 Demography 0938  
 Ethnic and Racial Studies 0631  
 Individual and Family Studies 0628  
 Industrial and Labor Relations 0629  
 Public and Social Welfare 0630  
 Social Structure and Development 0700  
 Theory and Methods 0344  
 Transportation 0709  
 Urban and Regional Planning 0999  
 Women's Studies 0453

**THE SCIENCES AND ENGINEERING**

**BIOLOGICAL SCIENCES**

Agriculture  
 General 0473  
 Agronomy 0285  
 Animal Culture and Nutrition 0475  
 Animal Pathology 0476  
 Food Science and Technology 0359  
 Forestry and Wildlife 0478  
 Plant Culture 0479  
 Plant Pathology 0480  
 Plant Physiology 0817  
 Range Management 0777  
 Wood Technology 0746  
 Biology  
 General 0306  
 Anatomy 0287  
 Prostatitics 0308  
 Botany 0309  
 Cell 0379  
 Ecology 0329  
 Entomology 0353  
 Genetics 0369  
 Limnology 0793  
 Microbiology 0410  
 Molecular 0307  
 Neuroscience 0317  
 Oceanography 0416  
 Physiology 0433  
 Radiation 0821  
 Veterinary Science 0778  
 Zoology 0472  
 Biophysics  
 General 0786  
 Medical 0760  
**EARTH SCIENCES**  
 Biogeochemistry 0425  
 Geochemistry 0996

Geodesy 0370  
 Geology 0372  
 Geophysics 0373  
 Hydrology 0388  
 Mineralogy 0411  
 Paleobotany 0345  
 Paleocology 0426  
 Paleontology 0418  
 Paleozoology 0985  
 Palynology 0427  
 Physical Geography 0368  
 Physical Oceanography 0415

**HEALTH AND ENVIRONMENTAL SCIENCES**

Environmental Sciences 0768  
 Health Sciences  
 General 0566  
 Audiology 0300  
 Chemotherapy 0992  
 Dentistry 0567  
 Education 0350  
 Hospital Management 0769  
 Human Development 0758  
 Immunology 0982  
 Medicine and Surgery 0564  
 Mental Health 0347  
 Nursing 0569  
 Nutrition 0570  
 Obstetrics and Gynecology 0380  
 Occupational Health and Therapy 0354  
 Ophthalmology 0381  
 Pathology 0571  
 Pharmacology 0419  
 Pharmacy 0572  
 Physical Therapy 0382  
 Public Health 0573  
 Radiology 0574  
 Recreation 0575

Speech Pathology 0460  
 Toxicology 0383  
 Home Economics 0386

**PHYSICAL SCIENCES**

**Pure Sciences**  
 Chemistry  
 General 0485  
 Agricultural 0749  
 Analytical 0486  
 Biochemistry 0487  
 Inorganic 0488  
 Nuclear 0738  
 Organic 0490  
 Pharmaceutical 0491  
 Physical 0494  
 Polymer 0495  
 Radiation 0754  
 Mathematics 0405  
 Physics  
 General 0605  
 Acoustics 0986  
 Astronomy and Astrophysics 0606  
 Atmospheric Science 0608  
 Atomic 0748  
 Electronics and Electricity 0607  
 Elementary Particles and High Energy 0798  
 Fluid and Plasma 0759  
 Molecular 0609  
 Nuclear 0610  
 Optics 0752  
 Radiation 0756  
 Solid State 0611  
 Statistics 0463  
**Applied Sciences**  
 Applied Mechanics 0346  
 Computer Science 0984

Engineering  
 General 0537  
 Aerospace 0538  
 Agricultural 0539  
 Automotive 0540  
 Biomedical 0541  
 Chemical 0542  
 Civil 0543  
 Electronics and Electrical 0544  
 Heat and Thermodynamics 0348  
 Hydraulic 0545  
 Industrial 0546  
 Marine 0547  
 Materials Science 0794  
 Mechanical 0548  
 Metallurgy 0743  
 Mining 0551  
 Nuclear 0552  
 Packaging 0549  
 Petroleum 0765  
 Sanitary and Municipal System Science 0790  
 Geotechnology 0428  
 Operations Research 0796  
 Plastics Technology 0795  
 Textile Technology 0994

**PSYCHOLOGY**

General 0621  
 Behavioral 0384  
 Clinical 0622  
 Developmental 0620  
 Experimental 0623  
 Industrial 0624  
 Personality 0625  
 Physiological 0989  
 Psychobiology 0349  
 Psychometrics 0632  
 Social 0451



For Martine - so in love with you am I!

# Table of Contents

## Table of Contents

## List of Tables

## List of Figures

## Abstract

## List of Abbreviations and Symbols

## Acknowledgements

<b>1. Introduction</b>	<b>1</b>
1.1 Dynamic models of flow beneath mid-ocean ridges .....	1
1.2 Extinct mid-ocean spreading centres .....	6
1.3 Thesis objectives .....	8
<b>2. Field Experiment and Data Reduction</b>	<b>9</b>
2.1 Seafloor spreading history of the Labrador Sea .....	9
2.2 Experimental configuration and procedure .....	11
2.3 Processing of seismic data .....	15
2.3.1 Reflection profiles .....	15
2.3.2 Sonobuoy refraction profiles .....	19
2.3.3 OBS refraction profiles .....	19
2.4 Time and range corrections .....	23
2.4.1 Sonobuoy data .....	23
2.4.2 OBS data .....	25
<b>3. One Dimensional Velocity Analysis</b>	<b>33</b>

3.1 Sediment correction method .....	33
3.2 Travel time solutions .....	38
3.2.1 Methods of analysis .....	38
3.2.2 Results .....	42
3.3 Synthetic seismograms .....	52
3.4 Discussion .....	56
<b>4. Two Dimensional Velocity Analysis</b> .....	<b>60</b>
4.1 Characteristics and selection of 2-D algorithm .....	61
4.2 Model parameterization .....	62
4.3 Initial velocity-depth model .....	64
4.3.1 Water layer .....	64
4.3.2 Sediment layers .....	64
4.3.3 Crustal and mantle layers .....	66
4.4 Considerations guiding model revisions .....	67
4.4.1 Uncertainty and identification of travel time picks .....	70
4.4.2 Assessment of model iterations .....	71
4.5 Final velocity-depth structure .....	72
4.5.1 Sediment layers .....	75
4.5.2 Crustal layers .....	78
4.5.3 Mantle layer .....	89
4.6 Error analysis .....	94
4.7 Synthetic seismograms .....	99

4.7.1 Comparison of WKBJ and TRAMP synthetics .....	100
4.7.2 Synthetic seismograms for receivers along line R2 .....	105
4.8 Summary .....	115
<b>5. Two Dimensional Gravity Modelling</b> .....	<b>117</b>
5.1 Observed free-air gravity anomaly .....	117
5.2 Gravity models based on 2-D seismic velocity structure .....	126
5.2.1 Initial gravity model .....	128
5.2.2 First revision: compensating basement high	
from 58 to 76 km .....	128
5.2.3 Second revision: lower mantle densities under the extinct	
spreading centre .....	132
5.2.4 Third revision: reduce regional asymmetry of	
calculated anomaly .....	134
5.2.5 Evidence for crustal thinning in the extinct spreading centre	142
5.3 Gabbroic root model .....	144
5.3.1 Free-air gravity anomaly of the root structure .....	149
5.3.2 Coupling of root structure to the line R2 gravity model	150
5.4 Summary .....	154
<b>6. Discussion</b> .....	<b>156</b>
6.1 Spreading rate history of the Labrador Sea preceding extinction	156
6.2 Nature of the crust and uppermost mantle at the extinct	
spreading centre .....	165

6.3 Implications for 2-D dynamic models of flow beneath	
mid-ocean ridges .....	171
6.4 Relationship to observations at slow spreading centres and	
fracture zones .....	181
6.4.1 Interplay between magmatism and volcanism .....	183
6.4.2 Applicability of 2-D thermal models .....	185
6.4.3 Cause of thinning at oceanic fracture zones .....	186
<b>7. Conclusions and Future Work</b>	<b>189</b>
7.1 Conclusions .....	189
7.2 Future work .....	190
7.2.1 Gravity .....	190
7.2.2 Thermal models .....	191
7.2.3 Seismic methods .....	192
<b>Appendix A. Refraction Profiles for Refraction Line R2</b>	<b>193</b>
<b>Appendix B. Refraction Profiles for Refraction Line R1</b>	<b>204</b>
<b>Appendix C. Boundary and Velocity Nodes in 2-D Seismic Modelling</b>	<b>209</b>
<b>References</b>	<b>213</b>

## List of Tables

-	2.1	Time corrections for OBSs .....	31
	2.2	Locations and water depths for OBSs .....	32
	3.1	Line R1, OBS plane layer solutions .....	43
	3.2	Line R2, OBS plane layer solutions .....	44
	4.1	Quality of fit for computed travel times in 2-D modelling along line R2	73
	4.2	Previous observations of high velocity lower crust northeast of the extinct spreading centre in the Labrador Sea .....	86
C		Velocity and boundary nodes for 2-D velocity-depth structure on line R2	210

## List of Figures

1.1	Mantle circulation beneath a mid-ocean spreading centre driven by plate spreading: (a) streamlines [Reid and Jackson, 1981]; (b) predicted relationship between crustal thickness and spreading rate [Reid and Jackson, 1981] ..	3
1.2	Mantle circulation beneath a mid-ocean spreading centre driven dominantly by localized buoyancy: (a) streamlines [Scott and Stevenson, 1989]; (b) predicted relationship between crustal thickness and spreading rate for various viscosities of the mantle [Sotin and Parmentier, 1990] .....	4
2.1	Map of bathymetry, magnetic lineations and fracture zones in the Labrador Sea .....	10
2.2	Location diagram for the seismic refraction experiment in the Labrador Sea .....	12
2.3	Single channel reflection profile along refraction shooting line R2	16
2.4	Single channel reflection profile along refraction shooting line R1	17
2.5	Processing stream for single channel reflection and sonobuoy data	18
2.6	Processing stream for seismic refraction data I: interpolated data file and construction of shot look up table .....	21
2.7	Processing stream for seismic refraction data II: plotting, SEG-Y conversion, plane layer solutions and $\tau$ - $p$ inversions .....	22
2.8	Travel time vs. range for the direct arrival at sonobuoy 11: (a) prior to range correction; (b) following range correction .....	24
2.9	Temperature vs. depth for the upper 600 m in the Labrador Sea during the 1987	

field season .....	27
2.10 Speed of sound in water for 1987 field season in the Labrador Sea	28
2.11 Contours of RMS fit between observed and computed ranges indicating the most probable location of OBS M .....	29
3.1 An interpretation of the single channel reflection profiles (Figures 2.3 and 2.4) along refraction lines R2 and R1 .....	35
3.2 Schematic of sediment travel time correction .....	36
3.3 Refraction profiles for OBS R2-L: (a) without sediment travel time corrections and (b) with sediment travel time corrections .....	37
3.4 Refraction profile for OBS R1-G in T-X space .....	45
3.5 Refraction profile for OBS R2-N in T-X space .....	46
3.6 Refraction profile for OBS R1-G in $\tau$ - $p$ space .....	47
3.7 Refraction profile for OBS R2-N in $\tau$ - $p$ space .....	48
3.8 1-D travel time solutions for line R1 .....	49
3.9 1-D travel time solutions for line R2 .....	50
3.10 1-D WKBJ synthetic seismogram for OBS R1-G .....	53
3.11 1-D WKBJ synthetic seismogram for OBS R2-N .....	54
3.12 Crustal structures arising from the 1-D WKBJ synthetic seismogram modelling: (a) OBS R1-G structure plotted with a compilation fracture zone crustal structures; (b) OBS R2-N structure plotted with a compilation of refraction results for typical mature crust in the Atlantic Ocean .....	58
4.1 Line R2: parameterization of the final 2-D velocity-depth structure	68

4.2	Line R2: the final 2-D velocity-depth structure represented by isovelocity contours .....	69
4.3	Line R2: ray coverage and travel time fits for the sediment layer	76
4.4	Line R2: ray coverage and travel time fits for the upper crust .....	81
4.5	Line R2: ray coverage and travel time fits for the lower crust .....	82
4.6	Line R2: ray coverage and travel time fits for wide angle reflections from the crust-mantle boundary .....	87
4.7	Line R2: ray coverage and travel time fits for mantle refracted arrivals at OBSs Q and O .....	91
4.8	Line R2: ray coverage and travel time fits for mantle refracted arrivals at OBSs E and N .....	92
4.9	Line R2: ray coverage and travel time fits for mantle refracted arrivals at OBSs M and L .....	93
4.10	(a) Degree of crustal thinning from 40 to 140 km along line R2 decreased in 10% intervals and (b) the corresponding effect on the residual travel time between observed and computed arrivals .....	97
4.11	Assessment of the average depth and velocity uncertainty of nodes comprising the crust-mantle boundary by introducing velocity and depth perturbations to the final velocity-depth structure (Fig. 4.2) and raytracing to obtain contours of (a) $T_{RMS}$ , (b) $\chi^2$ , (c) $n$ .....	98
4.12	(a) Source function used in comparison of synthetic seismogram algorithms. (b) source function used in line R2 synthetic seismograms. (c) 1-D velocity-depth	

	structure used in synthetic seismogram comparison .....	102
4.13	Comparison of synthetic seismograms generated using (a) Zelt's TRAMP and (b) Chapman's WKBJ .....	103
4.14	Synthetic seismic refraction profiles for OBSs Q and L .....	108
4.15	Synthetic seismic refraction profiles for OBS M .....	109
4.16	Synthetic seismic refraction profiles for OBS N .....	110
4.17	Synthetic seismic refraction profiles for OBS E .....	111
4.18	Synthetic seismic refraction profiles for OBS O .....	112
4.19	Synthetic seismic refraction profiles for Sonobuoys 11 and 12 .....	113
5.1	Free-air gravity anomaly along ship tracks in the vicinity of refraction lines R1 and R2. Observed values were gridded at BIO using a variable search radius .....	118
5.2	Free-air gravity anomaly along ship tracks in the vicinity of refraction lines R1 and R2. Observed values are gridded using a search area weighted by a gaussian function with a half-width of (a) 5 km and (b) 10 km .....	120
5.3	Free-air gravity anomaly along ship tracks in the vicinity of refraction lines R1 and R2. Observed values are gridded using a search area weighted by a gaussian function with a half-width of (a) 15 km and (b) 20 km .....	121
5.4	Profiles of the observed free-air gravity interpolated to positions along seismic refraction line R2 .....	124
5.5	Density-depth structure and calculated anomaly for the initial gravity model following the conversion of the final velocity-depth structure to a density-depth	

structure .....	129
5.6 First revision of the initial density-depth structure. Symmetry of the crust-mantle boundary from 60 to 130 km has been introduced .....	130
5.7 Second revision of the initial density-depth structure. Mantle densities within the extinct spreading centre (80 to 110 km) are reduced to $3.20 \text{ gcm}^{-3}$ .....	133
5.8 Third revision of the initial density-depth structure. The density of lower crust trapezoids from 0 to 60 km is increased by $0.07 \text{ gcm}^{-3}$ .....	136
5.9 Third revision of the initial density-depth structure. The thickness of the lower crust trapezoids is reduced by 0.51 km .....	137
5.10 Line R2: total mass in columns to 14 km depth, calculated at distance intervals of 10 km .....	138
5.11 Line R2 gravity model in which the crust has a constant thickness and the density of the mantle is uniform .....	143
5.12 Gabbroic root model: schematic of petrological and density structure, adapted from Fig. 1 in Hall <i>et al.</i> [1986] .....	146
5.13 Gabbroic root model: (a) calculation of the residual gravity anomaly in the Labrador Sea and (b) the residual gravity anomaly at numerous extinct spreading centres plotted as a function of spreading rate, adapted from Figs. 2 and 3 in Jonas <i>et al.</i> [1991] .....	147
5.14 Free-air gravity anomaly for the gabbroic root model .....	151
5.15 Free-air gravity anomaly for the gabbroic root model coupled with the initial density-depth structure from the line R2 seismic refraction results .....	152

6.1	Magnetic anomaly along selected ship tracks in the vicinity of refraction lines R1 and R2. Magnetic lineations following the interpretation of Roest and Srivastava [1989b] .....	157
6.2	Six potential spreading rate histories for the Labrador Sea from the time of anomaly 24 until the cessation of spreading. Spreading rate is plotted as a function of time (right panel) and as a function of distance from the accretionary axis (left panel) .....	161
6.3	Synthetic magnetic anomaly patterns underlain by their respective sequences of normal and reversed polarity blocks for the six potential pre-extinction spreading rate histories .....	162
6.4	Comparison of synthetic and observed magnetic anomaly patterns	163
6.5	Summary of geophysical information presented in this thesis. (a) Preferred spreading rate history, (b) free-air gravity anomaly, (c) total crustal thickness in vertical columns between nodes in the 2-D velocity-depth structure along line R2, (d) an isovelocity contour representation of the velocity-depth structure along line R2 .....	174
6.6	Crustal thickness predicted with the Reid and Jackson [1981] model for passive mantle upwelling for the six potential spreading rate histories in the Labrador Sea .....	176
A.1	Seismic refraction profiles for OBSs R2-L shooting southwest and R2-Q shooting northeast are plotted with a reducing velocity of 8 km/s and overlain with travel time curves from the 2-D ray tracing .....	194

A.2	Seismic refraction profiles for OBS R2-M shooting southwest and northeast are plotted with a reducing velocity of 8 km/s and overlain with travel time curves from the 2-D ray tracing .....	195
A.3	Seismic refraction profiles for OBS R2-N shooting southwest and northeast are plotted with a reducing velocity of 8 km/s and overlain with travel time curves from the 2-D ray tracing .....	196
A.4	Seismic refraction profiles for OBS R2-E shooting southwest and northeast are plotted with a reducing velocity of 8 km/s and overlain with travel time curves from the 2-D ray tracing .....	197
A.5	Seismic refraction profiles for OBS R2-O shooting southwest and northeast are plotted with a reducing velocity of 8 km/s and overlain with travel time curves from the 2-D ray tracing .....	198
A.6	Seismic refraction profiles for sonobuoys R2-11 and R2-12 shooting northeast are plotted with a reducing velocity of 8 km/s and overlain with travel time curves from the 2-D ray tracing .....	199
A.7	Seismic refraction profiles for sonobuoys R2-11 and R2-12 are plotted with a reducing velocity of 5 km/s and overlain with travel time curves from the 2-D ray tracing .....	200
A.8	Seismic refraction profiles for OBSs R2-L and R2-M are plotted with a reducing velocity of 5 km/s and overlain with travel time curves from the 2-D ray tracing .....	201
A.9	Seismic refraction profiles for OBSs R2-N and R2-E are plotted with a reducing	

	velocity of 5 km/s and overlain with travel time curves from the 2-D ray tracing .....	202
A.10	Seismic refraction profiles for OBSs R2-O and R2-Q are plotted with a reducing velocity of 5 km/s and overlain with travel time curves from the 2-D ray tracing .....	203
B.1	Seismic refraction profiles for OBSs R1-D shooting southeast and R1-H shooting northwest are plotted with a reducing velocity of 8 km/s .....	205
B.2	Seismic refraction profiles for OBS R1-E shooting southeast and northwest are plotted with a reducing velocity of 8 km/s. ....	206
B.3	Seismic refraction profiles for OBS R1-F shooting southeast and northwest are plotted with a reducing velocity of 8 km/s .....	207
B.4	Seismic refraction profiles for OBS R1-G shooting southeast and northwest are plotted with a reducing velocity of 8 km/s .....	208

## Abstract

Two dimensional dynamic models for mantle circulation beneath mid-ocean ridges are characterized by two end members. Models with passive upwelling induced by the separation of the lithospheric plates predict a broad region of partial melting, lateral migration of melt to the accretionary axis, and a dependence of crustal thickness upon spreading rate. Models with flow dominated by buoyancy forces localized beneath the spreading centre predict that upwelling occurs rapidly in a narrow zone and crustal thickness is independent of spreading rate. The Labrador Sea contains a rare example of an abandoned mid-ocean ridge where active accretion of oceanic crust ceased due to a change in the spreading geometry of lithospheric plates. As its thermal regime and spreading rate must have changed as spreading stopped, studying the crustal structure provides a means by which the predictions of thermal and petrological models for the processes and structure of active spreading centres may be assessed.

Seismic refraction data were collected along two refraction lines in the Labrador Sea, R1 along strike of the extinct ridge and R2 crossing it orthogonally. One and two dimensional analyses of the refraction data using travel time and synthetic seismogram techniques reveal major variations in crustal thickness and velocity. In the extinct spreading centre, a crustal thickness of approximately 4 km is determined, compared with 5.5 km for the flanks. Substantial lateral variations in P-wave velocities of the upper and lower crust are observed with a marked decrease within the extinct spreading centre. Low velocities are also observed in the uppermost mantle underlying the extinct spreading centre and are interpreted as being the result of hydrothermal alteration.

The anomalously low crustal velocities and crustal thinning are attributed to a decreasing supply of partial melt and increasing degree of tectonism at the slow spreading rates preceding extinction. The observations are consistent with thermal models which suggest a spreading rate dependence on crustal generation at slow spreading rates, though the thinning is not as appreciable as predicted. The seismic structure is also used to develop two dimensional gravity models along line R2. These models support the seismic observations of crustal thinning and demonstrate that the gravity field does not require a deep low density gabbroic root zone to underlie the extinct spreading centre.

## List of abbreviations and symbols

1-D	One dimensional
2-D	Two dimensional
BIO	Bedford Institute of Oceanography
DAL	Dalhousie University
GKS	Graphical Kernel System
HH	Hour
MM	Minute
OBS	Ocean bottom seismometer
PC	Personal computer
RMS	Root mean square
SEG-Y	Society of Exploration Geophysicists, format Y
TWTT	Two way travel time
T-X	Travel time - horizontal shot-receiver offset
$\tau$ - $p$	Travel time at zero offset (intercept time) - seismic ray parameter
VISTA	Viewpoints in seismic trace analysis, © Seismic Image Software Ltd.
XBT	Expendable bathythermograph
YR	Year

## Acknowledgements

I am indebted to many individuals and organizations for the technical and financial support, scientific dialogue, and encouragement which they provided. I would like to thank the officers and crew of the C.S.S. *Hudson*, Borden Chapman, Guy Fehn, and Neil Hamilton for their technical expertise during the course of the seismic refraction experiment. The analog refraction data was replayed and digitized using computing facilities at the Bedford Institute of Oceanography with the assistance of Steve Peary and Ian Reid. The development and maintenance of processing algorithms for the refraction data was assisted in its infancy by Greg Leger and the staff of the Dalhousie University Computing and Information Services and more recently by Deping Chian and Saeid Yazdanmehr. The research was supported by Energy, Mines and Resources grant 30/04/87 and Natural Science and Engineering Research Council of Canada grants OGP0008459, EQP0027418, and INF0001469. I also acknowledge the financial support provided by a fellowship from Dalhousie University.

I am grateful to the members of my thesis committee, Keith Thompson, Shiri Srivastava and Ian Reid for their interest in my research, ideas, constructive criticism, and comments on drafts of my thesis. Keith Loudon, my thesis supervisor, merits a special word of appreciation. I am grateful for the opportunities he provided to participate in field experiments and attend scientific conferences. I have benefitted from our many discussions and the contents of my thesis reflect his steady stream of ideas, "Have you tried looking at ...". I would also like to thank my fellow students in the Department of Oceanography for the stimulating social and scientific environment which they provided.

I have particularly enjoyed my many discussions with David Johnson and David Mosher about our research and the lighter side of life as a graduate student.

My wife, Martine, and son, Liam, also merit a special word of appreciation. More often than not, I was engrossed in my studies on weeknights and weekends. Their encouragement, patience, and understanding were instrumental in keeping up my spirits. I would also like to mention my parents and Martine's parents. Their financial assistance, prayers, and interest in my studies and well-being are most appreciated.

# **1. Introduction**

In plate tectonic theory, mid-ocean ridges mark boundaries between adjacent lithospheric plates and the location where new oceanic crust and lithosphere is formed when the plates are diverging. Extinct spreading centres are mid-ocean ridges where the active accretion of oceanic crust has ceased due to a change in the spreading geometry of the lithospheric plates. As such, extinct spreading centres represent a natural perturbation from the steady state situation and provide a unique environment to study aspects of crustal accretion. To this end, this thesis presents a geophysical study of a segment of the extinct spreading centre in the Labrador Sea, including: 1) a one and two dimensional analysis of seismic refraction data collected for this study; 2) gravity models which are based on the proposed seismic velocity-depth structure; and 3), a spreading rate history of the Labrador Sea based on modelling of the magnetic anomalies. The results are integrated in Chapter 6 to discuss the nature of the crust within the extinct spreading centre in the Labrador Sea and to assess the dynamic models of mantle circulation beneath mid-ocean ridges which are reviewed in the remainder of this introductory chapter.

## **1.1 Dynamic Models of Flow Beneath Mid-Ocean Ridges**

As spreading beneath a mid-ocean ridge stops, properties such as its spreading rate and thermal regime must change. A number of theoretical studies suggest that the processes of crustal accretion are dependent upon these properties [Bottinga and Allègre, 1978; Kusznir, 1980; Reid and Jackson, 1981]. The Reid and Jackson [1981] model treats the case of an isoviscous mantle in which upwelling (see streamlines Figure 1.1a) occurs

solely due to plate spreading. Crustal thickness, as defined by the total melt production, is predicted to decrease systematically with decreasing spreading rate (Figure 1.1b); this effect being most appreciable at half spreading rates below 20 mm/yr. Their work includes a compilation of seismic refraction measurements from active spreading centres; the most well constrained data (post 1970's) in apparent agreement with the dependence of crustal thickness upon spreading rate. However, in a more recent compilation of refraction data, Chen [1992] finds no systematic decrease in crustal thickness with spreading rate. Rather, large variations in crustal thickness are observed at slow spreading ridges (3-8 km for half rates < 20 mm/yr) and small variations at fast rates (5-7 km for half rates > 30 mm/yr). Chen [1992] speculates that these observations support a transition from a 3-D structure of crustal accretion at slow ridges to a 2-D accretion pattern at fast ridges.

More recent thermal models [Scott and Stevenson, 1989; Sotin and Parmentier, 1989; Parmentier and Phipps Morgan, 1990] include buoyant upwelling as an additional driving force for mantle circulation. A number of factors contribute to this buoyancy: 1) thermal expansion; 2) phase changes associated with partial melting; and most significantly 3) compositional density variations between the garnet lherzolite mantle source rock and the lower density harzburgite or dunite residual mantle which is left following partial melting of garnet and orthopyroxene. The relative importance of this buoyancy force depends upon spreading rate and mantle viscosity. Sotin and Parmentier [1989] find that at high mantle viscosity ( $10^{22}$  Pa s) upwelling due to plate spreading dominates and crustal thickness is predicted to be a strong function of spreading rate (Figure 1.2b). At lower mantle viscosity ( $10^{19}$  Pa s), buoyancy dominates upwelling and

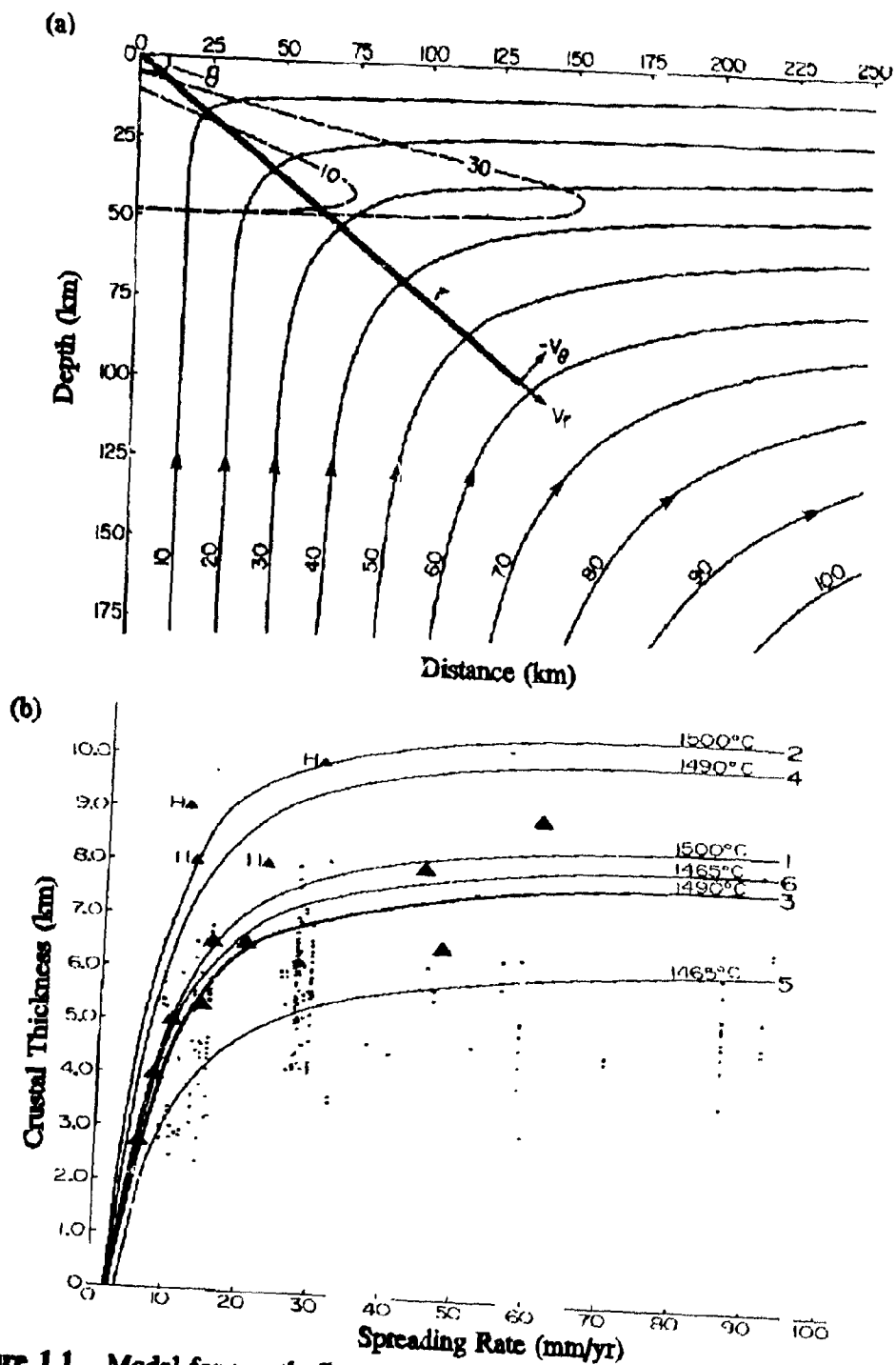


**Figure 1.1** Model for mantle flow in which circulation is driven by plate spreading: (a) Streamlines from Reid and Jackson [1981] and (b) Predicted relationship between crustal thickness and spreading rate [Reid and Jackson, 1981] for six combinations of mantle temperature and resident melt fraction to establish interconnected permeability (curves 1-6). Triangles are most reliable (post 1970's) observations from seismic refraction data.

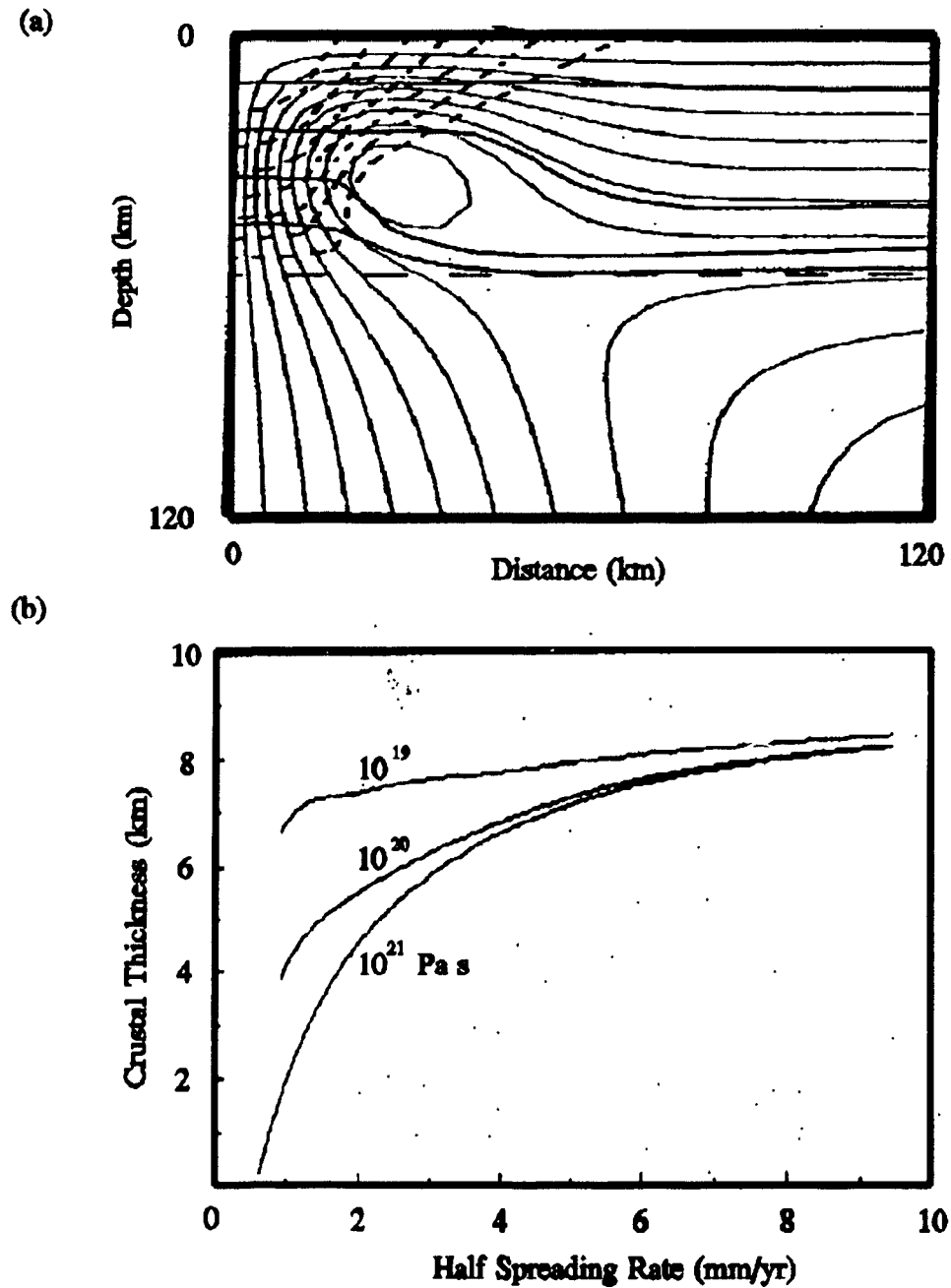


**Figure 1.2** Model for mantle flow in which circulation is dominated by localized buoyancy forces. (a) Streamlines (solid) and contours of 1% porosity (dashed lines) from Scott and Stevenson [1989] and (b) Predicted relationship between crustal thickness and spreading rate at different mantle viscosities [Sotin and Parmentier, 1990].

crustal thickness is nearly independent of spreading rate. In considering the role of the buoyant residual mantle, Scott and Stevenson [1989] predict that it becomes stably stratified under the newly formed plates (sub-horizontal streamlines beyond 80 km don't allow re-circulation, Figure 1.2a) thereby forcing upwelling to occur rapidly (faster than plate velocity) beneath the ridge axis with partial melting beginning at depths as great as 60 km.

The role of lateral melt migration remains unresolved in thermal models. It is generally agreed that melt is rapidly extracted from the mantle matrix [Ahern and Turcotte, 1979] since only a small melt fraction is required for interconnectedness of the melt [Daines and Richter, 1988]. However, a number of different views surround the ability of melt to move laterally from its source region to the accretionary axis. In modelling the melt production and melt migration at a ridge-transform intersection for a slow spreading centre, Phipps Morgan and Forsyth [1988] find a broad region of melting up to 100 km from the ridge axis and argue that a ridge suction force draws melt through an as yet undefined plumbing system to the ridge axis. Specifically, they note that melt production is only slightly reduced away from the fracture zone into the cold lithosphere, whereas melt migration is significantly reduced leading to an explanation for the observed extent of crustal thinning across fracture zones [Louden *et al.*, 1986].

Similarly, for flow induced by plate spreading [Reid and Jackson, 1981], a broad region of upwelling underlies mid-ocean ridges (out to 100 km). However, as a narrow neovolcanic zone (typically less than 5 km) is observed, partial melt must travel laterally to the accretionary axis. Spiegelman and MacKenzie [1987] propose that the extraction

of small melt fractions from a wide region and focusing of melt to the ridge axis arises from pressure gradients generated by corner flow of the mantle matrix when viscosities are sufficiently high ( $10^{21}$  Pa s). Sparks and Parmentier [1991] present a thermal model in which melts ascend vertically until it reaches the base of the newly formed lithosphere where it is able to migrate laterally to the ridge axis through a high permeability layer, driven by its along-layer component of gravity. The lithosphere, in this model, is treated as an impermeable layer underlain by a thin (200 m - 300 m) layer with a high permeability which arises from decompaction stresses in the narrow freezing region.

Scott and Stevenson [1989] argue that the non-hydrostatic forces introduced by plate spreading are inadequate for driving lateral melt migration. Consequently, the source region is restricted to a narrow zone directly underlying the ridge axis, as predicted in their buoyancy dominated models of mantle circulation. Further, their flow models complement petrological models, based on ophiolite studies, in which melt must be equilibrated at high pressures [Elthon *et al.*, 1982] and gravity models in which mid-ocean ridges are underlain by deep low density root zones [Hall *et al.*, 1986, Jonas *et al.*, 1991].

## 1.2 Extinct Mid-Ocean Spreading Centres

Failed rifting systems have been categorized by Batiza [1989] based on the length of their ridge segments and the offset between the inactive portion and its newly activated counterpart. The first category have small offsets (<50 km) and result from propagating/retreating rifts, migrating overlapping spreading centres, small non-overlapping offsets and deviations from axial linearity. The second category have offsets in the range 50 to 400 km and are related to the processes which form and destroy

microplates. The third category "extinct spreading centres" result from aborted spreading due to a change in the spreading geometry of lithospheric plates. They are large scale features separated by a ridge jump in excess of 400 km between the extinct spreading centre and the new locus of rifting [Batiza, 1989]. Coupling between the extinct spreading centre and the new rift may be weak or non-existent.

Extinct spreading centres are the least common type of failed rift. A number have been identified based on magnetic anomaly identifications and morphological expression [Mammerickx and Sandwell, 1986]. Those which have been identified include: the Mathematician Ridge [Klitgord and Mammerickx, 1982] and the Galapagos Ridge [Anderson and Sclater, 1972] in the Pacific Ocean; the Aegir Ridge in the Norwegian-Greenland Sea [Talwani and Eldholm, 1977]; the Central Basin Fault [Lewis and Hayes, 1980] and Shikoku Ridge in the Phillipine Sea [Tomoda *et al.*, 1975]; and ridges in the Tasman Sea [Weissel and Hays, 1977], Coral Sea [Weissel and Watts, 1979], and Labrador Sea [Srivastava *et al.*, 1981].

As detailed in section 1.3, studying the crustal structure of an extinct spreading centre provides unique opportunities to comment on the processes of crustal accretion which are ongoing at active spreading centres. Prior to the research detailed in this thesis (and preliminary results in [Osler and Loudon, 1992]), the only published refraction profiles in the vicinity of an extinct spreading centre were in the Shikoku basin in the Phillipine Sea [Nagumo *et al.*, 1980]. However, this is in an area with a complicated and ambiguous spreading history [Chamot-Rooke *et al.*, 1987] and the data only sampled the upper crust. Recently, there have been seismic refraction lines shot across the extinct

Aegir Ridge in the Norwegian-Greenland Sea, however, no results are yet available from this experiment [R.B. Whitmarsh, personal communication, 1992].

### **1.3 Thesis Objectives**

A study of the crustal structure at an extinct spreading centre provides an opportunity to comment on the different views of the processes which dominate crustal accretion (as reviewed in section 1.1) as the extinct spreading centre represents a frozen accretionary axis, free of the spatial complications of fracture zones and their effects on melt migration. In addition, for ridges which have been inactive for more than 40 - 60 Ma, the thermal effects associated with active spreading should have largely dissipated. Consequently, the uncertainties associated with the interpretation of a seismically defined crustal thickness and seismic velocity at active spreading centres will not influence this study. The observed crustal structure may reveal whether mantle upwelling at slow spreading rates is primarily governed by buoyant upwelling (uniform crustal thickness) or plate spreading (crustal thinning). Further, refraction measurements of the crust and upper mantle coupled with gravity modelling based on these seismic structures may reveal the extent of the source region which once supplied melt to the accretionary axis; in particular, whether mid-ocean ridges are underlain by low density gabbroic root zones which extend to significant depths in the mantle.

## 2. Field Experiment and Data Reduction

### 2.1 Seafloor Spreading History of the Labrador Sea

The Labrador Sea is a small ocean basin confined between the coasts of Labrador and Baffin Island to the west and Greenland to the east (Fig. 2.1). The presence of a buried extinct ridge in the Labrador Sea was first suggested by Drake *et al.* [1963] based on seismic reflection profiles, although at that time, the oceanic affinity of the crust in the basin was unclear [Van der Linden, 1975]. Several authors contended that the Labrador Sea was underlain by foundered continental crust with little or no seafloor spreading [*e.g.* Kerr, 1967; Meyerhoff, 1973]. An increased number of seismic profiles confirmed the morphological extent of the buried ridge and the identification of magnetic anomalies established the crust as having formed by sea-floor spreading [Srivastava *et al.*, 1981]. The name "Ran Ridge" was proposed for this extinct mid-Labrador Sea ridge; however, use of this name has not persisted. Curiously, the name for the extinct ridge in the Norwegian-Greenland Sea "Aegir Ridge" (Aegir being the husband of the sea god Ran) has been widely adopted.

From the detailed analysis of the magnetic anomalies in the Labrador Sea, the following sea-floor spreading history of the Labrador Sea has been most recently documented by Roest and Srivastava [1989a]. After a period of continental stretching, spreading was initiated in the Labrador Sea south of the Cartwright fracture zone at chron 34 (84 Ma) and was established in the northern Labrador Sea by chron 31 (69 Ma). Spreading continued in an east-northeast direction until chron 25 (59 Ma) when a major re-orientation of spreading occurred. This re-orientation to a more oblique spreading

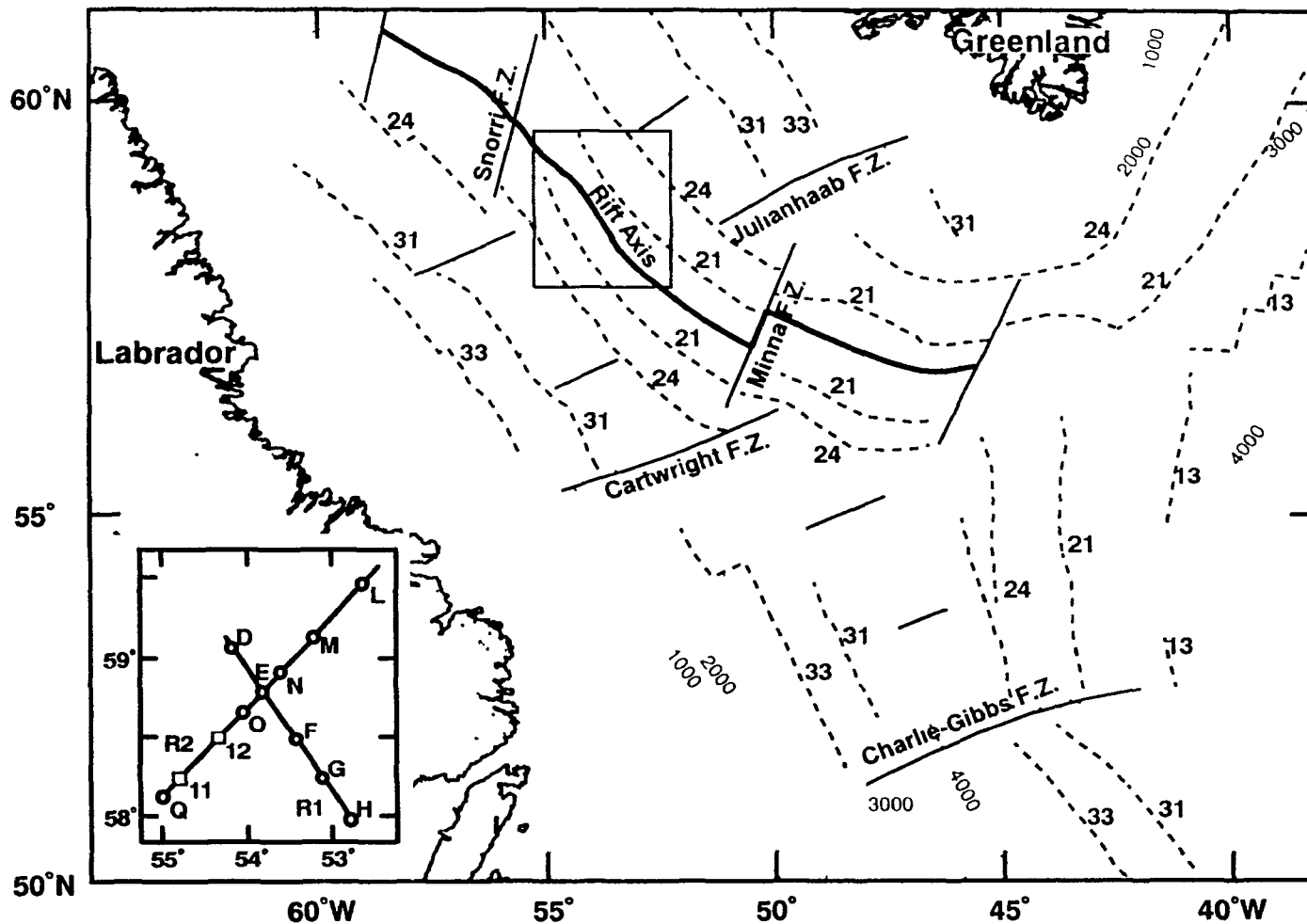


**Figure 2.1:** Location map for the seismic refraction experiment in the Labrador Sea. Inset shows the position of the OBSs (circles), sonobuoys (squares), and refraction shooting lines. Bathymetry contours (dotted) are displayed in metres. Selected magnetic anomaly lineations (dashed lines and corresponding chronological identifiers) and fracture zones are from Srivastava *et al.* [1988].

direction (north-northeast) was coincident with hot spot activity [Hyndman, 1973; Srivastava *et al.*, 1989] and the separation of Greenland from Eurasia initiating seafloor spreading on the Reykjanes Ridge, the northern extension of the present Mid Atlantic Ridge. The simultaneous seafloor spreading between North America and Greenland and Greenland and Eurasia between chron 24 (56 Ma) and chron 20 (45 Ma) formed the triple junction south of Greenland.

Spreading continued in the Labrador Sea until chron 20 (45 Ma) and was abandoned sometime before chron 13 (36 Ma) which is the first anomaly in the North Atlantic parallel to and continuous with the present mid-Atlantic ridge [Kristoffersen and Talwani, 1977]. The magnetic anomalies from chron 20 to chron 13 are not distinguishable in the Labrador Sea, hence they do not define whether spreading ceased instantaneously or gradually. In Chapter 6, synthetic magnetic anomaly patterns are generated for six potential spreading rate histories between chron 24 and the cessation of spreading. These are compared with the observed magnetic anomaly along ship tracks in the study area in an effort to constrain the spreading rate immediately preceding extinction.

## **2.2 Experimental Configuration and Procedure**

Two long refraction lines were shot at the extinct spreading centre in the Labrador Sea. Line R1 (Fig. 2.2), 150 km in length, was situated to sample crust along the strike of the extinct spreading centre. The position of the extinct spreading centre was inferred from a prominent low in the free-air gravity anomaly [Srivastava, 1986], the symmetry of the magnetic anomalies [Srivastava *et al.*, 1981], and an increased depth to basement

Seismic Refraction Experiment at the Extinct Spreading Centre in the Labrador Sea: Instrument and Shot Point Locations

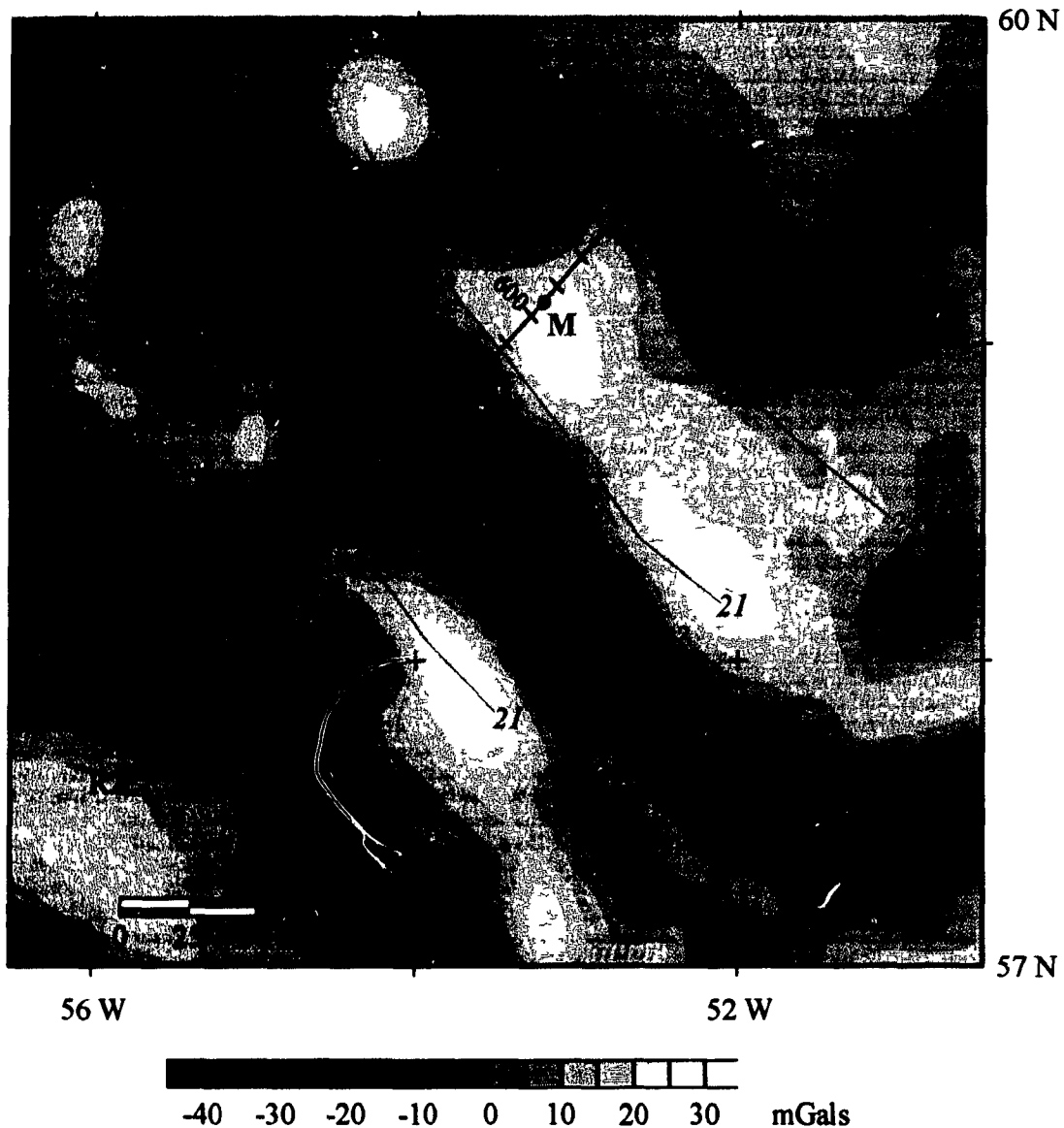


**Figure 2.2:** Shot point locations (dashes every 50th shot and numbers every 100) and receiver locations (OBSs - circles and sonobuoys - squares) for the seismic refraction experiment at the extinct spreading centre in the Labrador Sea. The gridded free-air gravity anomaly is a gray scale representation of Figure 5.1 where the free-air anomaly along track is also plotted. Identified magnetic lineations (following the interpretation of Roest and Srivastava [1989b]) and chronological identifiers (italicized numbers) are from Figure 6.1 where the magnetic anomalies on selected ship tracks in the vicinity of refraction lines R1 and R2 are also presented.

[Srivastava *et al.*, 1986; Oakey *et al.*, 1988] which is only determined by a sparse number of seismic reflection profiles and two additional profiles which we shot prior to the refraction lines.

Line R2 (Fig. 2.2), 220 km in length, was situated orthogonal to R1 and was designed to sample crust away from the area of the extinct spreading centre (out to chron 24) and to measure variations in crustal thickness as the extinct spreading centre is approached. The refraction line was oriented to follow the general direction of spreading following the major re-orientation at magnetic anomaly 25 [Srivastava, 1978]. A re-examination of the magnetic anomalies [Roest and Srivastava, 1989], subsequent to the collection of the refraction data, has altered the flow line of spreading direction by approximately 20°, closer to a north-northeast / south-southwest strike.

Both refraction lines were positioned to avoid known fractures zones in the area (Fig. 2.1), namely the Snorri Fracture Zone to the northwest and the Minna and Julianhaab fracture zones to the southeast [Srivastava *et al.*, 1988]. The determination of fracture zone locations in the Labrador Sea is guided chiefly by their signature in the free-air gravity anomaly where they appear as prominent low amplitude features which offset other anomalies. In positioning the refraction lines, these prominent features in the free-air gravity anomaly were avoided; however, the southwest end of line R2 is located in an area where a smaller offset feature is observed (see Fig. 5.1 and Chapter 5 for discussion of the gravity field). The potential that fracture zone features are influencing the seismically determined crustal structures along the refraction lines is thus considered minimal, but cannot be excluded.

Ocean Bottom Seismometers (OBSs) from Dalhousie University and the Atlantic Geoscience Centre at the Bedford Institute of Oceanography were deployed on the initial pass along a refraction line (locations in Fig. 2.2). The respective procedures for deploying and retrieving these instruments are detailed by Loncarevic [1983]. In brief, they are of the free-fall/pop-up variety, negatively buoyant when their anchors weights are attached and positively buoyant when released at a preset times programmed into their respective onboard computers. This imposes the logistical requirement that the ship return to the deployment location when the instrument is to be released. The OBSs are self contained with sensors, power supply, recording media, and recovery aids (an earlier version of the instrument is described by Heffler and Barrett [1979]). Data is recorded (DR) on an analog cassette tape and has a frequency response of roughly 5 to 20 Hz (Osler *et al.*, unpublished manuscript). The upper frequency limit is controlled by the tape transport speed and the lower frequency limit by the sensor response. The recording capacity is 28 days using four cascaded tapes and the dynamic range is estimated at 40 dB by an evolutionary spectral analysis (Osler *et al.*, unpublished manuscript).

Shooting occurred while the ship steamed at approximately 4 knots on the second pass along the refraction line. An array of 6 x 16.4 liter (6 x 1000 in<sup>3</sup>) air guns was used as the seismic source. The guns were detonated every 2 minutes yielding a trace separation of approximately 250 m (shot point locations in Fig. 2.2). While shooting the refraction lines, single channel reflection data were collected simultaneously using a 61 m (200 feet) hydrophone streamer. This signal was recorded on four track FM tape and plotted in real time on a chart recorder. Disposable sonobuoys were deployed between

OBS positions (Fig. 2.2). The radio signal transmitted back to ship from the sonobuoys was recorded on four channel FM tape and monitor records plotted on an X-Y pen plotter. The details of the timing and navigation in the data acquisition are discussed in section 2.4. All OBSs were successfully recovered on the third pass along the refraction line.

## **2.3 Processing of Seismic Data**

### *2.3.1 Reflection Profiles*

The single channel reflection data (Figures 2.3 and 2.4) were recorded on 4 track analog FM tape along with: 1) Dalhousie University format time code; 2) a trigger pulse denoting the instant of shot detonation and 3) radio telemetered sonobuoy data (when sonobuoys were deployed and within radio range). The data reduction process for the single channel reflection data is schematically presented in Figure 2.5a. The analog reflection data were digitized at 200 samples/sec at Dalhousie University using a PC based digitization system operating in a triggered mode. The direct arrival from shot to receiver served as the trigger signal to initiate digitization rather than the recorded trigger pulse, as its low amplitude and brief pulse duration did not suit the electronic criteria required by the digitizing board. The use of the direct arrival rather than the trigger pulse introduces a time shift for each shot of  $72 \pm 5$  msec relative to actual time of shot detonation. The time shift is the travel time required for the direct arrival to travel from the air gun array to the hydrophone streamer. Its uncertainty is known because time code was digitized concurrent with the reflection data. Offsets in the time code between all shots digitized did not exceed two sample points, which is 10 msec at 200 Hz. Given this stability, the time shift is treated as a static quantity by which all traces were delayed.



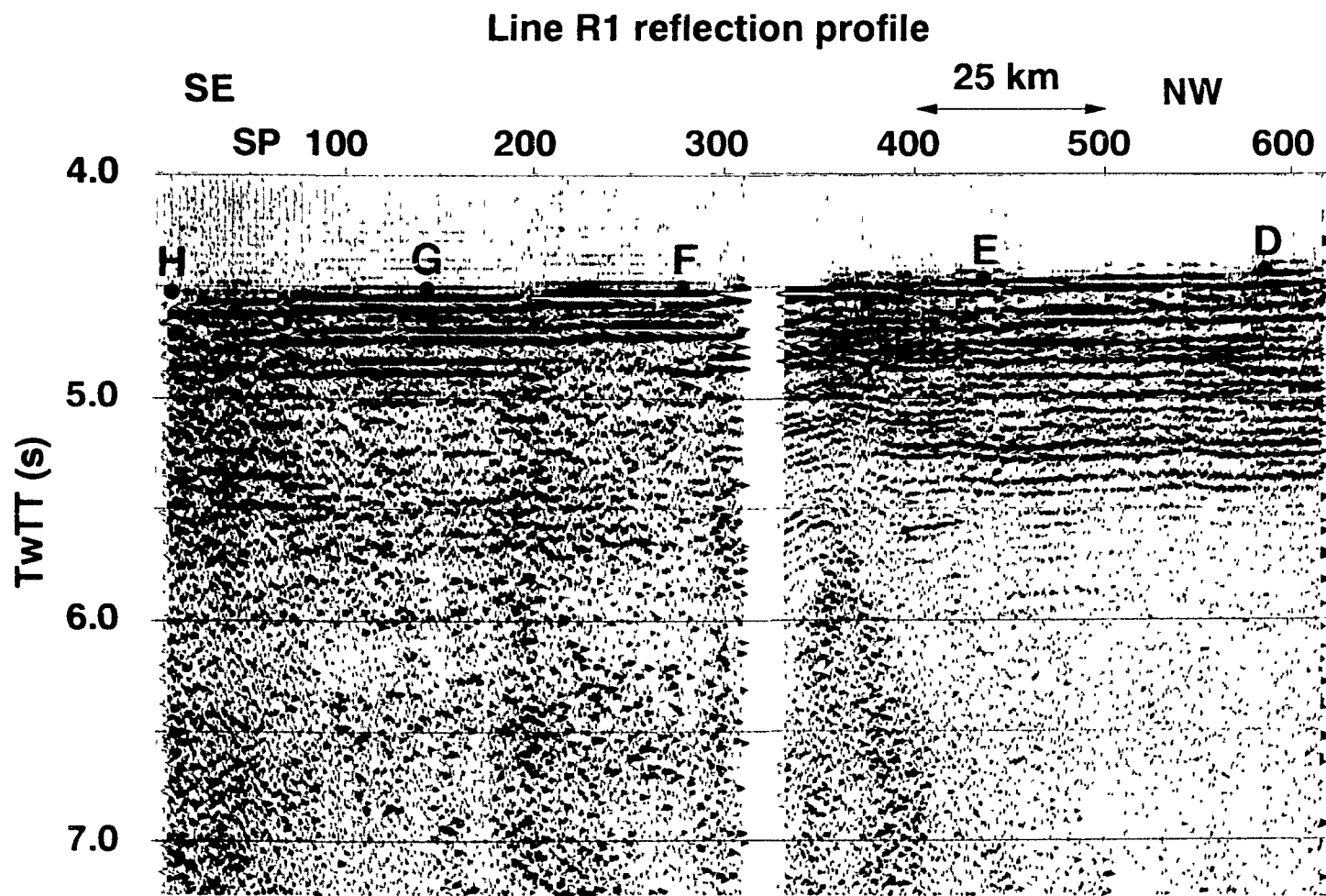
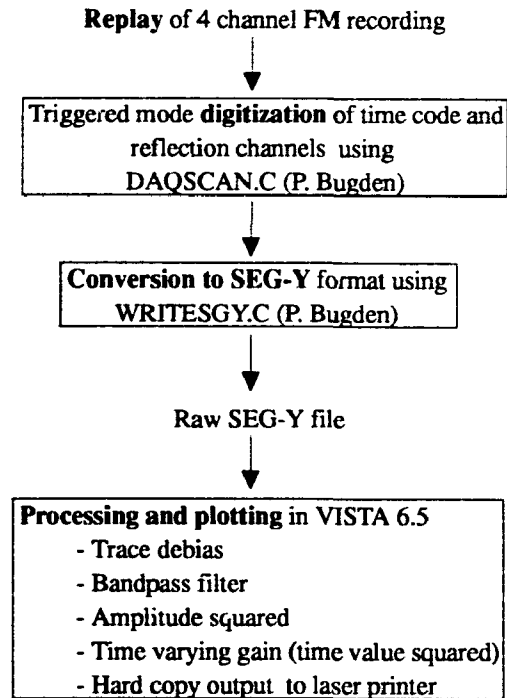


**Figure 2.4:** Line R1 reflection profile recorded while shooting the refraction data. The traces have been bandpass filtered from 6 to 36 Hz, amplitude squared to increase signal to noise and multiplied by a time varying gain function to compensate for energy loss due to spherical spreading. Dots mark the approximate locations of the OBSs. The location of the shot points (SP) is shown in Fig 2.2. Vertical exaggeration is approximately 30 1

(a) Single Channel Seismic Reflection Data Processing



(b) Sonobuoy Refraction Data Processing

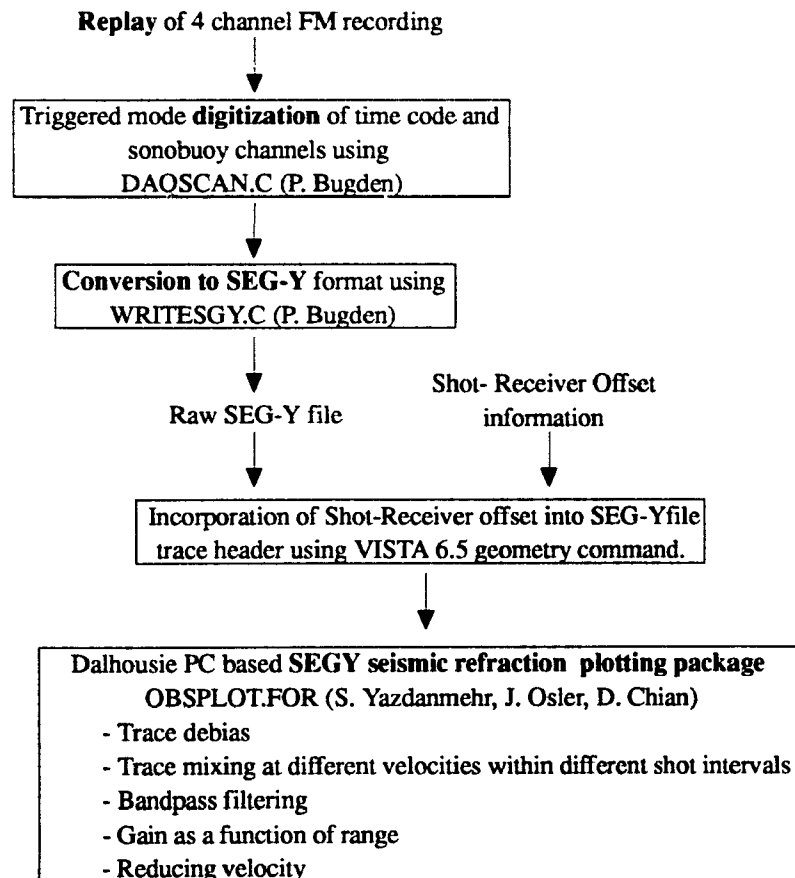


**Figure 2.5:** Processing stream and algorithms for reduction of (a) single channel seismic reflection data and (b) sonobuoy refraction data. Names of the primary authors of non-commercial software are parenthesized.

Following digitization of the analog data, the individual seismograms were converted into SEG-Y format for processing in VISTA 6.5, a PC based seismic reflection processing package. Processing steps in VISTA 6.5 were as follows: 1) Trace debias to remove drifting mean; 2) Bandpass filter from 6 to 36 Hz; 3) Amplitudes squared to increase signal to noise ratio; and 4) Multiplication by a time varying gain function (time value squared) to compensate for energy loss due to spherical spreading.

### *2.3.2 Sonobuoy Refraction Profiles*

As the sonobuoy data were recorded on the same 4 track analog FM tapes as the reflection data, the replay and digitization steps (Fig. 2.5b) were identical to those outlined for the seismic reflection data in Section 2.3.1. Once digitized, the individual traces were converted into SEG-Y format for processing. The GEOMETRY command in VISTA 6.5 was used to add shot-receiver offset information to all trace headers. Processing ensued in the PC based OBSPLOT.FOR as follows: 1) Trace debias; 2) Bandpass filtering and trace mixing with settings dependent upon the arrivals of interest; and 3) plotting with gain as a function of range and at reducing velocities appropriate for the arrivals of interest. The signal to noise ratios for crustal and deeper arrivals in the recorded data are low (*e.g.* Figs. A.6 and A.7). To supplement this data in the analysis, profiles plotted in real time for monitoring purposes during the refraction shooting were used in conjunction with the digitized data.

### *2.3.3 OBS Refraction Profiles*

The data reduction process for the seismic refraction data is considerably more involved. Initially, the steps may be divided into two streams (Fig. 2.6): processing of the

raw analog data to acquire an interpolated digital data file and the creation of a corresponding shot look up table containing all timing, navigation, and sediment corrections. These are brought together (Fig. 2.7) when refraction processing and plotting techniques in time-distance or  $\tau$ - $p$  space are subsequently pursued. Considering the data processing first (left panel, Fig. 2.6), the four channel OBS (hydrophone, vertical geophone, horizontal geophone, and time code) analog data was replayed at the Bedford Institute of Oceanography and digitized to a nominal frequency of 100 Hz. Second mark positions in the time code were then decoded and used to interpolate the data on a second by second basis to a fixed time base at 80 Hz. This adequately removes the effects of variable analog tape speed introduced during the recording or replay of the data.

The interpolated data for a given OBS is stored in a file which is a continuous stream of samples stored in binary format. Shot look up tables (right panel, Fig. 2.6) are constructed for each OBS. These tables indicate the position within the binary stream where the data for a given shot are to be found. Additionally, the tables contain: 1) shot times; 2) shot locations; 3) shot-receiver offsets and 4) timing corrections for each shot (see section 2.4.2). To prepare seismic refraction profiles, further treatment of the OBS data is accomplished through the use of TX\_OBSPLOT on the Dalhousie VAX 8800 mainframe or its PC-based SEG-Y equivalent OBSPLOT. The algorithm uses a workstation independent NCAR/GKS based graphics system for plotting seismic refraction data. The processing options selected vary upon the profile under consideration, but are drawn from the following options: 1) Trace debias; 2) Bandpass filtering; 3) Trace normalization; 4) Gain as a function of range; 5) Trace mixing at a specified reducing

## OBS Refraction Data: I - Processing

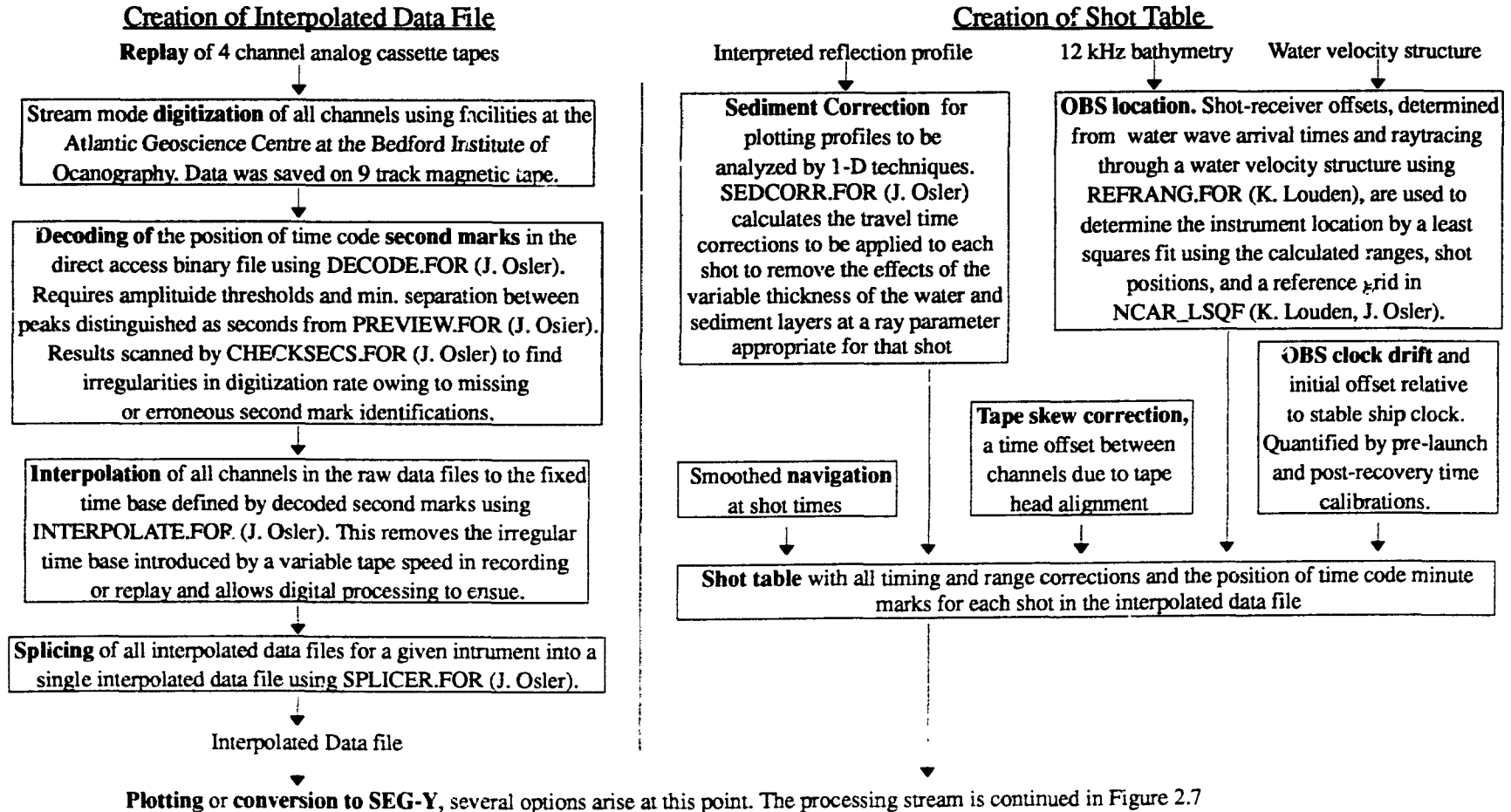


**Figure 2.6:** Processing stream and algorithms for reduction of seismic refraction data. Names of the primary authors of software are parenthesized.

## OBS Refraction Data: II - Plotting and 1-D Analysis

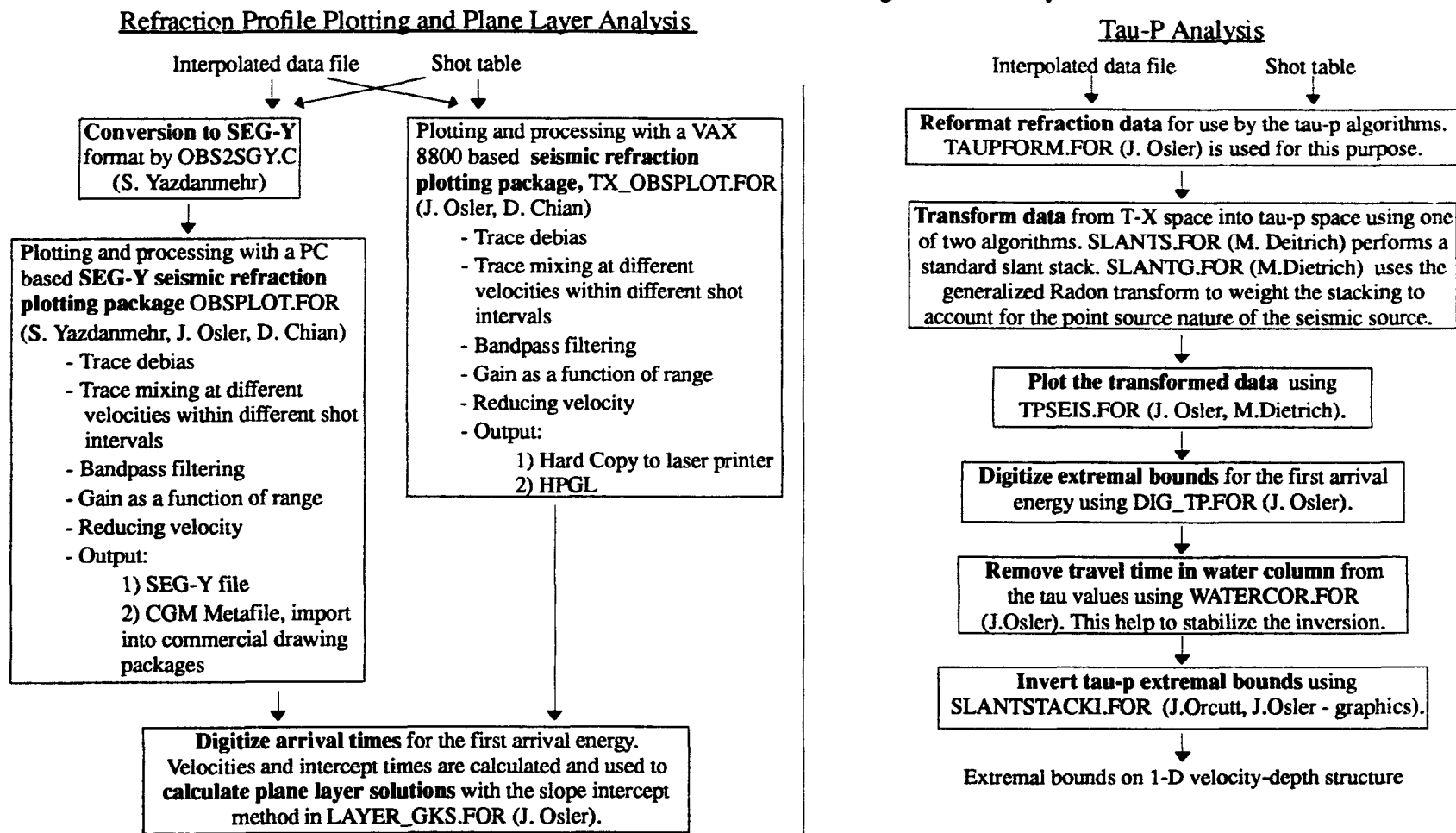


**Figure 2.7:** Processing stream and algorithms for plotting and 1-D analysis of seismic refraction data. Names of the primary authors of software are parenthesized.

velocity or coherency stacking within a range of reducing velocities; 6) Time code suppression.

## **2.4 Time and range corrections**

Crustal velocity structures determined from the interpretation of travel time versus shot-receiver range are highly dependent upon the time and range accuracy of the individual seismograms comprising the seismic refraction profile. As such, the application of time and range corrections received considerable attention and is detailed for the OBS and sonobuoy data in the following sections.

### *2.4.1 Sonobuoy data*

The position of the sonobuoy is not fixed; it is free to drift in response to wind or tidally generated currents. Determination of the shot-receiver offset for each trace requires that this drift be known for the period in which arrivals are being received. It can be quantified through an examination of the direct arrival from the shot to the sonobuoy. As an example, in Figure 2.8a, the travel time for the direct arrival is plotted as a function of range to a fixed assumed position for sonobuoy #11. The travel times have been plotted at a reducing velocity of 1.465 km/s, appropriate for surface waters in the Labrador Sea (Fig. 2.10). Following the assumption that this water velocity will be constant given the limited range (~40 km) and period in which arrivals are received at this sonobuoy (~4 hours), any deviations from a reduced travel time of 0 seconds are attributable to increases/decreases in travel time due to drift of the sonobuoy farther/closer from the shot location. The nature of the drift is such that it may be treated as a sinusoidal oscillation (Fig. 2.8a) whose removal through the appropriate adjustment of ranges leaves residual

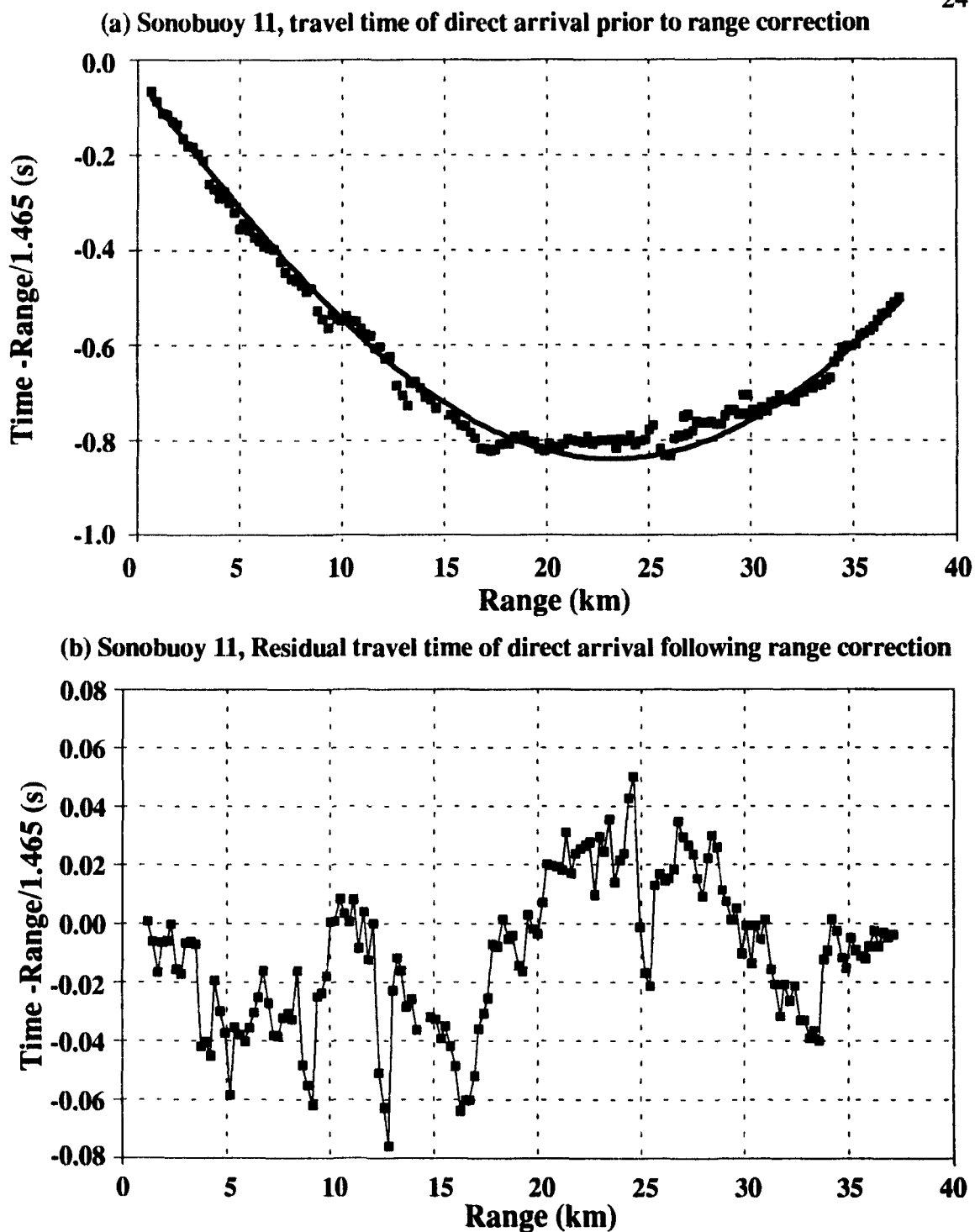


**Figure 2.8:** Travel time of the direct arrival for sonobuoy 11 plotted at a reducing velocity appropriate for surface waters in the Labrador Sea. (a) Travel time errors arise from the appreciable drift of the sonobuoy. To account for the drift, shot-receiver ranges are adjusted by removing the sinusoidal oscillation fit to the travel times. (b) Residual travel time following the range correction.

travel time variations of  $\pm 0.06$  seconds (Fig. 2.8b).

#### 2.4.2 OBS data

For the OBS data, corrections to the start time of each trace are required to account for: 1) an offset between OBS and ship clocks after synchronization; 2) drift in the OBS clocks during the experiment and 3) time offsets between analog data channels due to tape head alignment. The first of these corrections is constant for each OBS and obtained directly from the pre-launch time calibration. For the second correction, the difference in the offsets between the stable ship clock and an OBS clock at its pre-launch and post-recovery time calibrations is taken as the total amount of drift during the experiment. The drift correction is computed for each shot detonation time assuming a linear drift of the OBS clock between launch and recovery time calibrations. At the cold temperatures on the ocean floor, the OBS clocks are stable with deviations from the linear drift rate estimated at less than 10% in cold room experiments. During the 12 hour period in which arrivals are received for a 90 km long refraction profile (steaming at 4 knots), a 10% deviation in the highest drift rates (approximately 10 ms/hr, Table 2.1) could introduce a travel time error of 12 ms. This is equivalent to one sample point and not significant.

The last time correction arises from the skew between the magnetic tape and the recording head which introduces a time offset between channels. This timing error is the most significant and may be viewed as having a static and a dynamic component. The static component is the first order offset between channels (Table 2.1) which is quantified every 24 hours when identical signals are applied to all four channels on the tape. The

dynamic component is an irregular oscillation about the first order offset and can be as large as 1/4 of a seismic wavelength (approximately 37 ms for a dominant frequency of 6.8 Hz). No corrections are introduced to remove the dynamic component, though it is effectively removed by mixing of three or more traces in later processing.

Determining the shot-receiver offset for each trace requires the locations of the shot point and the OBS. Shot point locations were taken from the ship navigation data which was obtained using a combination of Loran C and transit satellite fixes. A running mean was applied along a six minute window of navigation data to smooth occasional jumps which occur at the time of Loran or satellite updates [following Reid, 1987]. To position each OBS (Table 2.2), the ranges for each first arrival water wave were first calculated by raytracing through the water velocity structure (Fig. 2.10). For the upper 528 m of the water column, the velocity of sound was computed with data from three XBT profiles obtained during the cruise (Fig. 2.9). For the remainder of the water column, velocities were obtained using tables relating velocity to temperature and depth in the Labrador Sea (area 4 in Matthews [1939]) at a constant salinity of 35 ppm and assuming a linear decrease in temperature from the 3.0°C observed at 528 m to a typical bottom water temperature of 1.7°C at 3300 m depth.

The ranges obtained by raytracing through the water velocity structure are then used to locate the most probable location for the instrument. This is accomplished by creating a reference grid and finding the grid location where there is a least squares minimum between (1) the ranges from the water wave arrival times to their respective shot points and (2) the ranges from a position on the reference grid to the shot points. As

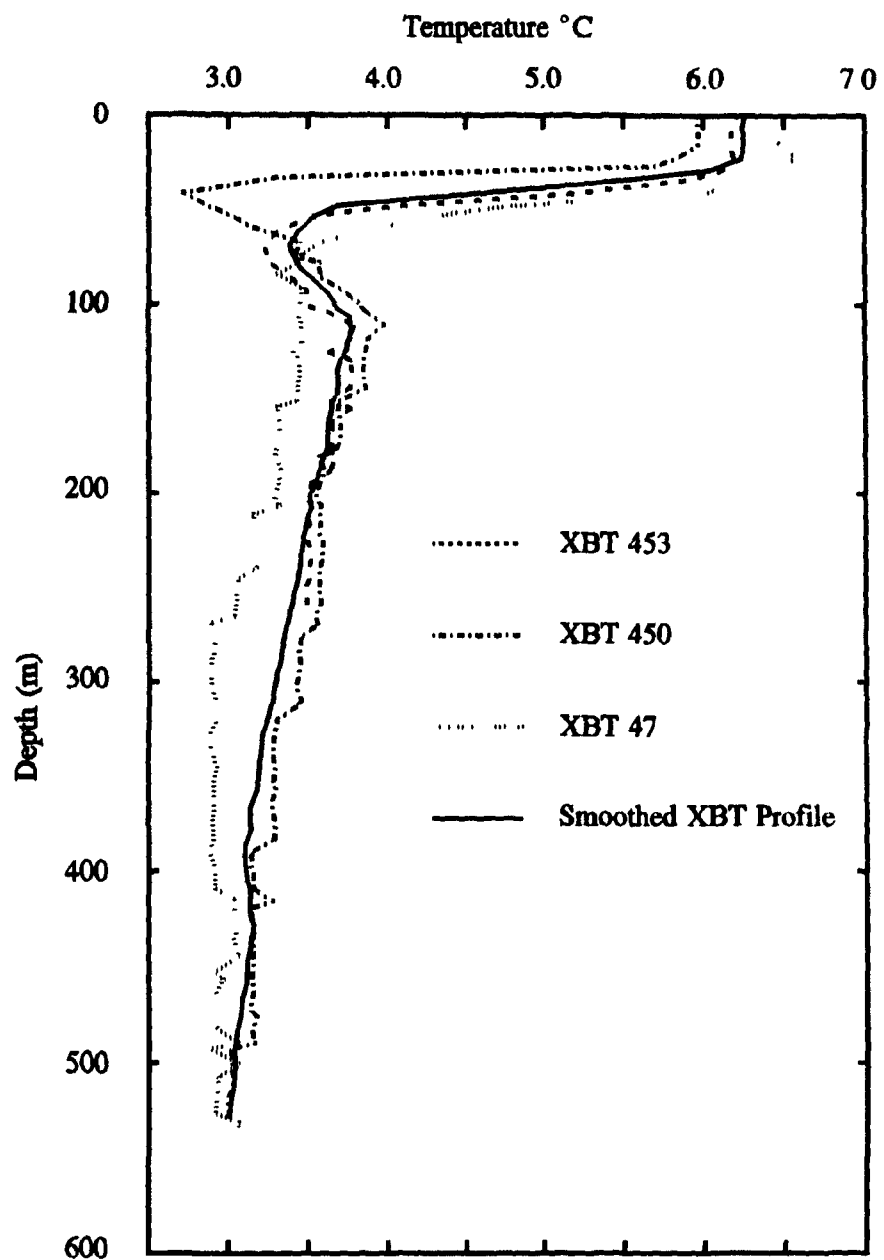


**Figure 2.9:** XBT temperature versus depth profiles for the upper 600 m of the water column in the Labrador Sea study area during the 1987 field season.

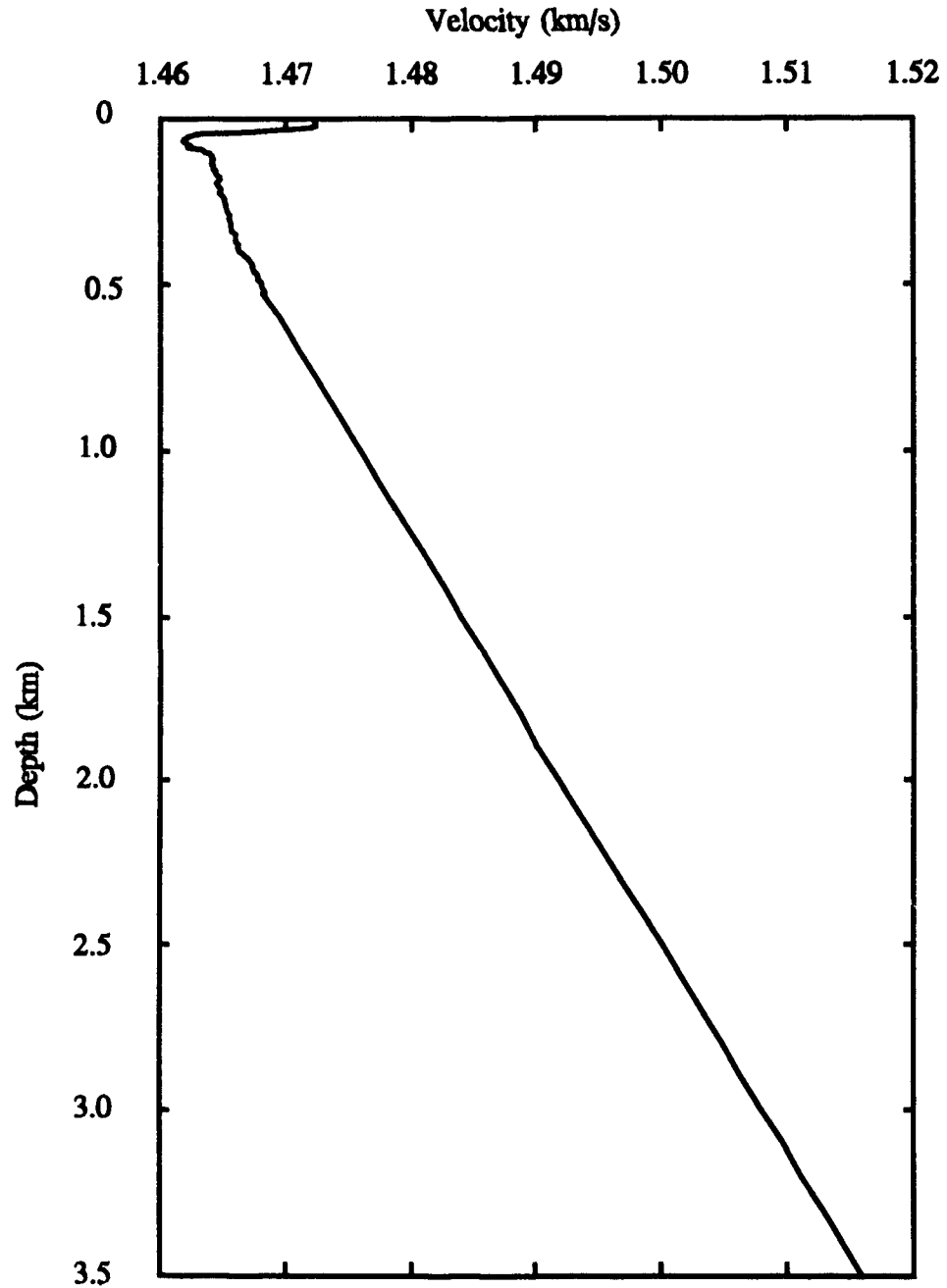


**Figure 2.10:** Velocity of sound in water for the Labrador Sea study area during the 1987 field season. Velocities for the upper 600 m of the water column are computed using the XBT data (Figure 2.9). Velocities for the remainder of the water column are computed from historical tables [Matthews, 1939] as discussed in the text.

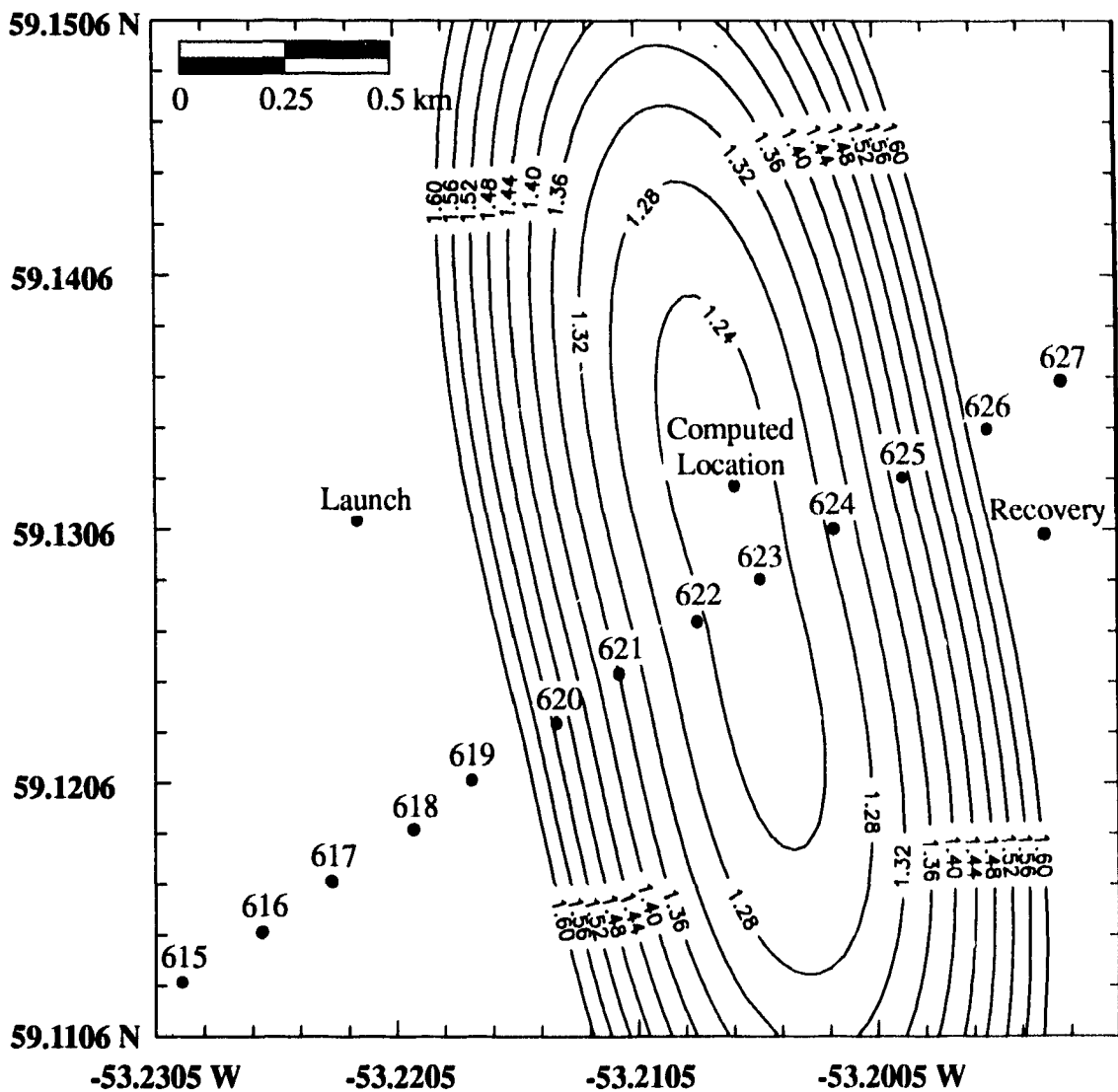


**Figure 2.11:** Determination of the position of OBS M. The least squares minimum (contours in km) between ranges calculated from water wave arrivals at each shot point and ranges between grid point locations and shot points is the most probable location of the instrument. The positions of the shot points, OBS launch and OBS recovery are marked by the annotated dots.

an example, in Figure 2.11 the positions of the shots, OBS launch, OBS recovery and contours of root mean square (in km) are presented for OBS M. As illustrated by the distortion of the contours, this methodology for locating the instrument has a higher resolution along the shooting line than across it. Further, it is the arrivals at shorter shot-receiver offsets which are most sensitive to the placement of an OBS off the line of shooting. As the shot-receiver offset increases, the angle between a line from the shot to the receiver and the actual shooting line decreases and eventually becomes insignificant.

For example, if an instrument were actually located 1 km off the line of shooting, but assumed to lie on the refraction line, the range errors incurred by this assumption would be 100 m at 5 km, 50 m at 10 km, 25 m at 20 km and so on. For crustal arrivals with a velocity of 5 km/s arriving between 5 and 10 km, the incorrect ranges would lead to the erroneous calculation of a velocity of 5.5 km/s. A similar calculation for mantle arrivals with a velocity of 8 km/s between 50 and 55 km leads to the calculation of a velocity of 7.99 km/s which would be indistinguishable from the actual velocity. In summary, the incorrect positioning of an instrument introduces a greater error for velocities calculated for the upper crust and sediment arrivals than for the deeper crustal and mantle arrivals.

**Table 2.1: OBS timing corrections**

Station	Timing Corrections						
	Tape Head Alignment Skew (ms) Relative to Channel 1				Time of OBS and Ship Clock Synchronization HH:MM/DAY/YR	Initial Offset (ms)	Drift rate (ms/hr)
	Chan 1	Chan 2	Chan 3	Chan 4			
R1-D	0	-13	-88	-125	16:30/202/1987	-58	-9.07
R1-E	0	-75	-125	-175	18:28/202/1987	+787	-3.94
R1-F	0	25	0	50	22:12/202/1987	-84	+0.03
R1-G	0	-63	-175	-238	22:34/202/1987	-5	-7.80
R1-H	0	-63	-163	-225	02:03/203/1987	-57	-10.42
R2-L	0	-88	-200	-300	18:46/208/1987	-53	-7.79
R2-M	0	-75	-213	-363	08:59/209/1987	-63	-9.98
R2-N	0	88	50	113	19:45/208/1987	+55	+0.36
R2-E	0	-100	-313	-438	18:28/202/1987	+787	-3.94
R2-O	0	-100	-188	-300	15:56/209/1987	-1	-9.32
R2-P					18:10/209/1987	-116	-1.57
R2-Q	0	-13	-75	-100	19:30/209/1987	-16	-8.03

**Table 2.2: OBS locations and depth**

Station	Position				Depth		
	Launch	Recovery	Computed	RMS min.(km)	Fathoms	TWTT (s)	km
R1-D	59.0698°N 54.1717°W	59.0647°N 54.1611°W	59.0678°N 54.1672°W	0.943	1808.8	4.522	3.3598
R1-E	58.7943°N 53.8305°W	58.7918°N 53.8141°W	58.7904°N 53.8116°W	0.717	1821.8	4.5545	3.3840
R1-F	58.4893°N 53.4129°W	58.4910°N 53.4285°W	58.4898°N 53.4169°W	0.718	1841.3	4.6033	3.4202
R1-G	58.2310°N 53.0864°W	58.2286°N 53.0955°W	58.2365°N 53.0964°W	0.915	1848.2	4.6205	3.433
R1-H	57.9685°N 52.7694°W	57.9752°N 52.7735°W	57.9756°N 52.7859°W	0.164	1861	4.6525	3.4568
R2-L	59.4660°N 52.6282°W	59.4580°N 52.6475°W	59.4625°N 52.6352°W	1.764	1836	4.590	3.4104
R2-M	59.1311°N 53.2223°W	59.1304°N 53.1935°W	59.1324°N 53.2065°W	1.405	1802.5	4.5063	3.3481
R2-N	58.9155°N 53.6105°W	58.9195°N 53.6075°W	58.9120°N 53.5960°W	1.581	1815	4.5375	3.3714
R2-E	58.7948°N 53.8073°W	58.7918°N 53.8141°W	58.7864°N 53.8111°W	1.383	1821.9	4.5548	3.3842
R2-O	58.6662°N 54.0415°W	58.6641°N 54.0420°W	58.6612°N 54.0335°W	1.603	1819.9	4.5498	3.3805
R2-P	58.3996°N 54.5080°W	58.4019°N 54.5216°W	see note (1)		1820	4.55	3.3807
R2-Q	58.1265°N 54.9800°W	58.1261°N 54.9803°W	see note (2)		1788.8	4.472	3.3227

- (1) OBS has poor amplitude response and severe crosstalk, data unusable.
- (2) The lack of shot points to the southwest of the OBS gave rise to unstable results in the least squares fitting process. As the launch and recovery positions are very close to each other, the launch position was taken as the position of the OBS.

### **3. One Dimensional Velocity Analysis**

One dimensional travel time solutions were developed for each OBS along refraction lines R1 and R2. These solutions assume that the gross structure of the extinct spreading centre may be treated as being piece-wise homogeneous. The 1-D solutions provide an overview of the structural variations between crust at the extinct spreading centre and crust in the basin which formed under typical spreading conditions. This comparison is pursued extensively in sections 3.3 and 3.4 by synthetic seismogram modelling of two OBSs which are representative of the distinct crustal types. Additionally, the 1-D solutions provide the initial crustal structure which is required in developing a 2-D structural model (Chapter 4).

#### **3.1 Sediment Correction Method**

Basement topography in the vicinity of the extinct spreading centre is appreciable (Figs. 2.3 and 2.4), necessitating the application of sediment travel time corrections to most OBSs before a 1-D analysis of deeper arrivals can be performed. An interpretation of single-channel reflection data collected during the refraction shooting along lines R1 and R2 is shown in Figure 3.1. Basement highs are well imaged while the basement low within the extinct spreading centre (Fig. 2.3, shot points 350-450) is difficult to discern. This is probably due to a weak impedance contrast between the higher velocity basal sediments and the low velocity upper crust observed within the extinct rift and not a lack of energy penetration.

The sediment travel time correction is an adaptation of the method employed by Whitmarsh [1975]. A schematic of the correction is presented in Figure 3.2. The travel

time correction accounts for the difference in travel time between the original path (refracted at the actual velocity interface) of a ray and the corrected path (forced to refract at the datum). Following the annotation in Figure 3.2, the travel time correction  $\Delta T_i$  at a given datum is:

$$\begin{aligned}\Delta T_i &= \frac{AD}{V_{i+1}} - \left( \frac{AB}{V_i} + \frac{BC}{V_{i+1}} + \frac{CD}{V_n} \right) \\ \Delta T_i &= \frac{\Delta H_i}{V_{i+1} \cos \theta_{i+1}} - \left( \frac{\Delta H_i}{V_i \cos \theta_i} + \frac{\Delta H_i (\tan \theta_{i+1} - \tan \theta_i)}{V_n} \right) \quad (\text{Eqn. 3.1}) \\ \Delta T_i &= \Delta H_i \left( \frac{\cos \theta_i}{V_i} - \frac{\cos \theta_{i+1}}{V_{i+1}} \right)\end{aligned}$$

The application of sediment travel time corrections is thus able to adjust the travel time of crustal and mantle arrivals to those which would have been recorded had all the shots, for a given OBS, been refracted at water bottom, sediment and upper crustal interfaces with uniform depths. The correction is computed at each of the four interfaces (shown in Figure 3.1) for each shot-receiver pair at an appropriate ray parameter ( $1/V_n$ ) based on the first arrival branch of the T-X plot. The corrections from the interfaces are summed to provide the cumulative travel time correction for each seismic trace. The datum levels were chosen differently for each OBS to minimize deviations from the datum  $\Delta H_i$  and reduce the magnitude of the travel time correction [Purdy, 1982].

The topography of two prominent internal sediment reflectors are employed in the sediment travel time correction. These reflectors can be related to those observed at ODP hole 646 [Arthur *et al.*, 1989], which allows velocity logs [Jarrard *et al.*, 1989] and the normal move out velocities of wide angle reflectors from a sonobuoy refraction profile

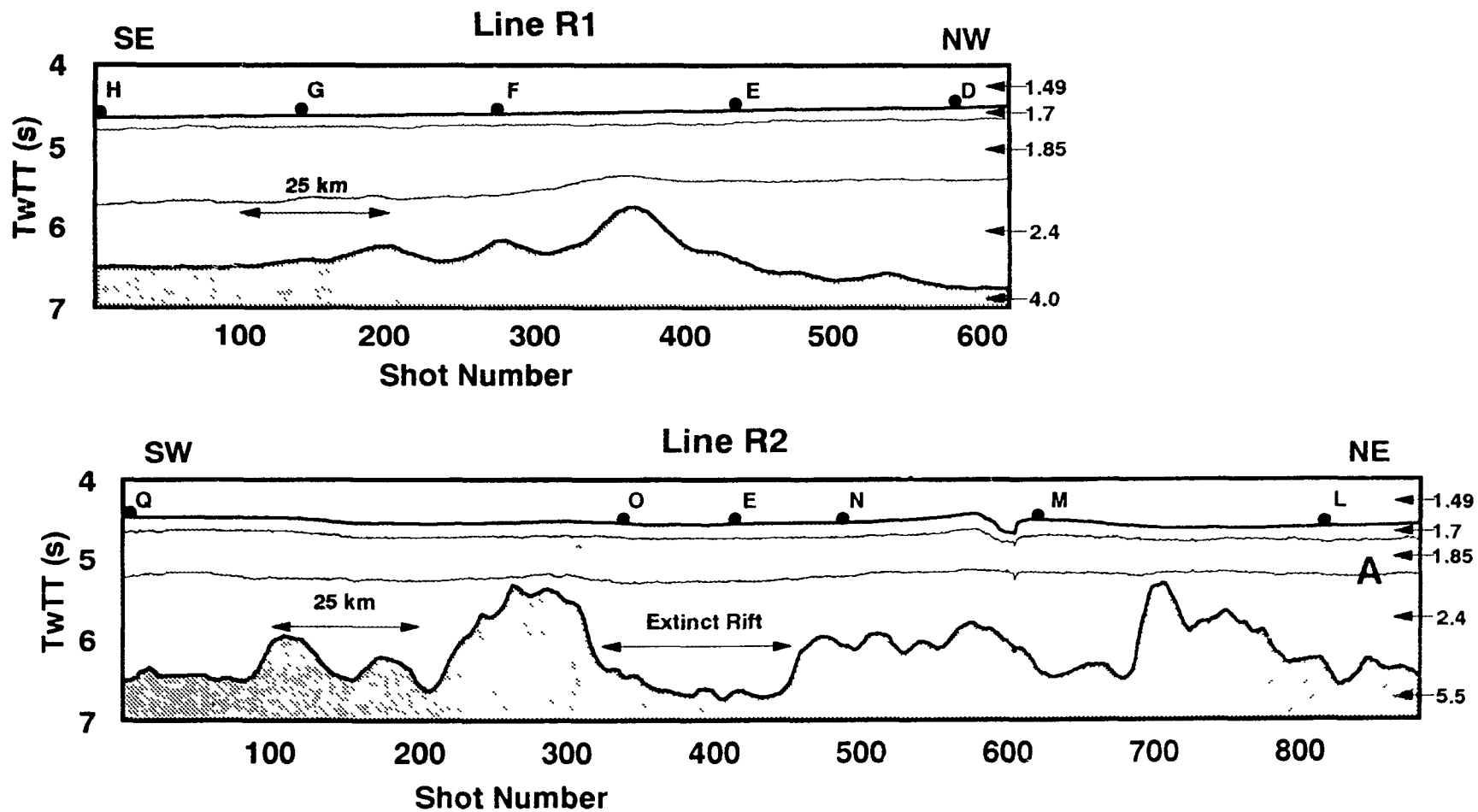


**Figure 3.1:** An interpretation of the reflection profiles along lines R1 and R2 (Figures 2.4 and 2.3 respectively). The water, sediment and crustal velocities are from a number of sources which are described in the text. The water layer has no shading, while the sediments are shaded light grey and the crust is shaded dark grey. Vertical exaggeration is approximately 10:1.

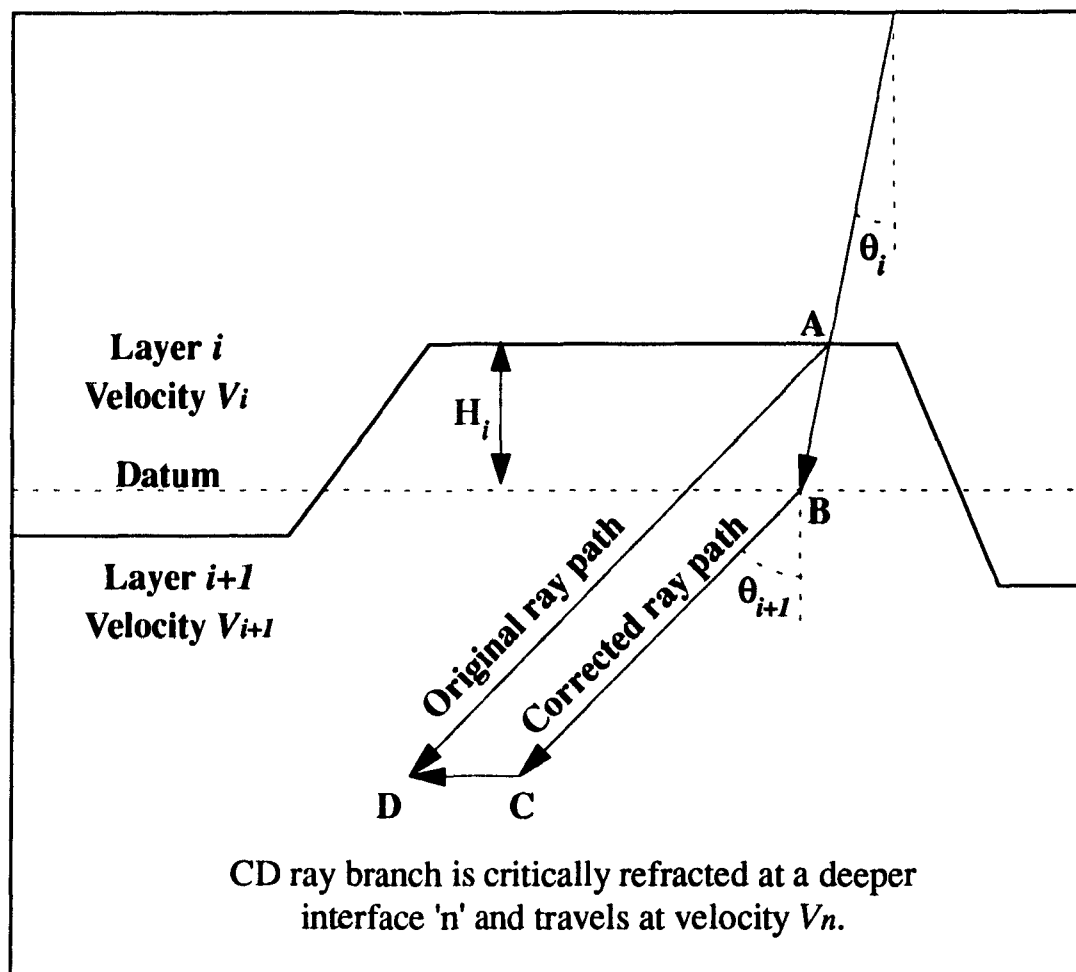


**Figure 3.2:** Schematic of sediment correction methodology (after Whitmarsh [1975]). The correction accounts for the travel time difference between the original ray path 'AD' and the corrected ray path 'AB+BC+CD' which forces the ray to refract at a datum.

### Refraction Profiles for OBSs L with and without Sediment Correction

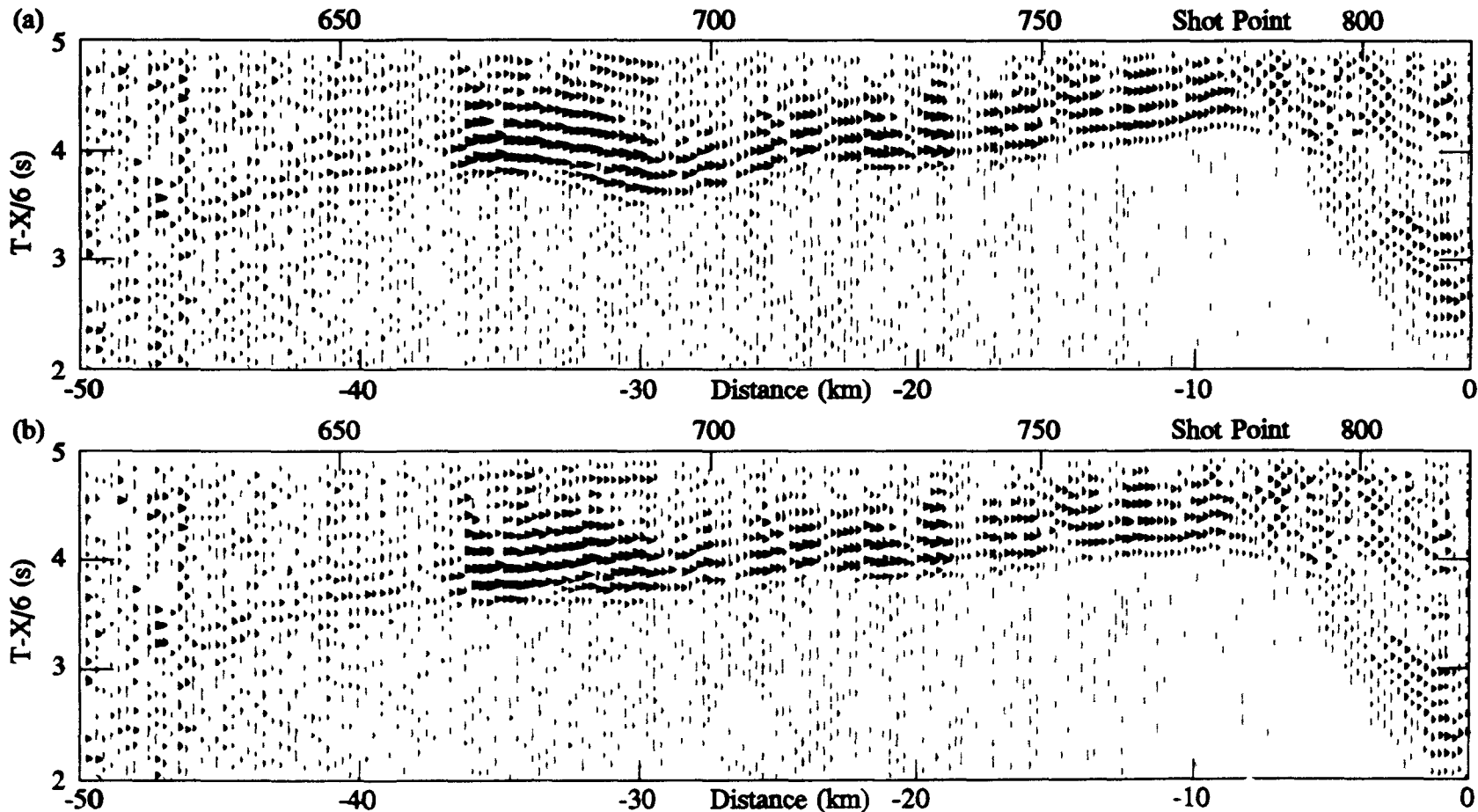


Figure 3.3: Refraction profiles for OBS L: (a) prior to the application of the sediment travel time correction and (b) following the application of the correction.

[Srivastava *et al.*, 1989] to be used in constraining the sediment velocity structure. In addition, a prominent sediment refractor (averaging 2.4 km/s) appears as a second arrival on all the refraction profiles. The upper crustal velocities used in the correction appear as first arrival branches in the refraction profiles, 5.5 km/s being an average for line R2 and 4.0 km/s an average for line R1.

To demonstrate the effectiveness of the correction method employed, two refraction profiles from OBS L are presented in Figure 3.3. In Figure 3.3a, the travel time of the mantle triplication point (~30 km range) is noticeably disturbed due to the prominent basement high in this area (Fig. 2.3, shot points 690-710). The application of sediment travel time corrections (Fig. 3.3b) has largely removed this unwanted travel time variation. The uncertainty in the corrected travel times is directly related to how well the sediment-crust boundary can be discerned in the reflection data as the travel time correction for topography on this boundary is an order of magnitude greater than the correction for any other boundary. For the reflection data, the uncertainty in the two way travel time picks is  $\pm 100$  msec for basement highs and  $\pm 250$  msec for basement lows. Corresponding uncertainties in the sediment travel time correction are  $\pm 26$  msec for basement highs and  $\pm 64$  msec for basement lows.

## **3.2 Travel time solutions**

### *3.2.1 Methods of Analysis*

Slope-intercept [Ewing, 1963] and  $\tau$ - $p$  extremal inversions [Garmany *et al.*, 1979; Orcutt, 1980] were pursued to determine end member p-wave velocity-depth structures for each OBS. The data reduction steps and associated algorithms for these methodologies

are summarized schematically in Figure 2.7. In the following paragraphs, their theoretical basis and relative advantages are briefly reviewed (following Kennett [1977]).

The slope-intercept method treats the velocity-depth structure as a stack of layers bounded by planar interfaces with the velocity in successive layers increasing. Each layer has a uniform velocity,  $v_j$ , and a thickness,  $h_j$ . For a ray traced through this structure, its ray parameter  $p = \sin(\theta_o/v_o)$ , where  $\theta_o$  is the inclination of the ray to the vertical at the source, remains constant along the ray in accordance with Snell's law (the ray parameter is also equal to the local slope of the travel time curve,  $p = dT/dX$ ). For a ray parameter  $p = 1/v_n$ , the ray refracted through the  $n$ th interface propagates parallel to the interface generating a head wave beyond the critical range where it is first refracted parallel to the interface. For the simplest case of the source and receiver both on the ocean surface, the travel time,  $T$ , of a head wave arrival at a range,  $X$ , is:

$$T = \frac{X}{v_n} + 2 \sum_{j=0}^{n-1} h_j (v_j^{-2} - v_n^{-2})^{1/2} \quad (\text{Eqn. 3.2})$$

which is a straight line with a slope  $1/v_n$ . The intercept of this straight line,  $\tau$ , on the time axis is:

$$\tau(v_n^{-1}) = T - \frac{X}{v_n} = 2 \sum_{j=0}^{n-1} h_j (v_j^{-2} - v_n^{-2})^{1/2} \quad (\text{Eqn. 3.3})$$

With estimates of the velocity of each refractor and its intercept time obtained by fitting straight line segments to the observed travel times, layer thicknesses,  $h_n$ , are calculated from the iterative relation:

Plane layer solutions were calculated for all OBSs by: 1) digitizing the first arrival

$$h_{n-1} = \frac{(\tau(v_n^{-1}) - 2 \sum_{j=0}^{n-2} h_j (v_j^{-2} - v_n^{-2})^{1/2})}{2(v_{n-1}^{-2} - v_n^{-2})^{1/2}} \quad (\text{Eqn. 3.4})$$

times in the sediment corrected refraction profiles; 2) partitioning these arrival times into neighbouring segments at points where changes in slope are observed; and 3) calculating the best fitting line of each segment in a least squares sense. The subjectivity and sensitivity of this method is described by Kennett [1976]:

"We see that these thickness estimates depend on those for shallower layers so the uncertainty in depth to an interface increases with its depth; whereas the velocities depend on a single slope determination... Unless there is a very distinct change in the nature of the arrivals the choice of cross-over points between successive straight lines is a somewhat subjective procedure. The assignment of travel time points to different lines will affect the slope and therefore the refractor velocity but particularly the intercepts and hence the thickness of the layers."

The  $\tau$ - $p$  method is a generalization of the slope-intercept method in which the velocity-depth structure is considered to have a continuous velocity stratification. First arrivals correspond to rays which have been continuously refracted through the velocity-depth structure. The intercept on the time axis,  $\tau(p)$ , is the intercept of a tangent to the travel time curve at a range,  $X$ , with slope  $p$ .

$$\tau(p) = T - pX \quad (\text{Eqn. 3.5})$$

Assuming that the velocity distribution,  $v(z)$ , is laterally homogeneous and a peice-wise continuous function of depth, the ray parameter remains constant along a ray path and is

related to  $\tau(p)$  by

$$\begin{aligned}\tau(p) &= 2 \int_0^{Z(p)} (v^{-2}(z) - p^2)^{1/2} dz \\ &= 2 \int_0^{Z(p)} (v^{-1}(z) \cos \theta(z)) dz\end{aligned}\tag{Eqn. 3.6}$$

where  $Z(p)$  is the depth at which the ray turns and  $\theta(z)$  is the local inclination of the ray to the vertical. The salient feature of Equation 3.6 is the direct relationship between  $\tau(p)$  and velocity-depth structure,  $v(z)$ . Solving for  $Z(p)$ ,

$$Z(p) = \frac{1}{\pi} \int_0^{\tau(p)} (q^2(\tau) - p^2)^{-1/2} d\tau\tag{Eqn. 3.7}$$

where  $q(\tau)$  is the inverse function to  $\tau(q)$ . From  $Z(p)$ , the velocity-depth structure may be constructed. In practice, upper and lower bounds are placed on  $\tau(p)$  and then iterative improvement is made to a trial velocity-depth structure until calculated  $\tau(p)$  values lie within error bounds for the observed  $\tau(p)$ , thereby producing extremal bounds on the velocity-depth structure. The  $\tau$ - $p$  methodology was used to develop velocity-depth structures for all OBSs by: 1) transforming the sediment corrected refraction data from T-X space to  $\tau$ - $p$  space (following Stoffa et al. [1981]); 2) digitizing upper and lower bounds on the first arrival times in the  $\tau$ - $p$  seismic profiles; and 3) using these bounds to calculate extremal velocity-depth structures.

The slope-intercept and  $\tau$ - $p$  approaches to obtaining velocity-depth travel time solutions are complementary. The  $\tau$ - $p$  methods, by their nature, deal appropriately with gradients in the velocity-depth structure. This is particularly important for crustal arrivals where the applicability of the slope-intercept method is tenuous. The slopes for these

refractors are not based on many first arrival picks and the partitioning of arrivals into distinct linear segments is ambiguous. In contrast, the slope-intercept method effectively treats arrivals which are refracted in layers with weaker velocity gradients, such as the mantle refraction. In the transformation into  $\tau$ - $p$  space, these refractors are mapped into a very small space (a single point if  $p=1/v_n$  is a constant, see Eqn. 3.5) making their subsequent inversion to a velocity-depth structure unreliable.

### 3.2.2 Results

Examples of the seismic refraction data from two OBSs used in this analysis are presented in T-X space (Figs. 3.4 and 3.5) and  $\tau$ - $p$  space (Figs. 3.6 and 3.7). These refraction profiles will also serve as archetypes in a first order comparison between the crustal structure within the extinct spreading centre and in the basin. Refraction profiles for all the instruments used in this study are presented in Appendices A and B. The velocity-depth structures resulting from the plane layer analysis are detailed in Tables 3.1 and 3.2 and depicted in Figures 3.8 and 3.9 along with the results from the  $\tau$ - $p$  analysis.

A comparison of the velocity-depth travel time solutions in Figures 3.8 and 3.9 shows general agreement between the slope-intercept and  $\tau$ - $p$  extremal inversion methods. Two notable discrepancies are: 1) the offset between the sediment-crust interface at OBSs O and N, which arise from difficulty in following the  $\tau$ - $p$  curve through the interval 0.4 to 0.25 sec/km where little energy is found (see relative amplitude curve in Figure 3.7); and 2) the offset between the position of the crust-mantle interface at OBS F, where the  $\tau$ - $p$  curve is of limited use as the energy from the mantle refractor is mapped into a narrow and noisy region and is difficult to define.

**Table 3.1:** Line R1, OBS plane layer solutions

Station		Layer					
		Sediment 1	Sediment 2	Sediment 3	Upper crust	Lower crust	Mantle
R1-D SE	Thickness (km)		0.69	1.13	1.82	2.37	
	Velocity (km/s)		1.85	2.60	3.56	5.76	8.01
R1-E SE	Thickness (km)	0.13	0.71	1.15	1.21	1.96	
	Velocity (km/s)	1.70	1.85	2.40	4.44	5.78	7.53
R1-E NW	Thickness (km)	0.13	0.71	1.04	1.89	0.74	
	Velocity (km/s)	1.70	1.85	2.40	3.99	6.29	7.25
R1-F SE	Thickness (km)	0.13	0.71	1.01	1.99	0.92	
	Velocity (km/s)	1.70	1.85	2.40	3.63	6.05	7.13
R1-F NW	Thickness (km)	0.13	0.71	0.89	3.08		
	Velocity (km/s)	1.70	1.85	2.4	4.48		7.71
R1-G SE	Thickness (km)		0.69	1.52	1.17	3.32	
	Velocity (km/s)		1.85	2.49	3.78	4.60	8.26
R1-G NW	Thickness (km)		0.69	1.59	2.80		
	Velocity (km/s)		1.85	2.40	4.00		7.95
R1-H NW	Thickness (km)		0.69	1.60	2.01	2.72	
	Velocity (km/s)		1.85	2.50	3.91	6.25	8.06
Extinct Spread- ing Centre Averag e	Thickness (km)				1.99	2.01	
	Velocity (km/s)				3.97	5.78	7.74

**Table 3.2:** Line R2, OBS plane layer solutions

Station		Layer					
		Sediment 1	Sediment 2	Sediment 3	Upper crust	Lower crust	Mantle
R2-L SW	Thickness (km)	0.13	0.42	1.39	1.38	4.35	
	Velocity (km/s)	1.70	1.85	2.40	5.13	7.03	8.03
R2-M NE	Thickness (km)	0.21	0.42	1.70	2.24	4.06	
	Velocity (km/s)	1.70	1.85	2.40	6.17	7.60	8.03
R2-M SW	Thickness (km)	0.21	0.42	1.48	1.88	4.21	
	Velocity (km/s)	1.70	1.85	2.40	5.33	6.91	8.05
R2-N NE	Thickness (km)	0.21	0.39	1.68	2.12	2.82	
	Velocity (km/s)	1.70	1.85	2.40	5.58	7.18	8.06
R2-N SW	Thickness (km)	0.15	0.44	1.85	2.54		
	Velocity (km/s)	1.70	1.85	2.4	5.85		7.87
R2-E NE	Thickness (km)	0.15	0.47	1.30	0.98	2.06	
	Velocity (km/s)	1.70	1.85	2.40	3.98	5.86	7.89
R2-E SW	Thickness (km)	0.15	0.47	1.30	0.71	3.06	
	Velocity (km/s)	1.70	1.85	2.40	4.30	6.07	7.93
R2-O NE	Thickness (km)	0.15	0.53	1.08	1.99	3.79	
	Velocity (km/s)	1.70	1.85	2.40	5.10	6.61	8.10
R2-O SW	Thickness (km)	0.15	0.53	1.17	0.85	3.85	
	Velocity (km/s)	1.70	1.85	2.40	5.15	6.65	7.98
R2-Q NE	Thickness (km)	0.15	0.51	1.62	2.02	2.14	
	Velocity (km/s)	1.7	1.85	2.40	5.74	6.94	7.73

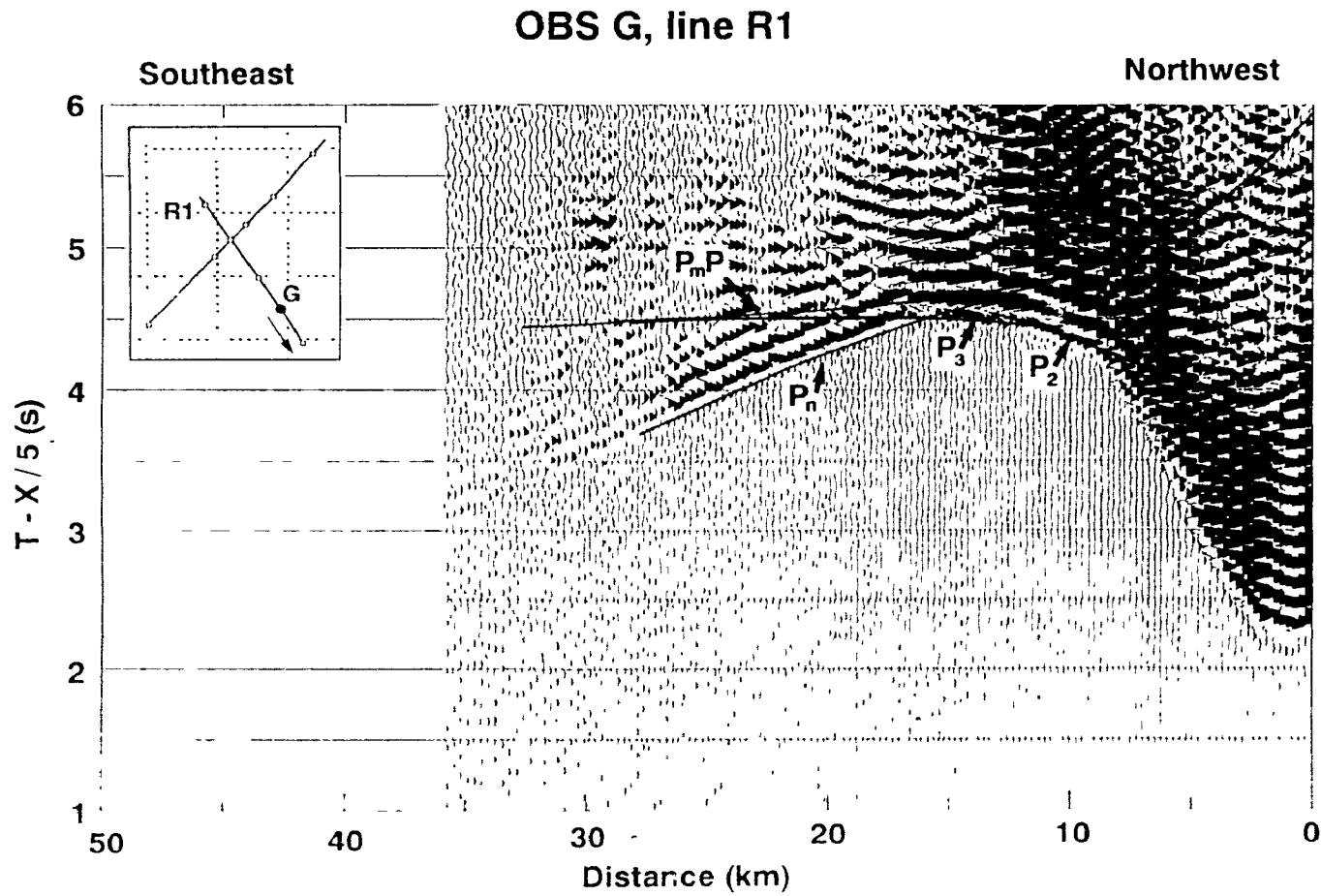


**Figure 3.4:** Seismic refraction profile for OBS G (shooting southeast) sampling crust within the extinct spreading centre along line R1. The instrument location is indicated in the inset. Traces are bandpass filtered from 4 to 12 Hz and multiplied by a gain which is a function of range ( $\text{Distance}^2/8$ ). Traces are plotted at a reducing velocity of 5 km s and peak amplitudes are clipped if their excursion exceeds 0.254 cm.

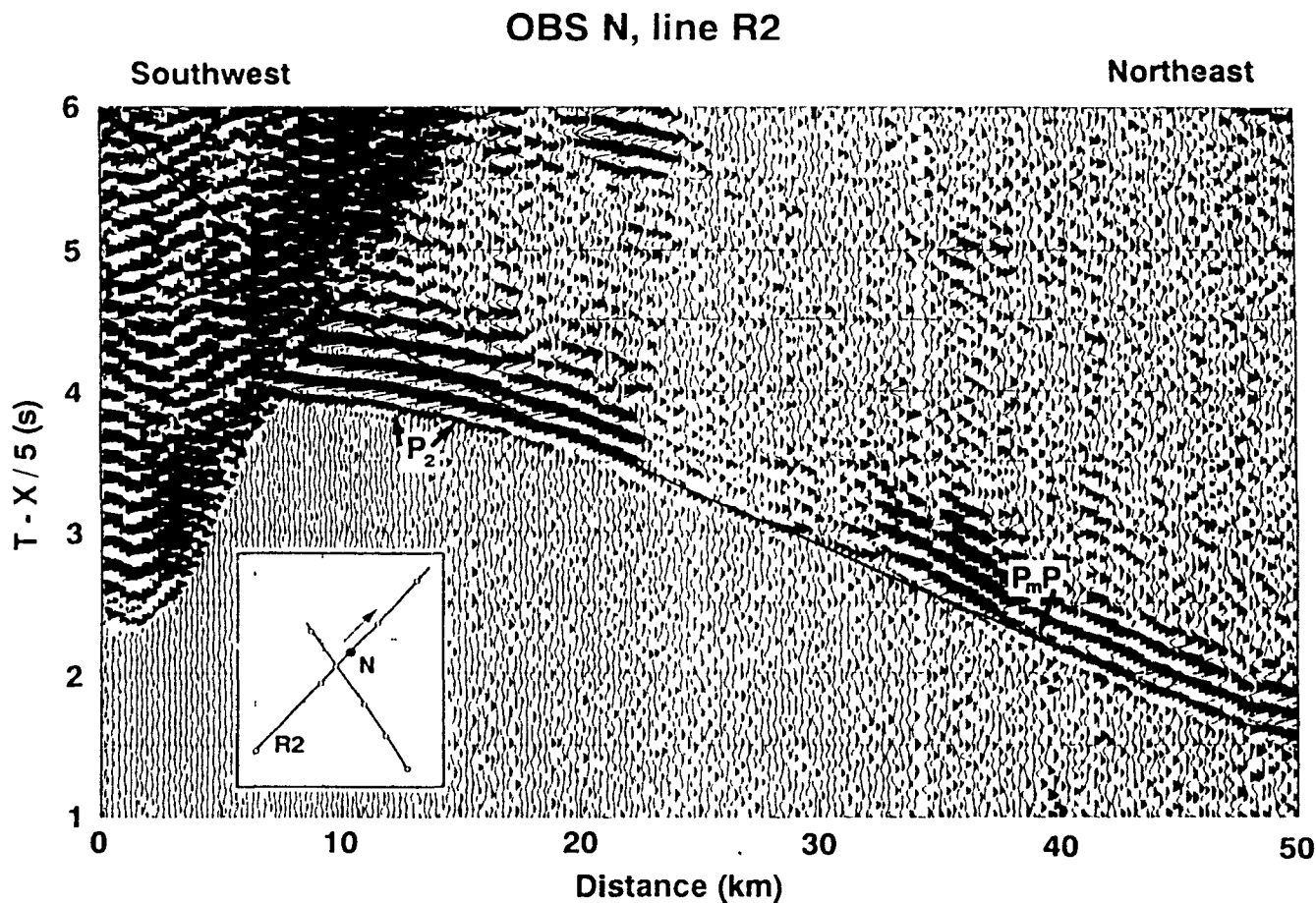


**Figure 3.5:** Seismic refraction profile for OBS N (shooting northeast) sampling crust in the Labrador Sea basin along line R2. The instrument location is indicated in the inset. The travel times have been sediment corrected (section 3.1). Traces are bandpass filtered from 4 to 12 Hz and multiplied by a gain which is a function of range ( $\text{Distance}/8$ ). Traces are plotted at a reducing velocity of 5 km/s and peak amplitudes are clipped if their excursion exceeds 0.254 cm.

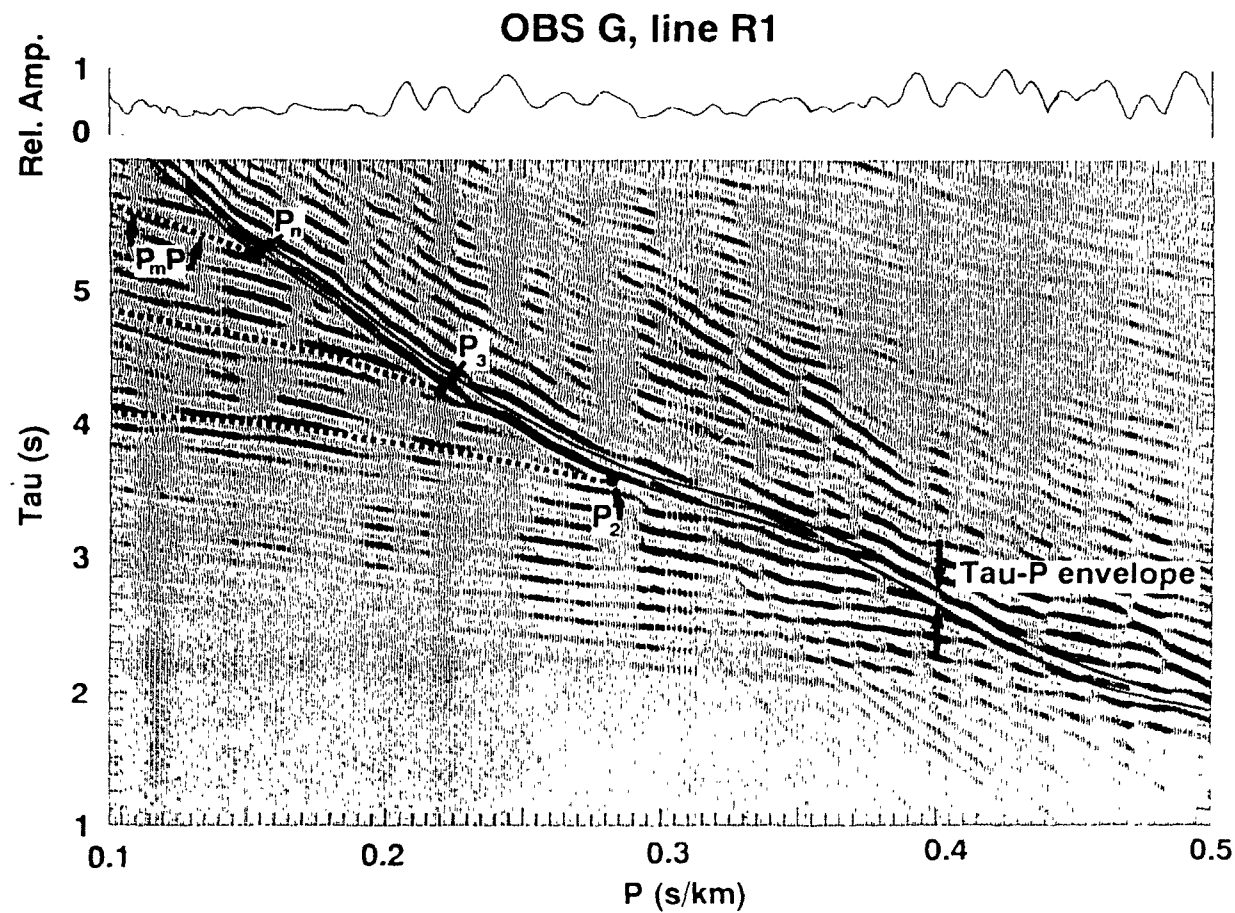


**Figure 3.6:** The seismic refraction profile for OBS G (Figure 3.4) after transformation into  $\tau$ - $p$  space. Traces have been normalized by their maximum amplitude, which is displayed above the data section at each ray parameter. The solid lines denote the envelope placed on the  $\tau$ - $p$  curve for the linearized inversion to velocity-depth. The dashed lines represent the location of pre-critical wide angle reflections which are terminated at their associated refractors (marked by dots).

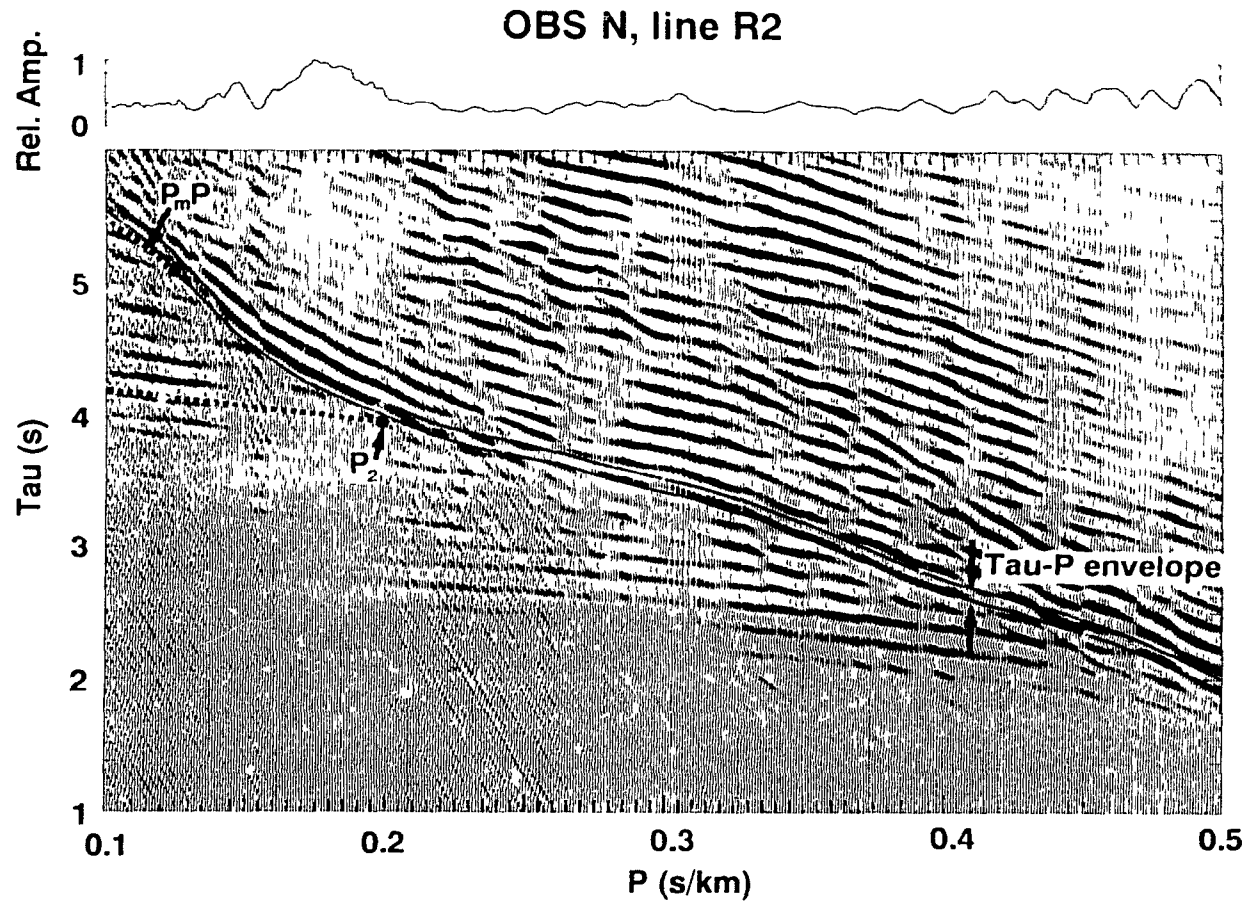


**Figure 3.7:** The seismic refraction profile for OBS N (Figure 3.5) after transformation into  $\tau$ - $p$  space. Traces have been normalized by their maximum amplitude, which is displayed above the data section at each ray parameter. The solid lines denote the envelope placed on the  $\tau$ - $p$  curve for the linearized inversion to velocity-depth. The dashed lines represent the location of pre-critical wide angle reflections which are terminated at their associated refractors (marked by dots).

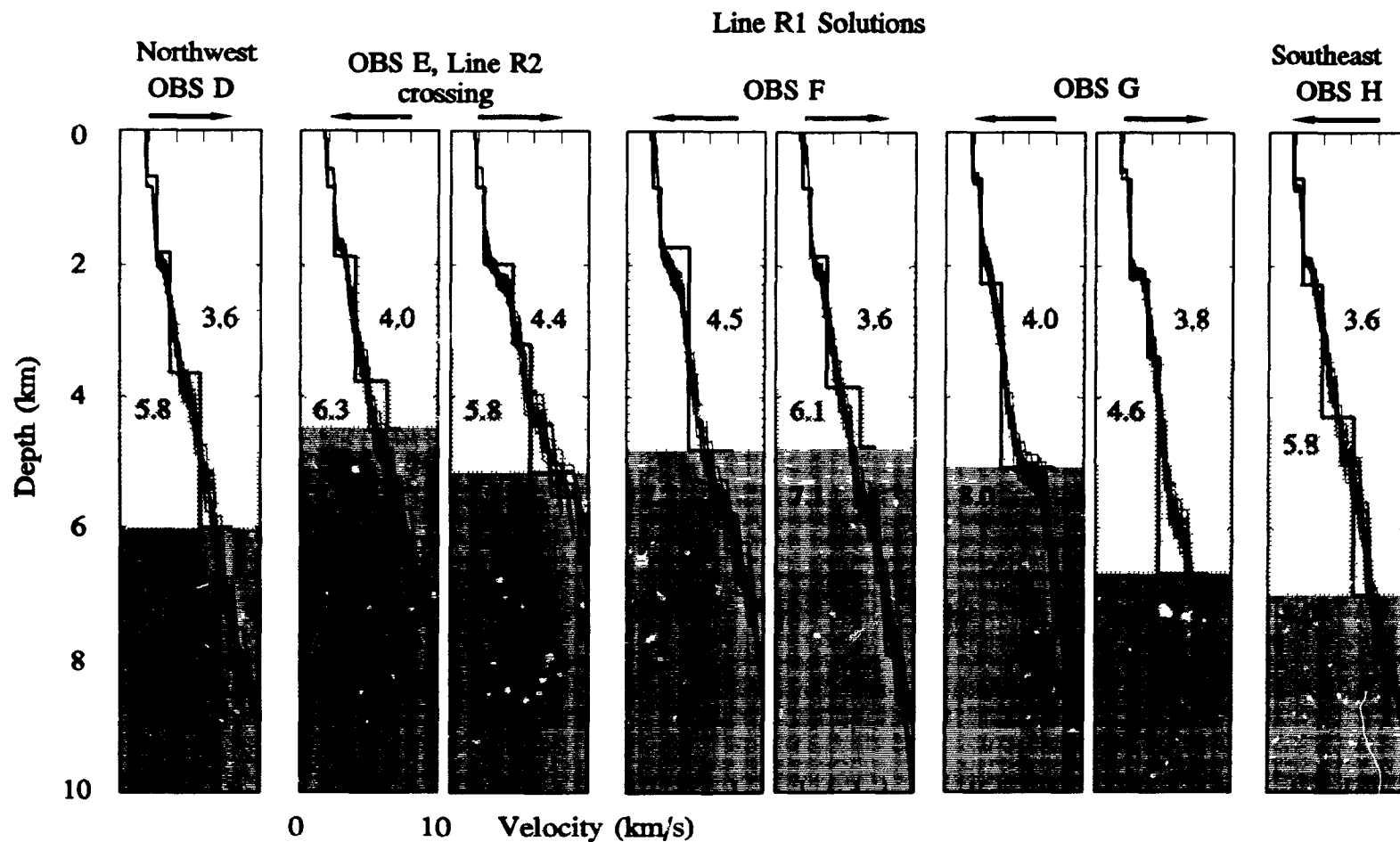


**Figure 3.8:** 1-D travel time solutions for line R1 along the axis of the extinct ridge. Solutions from the slope-intercept and tau-p inversions have been overlain for each OBS. Annotated velocities are those determined by the slope-intercept method. The upper crust is shaded light grey, the lower crust medium grey and the mantle dark grey based on the slope-intercept solutions.



The velocity-depth structures vary markedly from OBSs sampling crust within the extinct spreading centre to those sampling its flanks. For line R1 (Fig. 3.8), solutions for crustal structure along strike of the extinct spreading centre show exceptionally low upper crustal velocities (area shaded with light gray). The deeper crustal layer, shown shaded medium gray, exhibits the greatest degree of variability. It is present only at some of the OBSs where its thickness varies from less than 1 km (OBS F shooting southeast, OBS E shooting northwest) to 3.3 km (OBS G shooting southeast, OBS H shooting northwest) and low velocities ranging from 4.6 to 6.3 km/s are observed. The extremal bounds from the  $\tau$ - $p$  inversion emphasize the gradient nature of the crust within the extinct spreading centre. There is fairly little change in the velocity gradient, even as one enters into the mantle, shown shaded dark gray. Mantle velocities are also quite variable, ranging from extremes of 7.1 km/s to 8.3 km/s. Some of this variation can be explained by inadequacies of the 1-D methods employed; nonetheless, the mantle velocity in four of the seven refraction profiles is considerably lower than normal oceanic values away from active spreading centres [White *et al.*, 1984] and lower than those observed along line R2 for OBSs away from extinct spreading centre.

For line R2 (Fig. 3.9), the velocity-depth structures vary systematically in relation to the extinct spreading centre. OBSs L (shooting southwest), M, and N (shooting northeast) sample crust northeast of the extinct spreading centre. They exhibit more typical oceanic crustal structures; a high velocity gradient in layer 2 (light gray shading) and a low velocity gradient in layer 3 (medium gray shading). The thicknesses of layer 2 and layer 3 exhibit less variability; layer 2 varies between 1.4 and 2.2 km and layer 3

is 2.8 to 4.3 km thick. Typical velocities are observed for layer 2 (5.6 to 6.2 km/s) and for the mantle (8.0 to 8.1 km/s) while quite variable velocities are observed for layer 3 (6.9 to 7.6 km/s). Southwest of the extinct spreading centre, typical velocities are observed at OBS Q and O, 5.1 to 5.7 km/s for layer 2 and 6.6 to 6.9 km/s for layer 3. The crustal structure at OBS O is similar to that observed to the northeast of the extinct spreading centre, except for the high velocity lower crust. OBS Q exhibits some crustal thinning (1 to 2 km) relative to OBS O and a reduced mantle velocity.

### 3.3 Synthetic Seismograms

To define further the different velocity-depth structures found within and outside the extinct spreading centre, data at two OBSs, sampling crust representative of the different structures, were chosen for modelling by 1-D WKBJ synthetic seismograms [Chapman *et al.*, 1988]. The seismic profiles under consideration are OBS G (shooting southeast) and OBS N (shooting northeast) displayed in Figures 3.4 and 3.5 respectively. A qualitative examination of the record sections reveals profoundly different velocity structures. For OBS G, two low velocity first arrival branches ( $P_2$  and  $P_3$  in Figure 3.4) are followed by a mantle refractor ( $P_n$ ) at 18 km.  $P_n$  is strongly curved, with high amplitudes that decrease abruptly at 27 km indicating a velocity gradient in the uppermost mantle. For OBS N (Fig. 3.5), the first arrival branch ( $P_2$ ) emerges from the water-wave with a strong amplitude and curvature indicating a large velocity gradient in the upper crust. The amplitude of the upper crustal arrival decreases rapidly beyond 23 km. A high amplitude triplication from the mantle arrival dominates from ranges of 32 km and beyond.

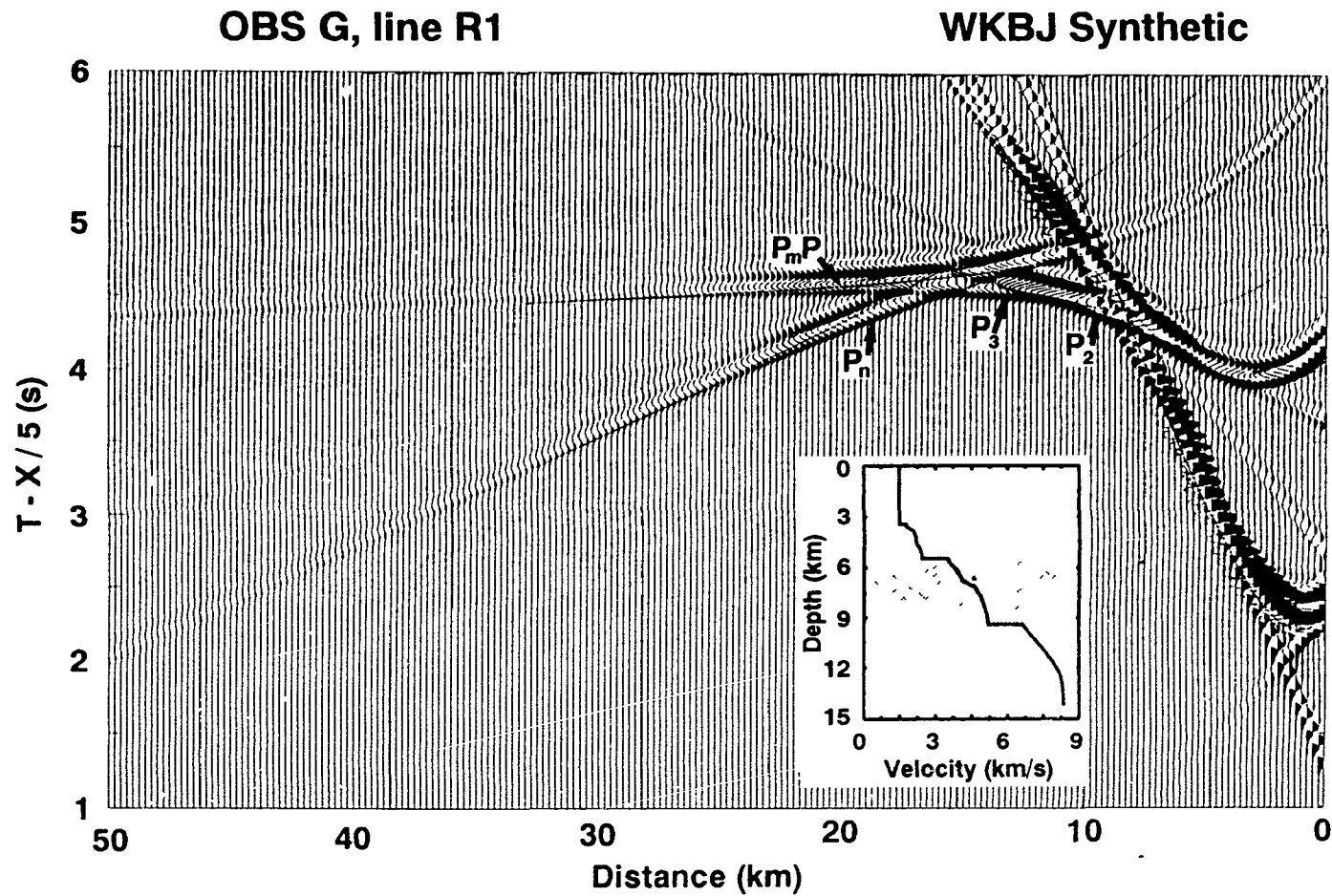


**Figure 3.10:** 1-D WKB synthetic computed for the OBS G refraction profile (Figure 3.4). The inset contains the corresponding velocity-depth structure which best models the data; the section of the curve representing crust has been shaded.

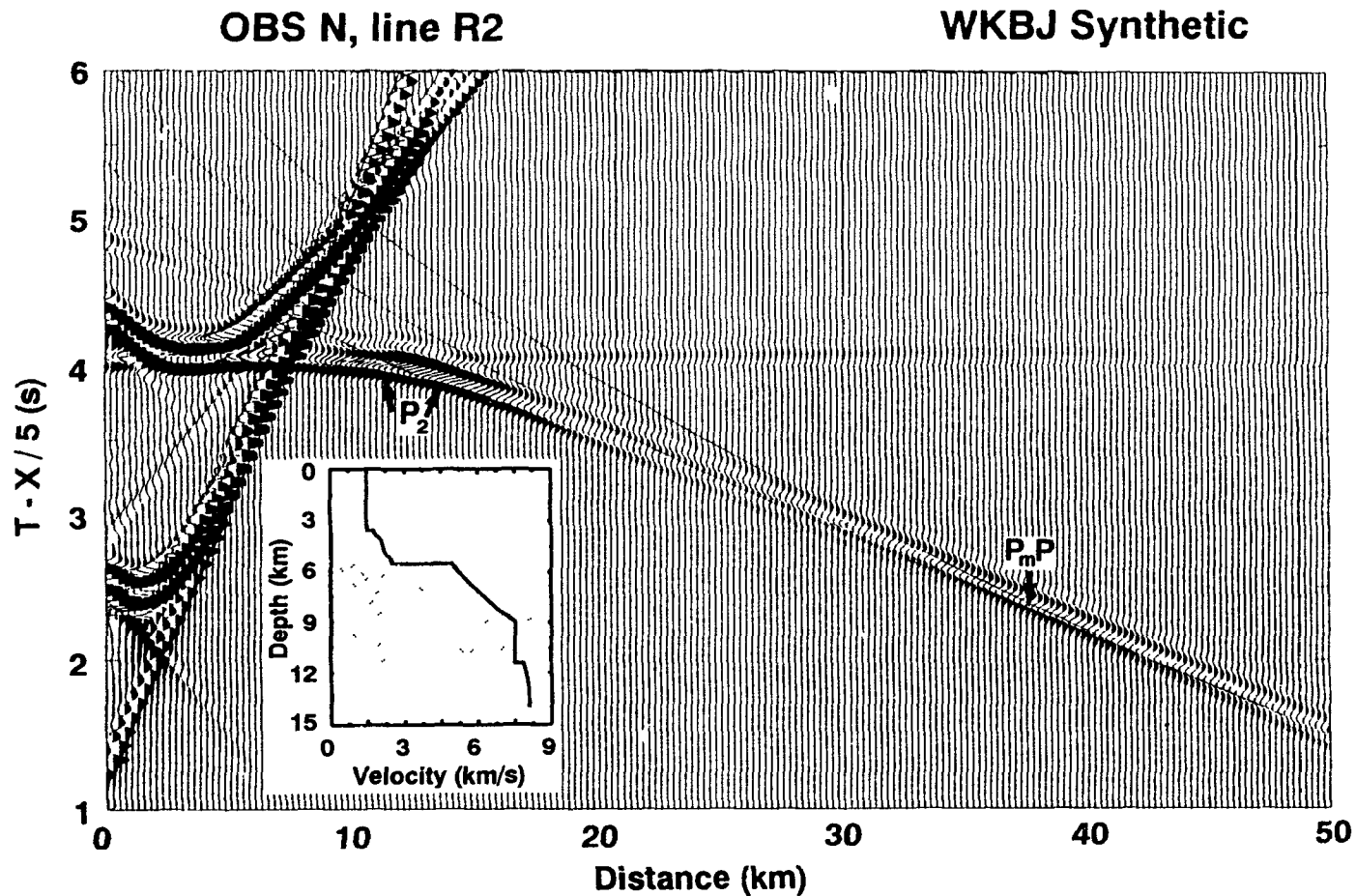


**Figure 3.11:** 1-D WKBJ synthetic computed for the OBS N refraction profile (Figure 3.5). The inset contains the corresponding velocity-depth structure which best models the data; the section of the curve representing crust has been shaded.

The synthetic seismograms developed for these seismic profiles and their corresponding velocity-depth structures are shown in Figures 3.10 and 3.11. The slope-intercept and  $\tau$ - $p$  solutions were used as end member starting solutions, the final models were produced by a process of forward iterative modelling. For both OBSs, the velocity-depth structures (insets in Figures 3.10 and 3.11) include the water depth and a sediment structure. The use of the sediment velocity structure for OBS N (which has sediment travel time corrections applied to the data) rather than the datum levels is of no consequence as the first arrival branches being modelled do not include any sediment refractors and the sediment travel time is the same as the datum structure.

For OBS G (Fig. 3.4),  $P_2$  and  $P_3$  are best modelled by two low velocity crustal units where the boundary between them is marked by an increase in the velocity gradient. A velocity discontinuity was initially sought to model the wide angle reflection  $P_3P$  appearing as a strong second arrival between 13 and 19 km. However, the magnitude of the velocity discontinuity required to model the amplitude of  $P_3P$  was not supported by the arrival times and velocities of the first arrival branch.  $P_n$  is well modelled, especially the energy decrease beyond 27 km, by a large velocity discontinuity between the crust and mantle and a large velocity gradient within the upper 3 km of the mantle followed by an abrupt decrease in the gradient.  $P_mP$  dominates the second arrival information in the synthetic (Fig. 3.10) more than desired because of the inability to partition sufficient energy into  $P_3P$  and by using a synthetic source function which is damped more rapidly than the true source signature.

For OBS N (Fig. 3.5),  $P_2$  is best modelled by a strong velocity gradient in the

upper crust with a slightly concave shape (see inset Figure 3.11). This gradient must be abruptly terminated to produce the rapid amplitude decrease at 22 km. Beyond this range, from 22 to 32 km, only low amplitude head wave energy from the base of the gradient layer arrives. The arrival time and range of the mantle arrival beginning at 32 km impose severe restrictions on the velocity and thickness of the deep crustal layer. If the velocity is decreased towards a more typical layer 3 velocity, then the resulting delay in the mantle arrival time is unacceptable. If the thickness of the layer is thinned in conjunction with the velocity decrease, the travel time is maintained but the critical range is moved to a shot-receiver range in which the seismic profile shows a clear lack of any strong returns. Given these criteria, the amplitude of  $P_mP$  is lower than desired in the synthetic seismogram.

### 3.4 Discussion

In comparing crustal structures within the extinct spreading centre to those on the flanks, gross differences are observed (section 3.2). OBSs sampling crust within the extinct spreading centre are D, E, F, G, H, O (shooting northeast), and N (shooting southwest). OBSs sampling crust which was formed before the time of anomaly 20 (45 Ma), when spreading rate is most likely to have decreased preceding extinction of the spreading centre (section 6.1), are OBSs L, M, N (shooting northeast), O (shooting southwest), and Q. The most significant difference between these two groups of OBSs is the dramatic thinning of the lower crustal unit (layer 3). Normal thicknesses are observed outside of the extinct spreading centre, while the thickness within the extinct spreading centre is either thinned or altogether absent. The degree of thinning in the upper crust is

not as appreciable. In this discussion, it must be emphasized that the division of the crust into upper and lower layers is difficult for some OBSs located within the extinct spreading centre as the change in the velocity gradient typically used for this distinction is not always present (eg. OBS G shooting northwest exhibits a linear gradient through the suite of crustal velocities). Nonetheless, the crust as a whole is seen to thin and those OBSs with clear changes in velocity gradient indicate severe thinning in the deeper crustal layer. A similar degree of variability is observed in the crustal P wave velocities. Within the extinct spreading centre, the velocities of the upper crust and especially the lower crust are lower than typical oceanic values [White *et al.*, 1984] and their counterparts elsewhere in the Labrador Sea basin [Van der Linden, 1975; Hinz *et al.*, 1979; Stergiopoulos, 1984; Srivastava *et al.*, 1989; Chian and Loudon, in preparation].

To focus the comparison of the extinct spreading centre and typical Labrador Sea crustal structures, the results from modelling travel time and amplitude data of the two representative OBSs by WKBJ synthetic seismograms (section 3.3) are displayed in Figures 3.12a and 3.12b. For comparative purposes, OBS N (Fig. 3.12b) is considered to be sampling crust typical of the Labrador Sea basin away from the extinct spreading centre, and is compared to a compilation of seismic refraction data for mature crust away from active spreading centres in the North Atlantic Ocean [White *et al.*, 1984]. The crustal structure at OBS N has a thickness comparable with mature oceanic crust. Its velocity gradient is somewhat higher than usual in the upper crust, but on the whole it follows the typical form, high in the upper crust and much decreased in the lower crust. The P wave velocity (7.5 km/s) in the lower crust is appreciably higher than normal (6.8

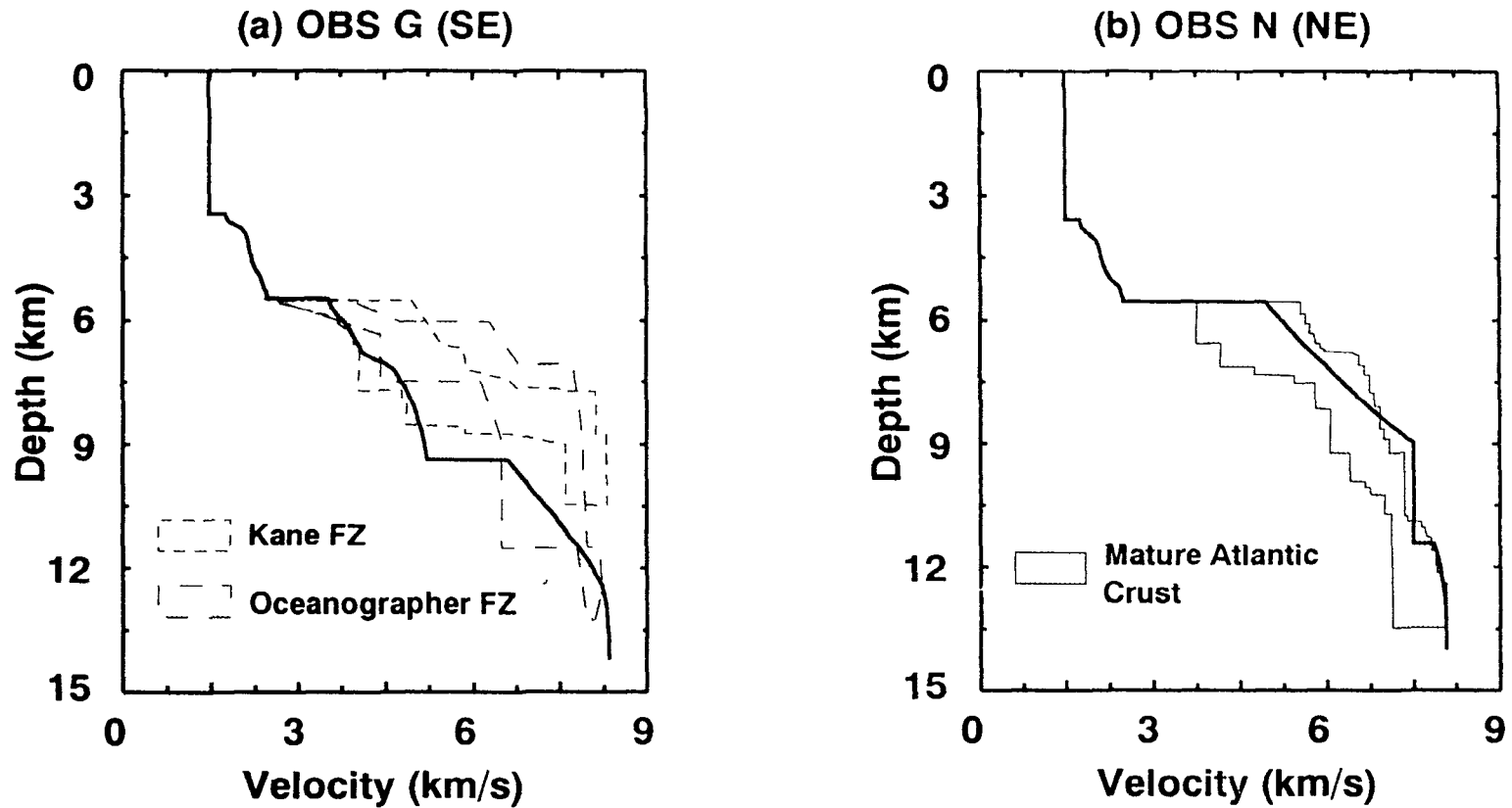


**Figure 3.12:** Crustal structures resulting from the modelling with 1-D synthetic seismograms are plotted against representative areas: (a) OBS G plotted with a compilation of refraction results from the Kane and Oceanographer fracture zones (sources discussed in text), (b) OBS N plotted with a compilation of refraction results for crust away from active spreading centres in the North Atlantic Ocean.

km/s). This high velocity may be characteristic in some areas of the eastern Labrador Sea as it has been previously observed in unreversed sonobuoy refraction profiles [Srivastava *et al.*, 1989; Hinz *et al.* 1979, 1973; Stergiopoulos, 1984] and is discussed further in section 4.5.2.

OBS G was situated to sample crust along the strike of the spreading centre and the results will be considered representative of the crust within the extinct spreading centre. The crustal structure obtained by the modelling with synthetic seismograms is quite different from normal ocean structures and more comparable to fracture zone structures (Fig. 3.12a). The crustal structure at OBS G shows appreciable thinning of the crust, by approximately 2 km, and velocities which are much lower than those observed in normal oceanic crust or elsewhere in the Labrador Sea basin. The compressional wave seismic structures at fracture zones have been typified by Sinha and Louden [1983]. Their type (a) structure is comparable to typical ocean crust except that layer 3 is slightly thinner (4.5 to 5 km thick), and has velocities ranging from significantly below normal to near normal values. This crustal type has been observed in the Vema fracture zone [Ludwig and Rabinowitz, 1980; Detrick *et al.*, 1980] and Oceanographer fracture zone [Sinha and Louden, 1983; Fox *et al.*, 1976]. Their type (b) structure is unlike typical oceanic crust. It is marked by low P wave velocities and a single high velocity gradient throughout. Mantle velocities are observed at depths as little as 2 to 3 km below the seafloor. This crustal type is found in the Kane fracture zone [Detrick and Purdy, 1980; Cormier *et al.*, 1984] and sections of the Oceanographer transform [Sinha and Louden, 1983] and Vema fracture zone [Louden *et al.*, 1986].

## 4. Two Dimensional Velocity Analysis

A two dimensional seismic model of the crust along refraction line R2, transversely crossing the extinct spreading centre, was developed and is described in this chapter. The 1-D travel time solutions and synthetics presented in Chapter 3 revealed a marked contrast in crustal structure within the extinct spreading centre from that along its flanks. Within the rift valley, the crust was found to be thin and of low p-wave velocity while on its flanks it was found to be more typically oceanic. As this crustal heterogeneity and its origin are the focus of the thesis, there is a clear impetus to develop a seismic crustal structure which is constrained in a 2-D sense.

Concerns regarding the reliability of the 1-D results for line R2 also motivated the development of a 2-D model for this refraction line. The 1-D solutions assumed piecewise homogeneity. Crustal structures were assumed to have horizontal planar interfaces and no lateral velocity variations within the shot-receiver offsets in which arrivals were received (at least 50 km). The degree of heterogeneity demonstrated by the 1-D travel time solutions from OBSs separated less than 50 km apart suggests that these fundamental assumptions of the 1-D methodology are not sufficiently satisfied in the study area. The applicability of the sediment correction algorithm in areas where refracting interfaces are sloped is a second related concern. The necessity and effectiveness of applying sediment travel time corrections to remove travel time variations arising from topography on the sediment-crust boundary prior to the calculation of 1-D solutions was demonstrated in Chapter 3. However, the geometry of the sediment correction method assumes that the refracted branch of the corrected ray path ('CD' in Fig. 3.2) travels on a boundary which

is parallel to the datum. In considering the 1-D results along line R2, dipping boundaries will be required, for example, on the crust-mantle boundary to accommodate the thinning of the crust as the extinct spreading centre is approached.

#### **4.1 Characteristics and Selection of 2-D Algorithm**

The algorithm selected for the purpose of developing a 2-D seismic crustal structure was the RAYINVR package written by Dr. Colin Zelt [Zelt and Smith, 1992]. Computed arrival times for user selected refracted, head wave or reflected phases are determined by raytracing through an irregular network of layered trapezoidal blocks which are used to parameterize the velocity structure. The blocks have dipping upper and lower boundaries, vertical left and right sides, and a velocity field which varies linearly along all four sides as determined by the velocity at the four corners of the trapezoid. The ray tracing through the velocity model is performed using zero-order asymptotic ray theory [Cerveny, 1977] in which the pair of first order ordinary differential equations for 2-D media are solved numerically by the Runge Kutta method.

Partial derivatives of travel time with respect to selected depth and velocity nodes are calculated analytically during the ray tracing along with travel time residuals. These may in turn be used by a complementary algorithm, DMPLSTSQ, which performs a damped least squares inversion to optimally fit computed travel times to observed travel times by adjusting the selected depth and velocity nodes. This ability to invert model parameters also allows the absolute uncertainty and spatial resolution of a velocity or depth node to be assessed and this application is discussed in section 4.6.

The algorithm was also selected because of its speed and suitability for use on a

486 PC. The computational efficiency is achieved by several features: 1) rays are not traced from receiver to shot (two point raytracing), rather the travel time at a shot point is calculated by interpolating between the travel times of rays which bracket the shot point; 2) the length of the linear segments which comprise a ray are adjusted automatically as a function of the vertical and horizontal velocity gradients; and 3) the take-off angle required to generate rays of a desired type from a specified boundary may be determined automatically through a trial raytracing and angle bisection routine. The distribution of rays about the take-off angle remains under the control of the user.

The RAYINVR package does not model seismic amplitudes. The use of a package which only seeks to fit observed travel times is justified because much of the amplitude response of the data in the study area is dominated by topographic focusing. The travel time information, therefore, impose the greatest constraint on the crustal structure. However, 2-D synthetic seismograms were generated (section 4.7) in the later stages of the travel time modelling and some revision of the velocity model was required in order to improve the fit to the amplitude information.

#### **4.2 Model Parameterization**

The distance coordinates at which layer boundaries and upper and lower velocities are specified can be completely general and independent between and within layers. There are, however, several criteria which guide the specification of nodes for each layer: 1) ray coverage - nodes may not be specified in areas where refracted or wide angle reflection phases are absent; 2) independent data sources - 12 kHz bathymetry and single channel reflection data (section 2.3.1); and 3) a trade-off between (a) minimizing RMS travel time

residuals,  $T_{\text{RMS}}$  (section 4.4.2), by increasing the number of nodes or (b) increasing the resolution of nodes and their stability in the inversion by decreasing the number of independent model parameters. The number and distribution of nodes (as delineated in Fig. 4.1) for each layer in the final model reflects the application of the aforementioned criteria. The final model has a basic nodal spacing of 10 km. This was selected after exploring the suitability of nodal spacings from 5 to 25 km. For nodal spacings beyond 10 km,  $T_{\text{RMS}}$  increased significantly while the resolution of nodes, from an inversion standpoint, remained problematic at all nodal spacings (section 4.6).

There are several areas of the model where the density of nodes deviates from the basic nodal spacing. On the sediment-crust boundary (between layers 3-4 or and 3-5 in Fig. 4.1), nodes are specified every 2.5 km as the observed travel time data exhibit variations which require this spatial definition (*e.g.* oscillation of the observed travel time of  $P_n$  arrivals for OBS M shooting southwest between 60 and 80 km in Fig. 4.9). The reflection data are able to provide this spatial definition while not compromising model parameter resolution as these nodes are never varied in a model inversion.

The absence of boundary and velocity nodes in the crust between 30 and 60 km (layers 5 and 7 in Fig. 4.1) is the most dramatic decrease from the basic nodal spacing. The paucity of raypaths travelling through this region precludes the specification of nodes. There are several additional areas in the sediment or crustal layers where a spacing of 20 or 30 km between velocity or boundary nodes exists. These are regions where (1) few, if any, of the rays refracted within the layer are able to constrain the node (*e.g.* no sediment phase information to define nodes along boundary between layers 2 and 3 at 170

and 180 km, Fig. 4.1) or (2) where lateral velocity variations are moderate and ably specified by the larger nodal spacing (*e.g.* the lower crust, layer 7, within the extinct spreading centre from 70 to 90 km, Fig. 4.1). The one exception to the criteria used in specifying nodes occurs at the ends of the refraction line (0 and 220 km) which are very poorly constrained, but required to satisfy the algorithm.

### **4.3 Initial Velocity-Depth Model**

A starting velocity-depth structure is required when performing either forward or inverse modelling of raypath travel times. The following sections detail the specification of the water, sediment, crust and mantle layers in the parameterization of the initial model.

#### *4.3.1 Water Layer*

At intervals of every tenth shot point (approximately 2.5 km), the 12 kHz bathymetry data were used to assign boundary nodes for the seafloor. Boundary nodes were then given a regular spacing by interpolating them onto a 2.5 km distance grid. The upper and lower velocities of the water layer were specified by solitary nodes whose value is applied to all trapezoids within the layer. The depth averaged velocity of 1.49 km/s (section 2.4.2) was assigned to both the upper and lower velocities thereby creating a layer with no vertical or horizontal velocity gradients.

#### *4.3.2 Sediment Layers*

The sediment column was divided into two layers; the first layer defined between the seafloor and a prominent internal sediment reflector (A in Fig. 3.1) and the second layer defined between the internal sediment reflector and the sediment-crust boundary.

The thickness of a layer,  $z_{lower}$ , at a shot point may be computed given (1)  $\Delta T$ , a vertical incidence travel time between reflectors defining the layer (from the interpreted reflection profile in Fig. 3.1), (2)  $V_{upper}$ , the upper boundary velocity; and (3)  $k$ , a linear velocity gradient such that  $V(z)=V_{upper}+ kz$  within the layer. At vertical incidence, the one-way travel time through a single layer with a linear velocity gradient is:

$$\Delta T = \int_0^{z_{lower}} \frac{1}{(V_{upper} + kz)} dz \quad (\text{Eqn. 4.1})$$

$$\Delta T = \frac{1}{k} \ln \left| 1 + \frac{kz_{lower}}{V_{upper}} \right|$$

From which the thickness of the layer and lower boundary velocity may be obtained:

$$z_{lower} = -\frac{V_{upper}}{k} (1 \pm \exp(k \Delta T)) \quad (\text{Eqn. 4.2})$$

$$V_{lower} = V_{upper} + kz_{lower}$$

For the upper sediment layer, the final velocity log at ODP site 646 [Figure 16 in Jarrard *et al.*, 1989] was used to assign  $V_{upper}=1.5$  km/s and  $k=0.96$  s<sup>-1</sup>. Using these values, the computed depth to the internal sediment reflector averages 0.63 km for refraction line R2, which coincides with the depth at which the velocity gradient decreases markedly in the site 646 velocity log. For the lower sediment layer, the observed travel times from rays refracted within the layer were used to select appropriate values of  $V_{upper}$  and  $k$  in computing the lower velocity nodes and sediment-crust boundary nodes. Several combinations of  $V_{upper}$  and  $k$  were tested by tracing rays through the test models and

comparing observed and computed travel times;  $V_{\text{upper}}=2.2$  km/s and  $k=0.2$  s<sup>-1</sup> were ultimately selected. The nodes computed with these values required little modification in the modelling except in the area of the extinct spreading centre where  $V_{\text{upper}}$  and  $k$  both increase. As with the water layer, nodes for both sediment layers were computed for every tenth shot point (approximately 2.5 km) and then used to establish a regular grid of nodes spaced 2.5 km apart. In the parameterization of the final model (Fig. 4.1), the initial 2.5 km spacing between nodes for the sediment layers was increased to 10 km as the denser nodal spacing was not required.

#### 4.3.3 Crustal and Mantle Layers

Boundary and depth nodes for the upper crust, lower crust and mantle layer were specified using the 1-D travel time solutions. For each OBS, the  $\tau$ - $p$  velocity-depth structures (section 3.2) were divided into upper and lower crustal layers. The boundary between these layers was placed at a depth where the velocity gradient was most appropriately split into two linear segments offset by a velocity discontinuity if required. The layer thicknesses and velocities so attained were used to define the structure of the crust at a point offset laterally from the receiver by 10 km in the direction of shooting. The boundary nodes were calculated by adding the layer thicknesses to the depth of the sediment-crust datum used in the sediment travel time corrections. In cases where the lateral offset causes structures from adjacent receivers to overlap (*e.g.* OBS O shooting northeast and OBS E shooting southwest), the structures were averaged and placed at a distance mid-way between receivers.

Mantle velocities were taken from the slope-intercept velocity-depth structures

(section 3.2). The  $\tau$ - $p$  solutions were not used in this instance as the mantle refractor is mapped to a narrow region in  $\tau$ - $p$  space and hence less reliable than the slope-intercept solution. As with the crustal boundary and velocity nodes, the mantle velocity nodes were also offset laterally from the receiver by 10 km in the direction of shooting. In practice, a mantle velocity from the slope-intercept method is an average of the actual mantle velocity variations present within the range over which arrivals are observed. Given considerable variability in this range interval for various OBSs, the 10 km offset was used, as it is the approximate range at which the critical angle for refraction at the crust-mantle boundary is reached.

For defining the lower boundary of the mantle layer, a velocity of 8.24 km/s was specified at a depth of 20 km. This introduces vertical velocity gradients which range from  $0.02 \text{ s}^{-1}$  to  $0.04 \text{ s}^{-1}$  depending upon the velocity at the upper boundary of the mantle layer. These velocity gradients exceed the typical range of the  $0.01$  to  $0.02 \text{ s}^{-1}$ . They arise from the low upper mantle velocities which are observed, particularly in the vicinity of the extinct spreading centre. For most OBSs, this gradient provides a suitable match for the critical range beyond which mantle refracted phases begin to be observed. The irregular distribution of boundary and velocity nodes for the crustal and mantle layers was then interpolated to form a regular grid with a nodal spacing of 5 km. In the parameterization of the final model (Fig. 4.1), this initial 5 km spacing between nodes for the crust and mantle layers was increased to 10 km as the denser nodal spacing was not justified by the resolution which the ray coverage provides.

#### **4.4 Considerations Guiding Model Revisions**

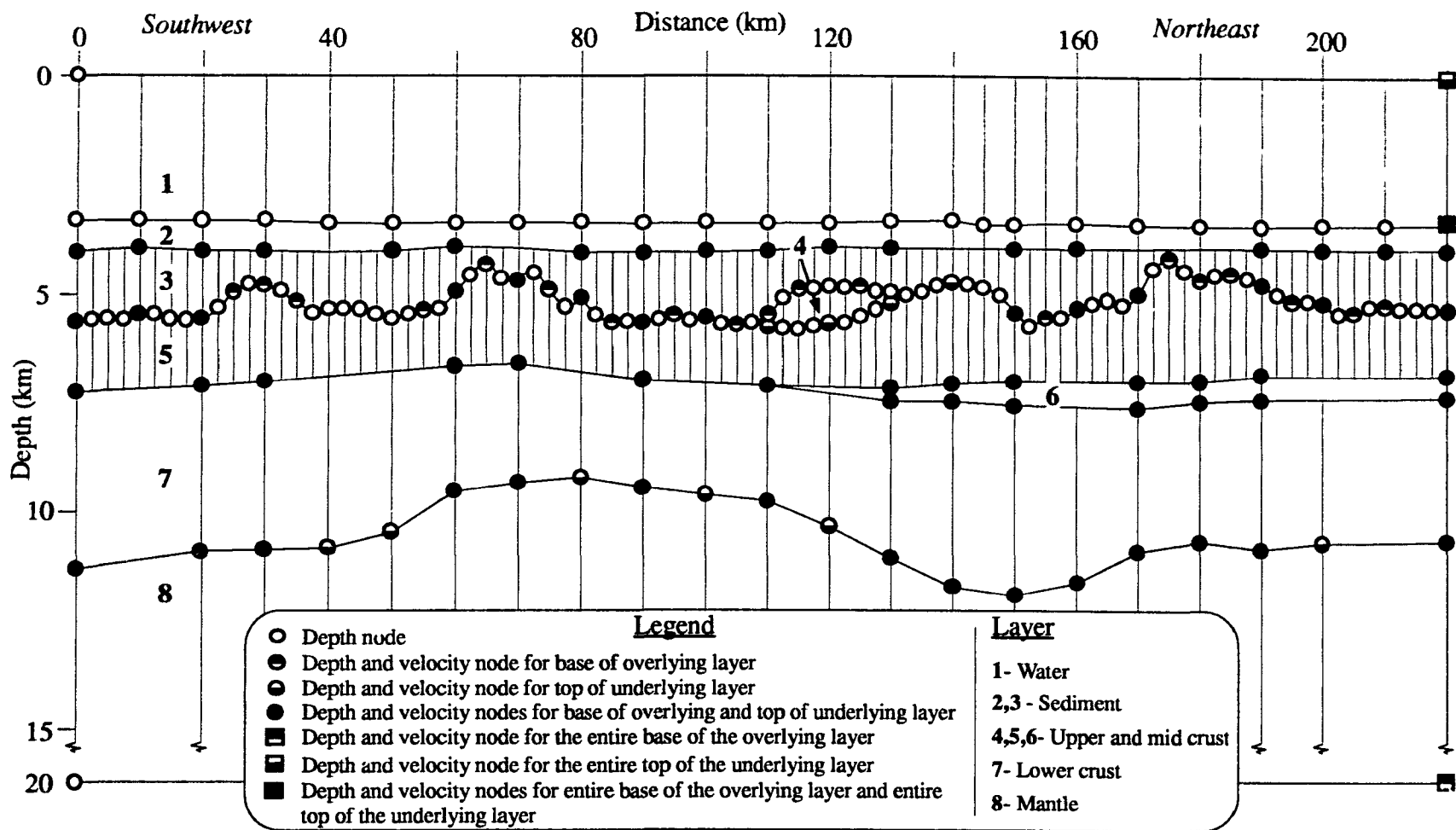


**Figure 4.1:** The velocity-depth structure for 2-D seismic modelling of refraction line R2 is parameterized by a series of layered trapezoidal blocks. Each layer is defined by a series of boundary nodes along its upper surface and velocity nodes along its upper and lower surfaces (see Legend). The number and distribution of nodes is dictated by the three criteria detailed in section 4.2: model resolution, subsurface ray coverage, and constraints from the reflection data.

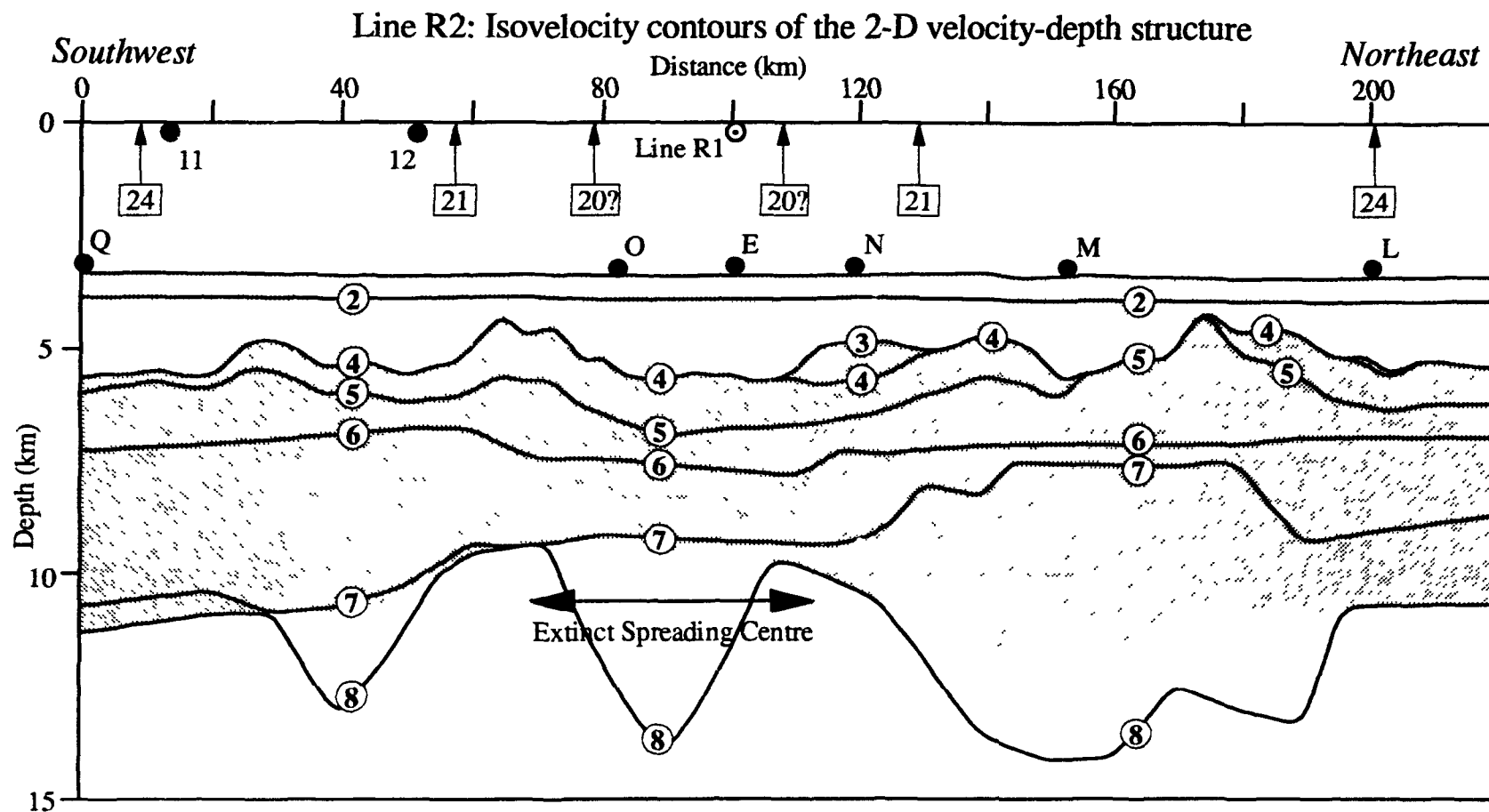


**Figure 4.2:** The 2-D velocity-depth structure is represented by isovelocity contours which were computed at 1 km distance intervals and smoothed with a three point filter. Velocity contours can become coincident along model boundaries where a velocity discontinuity is present. The light grey area marks the sediment layers (2 and 3 in Fig. 4.1) and the medium grey area marks the crustal layers (4,5, and 6 in Fig. 4.1). Receivers are denoted by the solid circles. The arrows and corresponding chronological identifiers mark the intersection of magnetic anomaly lineations with line R2 (Figs. 2.2 and 6.1).

#### *4.4.1 Uncertainty and Identification of Travel time Picks*

In raytracing, an optimal fit between observed and computed travel times is sought by adjusting the velocity and boundary nodes comprising the 2-D velocity-depth structure. In forward modelling, the uncertainty assigned to the picks serves as a criteria by which the quality of a computed travel time fit may be assessed (see discussion of  $\chi^2$  in section 4.4.2). In model inversions, the uncertainties have a direct influence by weighting the relative adjustment made to individual nodes selected for inversion in the velocity-depth structure.

For all travel time picks, a base uncertainty of  $\pm 0.02$  s was chosen to account for the timing uncertainties inherent to the refraction data, as described in section 2.4.2. A further uncertainty was added to reflect the quality of the pick itself. The largest uncertainties were assigned to second arrivals or first arrivals at large source-receiver offsets. In the former case, the  $P_mP$  and sediment refraction arrivals are difficult to pick because of interference with the wavetrain from the first arrivals. In the latter case,  $P_n$  arrivals are difficult to pick because their amplitude barely exceeds the noise floor. The maximum uncertainty assigned was  $\pm 0.12$  s, which is slightly less than  $\pm$  one full seismic wavelength (0.147 s) for arrivals with a dominant frequency of 6.8 Hz. In presenting the raytracing results in Figures 4.3 to 4.9, the observed travel times are represented by the stippled areas whose height at a given distance denotes the uncertainty of the picks.

As mentioned, adjustments to the velocity-depth structure are made by optimally fitting the computed arrival times of rays to their associated observed travel times. A proper identification of the layer in which an observed arrival is thought to have been

refracted or the boundary from which it was reflected is central to this 2-D raytracing methodology. Failing to properly identify arrivals leads to the inappropriate adjustment of boundary or velocity nodes, and ultimately, inaccuracies in the 2-D velocity-depth structure. For some receivers, particularly those with travel time and amplitude variations originating from the basement topography, the proper identification of arrivals is difficult. To minimize this source of error in the modelling, the identification of travel time picks was continually re-assessed; raytracing through successive iterations of the velocity-depth structure tended to clarify the proper identification of the picks.

#### 4.4.2 Assessment of Model Iterations

To assess the quality of a model iteration, three values were routinely calculated and compared with the results from alternate revisions. The first quantity,  $n$ , is the number of observed travel times which are reached by the computed arrivals. Assuming that the observed travel times have been properly identified, one clearly seeks to construct a velocity-depth structure which will be able to trace rays to most observed locations. Otherwise, the model is deficient in one manner or another: geometric shadow zones, inappropriate velocity gradients, or boundary dips.

Two further quantities,  $T_{RMS}$  and  $\chi^2$ , quantify the fit between the observed and computed arrival times for a given ray group and are defined as follows:

$$T_{RMS} = \left( \frac{\sum_{i=1}^n (Tobs_i - Tcalc_i)^2}{n} \right)^{1/2} \quad (\text{Eqn. 4.3})$$

$$\chi^2 = \left( \frac{\sum_{i=1}^n \left( \frac{Tobs_i - Tcalc_i}{Uobs_i} \right)^2}{n} \right)^{1/2}$$

Where:  $T_{obs}$  = Observed travel time  
 $T_{calc}$  = Calculated travel time  
 $U_{obs}$  = Uncertainty of the observed travel time  
 $n$  = Number of calculated travel times reaching observed arrivals

For values of  $\chi^2 \leq 1$ , the computed arrivals fit the observed arrivals within the uncertainties of the observed travel times. This criteria was set as the minimum standard which computed arrivals must achieve for a model revision to be deemed acceptable. It was relaxed only in instances where multiple raypaths from different receivers overlapped, but no structure could be devised which was capable of allowing  $\chi^2 \leq 1$  for raypaths at all receivers. The values of  $n$ ,  $T_{RMS}$ , and  $\chi^2$  in the final velocity-depth structure are presented in Table 4.1 and discussed in section 4.5.

#### **4.5 Final Velocity-Depth Structure**

This section details the characteristics of the final velocity-depth structure along line R2, while leaving an interpretation of the structure and its relationship to the thesis objectives for discussion in Chapter 6. The final model is the product of travel time modelling which followed a layer by layer approach. That is, revisions to a model layer involved the observed travel times, from all receivers, identified as having emanated from that layer. Arrivals from all layers were frequently viewed on a receiver by receiver basis as well to ensure that observed travel times were properly identified (section 4.4.1).

As the structure of an overlying layer influences the computed travel times for an underlying layer, revisions to model layers proceeded from the surface layer downwards. Revisions to an underlying layer in the model layer can also influence the structure of an

Table 4.1: Quality of fit for computed travel times in 2-D modelling along line R2

		Sed. Refr.	P <sub>2</sub>	P <sub>3</sub>	P <sub>m</sub> P	P <sub>n</sub>
R2-L NE	n	25	7			
	T <sub>rms</sub>	.020	.060	No	No	No
	χ <sup>2</sup>	.120	1.664	Arrivals	Arrivals	Arrivals
R2-L SW	n	26	11	103	22	163
	T <sub>rms</sub>	.016	.034	.035	.171	.086
	χ <sup>2</sup>	.057	.350	.341	3.053	1.146
R2-M NE	n	29	41	37	56	93
	T <sub>rms</sub>	.024	.045	.080	.132	.119
	χ <sup>2</sup>	.123	1.010	2.164	3.802	1.580
R2-M SW	n	25	25	70	80	163
	T <sub>rms</sub>	.020	.022	.049	.085	.070
	χ <sup>2</sup>	.097	.199	.655	0.583	.536
R2-N NE	n	8	14	89	60	118
	T <sub>rms</sub>	.031	.028	.068	.101	.082
	χ <sup>2</sup>	.205	.407	1.739	1.778	.788
R2-N SW	n	14	11	15	No	222
	T <sub>rms</sub>	.019	.076	.018	Arrivals	.066
	χ <sup>2</sup>	.150	3.944	.185		.485
R2-E NE	n	32	14	15	No	76
	T <sub>rms</sub>	.059	.013	.024	Arrivals	.062
	χ <sup>2</sup>	.356	.042	.143		.578
R2-E SW	n	33	13	28	No	209
	T <sub>rms</sub>	.042	.013	.031	Arrivals	.045
	χ <sup>2</sup>	.180	.018	.242		.239
R2-O NE	n	38	18	27	No	106
	T <sub>rms</sub>	.029	.023	.041	Arrivals	.060
	χ <sup>2</sup>	.109	.266	.491		.452
R2-O SW	n	20	15	11	No	199
	T <sub>rms</sub>	.047	.046	.049	Arrivals	.081
	χ <sup>2</sup>	.303	.464	.418		.721
R2-12 NE	n	19	19	21	No	No
	T <sub>rms</sub>	.018	.064	.086	Arrivals	Arrivals
	χ <sup>2</sup>	.141	1.317	1.181		
R2-11 NE	n	18	27	31	No	No
	T <sub>rms</sub>	.030	.030	.079	Arrivals	Arrivals
	χ <sup>2</sup>	.379	.185	1.423		
R2-Q NE	n	42	29	27	No	109
	T <sub>rms</sub>	.024	.027	.027	Arrivals	.083
	χ <sup>2</sup>	.140	.202	.157		1.220

overlying layer as they share a common boundary. If these boundary nodes are subject to modification, the velocity gradient structure of the overlying layer and depth to which rays are refracted will be altered. A suitable fit for arrivals from an overlying layer may then be degraded by the boundary modifications which are required to fit the arrival times for an underlying layer. This interdependency was minimized by repeating the sequence of top to bottom revisions three times, with the magnitude of the changes to boundary and velocity nodes decreasing with each repetition.

In Figure 4.2, the final velocity-depth structure is represented by smoothed isovelocity contours. The points comprising the contours were calculated every 1 km by a linear interpolation between the velocity and boundary nodes for the trapezoid in which they are bounded. As such, the contours can become coincident along model boundaries (such as the sediment-crust boundary) where there is a velocity contrast. The contours provide a sense of the vertical and horizontal gradients which rays travelling through a given trapezoid would experience. In Figure 4.2, the sediment and crustal layers, as defined by boundary nodes in the model parameterization (Fig. 4.1), are shaded light and medium grey respectively. The depth and distance coordinates and velocity of each node comprising the final model are listed in Appendix C. Figures 4.3 through 4.9 present raytracing through the layers of the final velocity-depth structure and the associated observed and computed travel times. Table 4.1 lists the values of  $n$ ,  $T_{\text{RMS}}$ , and  $\chi^2$  which quantify the quality of fit of the computed arrivals (section 4.4.2) from each layer at all the receivers. The following sections use these tables and figures to discuss the details of the sediment, crust and mantle in the final 2-D velocity-depth structure. Note that

reducing velocities and time scales appropriate for the arrivals from each layer have been selected in presenting the travel time observations and computed arrivals. Further, raypaths and travel times at adjacent receivers have been split into upper and lower panels so they will not overlap.

#### *4.5.1 Sediment Layers*

The sediment layers are numbered 2 and 3 in the model parameterization (Fig. 4.1) and shaded light grey in the velocity-depth structure (Fig. 4.2). Ray paths and associated travel times for sediment refractions are found in Fig. 4.3. The initial velocity-depth structure (section 4.3.2) provided an excellent starting solution which required little subsequent modification for receivers on the rift flanks. Computed arrivals for OBSs L, M, and Q (shooting northeast) exemplify the quality of this structure with  $\chi^2$  values from 0.057 to 0.140. Further, the maximum shot-receiver offsets at which the computed sediment refractions arrive correspond very closely with the respective maximum offsets at which observed travel times are seen. This offset is a function of the depth of the layer and the velocity gradient. These dictate respectively, how deep and how rapidly rays will be refracted. The close match between the observed and computed maximum offsets thus serves as an additional indication that the vertical velocity gradients in the sediment layer have been appropriately specified. Sonobuoy 11 is the only receiver at which rays are not traced to most observed arrivals. The first 18 travel time picks are reached, but the deeper rays required to reach the remainder are stopped when they intercept the basement high at 25 km.

Sediments loosely defined as being within the bounds of paleo-rift axial valley

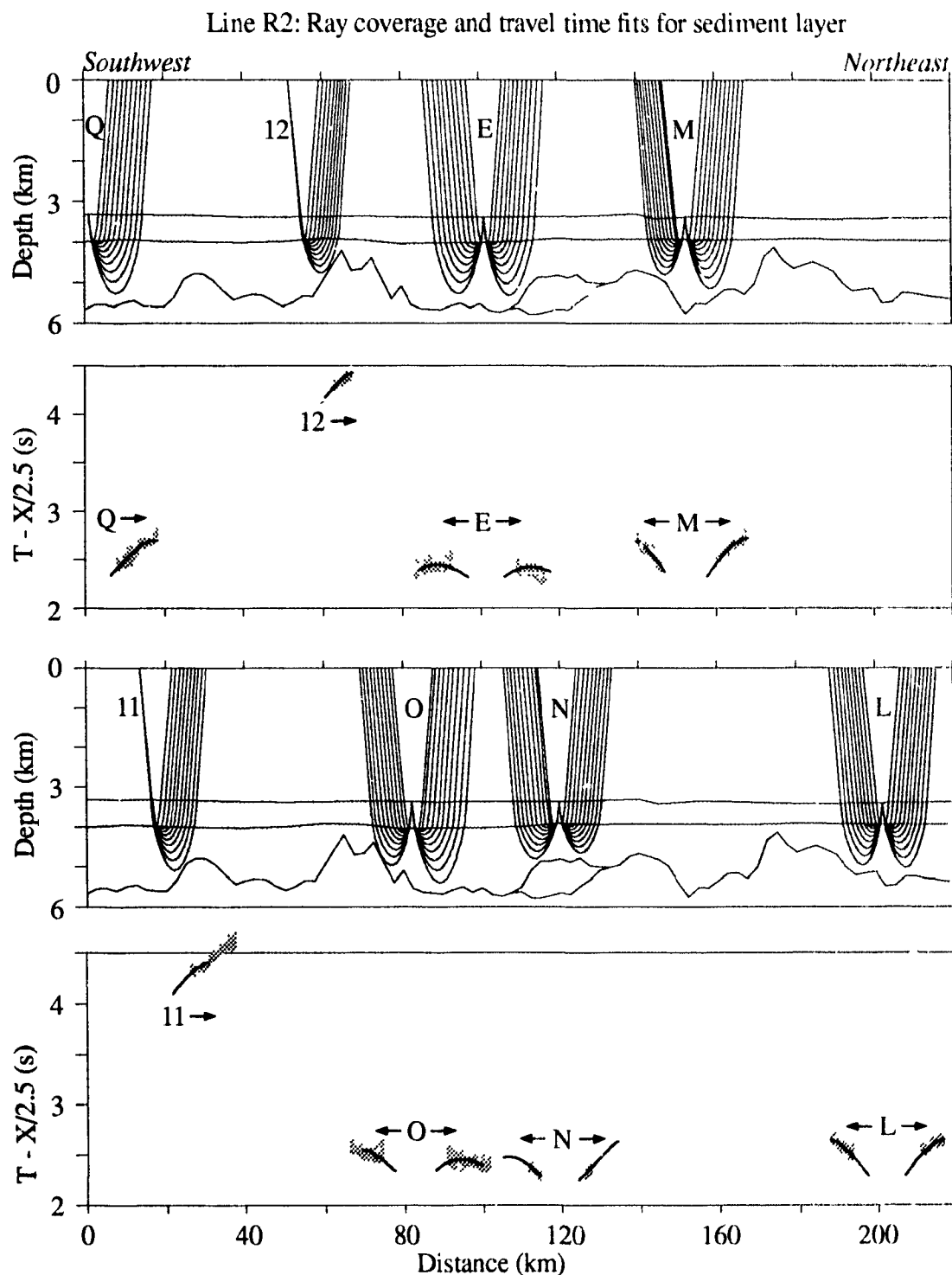


**Figure 4.3:** Computed ray paths and travel times for refractions in the sediment layer (shaded grey) using the 2-D velocity-depth structure along line R2 (Fig. 4.2). Observed travel times and their uncertainties are represented by the stippled areas through which the computed arrival times are traced. Ray paths converge to their corresponding receivers.

(nodes from 80 to 120 km ) depart from the initial solution. The velocity of nodes along the top and bottom of layer 3, the lower sediment layer, must be increased in this region. The requirement for higher velocities is apparent in a quick examination of the observed travel times (Fig. 4.3). Using the reducing velocity as a guide, OBS E and OBS O (shooting northeast) have velocities exceeding 2.5 km/s while receivers outside this region have velocities slower than 2.5 km/s.

The topography of the sediment-crust boundary (3-4 or 3-5 in Fig. 4.1) was modified from its specification in the initial velocity-depth structure to improve the travel time fit of the crustal and mantle arrivals. In the initial 2-D model, the depth of these nodes was computed by a travel time to depth conversion (Eqn. 4.2) using travel times from the interpreted reflection profile (Fig. 3.1). This required assumptions about the velocity structure of the sediments (section 4.3.2) and also has some inherent uncertainty. Specifically, travel times for the basement reflector are difficult to pick in regions where the reflection amplitudes are low. Therefore, when merited by unresolved travel time misfits in lower layers, the sediment-crust boundary was subject to manual revision.

In practice, the required revisions were minor in all but two cases which are described in greater detail. First, shorter wavelength oscillations were introduced on the basement high from 60 to 80 km. These variations on the sediment-crust boundary are required to reproduce the travel time oscillations observed in  $P_n$  for OBS N shooting southwest (Fig. 4.8), OBS E shooting southwest (Fig. 4.8) and OBS M shooting southwest (Fig. 4.7). The second revision was a deepening of the sediment-crust boundary below OBS M. This was required to delay crustal arrivals for OBS M and is neither supported

nor in conflict with the reflection data as the basement is very difficult to pick in this region.

#### *4.5.2 Crustal Layers*

The model layers which define the crust are numbered 4,5,6 and 7 in the model parameterization (Fig. 4.1) and shaded medium grey in the velocity-depth structure (Fig. 4.2). Ray paths and travel times for the upper crust are presented in Figure 4.4 and ray paths for the lower crust are presented in Figure 4.5. Two of the model layers, 4 and 6, are only found in specific regions of the model to satisfy travel time or amplitude considerations. There are no arrivals from these layers so the nodal values are not defined by directly fitting observed travel times with computed arrivals.

Layer 4 was introduced to delay the  $P_2$  arrival times of OBS N. This is not a timing error in the refraction data as it would have been detected for earlier arrivals, the sediment refraction and direct ray path from the surface to the OBS. Two modifications could be introduced to account for the time offset: 1) treat the strong basement reflection (shot points 470 to 520 in Fig. 2.2) as an off axis feature and deepen the sediments underlying OBS N accordingly or 2) attribute the travel time delay to a lower velocity (decreased by roughly 1 km/s) in the upper 0.8 km of crust. The latter option was selected in the model parameterization, partly because ray paths from OBS E shooting northeast (Fig. 4.5) through this region are also delayed. In either case, the travel time accommodation which this layer provides has little bearing on the final model as the layer only exists over a narrow 20 km region.

Layer 6, on the northeast flank of the extinct spreading centre, was introduced into

the velocity-depth structure when it was apparent that the two layer model with linear velocity gradients could not adequately parameterize the structure. The lower crust (layer 7 in Fig. 4.1) requires (1) high velocities to fit the observed travel times (OBSs M, L shooting southwest, and N shooting northeast in Fig. 4.5) and (2) a weak velocity gradient in the layer to allow  $P_3$  and  $P_mP$  for these OBSs (Fig. 4.6) to extend to shot-receiver offsets of approximately 40 km (Figs. 4.6 and 4.5 respectively). If the boundary between the upper and lower crust is held at a fairly uniform depth across the whole model, the high velocity lower crustal refractions from OBS N shooting northeast, OBS M, and OBS L shooting southwest arrive too early. The delay could be accommodated by thickening the upper crust, layer 5, but this is undesirable for several reasons. First, it introduces an upper crustal asymmetry between the flanks of the extinct spreading centre. Second, it produces a strong mid-crustal velocity contrast from which wide angle reflections should be observed. There is supporting evidence from the upper crustal velocity structure at OBS N, as determined by 1-D WKBJ synthetic seismograms (Fig. 3.11), that a stronger velocity gradient exists just above the boundary with the lower crust. A similar layer may exist on the southwest flank, but cannot be specified given the number of ray paths in that area.

The 2-D velocity-depth structure (Fig. 4.2) quantifies the lateral variations which exist as one crosses the extinct spreading centre along a southwest-northeast striking refraction line. As anticipated from the 1-D travel time solutions, two principal variations in crustal structure emerge. These are the variation in the velocity and thickness of the crust as a function of range from the extinct spreading centre and the asymmetry between

flanks of the extinct spreading centre. The observations and 2-D modelling which define these variations dominates the discussion in the remainder of this section

Arrivals at OBS O shooting northeast, OBS E, and OBS N shooting southwest are used to define the upper and lower crustal structure within the extinct spreading centre (Figs. 4.4 and 4.5 respectively). If one compares the slopes which the observed arrivals define with the reducing velocity of 5 km/s, the velocities from the upper crust at receivers within the extinct spreading centre do not exceed the reducing velocity. This crude observation is borne out in the final velocity-depth structure (Fig. 4.2) where velocities of much of the upper crust are within the 4 and 5 km/s isovelocity contours. Further evidence for the low upper crustal velocities is found by noting the marked delay in  $F_3$  arrivals at OBSs E, N shooting southwest, and O shooting NE (Fig. 4.5). These arrivals are delayed with respect to lower crustal arrivals at other receivers because their ray paths travel through the region of low upper crustal velocities within the extinct spreading centre. For arrivals from the lower crust (Fig. 4.5), the direct observation of lower velocities at these OBSs is even more pronounced. These low velocities are expressed in the final model by the pushing down of the 6 km/s isovelocity contour as the extinct spreading centre is entered and the proximity of the 7 km/s contour to the crust-mantle boundary.

The influence of the extinct spreading centre is broad with appreciable crustal thinning observed over a 60 km range from 50 to 110 km (Fig. 6.5c). The transition to the extinct spreading centre type structures occurs rapidly between 60 and 80 km on the southwest rift flank and 110 to 130 km on the northeast flank. The crust within the extinct

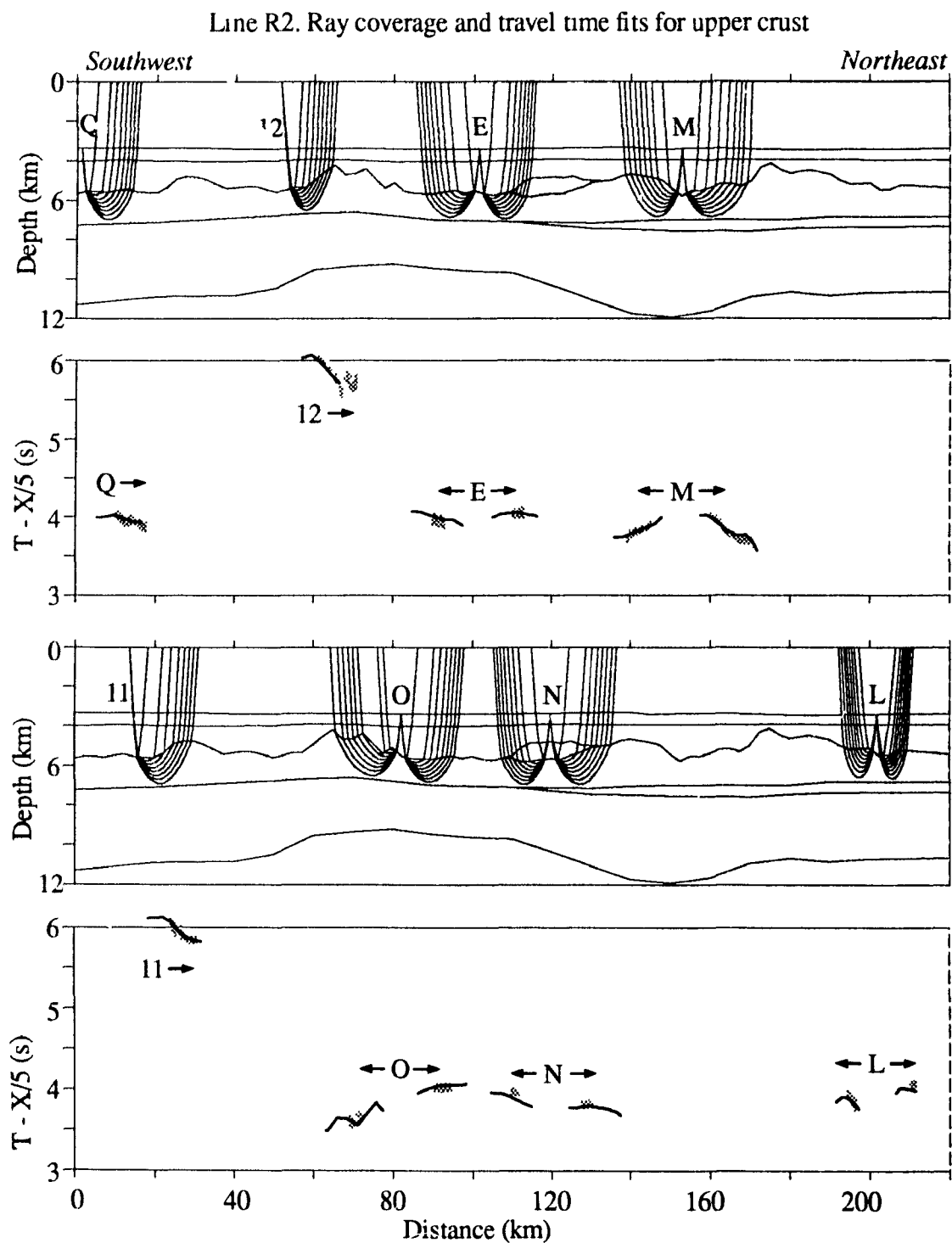


**Figure 4.4:** Computed ray paths and travel times for refractions,  $P_2$ , in the upper crust (shaded grey) using the 2-D velocity-depth structure along line R2 (Fig. 4.2). Observed travel times and their uncertainties are represented by the stippled areas through which the computed arrival times are traced. Ray paths converge to their corresponding receivers.

## Line R2: Ray coverage and travel time fits for lower crust

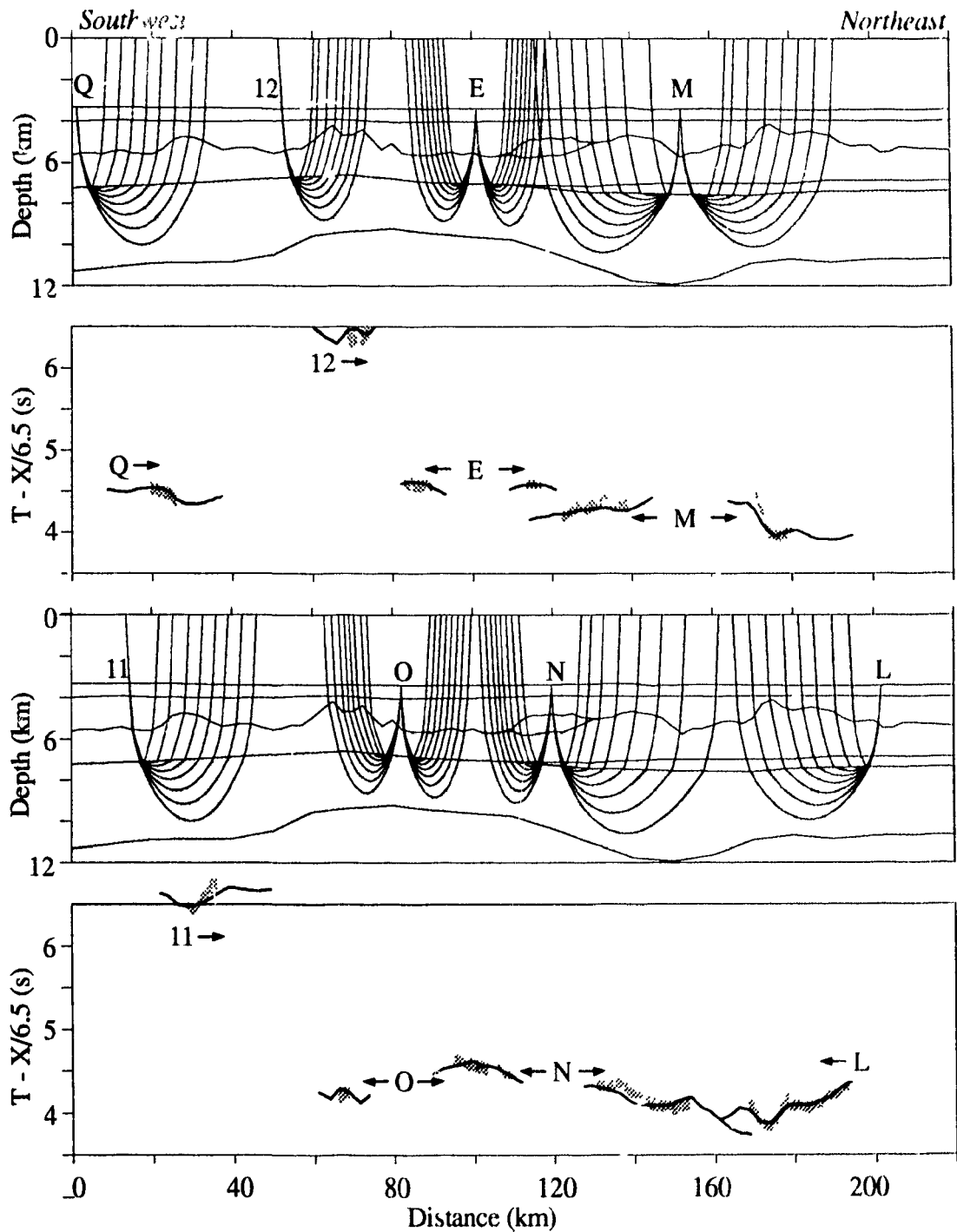


**Figure 4.5:** Computed ray paths and travel times for refractions, P<sub>3</sub>, in the lower crust (shaded grey) using the 2-D velocity-depth structure along line R2 (Fig. 4.2). Observed travel times and their uncertainties are represented by the stippled areas through which the computed arrival times are traced. Ray paths converge to their corresponding receivers.

spreading centre itself, as bounded by the paleo-rift axial valley from 80 to 110 km, is remarkably homogeneous with crustal thickness only varying between 3.77 and 4.24 km. This degree of homogeneity within the extinct spreading centre was not present in the initial velocity-depth structure as defined by the line R2 1-D travel time solutions (Fig. 3.9). OBS O shooting northeast, for example, was more typical of a flank structure with thicker crust and higher velocities and OBS N shooting southwest did not exhibit the low velocities in the upper crust.

There is confidence in the 2-D velocity-depth structure within the extinct spreading centre. Receivers were, in this instance, situated such that there are many overlapping ray paths for the lower crust, and some in the upper crust. Further, the four refraction profiles sampling crust in this region have  $T_{\text{RMS}} \leq 0.41$  s and  $\chi^2 \leq 0.49$  (Table 4.1). In addition, the short shot-receiver offsets over which computed and observed refracted phases are present is an indication of the crustal thinning in the extinct spreading centre, confirmed by a consideration of the  $P_n$  arrivals in section 4.5.4.

Turning to a discussion of the velocity structure observed on the flanks, beyond the influence of the extinct spreading centre, from 0 to 60 km to the southwest and from 130 to 220 km to the northeast, the seismic behaviour of the crust is very different from the crust within the extinct spreading centre. There are several indications of this distinction: 1) higher velocities; 2) greater range to which refracted arrivals are observed; 3) 2 to 3 times more observed arrivals; and 4) clearly discernable  $P_mP$  arrivals.

The southwest flank is less well constrained than the northeast flank, despite the inclusion of arrivals from two sonobuoys which were not considered in the 1-D analysis.

The travel times at these sonobuoys are helpful in defining the crustal velocity structure, but limited by the quality of their mantle arrivals (Fig. A.6), which were omitted in determining the final solution. The southwestern flank is defined by arrivals from OBS Q, sonobuoys 11 and 12, and OBS O shooting southwest. However, the last two of these receivers are better suited to defining the transitional area from the southwest flank into the extinct spreading centre. The range from 0 to 30 km is well defined by the ray paths from OBS Q and sonobuoy 11. A typical oceanic structure is observed in this region with a high velocity gradient in the upper crust (isovelocity contours 4 km/s to 6 km/s in Fig. 4.2), a lower velocity gradient in the lower crust (isovelocity contours 6 km/s to 8 km/s in Fig. 4.2), and a nominal crustal thickness of 5.5 km (Fig. 6.5c). The model parameterization effectively extends this structure from 30 to 60 km because no velocity or boundary nodes are specified in this interval (Fig. 4.1). The apparent homogeneity in the final velocity-depth structure from 30 to 60 km is thus an artifact of nodal density in this region.

The northeast flank, by contrast, is well resolved with better ray coverage and additional information from the  $P_mP$  arrivals. The  $P_3$  (Fig. 4.5) and  $P_mP$  (Fig. 4.6) arrivals from OBS N shooting northeast, OBS M shooting both directions, and OBS L shooting southwest define the features of this region. The character of the observed travel times from the lower crust differs appreciably for these four refraction profiles when compared to arrivals from the OBSs sampling the southwest flank or the extinct spreading centre. The arrivals at the northeast flank receivers are of considerably higher velocity and extend to greater shot-receiver offsets. To model the lower crust refractor velocities, upper

boundary velocities from 6.89 km/s to 7.19 km/s and lower boundary velocities from 7.54 to 7.71 km/s are required in the fastest region from 130 to 170 (Appendix C). In addition, a thickening of the crust (by approximately 1 km) and weak velocity gradient are required to match the shot-receiver offsets to which  $P_3$  and  $P_mP$  arrivals are observed. From 190 to 220 km, the crustal thickness (Fig. 6.5c) is comparable to that observed on the southwest flank from 0 to 50 km, but the high velocities in the lower crust remain.

There are several observations of a high velocity lower crustal layer in the Labrador Sea (Table 4.2) at widely spaced locations northeast of the extinct spreading centre. However, it is not possible, at this time, to assess the prevalence of this material because all but one of these observations (Line F, Stergiopolous [1984]) are from unreversed sonobuoys which may be influenced by sediment thickness variations or dipping interfaces. In addition, there are observations of normal lower crustal velocities northeast of the extinct spreading centre (Sonobuoys 3, 22, and possibly 20 [Hinz *et al.*, 1979]). The presence of this high velocity lower crustal material northeast of the extinct spreading centre on line R2 may be related to hot spot activity from the time of anomaly 24 until the cessation of spreading [Srivastava *et al.*, 1989], but knowledge of its regional extent will be required to address this speculation.

On the northeast flank of the extinct spreading centre,  $P_mP$  arrivals were also observed and used to define the velocity gradient structure of the lower crust. They are second arrivals which are difficult to pick because of interference with the wavetrain from earlier arrivals. Accordingly, they were assigned the largest uncertainties of all arrivals and are intentionally the most poorly fit ( $0.6 \leq \chi^2 \leq 3.8$ ). The final velocity-depth

**Table 4.2:** Previous observations of high velocity lower crust northeast of the extinct spreading centre in the Labrador Sea

Station Identifier	Latitude	Longitude	Magnetic Anomaly	Lower Crustal Velocity (km/s)	Type of Observation	Interpretation Techniques	Reference
Line A	line midpoint 61.5°N	line midpoint 50.8°W	In quiet zone off Greenland Margin	7.64	Unreversed refraction profile for sonobuoy 1A	1-D raytracing with head wave arrivals	Stergiopoulos [1984]
Line F	line midpoint 60.0°N	line midpoint 52.0°W	Between 27 and 28	7.22	Reversed refraction profile for sonobuoys 10 and 11	1-D raytracing with head wave arrivals	Stergiopoulos [1984]
ODP site 646	58.13°N	48.23°W	24	7.5	Unreversed sonobuoy refraction profile	1-D synthetic seismograms	Srivastava <i>et al.</i> [1989]
15/77	62.0°N	55.3°W	In quiet zone off Greenland Margin	7.5	Unreversed sonobuoy refraction profile	1-D plane layer solution	Hinz <i>et al.</i> [1979]

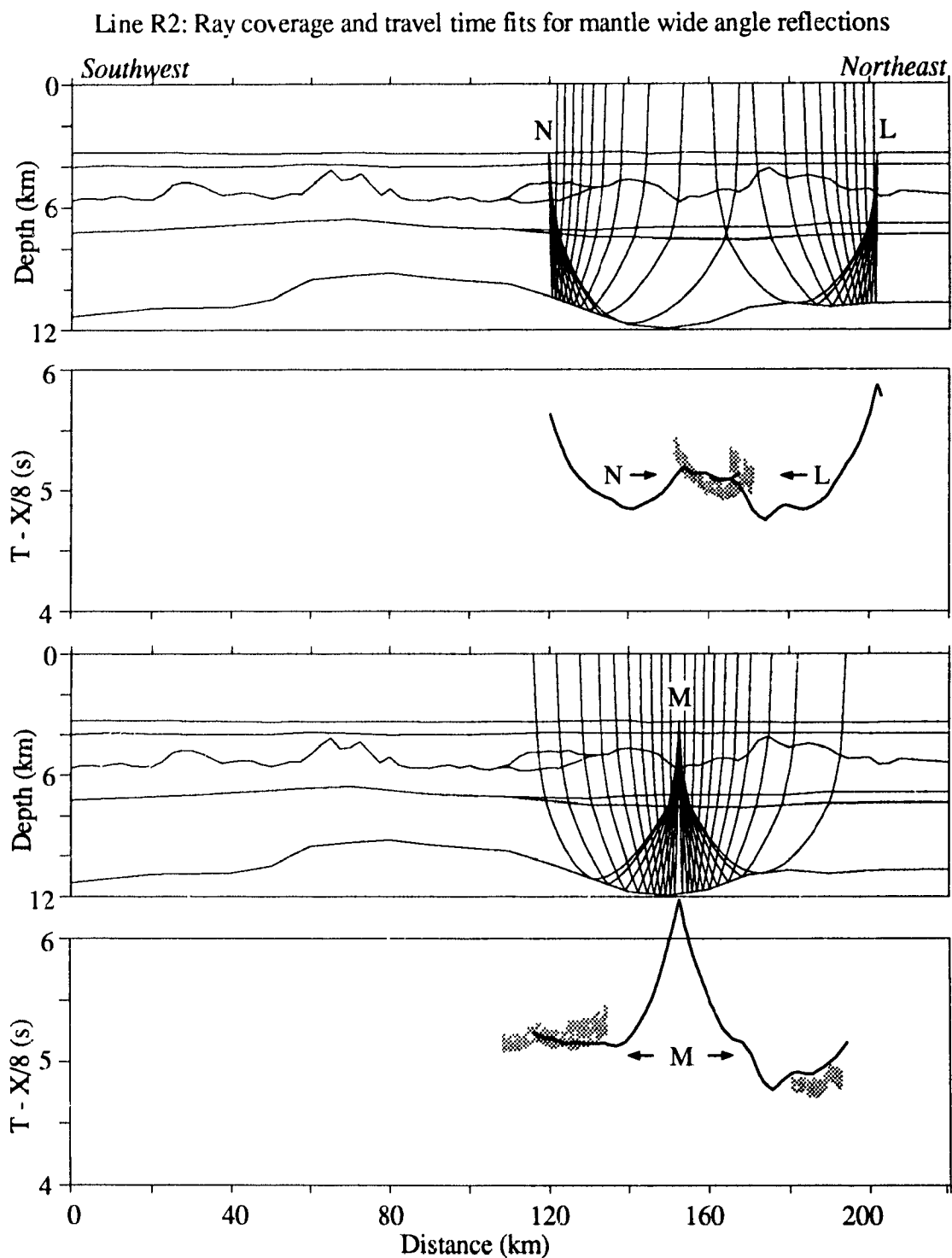


**Figure 4.6:** Computed ray paths and travel times for the mantle wide angle reflection, PmP, at OBSs L, M, and N using the 2-D velocity-depth structure along line R2 (Fig. 4.2). Observed travel times and their uncertainties are represented by the stippled areas through which the computed arrival times are traced. Ray paths converge to their corresponding receivers.

structure which accommodates the four sets of observed  $P_mP$  arrivals from OBS M, OBS L shooting southwest, and OBS N shooting northeast is a compromise between a number of competing factors as demonstrated by the following examples.

First, consider the region of rapid crustal thinning from 140 to 120 km (Figs. 4.1 and 6.5c). OBS M shooting southwest requires a combination of slope on the crust-mantle boundary and high lower crustal velocities to reproduce the high (greater than 8 km/s) apparent move-out velocities of  $P_mP$ . The fit of computed  $P_mP$  arrivals for this OBS ( $\chi^2=0.58$ ) and for OBS N shooting northeast ( $\chi^2=1.78$ ) could be improved by more rapid crustal thinning, producing a steeper slope on this boundary. However, the  $P_n$  arrivals from OBS N shooting northeast (Fig. 4.8) are very sensitive to the slope of this boundary. A steeper slope broadens the shadow zone which is produced by rays entering the mantle in a region of crustal thinning and then being refracted below a region of crustal thickening. As the shadow zone broadens, the number of observed arrivals to which rays are traced decreases, which is clearly an undesirable consequence.

For a second example of these compromises, consider the  $P_mP$  arrivals from OBS M shooting northeast and OBS L shooting southwest (Fig. 4.6). The observed arrivals are from reflections off neighbouring regions of the crust-mantle interface (~180 to 190 km for OBS L and 170 to 180 km for OBS M) and the upward branch of their ray paths overlap the same region of the crust. However, the arrival times at OBS L are too early ( $T_{RMS}=0.171$  s) while those at OBS M are too late ( $T_{RMS}=0.132$  s). To reduce  $T_{RMS}$  for  $P_mP$  arrivals, the travel time of the downward branch of the ray paths would have to be adjusted by revisions to the crustal velocity or thickness near the OBSs. Such changes,

however, degrade the quality of the first arrival  $P_2$ ,  $P_3$ , and  $P_n$  travel time fits. Given that  $P_mP$  is a second arrival, revisions near the OBS were only made to the extent of balancing the travel time misfits of  $P_mP$  as evenly as possible and not necessarily minimize it.

#### 4.5.3 Mantle Layer

The model layer defining the mantle is number 8 in the model parameterization (Fig. 4.1). Ray paths and travel times for  $P_n$  are displayed in Figures 4.7 through 4.9, with the shooting for each receiver being plotted on a separate plot panel.  $P_n$  arrivals are used to define the thickness of the crust and the velocity of the uppermost mantle. These two quantities exhibit significant variations along length of line R2, primarily in relation to the extinct spreading centre.

In fitting the observed arrivals for  $P_n$ , a concerted effort was made to minimize  $T_{RMS}$  at all receivers and keep it within the uncertainty of the travel time picks (*i.e.*  $\chi^2 \leq 1$ ). This goal was achieved for 7 of the ten 10 sets of observed arrivals (Table 4.1). The final velocity-depth structure (Fig. 4.2) is an optimal fit in the sense that further revisions to the model to minimize  $T_{RMS}$  for one receiver would increase  $T_R$  for another receiver. For example, the largest of the  $P_n$  travel time residuals ( $T_{RMS} = 0.119$  s) at OBS M shooting northeast (Fig. 4.9) may be reduced by thinning the crust or increasing the mantle velocity between 170 and 220 km. However, the arrivals for OBS L shooting southwest (Fig. 4.9) also travel through this region of the mantle and arrive too early ( $T_{RMS} = 0.86$ ). A modification to reduce  $T_{RMS}$  at OBS M would therefore increase  $T_{RMS}$  at OBS L. Once such limits to the model revisions are encountered, the remaining travel time residuals may be attributed to the following: 1) limitations of 2-D methodology, with

rays travelling outside of the distance-depth plane assumed in the 2-D velocity-depth structure; 2) there are variations in the structure of an overlying layer which are not adequately resolved by the existing data; or 3) unaccounted timing errors remain at various receivers.

The isovelocity contours in Figure 4.2 show low velocities (less than 8 km/s) in the uppermost mantle in three locations. While these contours are only defined by nodes along the upper and lower boundary of the mantle layer, they do correctly represent the velocity gradient structure which rays encounter while refracting through the mantle. Based on these contours, the thickest of these low velocity regions underlies the extinct spreading centre and extends to a maximum depth of 4.3 km below the crust-mantle boundary. The upper mantle velocities within the extinct spreading centre are the most well constrained in the model because of the number of overlapping ray paths and the confidence in the crustal structure overlying the mantle (section 4.5.2). The quality of the travel time fits is particularly good ( $0.239 \leq \chi^2 \leq 0.578$ ) for the receivers which have  $P_n$  ray paths crossing, or entering the mantle within, the extinct spreading centre (OBS E, OBS O shooting northeast, OBS N shooting southwest, and OBS M shooting southwest).

The depth extent of the low velocity zone underlying the extinct spreading centre complements the results obtained by 1-D synthetic seismogram modelling for OBS G (Fig. 3.10). This 1-D synthetic seismogram suggested that a relatively strong gradient existed in the uppermost mantle to a depth of 3 km below the crust-mantle boundary. The lowest nodal velocity along the crust-mantle boundary is 7.82 km/s and occurs at 90 km. This is 1% higher than the line R1 average mantle velocity of 7.74 km/s (Table 3.1).

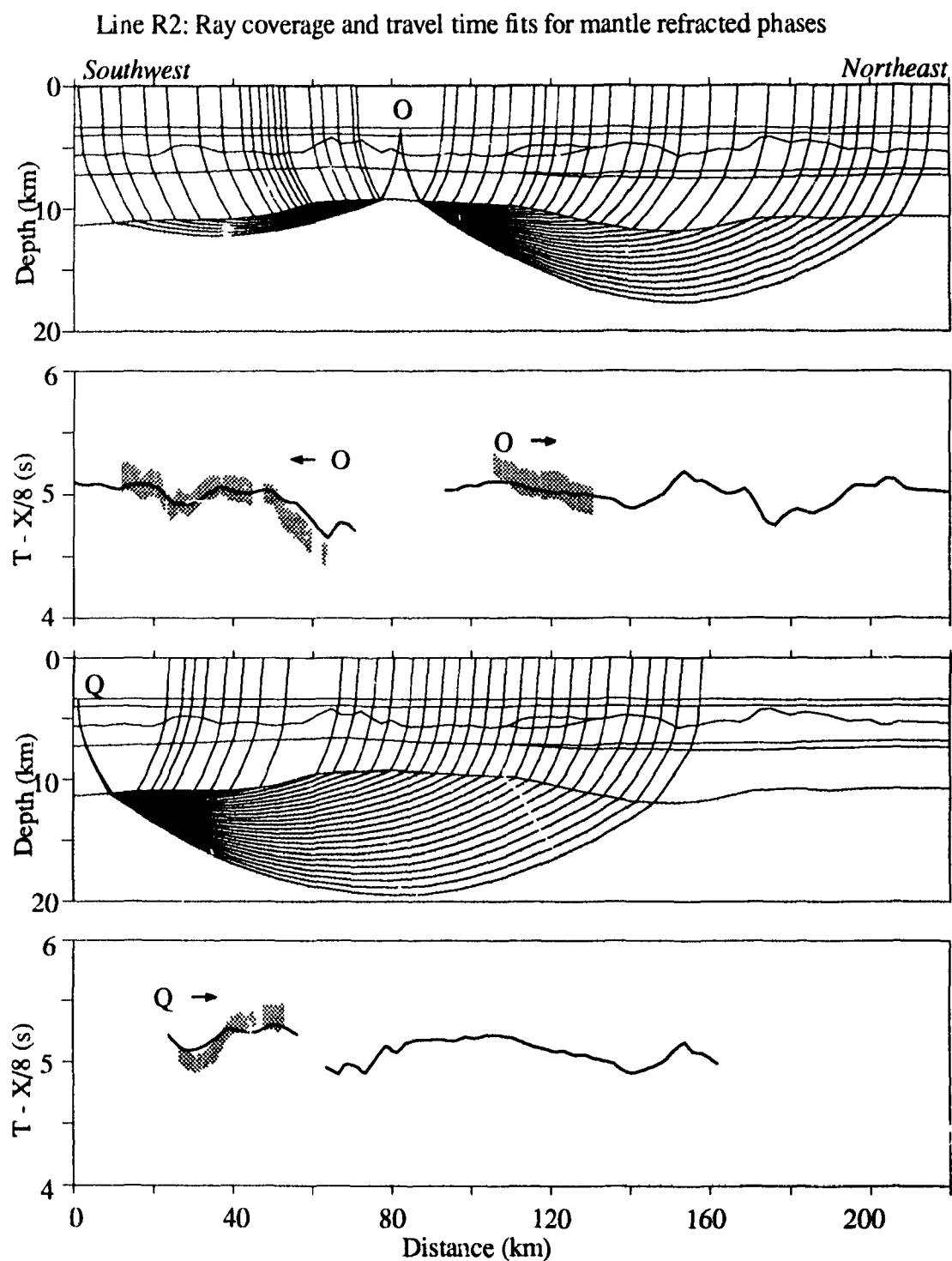


**Figure 4.7:** Computed ray paths and travel times for refractions,  $P_n$ , in the mantle (shaded grey) at OBSs O and Q using the 2-D velocity-depth structure along line R2 (Fig. 4.2). Observed travel times and their uncertainties are represented by the stippled areas through which the computed arrival times are traced. Ray paths converge to their corresponding receivers.

Line R2: Ray coverage and travel time fits for mantle refracted phases

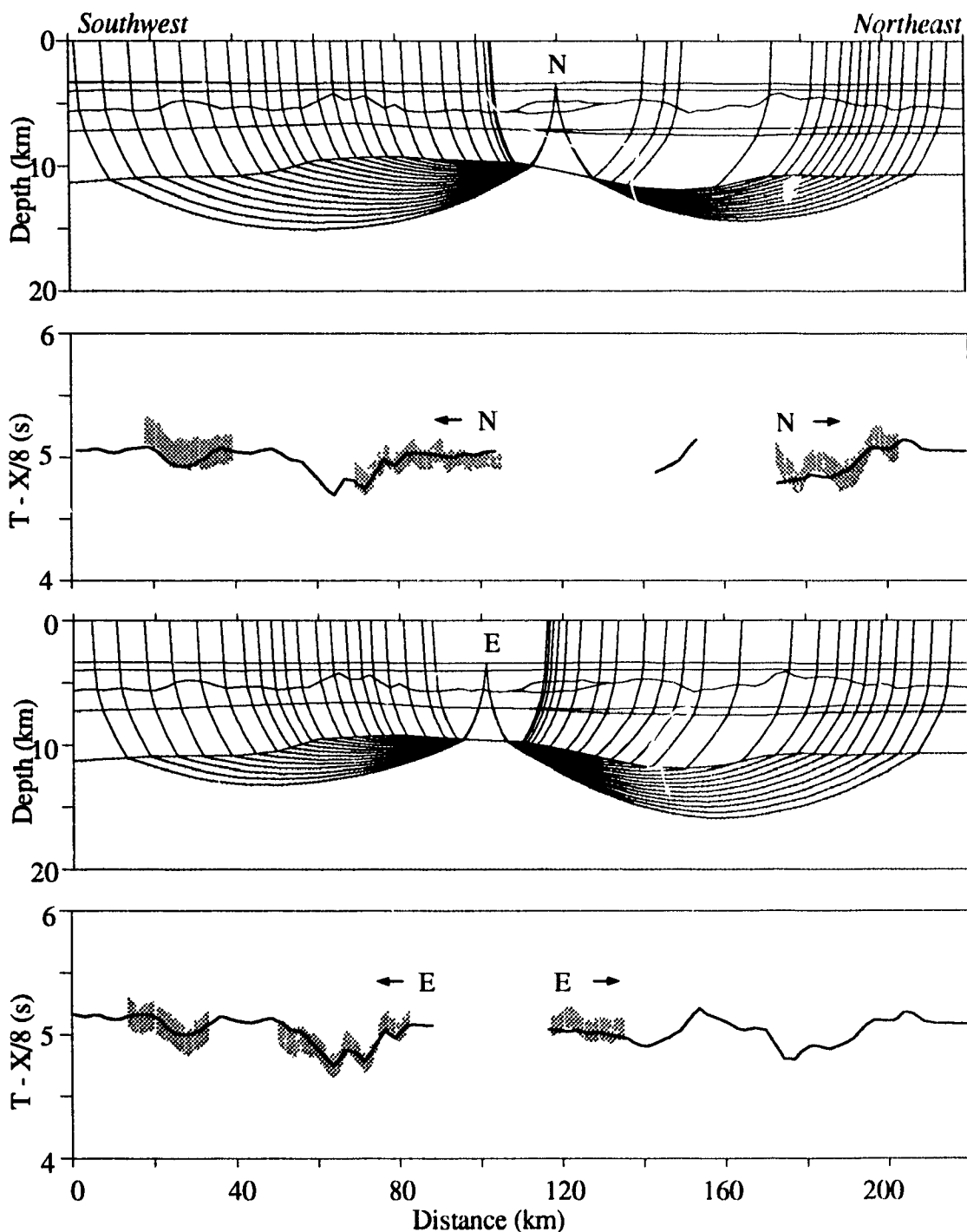


**Figure 4.8:** Computed ray paths and travel times for refractions, P<sub>n</sub>, in the mantle (shaded grey) at OBSs N and E using the 2-D velocity-depth structure along line R2 (Fig. 4.2). Observed travel times and their uncertainties are represented by the stippled areas through which the computed arrival times are traced. Ray paths converge to their corresponding receivers.

## Line R2: Ray coverage and travel time fits for mantle refracted phases

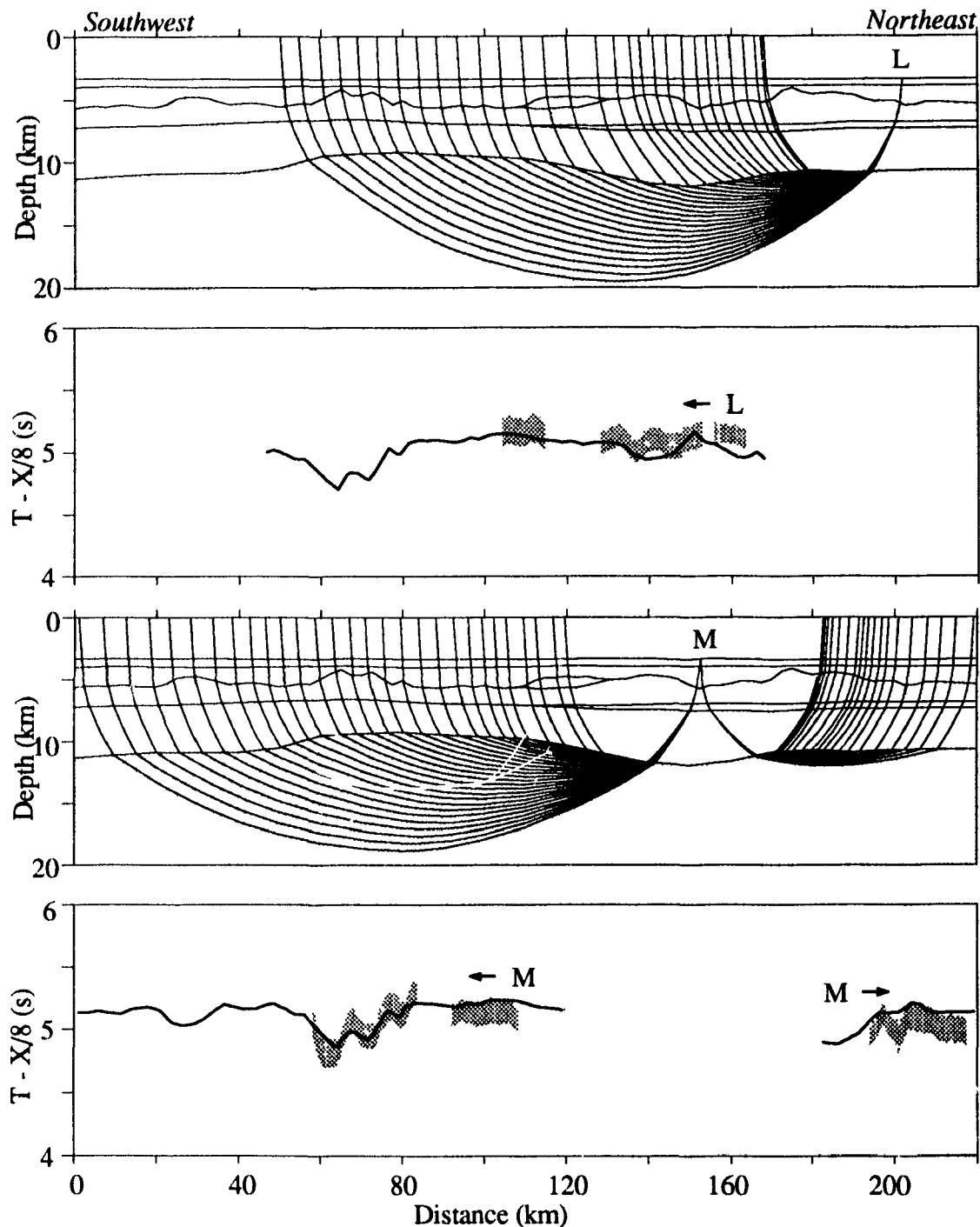


**Figure 4.9:** Computed ray paths and travel times for refractions,  $P_n$ , in the mantle (shaded grey) at OBSs L and M using the 2-D velocity-depth structure along line R2 (Fig. 4.2). Observed travel times and their uncertainties are represented by the stippled areas through which the computed arrival times are traced. Ray paths converge to their corresponding receivers.

The role of the mantle arrivals in defining the transition from typical oceanic crustal structures to the distinct crustal type within the extinct spreading centre was eluded to in section 4.5.2.  $P_n$  arrivals from OBS O shooting southwest (Fig. 4.7) are particularly helpful in defining this transition for the southwest flank of the extinct spreading centre. The slope on the crust-mantle boundary is revealed as arrivals from 45 to 60 km are up to 0.4 s earlier than those from 10 to 45 km. OBS Q shooting northeast (Fig. 4.7) also defines the crust-mantle boundary on the southwest flank. For this receiver, the  $P_n$  arrivals terminate abruptly at 55 km at a shadow zone generated by the rapid crustal thinning.

The transition from the thin crust within the extinct spreading centre to normal thicknesses on the northeast flank is not as easily discerned. In this case, the high velocity lower crust in this region (section 4.5.2) counteracts the delay which  $P_n$  would otherwise exhibit as the crust thickens. However, as discussed in section 4.5.2, there is evidence for slope on the crust-mantle boundary from the move-out of  $P_mP$  and the shadow zone generated for  $P_n$  arrivals from OBS N shooting northeast.

#### **4.6 Error Analysis**

A unique feature of the RAYINVR algorithm is the ability to provide quantitative estimates of the spatial resolution and absolute uncertainty of representative boundary and velocity nodes. A final model which was determined by an inversion is a pre-requisite for the procedures to obtain these estimates. Following Zelt and Smith [1992], an estimate of the parameter's absolute uncertainty is obtained by: 1) perturbing the value of a node from that in the final model; 2) inverting the observed data and involving all other parameters determined at the same time as the perturbed parameter during inversion for

the final model; 3) repeating steps 1 and 2 while increasing the perturbation until the new inverted model is unable to fit the observed data as well as the original final model.

Spatial resolution about a single node in the final model may be assessed by the following steps: 1) perturb the value of the node by an amount on the order of its estimated uncertainty; 2) trace rays through the perturbed model to calculate the associated travel times; 3) interpolate these at the observed locations and assign the observed travel time uncertainty at each location; 4) reset the value of the node to its value in the final model and 5) invert the calculated data involving all model parameters that were determined at the same time as the selected parameter during the inversion for the final model. The spatial resolution is indicated by the amount by which the values of adjacent parameters differ from corresponding values in the final model.

The choice of matrix inversion methodology employed in the DMPLSTQ inversion algorithm presupposes that the number of model parameters is much less than the number of observations. In an attempt to meet this requirement and produce a "final" model determined through an inverse step, the number of nodes was reduced from the initial model parameterization (section 4.3) and beyond that displayed in the parameterization of the actual final model (Fig. 4.1). The nominal spacing between nodes was increased to as much as 25 km; however, the quality of models determined by inversions remained problematic. Inversions might give rise to low velocity zones or, more commonly, boundary oscillations which produced geometric shadow zones and a decrease in the number of rays traced to observed locations. Further, reducing the number of nodes to stabilize the inversion resulted in a marked decrease in the quality of the travel time fits;

the denser distributions of nodes was required to adequately parameterize the heterogeneous structure.

A noteworthy example among the attempts to perform error analysis on the final model (Fig 4.2) involved the nodes defining the crust-mantle boundary from 70 to 120 km. These nodes define a significant crustal thinning in the area of the extinct spreading centre. This is an important observation and one for which estimates of the absolute parameter uncertainty are desirable. These nodes should also be among the most well constrained as 5 receivers have observed travel times for mantle ray paths crossing the crust-mantle boundary. In practice, iterations of model inversions would never converge to a final solution and usually generated geometric shadow zones, particularly for OBS E (shooting northeast) and OBS N (shooting southwest) which are quite sensitive to changes in the crust-mantle boundary which exceed 0.2 km.

As an alternative to the inverse techniques of Zelt and Smith [1992], error analysis of the model parameters defining the crust-mantle boundary was performed by perturbing model parameter values and then raytracing through the perturbed model. In the first of two approaches, the degree of crustal thinning within the extinct spreading centre, as defined by boundary nodes from 40 to 140 km along line R2, was progressively decreased (Fig. 4.10a) until the crust-mantle boundary was linear between the 40 km and 140 km endpoints. The degree of crustal thinning was decreased in 10% intervals; in Figure 4.10b,  $\chi^2$  values using mantle arrivals at all OBSs are presented for each of these perturbed models. Following the criteria of fitting computed arrivals to within the uncertainty assigned to the observed travel time picks ( $\chi^2 \leq 1$ ), no more than 25% of the crustal

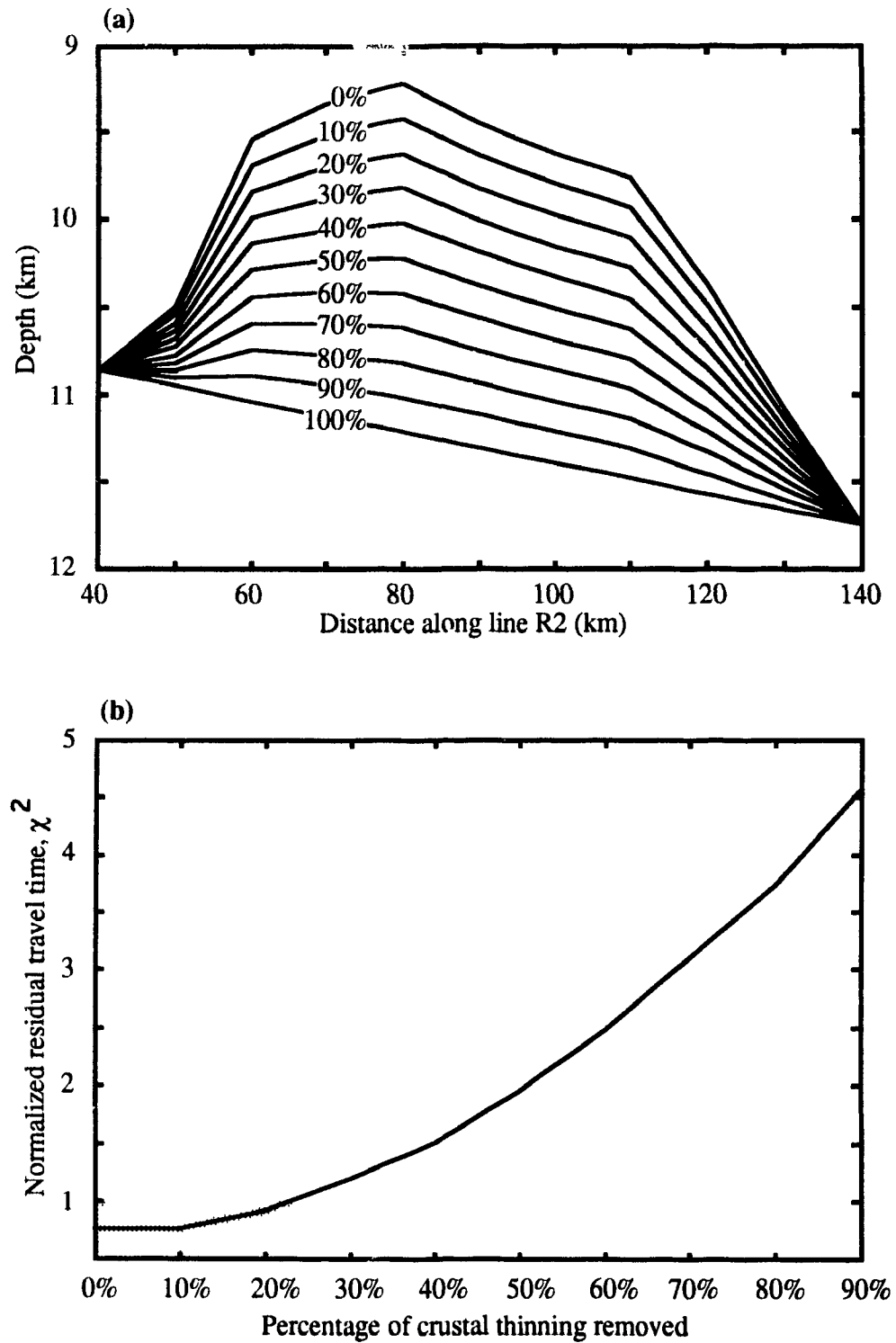


**Fig. 4.10:** (a) Percentage of crustal thinning removed within the extinct spreading centre from 40 to 140 km along line R2 and (b) the influence of decreasing the degree of crustal thinning on the quality of fit between observed and calculated arrival times for all mantle arrivals.

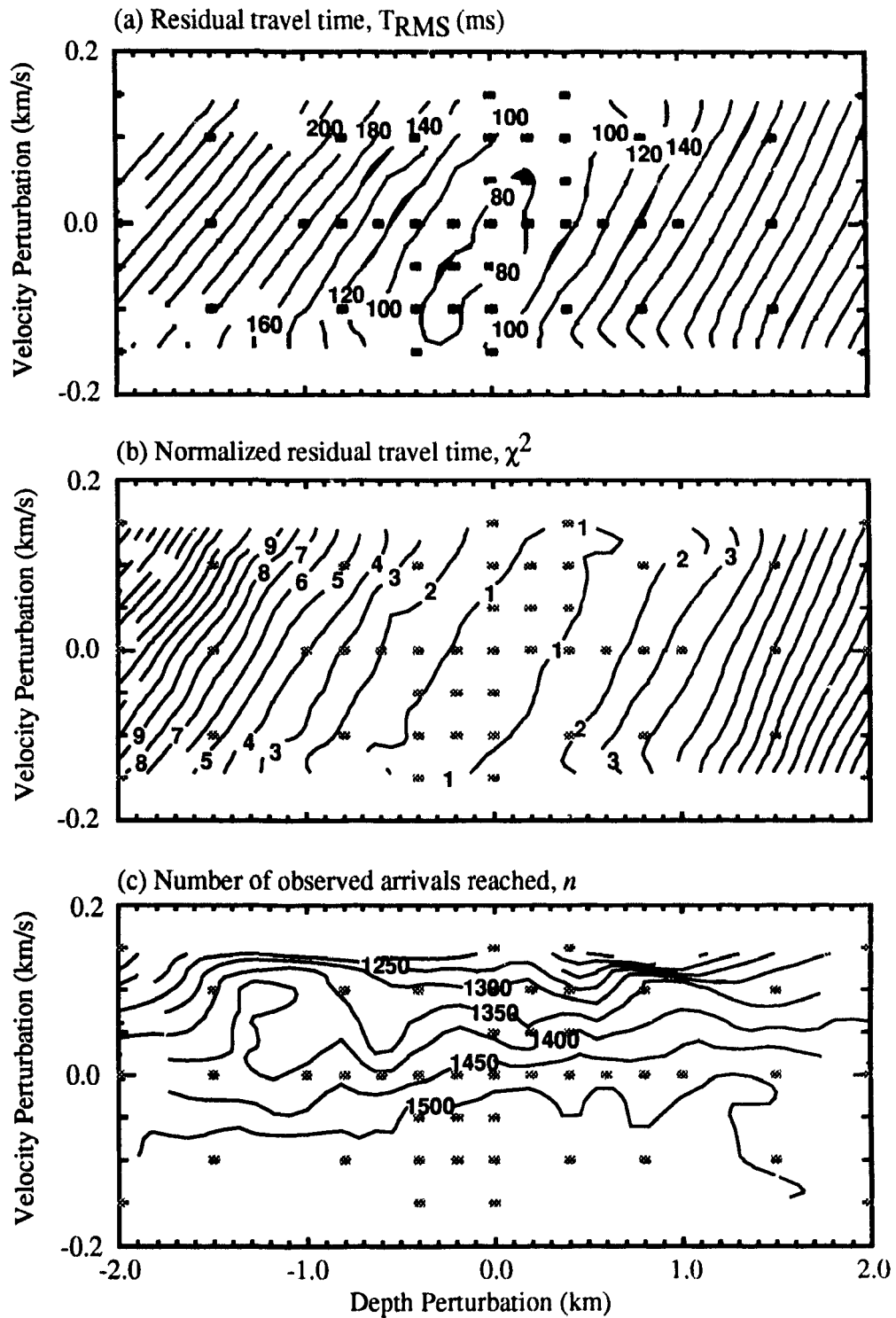


**Fig. 4.11:** Velocity and depth perturbations (star symbols) are introduced to nodes which form the crust-mantle boundary in the final velocity-depth structure for line R2 (Fig. 4.2). The effect of these perturbations on the quality of the model fit is assessed by plotting contours of (a)  $T_{RMS}$ , (b)  $\chi^2$  and (c)  $n$

thinning may be removed before travel time fits are no longer acceptable.

In the second approach, a constant velocity and/or depth perturbation was applied to all nodes comprising the crust-mantle boundary. Raytracing ensued with the calculation of an average  $T_{\text{RMS}}$ , an average  $\chi^2$ , and  $n$  using the mantle arrivals at all OBSs. Contours of these quantities are presented in Figures 4.11a, 4.11b, and 4.11c respectively as a function of the velocity and depth perturbation magnitude. The  $T_{\text{RMS}} = 80$  msec and  $\chi^2 = 1$  contours show a preferred orientation to plausible perturbations. Increases in  $P_n$  velocity are complementary with positive depth perturbations (crustal thickening) and decreases in  $P_n$  velocity are complementary with negative depth perturbations (crustal thinning). However, for positive velocity perturbations exceeding 0.05 km/s, the number of observed arrivals which are reached by the rays begins decreasing markedly (Fig. 4.11c). This arises because increases in the upper mantle velocities decrease the velocity gradient of the mantle layer to a point where it is too weak to refract rays to the shorter shot-receiver offsets for mantle arrivals. On the basis of the dimensions of the 80 msec  $T_{\text{RMS}}$  contour and the rejection of positive velocity perturbations, average uncertainties of  $\pm 0.25$  km and  $\pm 0.08$  km/s can be assigned to the depth and velocity nodes comprising the crust-mantle boundary.

#### 4.7 Synthetic Seismograms

Synthetic seismic refraction profiles were generated for the receivers along line R2 using the final velocity-structure (section 4.5). The synthetic seismograms were computed using TRAMP, a geometrical ray theory algorithm for inhomogeneous structures written by Zelt [1992]. The impulse response seismograms generated by the

program contain the time, theoretical amplitude and phase of arrivals for a given shot-receiver offset and region of the velocity-depth structure. The impulse response is subsequently convolved with a user specified source function, representative of the source used in the experiment. In this case, the exponentially damped cosine function of Cerveny [1977] was used as the source function:

$$f(t) = \exp\left(-\left(\frac{2\pi f_m}{\gamma}\right)^2 t^2\right) \cos(2\pi f_m t + v) \quad (\text{Eqn. 4.4})$$

Where:  $f_m$  = Dominant frequency of source

$\gamma$  = damping factor

$v$  = phase shift

The wavelet used in producing the synthetic seismograms for receivers along line R2 is shown in Figure 4.12b while the wavelet used in the comparison between synthetic seismogram algorithms (section 4.7.1) is shown in Figure 4.12a. In the latter case, the wavelet has a shorter time duration and is damped rapidly, allowing for the first and second arrivals in the synthetics to be readily distinguished. The opposite effect is sought in producing synthetic seismograms for the receivers along line R2, where a long wavetrain, 3 full wavelengths (approximately 450 ms), often obscures the second arrival information. To represent these characteristics of the source function, the wavelet for the line R2 synthetics has a weak damping ( $\gamma=5.6$ ) and a phase shift ( $v=\pi/3$ ) to move the peak positive amplitude earlier in the wavelet and suppress the amplitude of the first peak in the wavetrain (centred at -0.16 s in Fig. 4.12b).

#### 4.7.1 Comparison of WKBJ and TRAMP synthetic seismograms

As the TRAMP algorithm is new, a test was conducted to compare the amplitude

distribution which it computes with that of a more well established algorithm, Chapman's 1-D WKBJ [1977]. The 1-D velocity-depth structure in Figure 4.12c was devised for this purpose. It has layer thicknesses, velocities, and velocity gradients which are typical of those found for the flanks of the extinct spreading centre in the final velocity-depth structure (section 4.5). The 1-D test synthetic seismograms (Fig. 4.13) include (1) head waves and wide angle reflections from the sediment-crust and successively deeper boundaries and (2) refracted (diving) rays from the sediment, crust and mantle layers. Arrivals from the uppermost layers were not considered as these high amplitude reflections aren't typically used in seismic refraction interpretation and their inclusion masks the emergence of the lower amplitude refracted arrivals at short shot-receiver offsets.

The traces in both synthetic refraction profiles have received the same scaling as a function of shot-receiver offset. The global gain applied to all traces in a refraction profile was adjusted such that the amplitude of the crustal refractions (first arrivals from 10 to 20 km) matches in the two profiles. These arrivals were chosen for the point of normalization as they are arrivals for which asymptotic ray theory is entirely valid. There is a static time shift of 0.1 s between the two synthetic refraction profiles. This stems from the convolution, as the WKBJ algorithm performs the convolution in frequency space with the peak amplitude of the wavelet centred about the impulse function response. The TRAMP algorithm, by contrast, performs the convolution in the time domain and offsets the peak amplitude of the wavelet by one half of its time length.

In comparing the TRAMP synthetics (Fig. 4.13a) with the WKBJ synthetics (Fig.

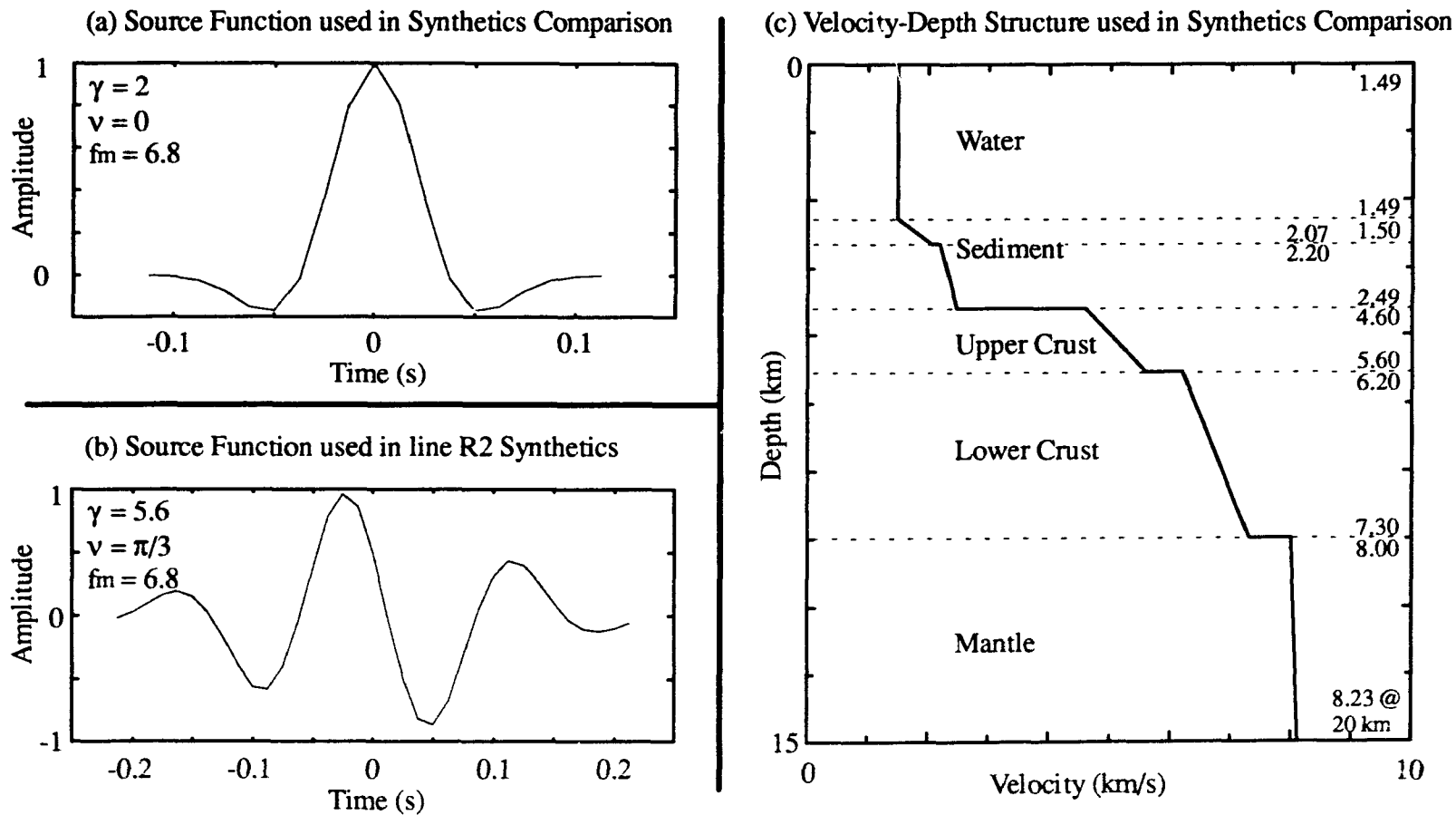


**Figure 4.12:** Source functions convolved with the impulse response to produce the synthetic seismograms for (a) 1-D test between WKBJ and TRAMP algorithms and (b) for receivers along line R2 using the 2-D velocity-depth structure. Panel (c) presents the 1-D velocity-depth structure used in testing the synthetic seismogram algorithms. Layer boundaries are marked by dashed with velocities (km/s) as marked above and below the boundaries.

### Comparison of Synthetic Seismogram algorithms

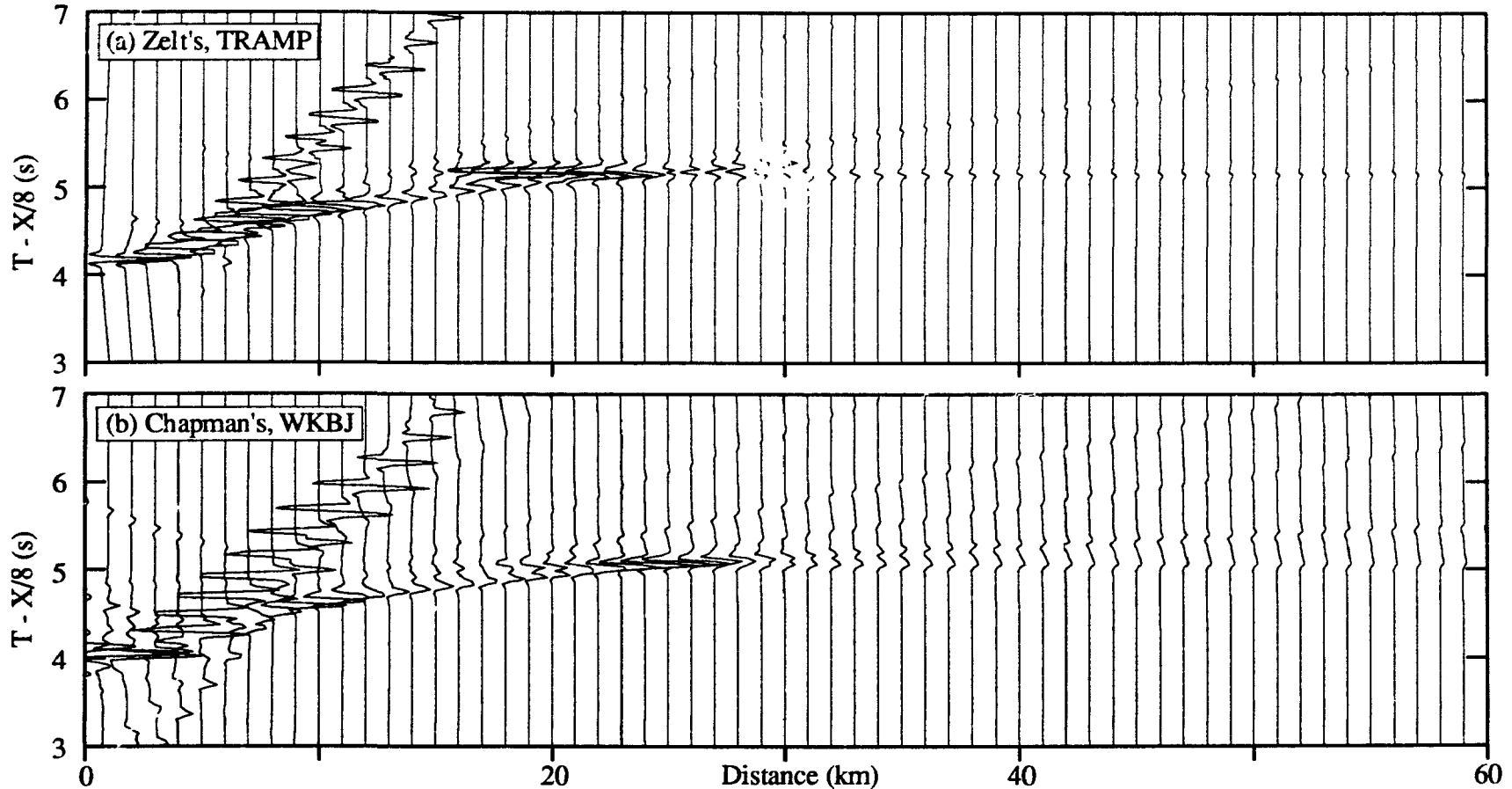


**Figure 4.13:** Synthetic seismograms through the 1-D velocity-depth structure in Fig. 4.10. (a) Using Chapman *et al.*'s [1988] WKBJ algorithm and (b) using Zelt's 2-D asymptotic ray theory algorithm. Both synthetics use the same source function (Fig. 4.10a) and gain as a function of range. Head waves, wide angle reflections and refracted arrivals from all layers/boundaries deeper than the mid-sediment boundary are included in the synthetics as detailed in the text.

4.13b), the prevalent distinction is the position and amplitude of the  $P_mP$  arrivals. They are the prominent high amplitude second arrivals from 16 to 24 km for the TRAMP algorithm (Fig. 4.13a) and from 18 to 27 km for the WKBJ algorithm (Fig. 4.13b). The shot-receiver offset at which the peak amplitude of  $P_mP$  arrivals is observed is 6 km greater in the WKBJ synthetics and the WKBJ synthetics also show energy from  $P_mP$  and  $P_3P$  beyond the critical point. Further, the amplitude of the  $P_mP$  phase builds up very rapidly in the TRAMP synthetics while it is more gradual in the WKBJ synthetics. The amplitudes of the refracted arrivals compare favourably except for the mantle refraction in an interval from just beyond the critical point to a range of 40 km. In the TRAMP synthetics (Fig. 4.13a), the amplitude of this refractor is lower than its counterpart in the WKBJ synthetics.

These observations are consistent with previous comparisons of asymptotic ray theory and its extensions (the WKBJ approximation) [*e.g.* Chapman, 1985]. Specifically, asymptotic ray theory breaks down in a number of situations: caustics, critical points, diffractions. In these cases, the amplitude function can vary rapidly and does not properly determine amplitudes. The WKBJ approach, by contrast, is more general and its amplitude function remains valid. As the distinctions observed between the TRAMP and WKBJ synthetics (Fig. 4.13) are centred about the critical point for the mantle arrivals, the limitations of asymptotic ray theory are most likely responsible. These limitations faced by the TRAMP synthetics should be recalled when considering the synthetic seismograms in Figures 4.14 to 4.19. The prime differences which emerge from the comparison of observed and synthetic refraction profiles in section 4.7.2 are the shot-receiver offsets to

which  $P_mP$  arrivals are traced, their rapid cut-off, and the low amplitude of the mantle refractor just beyond the critical point.

#### *4.7.2 Synthetic seismograms for receivers along line R2*

Confidence that a velocity-depth structure is an adequate representation of the actual seismic crustal structure can be gained by visually comparing synthetic and observed refraction profiles. If the observed amplitude variations are reproduced successfully, then the velocity-depth structure is qualitatively validated. To this end, 2-D synthetic seismograms were generated for line R2 as a means whereby the final velocity-depth structure obtained by travel time modelling (section 4.6) may be further validated. In practice, the amplitude modelling spawned a further round of revisions to the velocity-depth structure produced by the travel time modelling. In particular, modifications were required to reproduce the  $P_mP$  amplitude patterns for OBSs on the northeast flank of the extinct spreading centre.

The synthetic seismograms for receivers along line R2 were computed using the final velocity-depth structure (Fig. 4.2) and are presented in Figures 4.14 to 4.19. For each synthetic refraction profile, the location of the receiver and direction of shooting are indicated by the small insets superimposed on the profile. The synthetic refraction profiles may be compared directly with the observed data (Figures A.1 - A.6) as they have been plotted with identical time scales, reducing velocity, and gain function. Travel time curves from the 2-D raytracing are also superimposed on the observed refraction profiles.

OBS L: The synthetic refraction profile for OBS L shooting northeast is presented in Figure 4.14a and the observed profile is presented in Figure A.1. The amplitude

build up of the  $P_mP$  arrivals at 30 km due to topographic focusing, the interference of  $P_3$  and  $P_mP$  from 25 to 27 km, and the rapid amplitude decrease and transition to  $P_n$  arrivals by 40 km are well modelled in the synthetics. The most poorly matched feature in this synthetic is the amplitude of  $P_3$  from 12 to 19 km; it decreases rapidly in the synthetics while remaining relatively strong in the observed data. This lack of energy in the synthetics arises from the strong velocity gradient in the upper crust which was required to match the travel time information.

OBS M: The synthetic refraction profiles for OBS M are presented in Figures 4.15a (shooting southwest) and 4.15b (shooting northeast) and the observed profiles are presented in Figure A.2. Shooting southwest, the high amplitude  $P_mP$  arrivals from 18 to 48 km in the observed data are matched in the synthetics from 18 km to 39 km, at which point the  $P_mP$  arrivals terminate abruptly. The gap with no second arrivals and weaker first arrivals from 15 to 19 km in the observed data is also produced in the synthetics, but the interval is shifted to 17 to 21 km. The observed  $P_n$  arrivals for this receiver are particularly strong from 80 to 90 km as rays enter the southwest flank of the extinct spreading centre. The synthetics do not replicate this behaviour. Shooting northeast, the synthetic is a particularly good representation of the data. The low amplitudes surrounding the basement high (shot point 700) are present in both the synthetics and observed data from 19 to 24 km. On either side of this feature, the synthetics match the high amplitude arrivals from 10 to 19 km and 25 to 45 km.

OBS N: The synthetic refraction profiles for OBS N are presented in Figures 4.16a (shooting southwest) and 4.16b (shooting northeast) and the observed profiles are

presented in Figure A.3. The observed arrivals for OBS N exhibit a tremendous asymmetry between shooting directions, into the extinct spreading centre to the southwest and into a flank structure to the northeast. This asymmetry is well replicated in the synthetics. For arrivals shooting to the northeast, the broad range (20 to 50 km) over which  $P_mP$  arrivals exist and the abrupt termination at 50 km are well modelled. The prevalent amplitude build up from 34 to 50 km in the observed data is not emphasized in the synthetics which have shifted the locus of energy to the 26 to 33 km range where weak arrivals are found in the observed data. Shooting to the southwest, the strong amplitudes from crustal arrivals and absence of a discernable  $P_mP$  phase are well modelled in the synthetics. The energy in the  $P_n$  arrivals in the observed data from 23 to 45 km (and OBSs, see discussion for OBS E) is not produced in the synthetics.

OBS E: The synthetic refraction profiles for OBS E are presented in Figures 4.17a (shooting southwest) and 4.17b (shooting northeast) and the observed profiles are presented in Figure A.4. The observed arrivals and synthetics are very similar to those for OBS N shooting southwest. Once again, the amplitude of the upper and lower crust refractors is strong and well modelled in the synthetics as the energy is refracted by the near linear velocity gradient throughout the crust within the extinct spreading centre. As with OBS N shooting southwest, the high amplitudes in the observed crustal arrivals are followed by strong  $P_n$  arrivals from 20 to 30 km. The synthetics put very little energy into these  $P_n$  arrivals just beyond the critical point despite a relatively strong velocity gradient ( $0.04 \text{ s}^{-1}$ ) for the upper mantle in this region.

OBS O: The synthetic refraction profiles for OBS O are presented in Figures

### Synthetic Seismic Refraction Profiles for OBSs Q and L

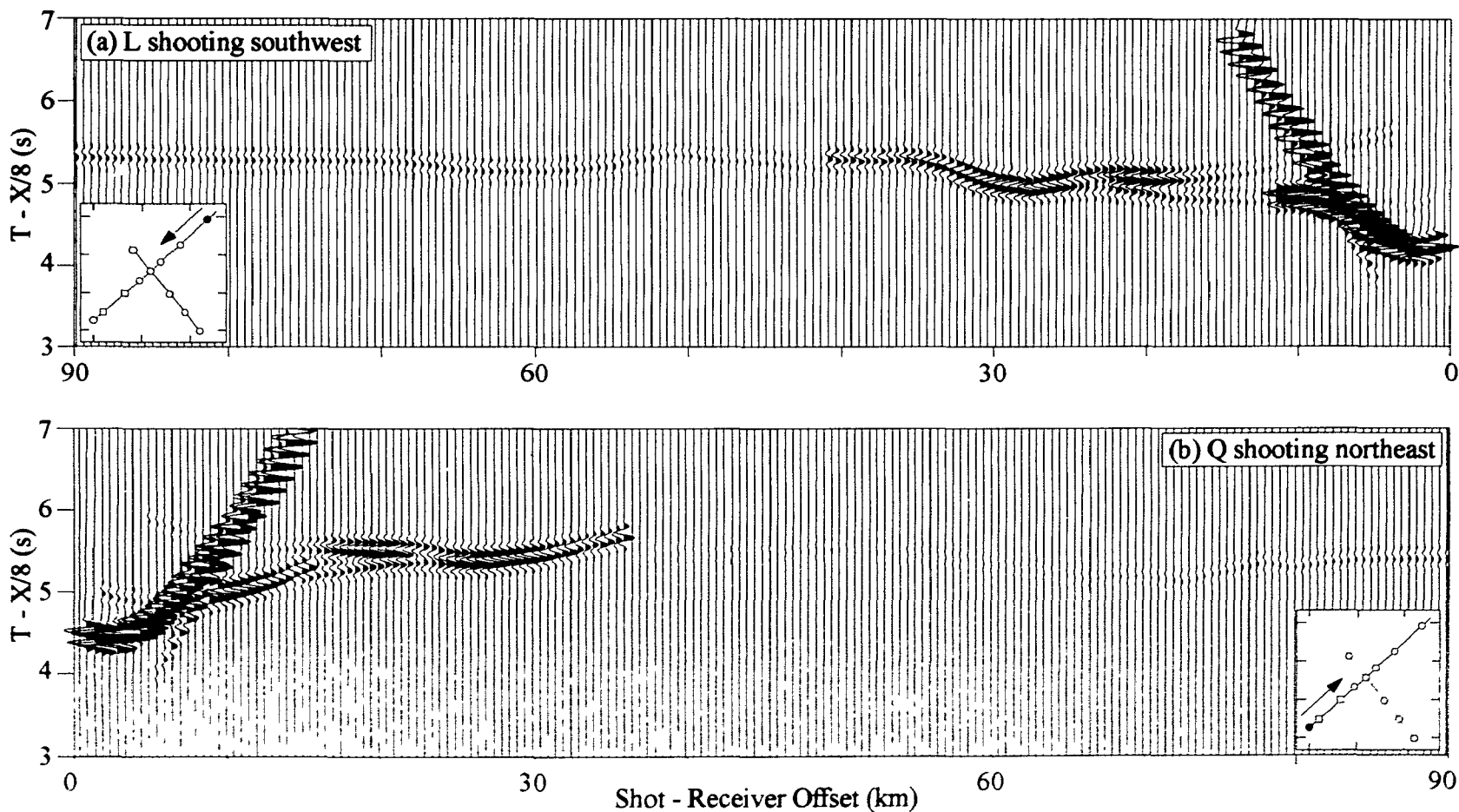


**Figure 4.14:** Synthetic seismic refraction profile for (a) OBS L shooting southwest and (b) OBS Q shooting northeast using the 2-D velocity-depth structure in Fig. 4.2. Gain has been applied as a function of range and traces are plotted at a reducing velocity of 8 km/s.

### Synthetic Seismic Refraction Profiles for OBS M

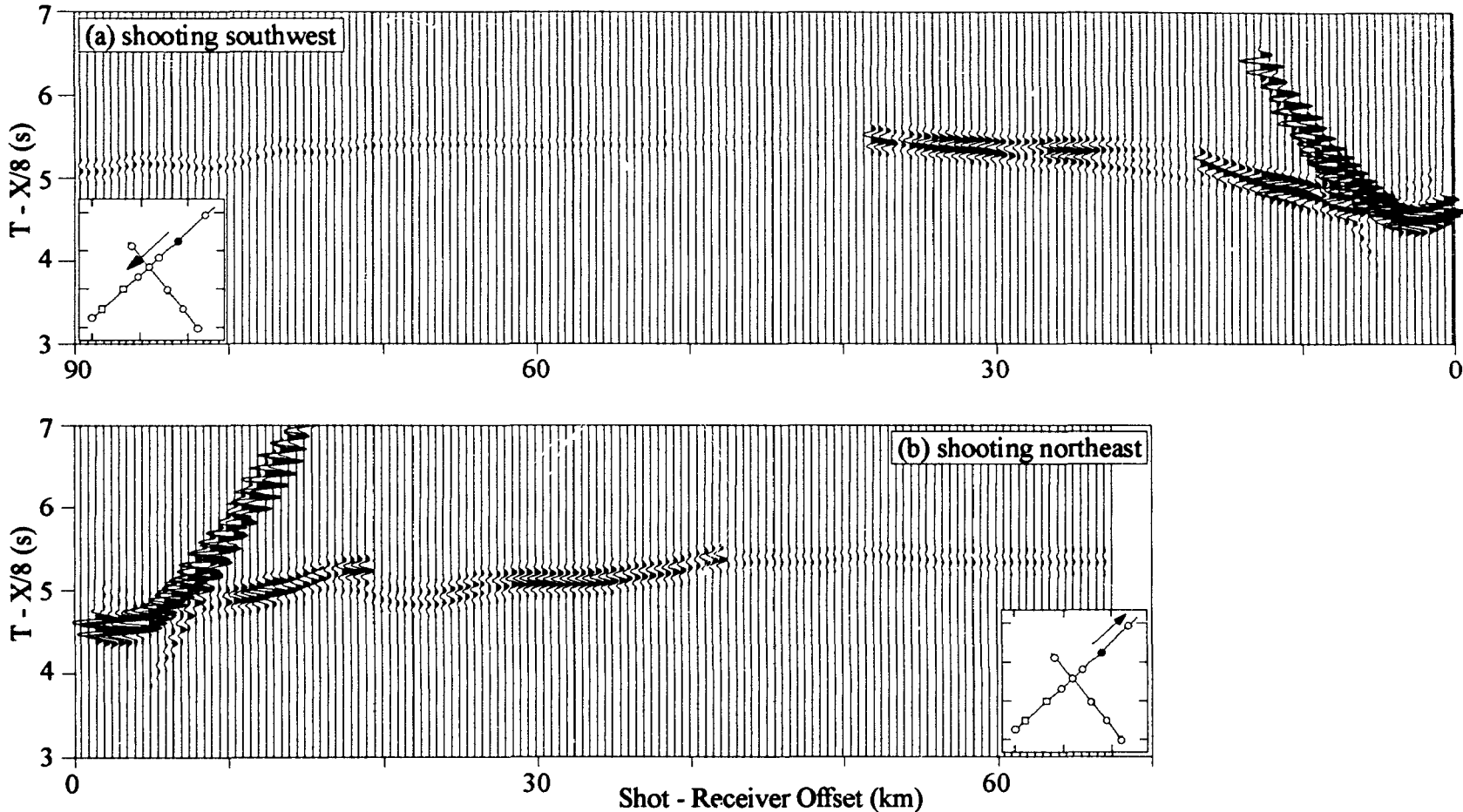


**Figure 4.15:** Synthetic seismic refraction profile for OBS M (a) shooting southwest (b) shooting northeast using the 2-D velocity-depth structure in Fig. 4.2. Gain has been applied as a function of range and traces are plotted at a reducing velocity of 8 km/s.

### Synthetic Seismic Refraction Profiles for OBS N

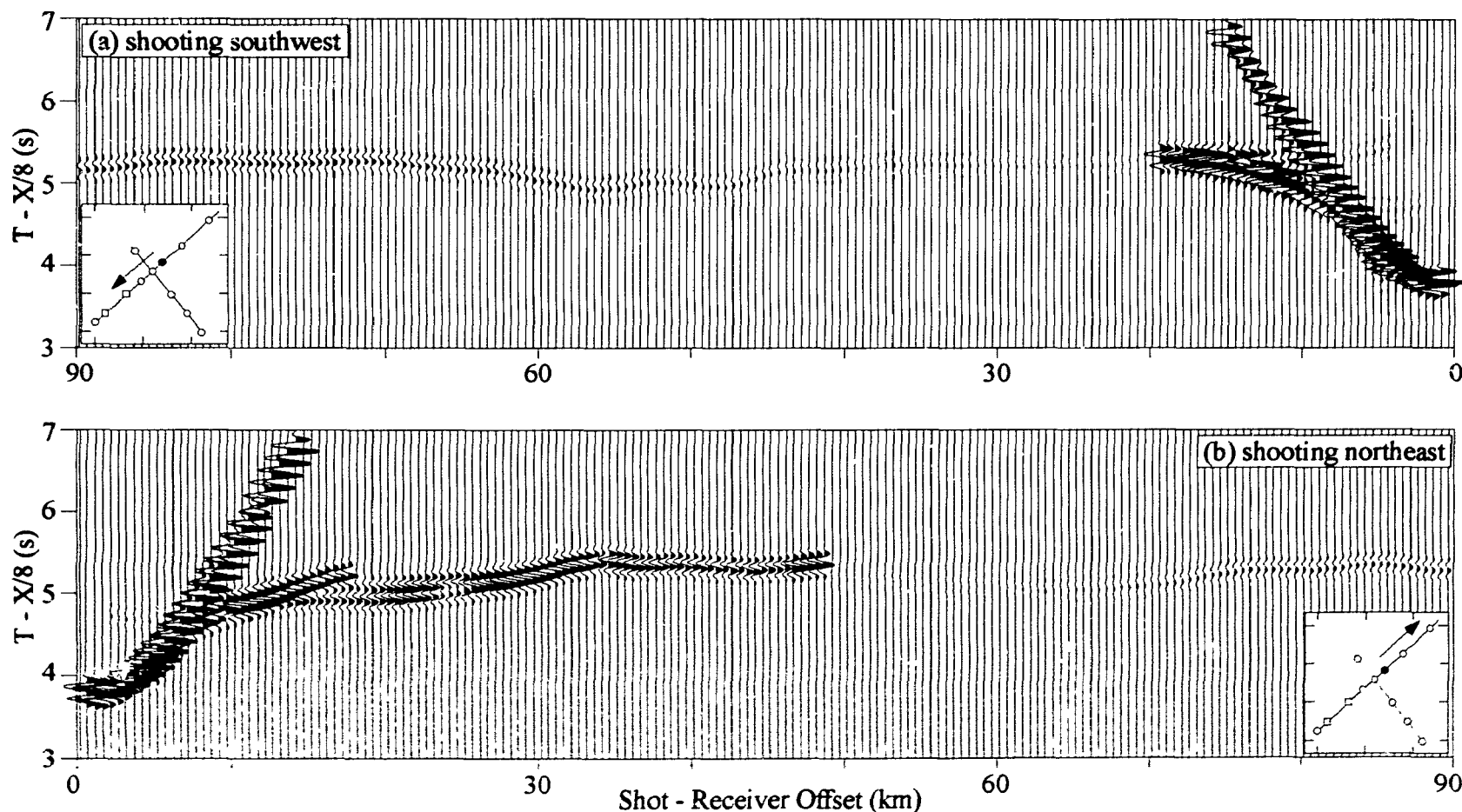


**Figure 4.16:** Synthetic seismic refraction profile for OBS N (a) shooting southwest (b) shooting northeast using the 2-D velocity-depth structure in Fig. 4.2. Gain has been applied as a function of range and traces are plotted at a reducing velocity of 8 km/s.

### Synthetic Seismic Refraction Profiles for OBS E

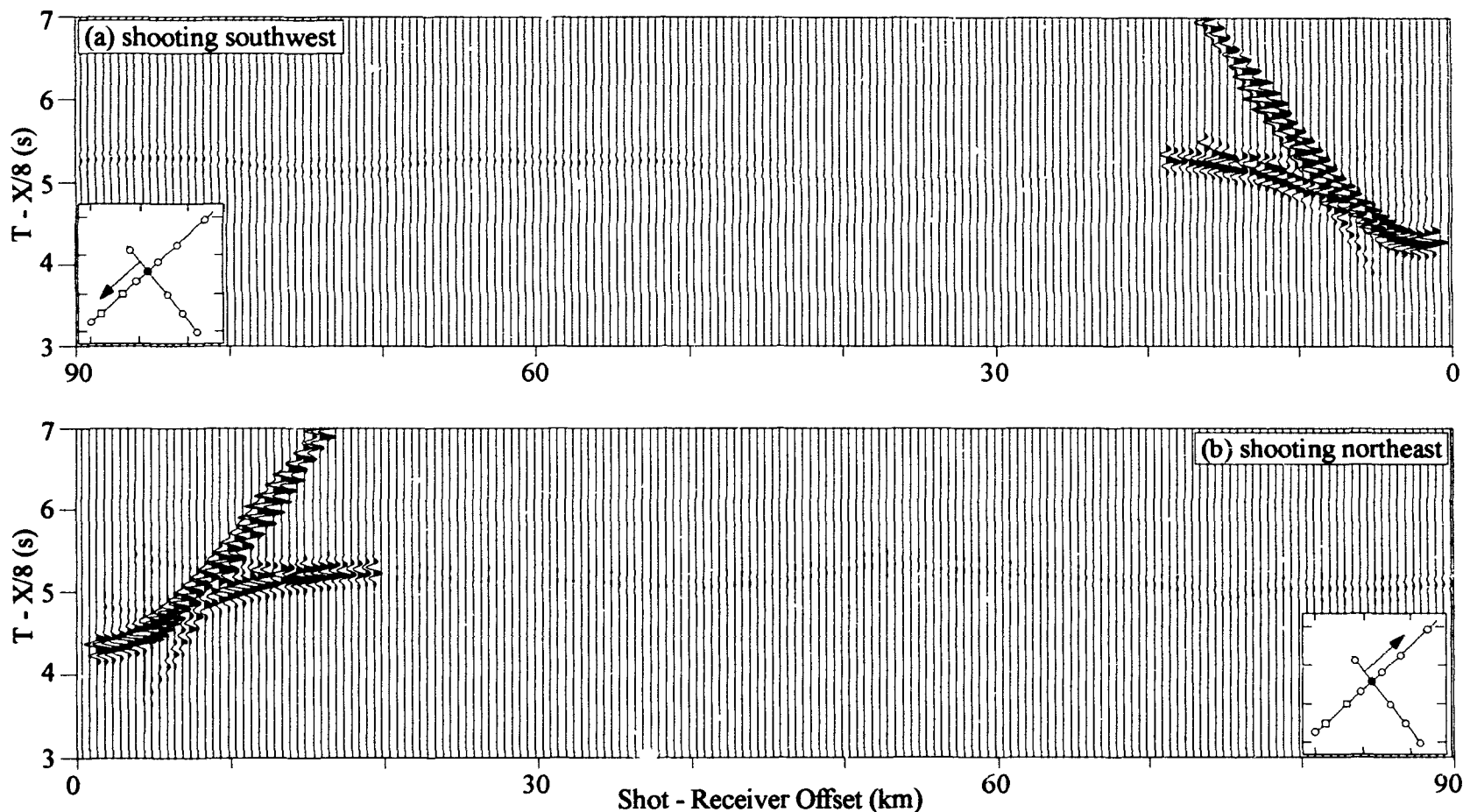


**Figure 4.17:** Synthetic seismic refraction profile for OBS E (a) shooting southwest (b) shooting northeast using the 2-D velocity-depth structure in Fig. 4.2. Gain has been applied as a function of range and traces are plotted at a reducing velocity of 8 km/s.

### Synthetic Seismic Refraction Profiles for OBS O

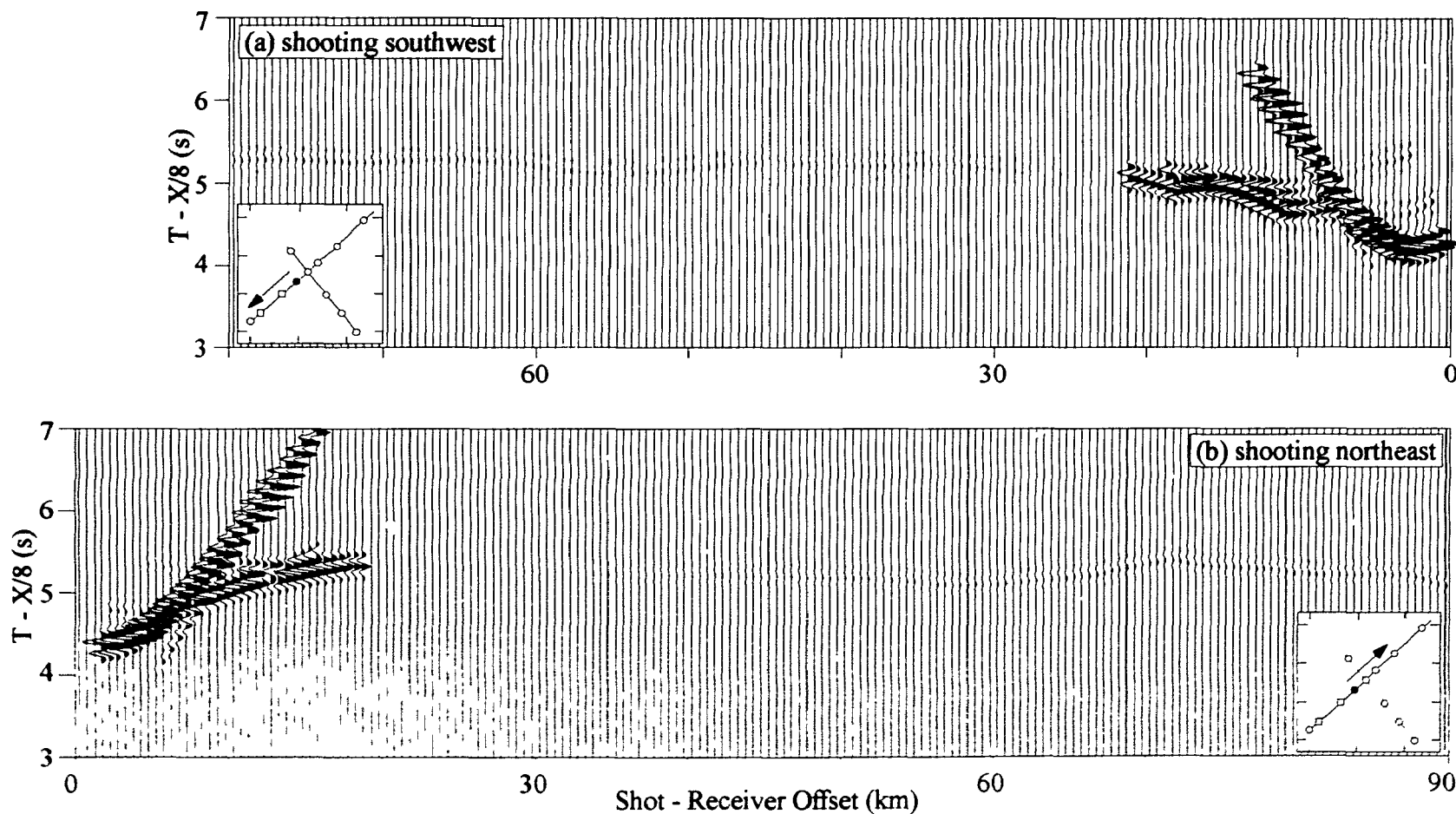


**Figure 4.18:** Synthetic seismic refraction profile for OBS O (a) shooting southwest (b) shooting northeast using the 2-D velocity-depth structure in Fig. 4.2. Gain has been applied as a function of range and traces are plotted at a reducing velocity of 8 km/s.

### Synthetic Seismic Refraction Profiles for Sonobuoys 11 and 12

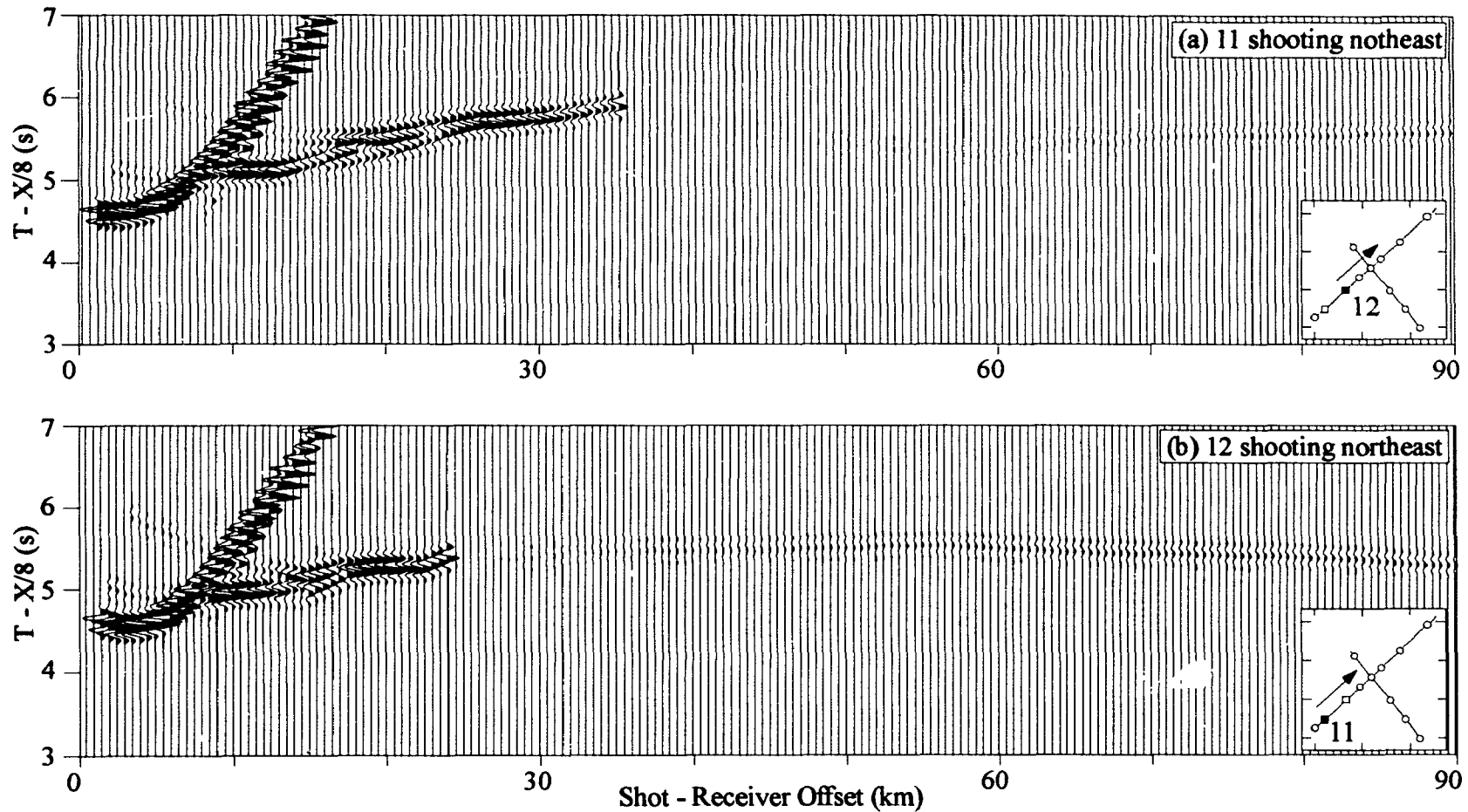


**Figure 4.19:** Synthetic seismic refraction profile for (a) Sonobuoy 11 shooting northeast and (b) Sonobuoy 12 shooting northeast using the 2-D velocity-depth structure in Fig. 4.2. Gain has been applied as a function of range and traces are plotted at a reducing velocity of 8 km/s.

4.18a (shooting southwest) and 4.18b (shooting northeast) and the observed profiles are presented in Figure A.5. Shooting to the northeast into the extinct spreading centre, the strength of crustal refractors is once again matched in the synthetics. For this receiver, there is little energy observed beyond 22 km, the amplitude drop in the synthetics and observed data relates to the range at which crustal level arrivals are no longer received. Shooting to the southwest, the observed arrivals show low amplitudes for the crustal arrivals from 7 to 10 km followed by a region of high amplitude arrivals from 10 to 17 km. The amplitude decrease is a topographic effect and well modelled by the synthetics. Meanwhile, the region of higher amplitudes (10 to 17 km) is a combination of  $P_1$  and  $P_mP$  arrivals and extends to 22 km in the synthetics, 5 km farther than that in the observed data.

OBS Q: The synthetic refraction profile for OBS Q shooting northeast is presented in (Fig. 4.14b) and the observed profile is presented in Figure A.1 The high amplitude of arrivals from 10 to 17 km and rapid amplitude drop from 17 to 19 km are both well modelled as is the  $P_n$  shadow zone created by the zone of crustal thinning from the southwest flank into the extinct spreading centre. The  $P_mP$  arrivals are the most poorly matched in this synthetic, they terminate abruptly at a shot-receiver offset of 36 km while actual termination in the observed data occurs at an offset of 44 km in the observed data

In summary, the synthetic and observed refraction profiles compare favourably as the major amplitude variations for  $P_2$ ,  $P_3$ , and  $P_mP$  arrivals are matched, though the patterns of amplitude variations are shifted by several kilometres in some instances. The greatest shortcomings of the synthetics are the low amplitude of the  $P_n$  arrivals and the

very rapid termination of the  $P_mP$  arrivals. Based on the comparison of the TRAMP and WKBJ algorithms (section 4.7.1), it is felt that both of these shortcomings stem in part from limitations of the asymptotic ray theory which the TRAMP algorithm employs and not solely from inadequacies in the final velocity-depth structure.

#### 4.8 Summary

A 2-D seismic velocity-depth structure (Figs. 4.1 and 4.2) was developed for refraction line R2 transversely crossing the extinct spreading centre in the Labrador Sea (location in Fig. 2.2). Information from 12 kHz bathymetry data, seismic reflection data, and plane-layer and  $\tau$ - $p$  travel time solutions from the 1-D velocity analysis were used to develop an initial velocity-depth structure. The final velocity-depth structure was obtained by revising this initial velocity-depth structure to: 1) quantitatively improve the quality of fit between arrival times calculated by raytracing and their observed counterparts and 2) to qualitatively improve the fit between amplitude patterns in synthetic and observed refraction profiles. The revisions based on raytracing were largely introduced by forward modelling with the RAYINVR package [Zelt and Smith, 1992]. This package is also capable of operating in an inverse sense and can be used to perform error analysis. In practice, inverse steps were only helpful in guiding revisions to the model as they did not converge to plausible velocity structures.

The results of the 2-D modelling affirm the results obtained in the 1-D velocity analysis. The crust within the extinct spreading centre is thinner and of lower p-wave velocity than on its flanks. The 2-D velocity analysis goes beyond the 1-D analysis as it defines the breadth of the region in which these low velocities and crustal thinning are

observed and defines the lateral transition from the flanks into the extinct spreading centre. Further, the 2-D results adequately treat the variations in sediment thickness and heterogeneity in the crustal structure, two concerns which limited the reliability of the 1-D analysis.

## 5. Two Dimensional Gravity Modelling

In this chapter, 2-D gravity models are calculated along line R2, the seismic refraction line which transversely crosses the extinct spreading centre (Fig. 2.2). These models all stem from a conversion of the final velocity-depth structure (Fig. 4.2) into a density structure. The comparison of calculated and observed free-air gravity anomalies provides an independent check on the suitability of the final seismic velocity-depth structure and the extent to which revisions to this structure are merited. In addition, the gravity modelling is used to assess the viability of an alternate model for crust and upper mantle structures underlying mid-ocean spreading centres proposed by Hall *et al.* [1986]. In this model, a low density gabbroic root structure underlies both active and extinct spreading centres and is used to model the axial gravity low at the extinct spreading centre in the Labrador Sea.

### 5.1 Observed Free-Air Gravity Anomaly

In Figure 5.1, the free-air gravity anomaly along ship tracks in the vicinity of the seismic refraction lines R1 and R2 (blue lines) and the OBS and sonobuoy receivers (magenta crosses) are presented. The excursion of the black dots perpendicular to the gravity measurements along the ships track (black lines) represent the amplitudes of the observed anomalies. Positive anomalies are plotted to the north of the ship track and negative anomalies to the south. The track coverage is dominated by the 1974 Minna cruises which cross the extinct spreading centre with a bearing of  $65^\circ$  (clockwise from north). The spacing between these tracks is approximately 34 km.

The track coverage is sufficient for the free-air gravity anomaly to reveal some

## Labrador Sea, Free-Air Gravity Anomaly

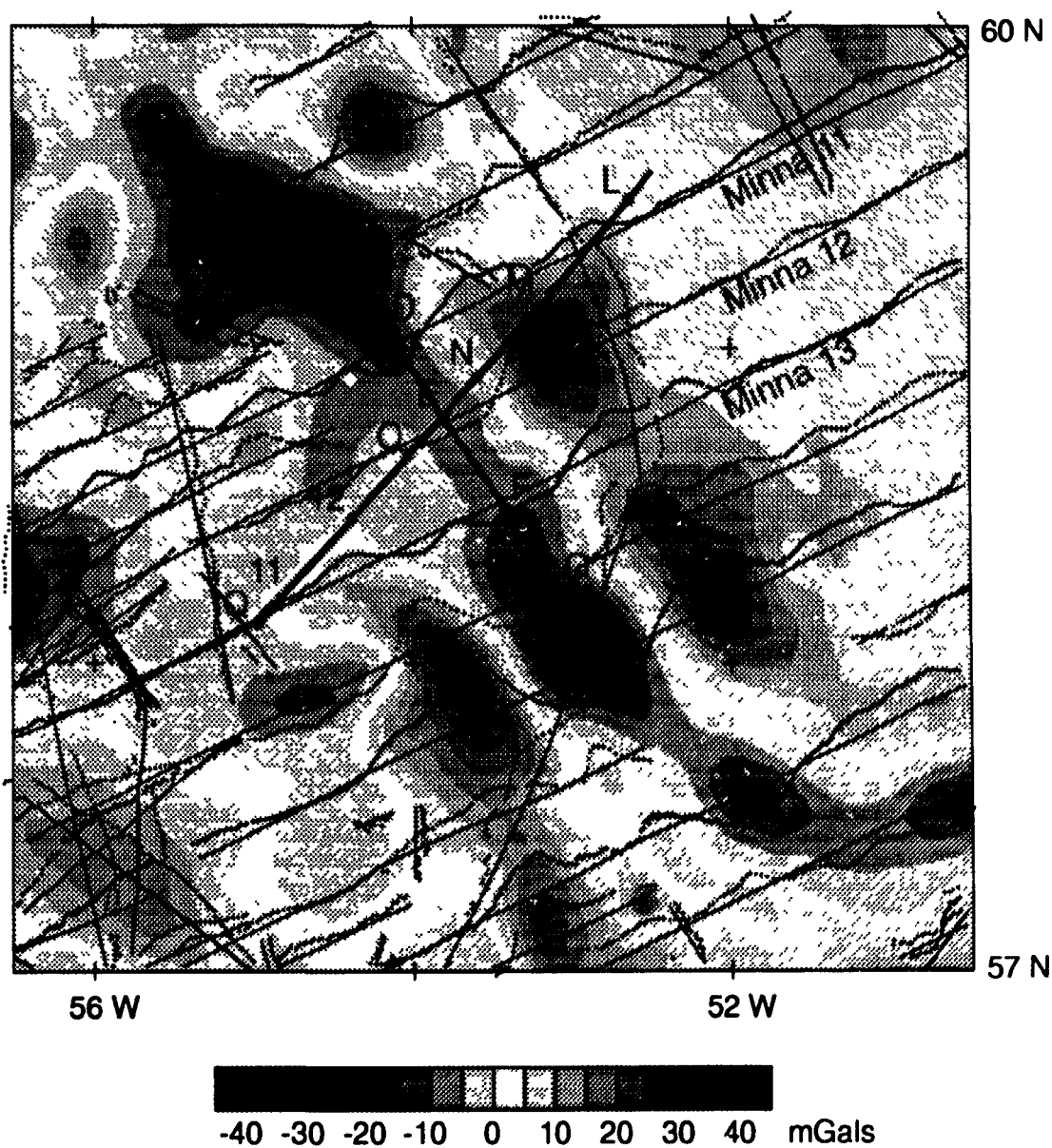


Figure 5.1: The free-air gravity anomaly along ship tracks (black lines) in the vicinity of refraction lines R1 and R2 (blue lines) in the Labrador Sea. Anomalies are plotted perpendicular to the ship track with positive values to the north. Receiver locations are marked in magenta. The gridding of the observed values was performed at the Bedford Institute of Oceanography using a variable search radius.

prominent features of the Labrador Sea basin: 1) The extinct spreading centre is characterized by an axial low (the north-northwest to south-southeast trending anomaly in Figure 5.1) which is flanked by highs. Two factors contribute to the axial gravity low. First, the increased depth to basement (*i.e.* thicker sediments) overlying the extinct spreading centre [Srivastava *et al.*, 1986] as determined from the single channel Minna reflection profiles and a lesser number of multichannel reflection lines. Second, the relatively low velocity/density of the crust and upper mantle within the extinct spreading centre (Chapters 3 and 4). 2) A basin wide asymmetry exists in the Labrador Sea [Srivastava, 1981; Vogt *et al.*, 1982] with a predominance of positive anomalies to the northeast of the extinct spreading centre and negative anomalies to the southwest. 3) The position of fracture zones is inferred from gravity lows parallel to paleo-spreading directions.

The ability of the observed data to resolve shorter wavelength features is more limited. In particular, there is no gravity data coincident with refraction line R2 so the free-air anomalies computed for the gravity models may only be compared with the observed values at track crossings and with a profile of the observed anomaly along track which is extracted from the gridded gravity anomaly (colour contours in Figures 5.1, 5.2, and 5.3). To illustrate the spatial resolution which the density of the ship tracks imposes, the observed values of the free-air gravity anomaly are used to produce the gridded data sets in Figures 5.2 and 5.3. In each of the four gridded data sets displayed, grid points are determined every 8 km, but use different search areas to determine the amplitude of the free-air anomaly. The search areas are circular and apply a weighted average to any

### Labrador Sea, Free-Air Gravity Anomaly: Ship Tracks and Interpolated Grid

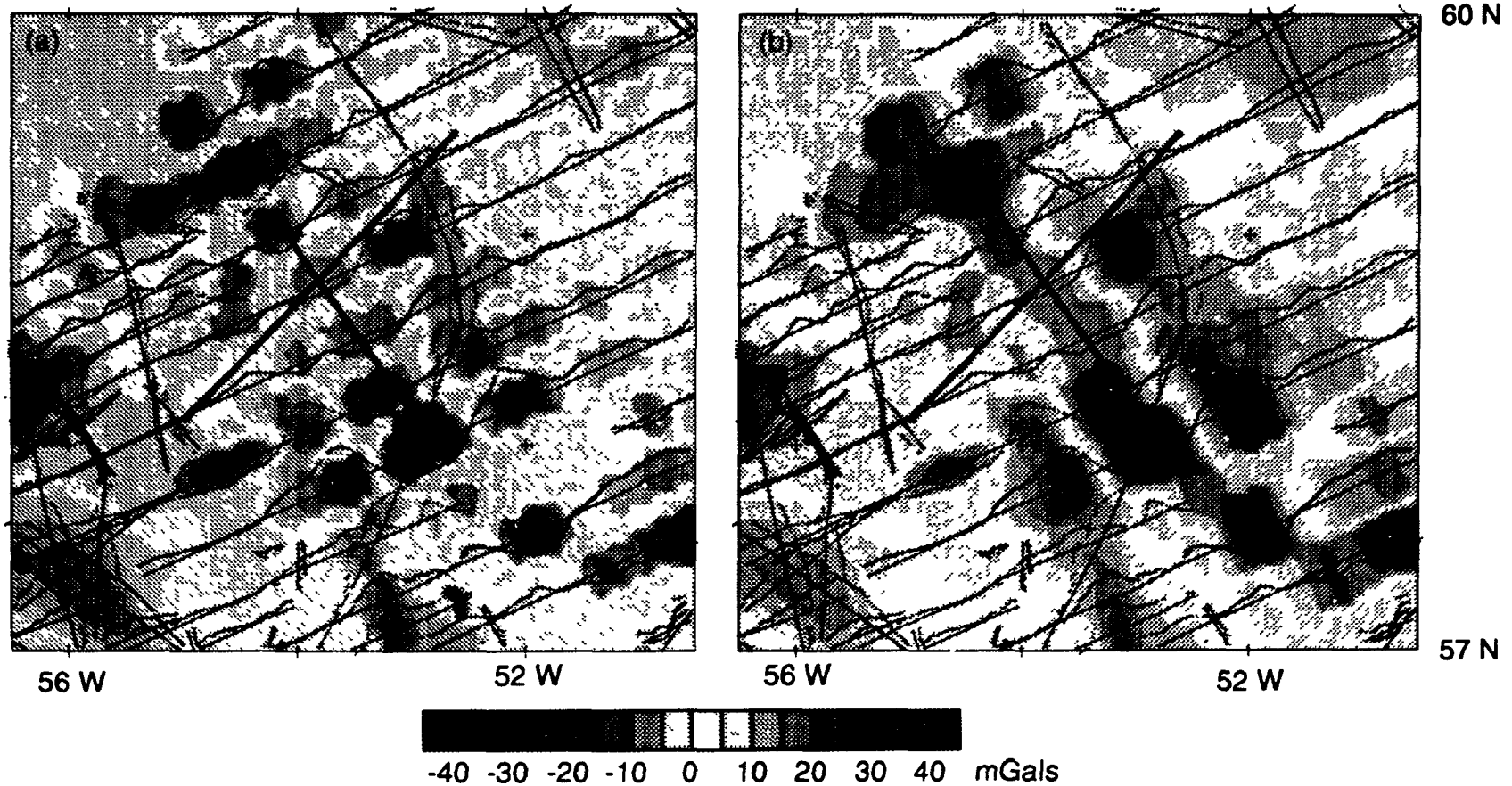


Figure 5.2: The free-air gravity anomaly along ship tracks (black lines) in the vicinity of refraction lines R1 and R2 (blue lines) in the Labrador Sea. Anomalies are plotted perpendicular to the ship track with positive values to the north. The observed values are interpolated to form a regular grid with an 8 km spacing by searching a radius of 3 gaussian half widths of (a) 5 km and (b) 10 km.

### Labrador Sea, Free-Air Gravity Anomaly: Ship Tracks and Interpolated Grid

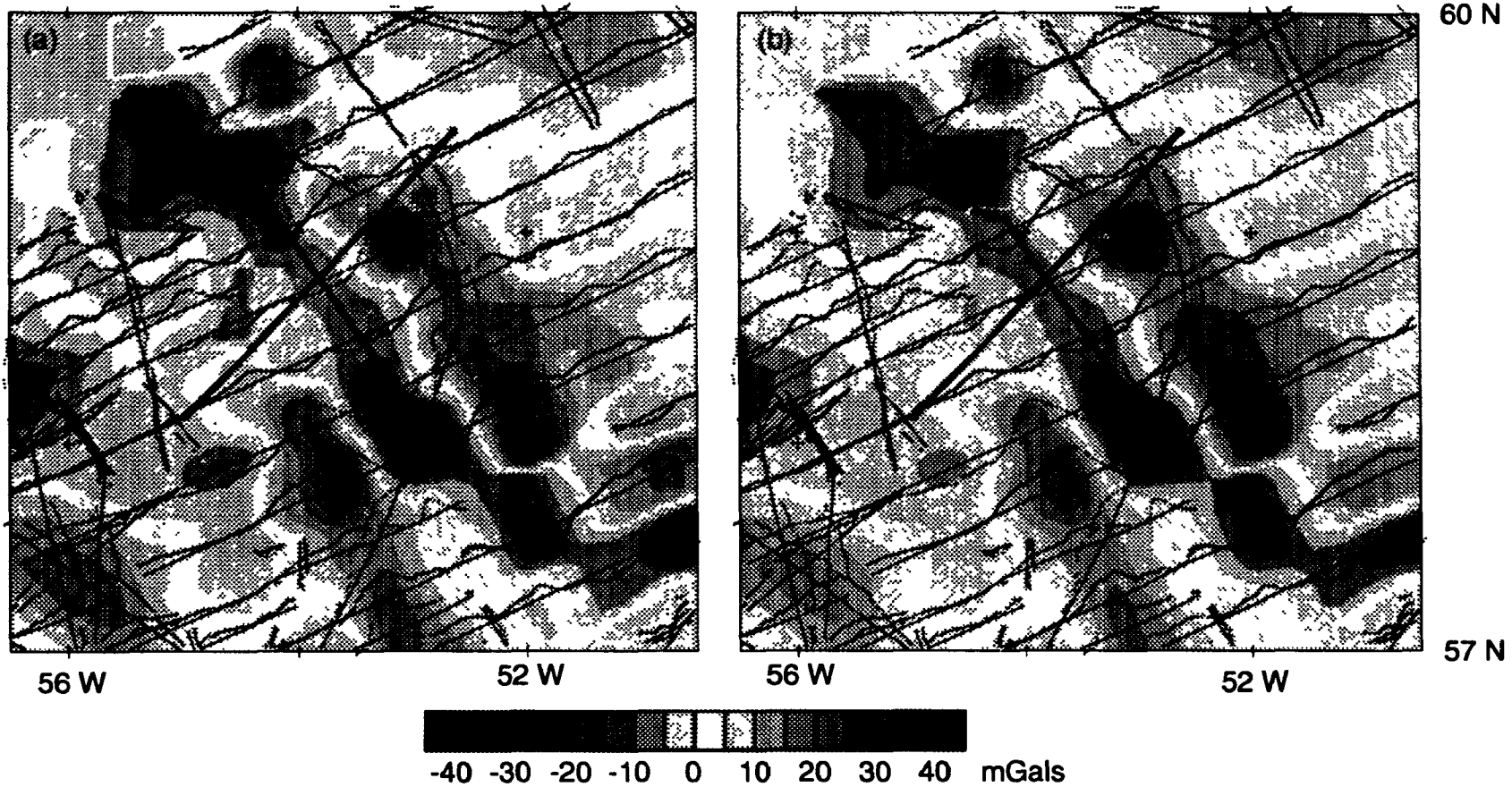


Figure 5.3: The free-air gravity anomaly along ship tracks (black lines) in the vicinity of refraction lines R1 and R2 (blue lines) in the Labrador Sea. Anomalies are plotted perpendicular to the ship track with positive values to the north. The observed values are interpolated to form a regular grid with an 8 km spacing by searching a radius of 3 gaussian half widths of (a) 15 km and (b) 20 km.

observations which lie within their bounds. The weighting,  $w(x)$ , is defined by a gaussian function with a specified half-width controlling how rapidly it is dampened as a function of distance from the grid point:

$$w(x) = \frac{1}{a\sqrt{2\pi}} e^{-\frac{x^2}{2a^2}} \quad (\text{Eqn. 5.1})$$

The gridded data sets which result from applying different search radii are presented in Figures 5.2a, 5.2b, 5.3a, and 5.3b where the respective search areas are 3 times a gaussian half-width of 5, 10, 15, and 20 km. For the 5 and 10 km half-widths, the tracks remain largely independent with little or no averaging of values between tracks, except in regions to the southwest of the extinct spreading centre where the track density is higher. The motivation to grid the observed values is the establishment of a 2-D field which is representative of the observed gravity field along track. For the search areas with the 5 and 10 km half-widths, the granularity in the 2-D field due to the track spacing has not been removed and the search areas are therefore considered too small. For the 15 and 20 km half-widths, there is appreciable averaging across and along tracks. Spatial continuity in the 2-D field is achieved, at least in the vicinity of the seismic refraction lines R1 and R2. As the search area increases, the peak to peak amplitudes generally decrease (*e.g.* -25 to 30 mGals for a 15 km half-width and -20 to 25 mGals for a 20 km half-width ) and shorter wavelength features are progressively removed by the greater extent of averaging.

From each of these grids, profiles of the free-air gravity anomaly along line R2

have been extracted and displayed in Figure 5.4 along with the four observed values and their observational uncertainties [Geophysical Data Centre, Geological Survey of Canada, Personal Communication, 1991] at track crossing points (distances of 5.9, 94.8, 175.3, and 181.3 km along line R2). A fifth profile is also displayed. It is extracted from the BIO grid (Figure 5.1), which employs a search area which varies with the regional track density. In general, the profiles extracted from the 5, 10, 15, and 20 km half-width grids show a progressive decrease in peak to peak amplitudes and loss of shorter wavelength features as the search area broadens.

Considering specific features of these profiles, the search area with a 5 km half-width is not wide enough to span tracks, so the interpolated profile either drops to zero midway between tracks or it is quite variable in these regions. However, it involves the least averaging and consequently it is best able to pass through the observed values at track crossings. Nonetheless, it has a consistently lower peak to peak excursion than the observed values at the track crossing points. This behaviour is noted for all of the search areas and is most dramatic for the track crossing at 175 km where profile values are 1.5 to 5 mGals less than the observed value. The profile values at this location are influenced by the rapid decrease in the observed values for the three gravity measurements on the ship track bearing north-northwest.

The signature of the basement highs and lows is also obscured in the profile of the observed anomaly. There are four basement highs along line R2: 24 to 34 km; 58 to 76 km; 112 to 148 km; and 170 to 194 km (shot point intervals 70-145, 215-345, 460-620, 685-795 in Figure 2.3). These all have an expression in the free-air gravity anomaly

### Interpolated Free-Air Gravity Anomaly along Refraction Line R2

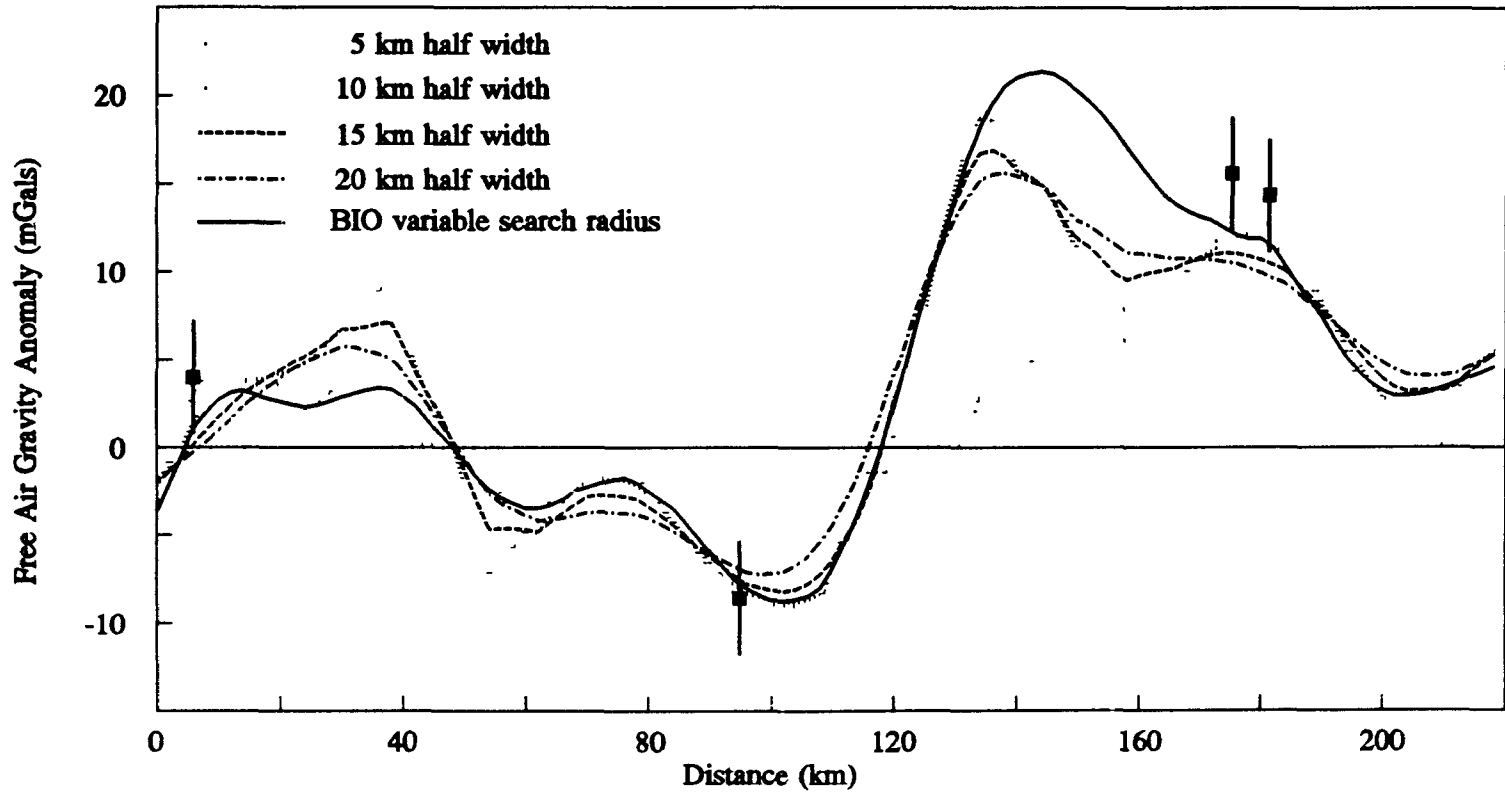


Figure 5.4: The free-air gravity anomaly along line R2 interpolated from the gridded data sets in Figures 6.2 and 6.3 which use different search areas. Observed values at track crossing points are denoted by the solid squares and the vertical bars represent the uncertainty of these values.

along track, but their distinctiveness weakens as the search area increases. For example, the basement low around shot point 650 (Fig. 2.3) influences the gravity field on the Minna 11 ship track (north of OBS M in Fig. 5.1). In the profiles extracted from the BIO and 20 km half-width grids, the expression of this basement low (at 160 km in Fig. 5.4) is largely removed through the averaging. Given these considerations, the profile extracted from the observed values gridded with a search radius of 3 times a gaussian half-width of 15 km is used as the best approximation to a true "observed" free-air gravity anomaly along refraction line R2, to which the calculated free-air gravity anomalies are compared.

Two further caveats limit the results of the gravity modelling. The first pertains to the profile of the observed anomaly along track. The effects of the search area employed has already been noted. The separation between a feature, basement topography or otherwise, and the point of observation is a further consideration. A feature which lies between ship tracks is not the central contribution to the observed gravitational acceleration at a measurement location: the influence of a mass anomaly varies inversely with the square of the distance separating the mass anomaly from the observation point. Therefore, if the spatial extent of a feature is less than the distance separating ship tracks, it will not be fully resolved on these ship tracks.

The second caveat pertains to the 2-D nature of the gravity calculation [Talwani *et al.*, 1959]. The gravity field is calculated over constant density polygonal prisms which are assumed to extend infinitely into the third dimension, perpendicular to the strike of the density-depth section. The gravity anomaly for a basement high, for example, is computed as if it were actually a ridge. If this is not the case, the computed anomaly will

overestimate the influence of the feature. Line R2 is situated in an area where the positive gravity anomalies from the southwest and northeast flanks of the extinct spreading centre (Figure 5.1) begin to terminate. In terms of satisfying the assumptions in the methodology of the 2-D gravity modelling, it would have been desirable to have placed the refraction line further south where the gravity anomaly from the axial flanks is continuous.

In summary, the profile of observed values will underestimate the actual contribution of a feature, positive or negative, to the gravity anomaly because of the averaging in the gridding process. If the wavelength of the feature is less the separation between the ship tracks on which it is observed, then its influence in the profile of observed values is further underestimated. Meanwhile, the calculated anomaly for a feature will be overestimated due to the 2-D nature of the gravity calculation.

## 5.2 Gravity Models Based on 2-D Seismic Velocity Structure

To construct a density-depth structure from the final 2-D seismic velocity-depth structure along line R2 (Chapter 4), densities were assigned to each of the model trapezoids defined by the boundary nodes (Fig. 4.1). A density for each trapezoid is computed by averaging the four velocity nodes and then converting velocity to density using the following 4th order polynomial relationship which fits the empirical data of the Nafe-Drake curve [Ludwig et al., 1970] for  $1 < V_p < 9$  km/s:

$$\rho = -0.00283 V_p^4 + 0.0704 V_p^3 - 0.598 V_p^2 + 2.23 V_p - 0.700 \quad (\text{Eqn 5.2})$$

Where:

$\rho$  = density in  $\text{gcm}^{-3}$

$V_p$  = seismic p-wave velocity

For the mantle layer (8 in Fig. 4.1), the bottom boundary is set at 14 km in the gravity models and the density of mantle trapezoids is calculated using the velocity of the upper boundary nodes alone. In the velocity-depth structure, the mantle layer must be deep enough to allow the rays at the large source-receiver offsets to be refracted; the depth is otherwise arbitrary. It is the depth and velocity nodes for the upper boundary which primarily control the velocity gradient structure of the mantle trapezoids since the lower boundary is horizontal and of constant velocity. If the bottom boundary velocity is included in the density calculation, then the density variations in the upper mantle are muted. If the 20 km depth to the lower boundary is retained, while excluding the lower boundary velocity nodes from the density calculation, then the influence of the upper boundary velocity variations is carried to a depth of 20 km and their influence is too great. The 14 km depth is selected as a reasonable depth to which these density variations extend. In section 5.3, an alternate model for the structure of a mid-ocean ridge is explored with density variations extending to depths  $> 30$  km into the mantle.

In Figures 5.5 to 5.9, gravity models emanating from the seismic velocity-depth structure along refraction line R2 are presented. In these figures, the upper plot panel contains the computed free-air gravity anomaly (solid line), the observed value (dotted line), crossing points (solid squares with uncertainties), and a profile of observed values along track (dashed line) obtained using the search area with a 15 km half-width (section 5.1). The lower plot panel contains the 2-D density-depth structure. The density of each trapezoid is printed within its confines. For the lower sediment and upper crustal layers (3,4, and 5 in Fig. 4.1), the spacing of boundary nodes along the sediment-crust boundary

gives rise to trapezoids every 2.5 km. As the densities of these trapezoids do not vary rapidly, the density of every fourth trapezoid is printed in the figures. The calculated anomalies and profile of observed values are extended an additional 20 km beyond the ends of the refraction line to provide a greater sense of the regional trend of these anomalies (section 5.2.4). Values of the calculated anomaly are determined every 2 km.

### *5.2.1 Initial Gravity Model*

The gravity model obtained from the final velocity-depth structure (Fig. 4.2) is presented in Figure 5.5. The calculated anomaly, a relative quantity, is plotted so that it falls within the uncertainty bounds of three of the four observed values at the track crossings. When compared to the profile of observed values and the fourth track crossing, the calculated anomaly does not fit particularly well. First, the calculated free-air gravity anomaly to the southwest of the extinct spreading centre is 18 mGals below the observed value at the Minna 13 track crossing at 5.9 km and the profile values from 0 to 50 km. Second, the calculated anomaly for the basement high from 58 to 76 km overestimates the peak to peak amplitude of this feature by 16 mGals. Third, the peak to peak amplitude of the basement high from 112 to 148 km is underestimated by up to 13 mGals. Revisions to the density structure, which are plausible given the constraints which the refraction data impose, are introduced in an effort to reduce the magnitude of these discrepancies.

### *5.2.2 First Revision: Compensating Basement High from 58 to 76 km*

The first of these revisions is presented in Figure 5.6. The crust-mantle boundary has been modified to thicken the crust beneath the basement high from 58 to 76 km. This provides partial compensation for the basement high, reducing the contribution from the

### Line R2 Gravity Model: Final Velocity-Depth Structure

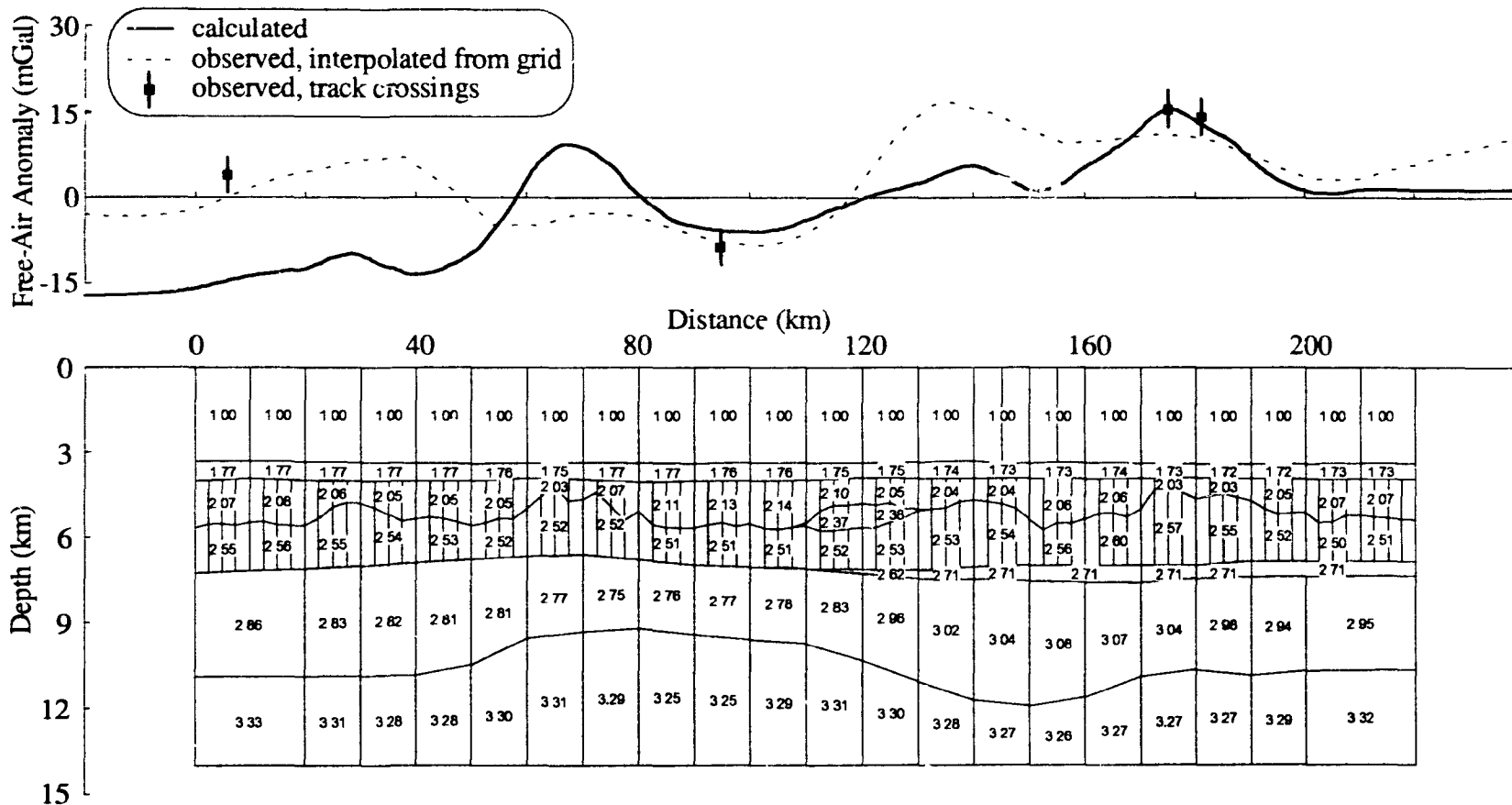


**Figure 5.5:** 2-D gravity model using the final velocity-depth structure (Fig. 4.2). The seismic velocities have been converted to density using the relationship in Equation 5.1. Densities are in g/cc and printed within the bounds of the model trapezoids used in the gravity calculations.

### Line R2 Gravity Model: Symmetry of Crust-Mantle Boundary from 60 to 130 km

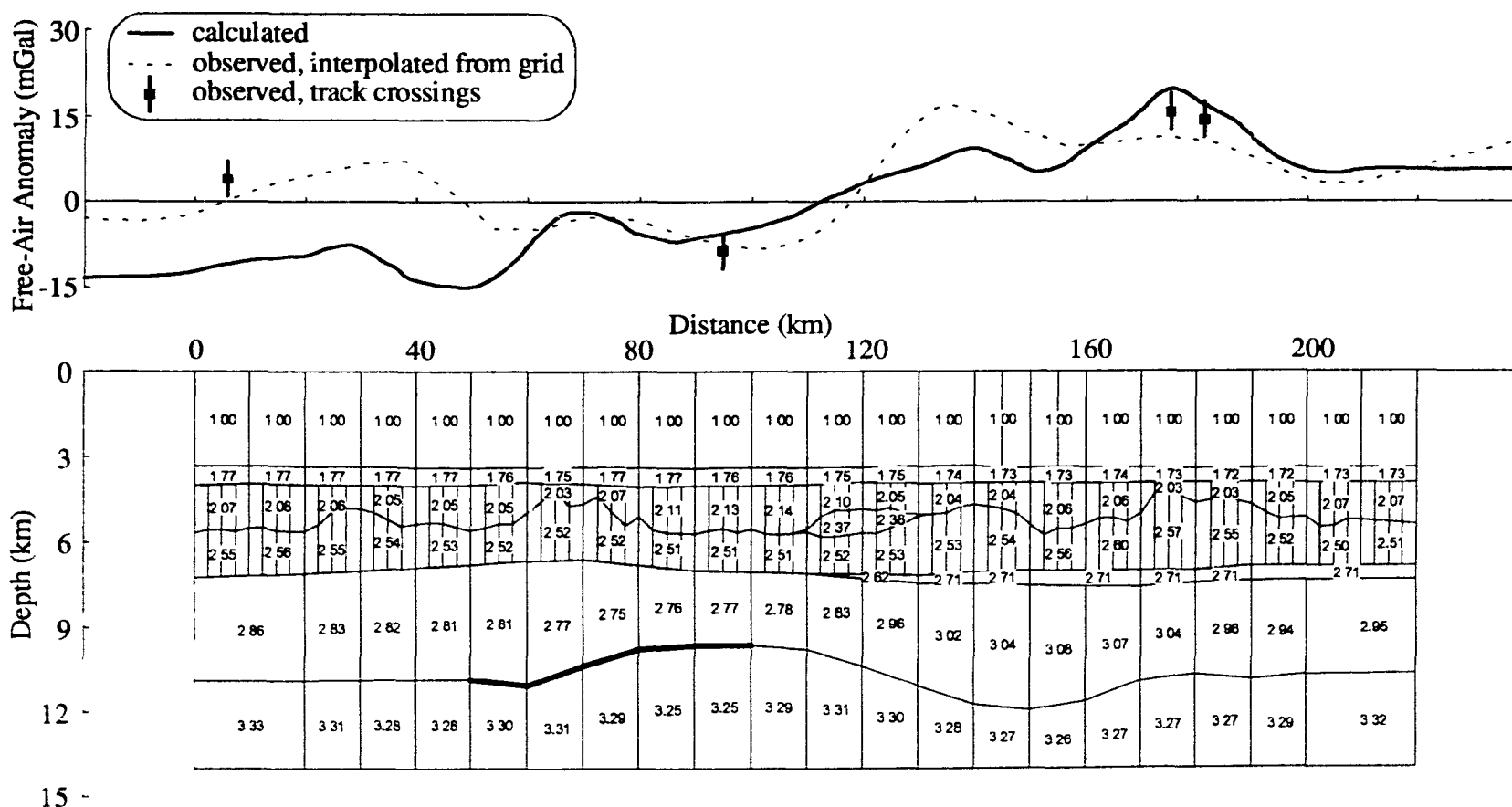


**Figure 5.6:** The initial density structure (Fig. 5.5) has been modified (as indicated the bold lines) to introduce symmetry on the crust-mantle boundary from 60 to 130 km about a midpoint of 95 km within the extinct spreading centre. This helps to compensate the contribution to the calculated anomaly from the basement high from 58 to 76 km.

mantle layer to the calculated gravity anomaly. The thickening is introduced by making the crust-mantle boundary symmetric from 60 to 130 km, centred about a midpoint at 95 km. The depth nodes for the crust-mantle boundary from 60 to 90 km are assigned the corresponding values of the nodes from 100 to 130 km.

The crust-mantle boundary in this region is constrained by the  $P_n$  arrivals from OBS O shooting southwest (Fig. 4.7), OBS N shooting southwest (Fig. 4.8), OBS M shooting southwest (Fig. 4.9), OBS E shooting southwest (Fig. 4.7), and the shadow zone for OBS Q shooting northeast (Fig. 4.7). In specifying a symmetric crust-mantle boundary, the lower crustal thickening which is introduced attains a maximum value of 1.54 km at 60 km. The maximum delay in  $P_n$  travel times is localized at this point and averages 0.14 s for the aforementioned OBSs. The overall fit of computed to observed travel times for  $P_n$ , as quantified by an average  $T_{RMS}$  for these receivers, increases from 0.069 s to 0.113 s. These measures of the degradation in the quality of fit of computed  $P_n$  travel times may be compared with the maximum uncertainty of 0.12 s which was assigned to observed travel time picks (section 4.4.1). The travel time delays introduced by thickening the crust are at the limit which can be accepted given the uncertainty of the seismic refraction data.

The thickening of the crust decreases the contribution of the basement high to the free-air anomaly by approximately 10 mGals. The discrepancy which remains cannot be reasonably accommodated by modifications to the velocity-depth structure and other potential sources merit discussion. This basement high may be part of continuous feature parallel to ridge strike as there are similar short wavelength peaks in the observed free-air

gravity anomalies along the Minna 11, 12, and 13 ship tracks (marked by white dots in Fig. 5.1). While this gives some confidence that the 2-D assumption which the gravity model presupposes is valid, it remains possible that line R2 intersected the ridge at a basement high. In addition, the amplitude ascribed to the basement high is too low in the line R2 profile of observed values. The peak to peak amplitudes are approximately 9 mGal on the Minna 11,12, and 13 tracks. This anomaly has a relatively short wavelength (15 - 20 km) and the gridding has been shown to reduce the amplitude of short wavelength highs which are adjacent to lower amplitude values (section 5.1). For the search area using a 15 km half-width weighting for the gaussian function, the peak to peak amplitude of this feature is no more than 4 mGal in the profile of observed values (Fig. 5.4).

### *5.2.3 Second Revision: Lower Mantle Densities Under the Extinct Spreading Centre*

In the second revision (Fig. 5.7), the density of the mantle trapezoids from 80 to 110 km is decreased to  $3.20 \text{ gcm}^{-3}$ . This adjustment is justified as follows. First, the velocity nodes on the upper boundary of the mantle layer along line R2 are sampling the mantle in the fast direction [Christensen, 1984]. Anisotropy of the mantle, can lead to a velocity difference of 5% between velocities in the ridge parallel (slow) and ridge perpendicular (fast) directions [Bibee and Shor, 1976]. Second, and more directly, the  $3.20 \text{ gcm}^{-3}$  is calculated using the average velocity of 7.74 km/s (Table 3.1) along line R1 and the velocity to density relationship (Equation 5.2).

The introduction of these lower densities has several desirable consequences. The amplitude of the calculated anomaly to the southwest from 0 to 50 km is increased



relative to that within the extinct spreading centre. The discrepancy between observed and calculated values for the basement high from 112 to 148 km is marginally decreased and the rapid transition from a gravity low to a gravity high from 110 to 130 km is improved. A further improvement in fitting the profile of observed values can be achieved by a more substantial reduction in the density. In doing so, however, the fit to the observed values at the 95 and 180 km track crossings is then lost and the density decreases below that which can be quantitatively justified by the line R1 refraction results.

#### *5.2.4 Third Revision: Reduce Regional Asymmetry of Calculated Anomaly*

This section considers the asymmetry in the calculated free-air anomaly along line R2 which is too negative to the southwest of the extinct spreading centre and too positive to the northeast (Fig. 5.5). Two alternate views of this asymmetry are explored. In the first, it is considered an undesirable artifact of the velocity-depth structure and gravity models which largely remove this asymmetry are devised. In the second view, the asymmetry stemming from the velocity-depth structure is treated as actually being present in the region, but not well expressed in the observed gravity anomaly along line R2.

The asymmetry in the calculated free-air gravity anomaly is indicative of an isostatic imbalance between the eastern and western flanks of the extinct spreading centre. This imbalance is quantified in Figure 5.10 where the total mass in columns is calculated at distance intervals of 10 km along refraction line R2. The layer thicknesses used in this calculation are from the final velocity-depth structure (Fig. 4.2). The densities are calculated from Equation 5.2 using an average of the upper and lower velocity nodes of a layer at a given position. This differs from the calculation of densities for model

trapezoids where the average velocity was calculated using the velocities at the four corners defining the trapezoid. For distance intervals at which boundary and/or velocity nodes are not present in the final model parameterization (*e.g.* 10 km position for layers 7 and 8 in Figure 4.1), the values have been interpolated from those at neighbouring nodes. The mass in the mantle (layer 8 in Fig. 4.1 and 5.9) is calculated from the base of the crust to a depth of 14 km, the same depth used in specifying the base of the mantle layer in the gravity calculations.

Figure 5.10b is a stacked bar representation of the mass which each layer contributes to the total mass of the column. The upper plot panel (Fig. 5.10a) presents the total mass in each column and a linear regression between the values. The difference in mass between the columns at 0 and 220 km is  $0.44 \times 10^6 \text{ kgm}^{-2}$  and the difference between the endpoints of the regression line at 0 and 220 km is  $0.53 \times 10^6 \text{ kgm}^{-2}$ . For a Bouguer slab calculation,

$$g_B \text{ (mGals)} = \frac{2\pi G(\Delta M)}{10^{-5}} \quad (\text{Eqn. 5.3})$$

Where:

$$G = \text{gravitational constant} = 6.67 \times 10^{-11} \text{ (m}^3\text{kg}^{-1}\text{s}^{-2}\text{)}$$

$$\Delta M = \text{Mass in a column (kgm}^{-2}\text{)}$$

the differences in mass at 0 and 220 km would generate gravity anomalies of 18.1 and 22.2 mGals respectively. This may be compared with the difference of 18.5 mGals which exists between the calculated free-air gravity anomaly at 0 and 220 km in Figure 5.5. As gravity modelling is non-unique, there are numerous revisions which could be introduced

### Line R2 Gravity Model: Increased Density of Lower Crust from 0 to 60 km

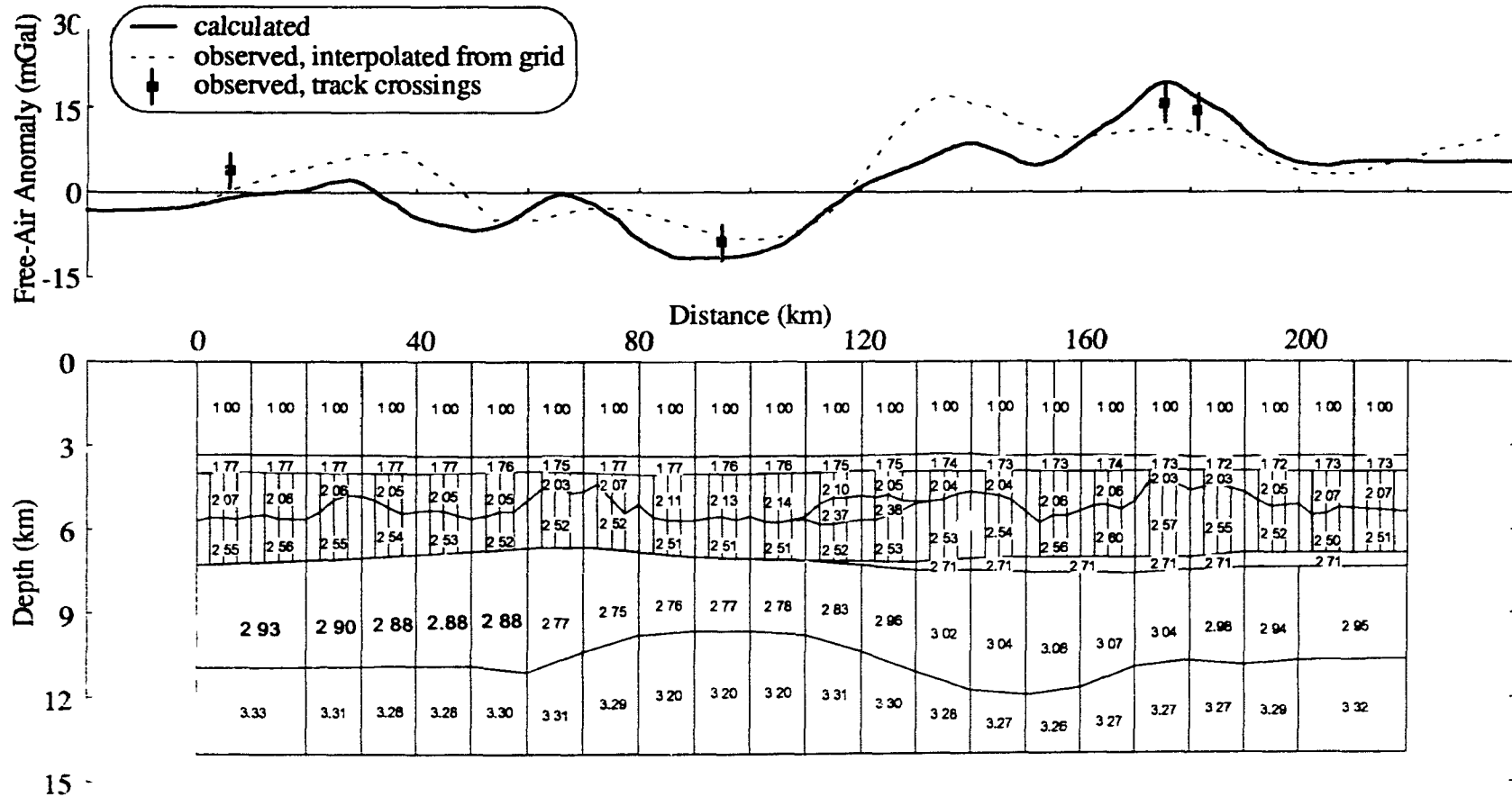


**Figure 5.8:** The density structure in Figure 5.7 has been modified by increasing the densities of the lower crust trapezoids from 0 to 60 km by 0.07 g/cc (bold and enlarged text in lower plot panel). This reduces the regional asymmetry between the flanks of the extinct spreading centre by reducing the degree of isostatic imbalance which is present in the density structure.

### Line R2 Gravity Model: Thinning of Lower Crust from 0 to 60 km

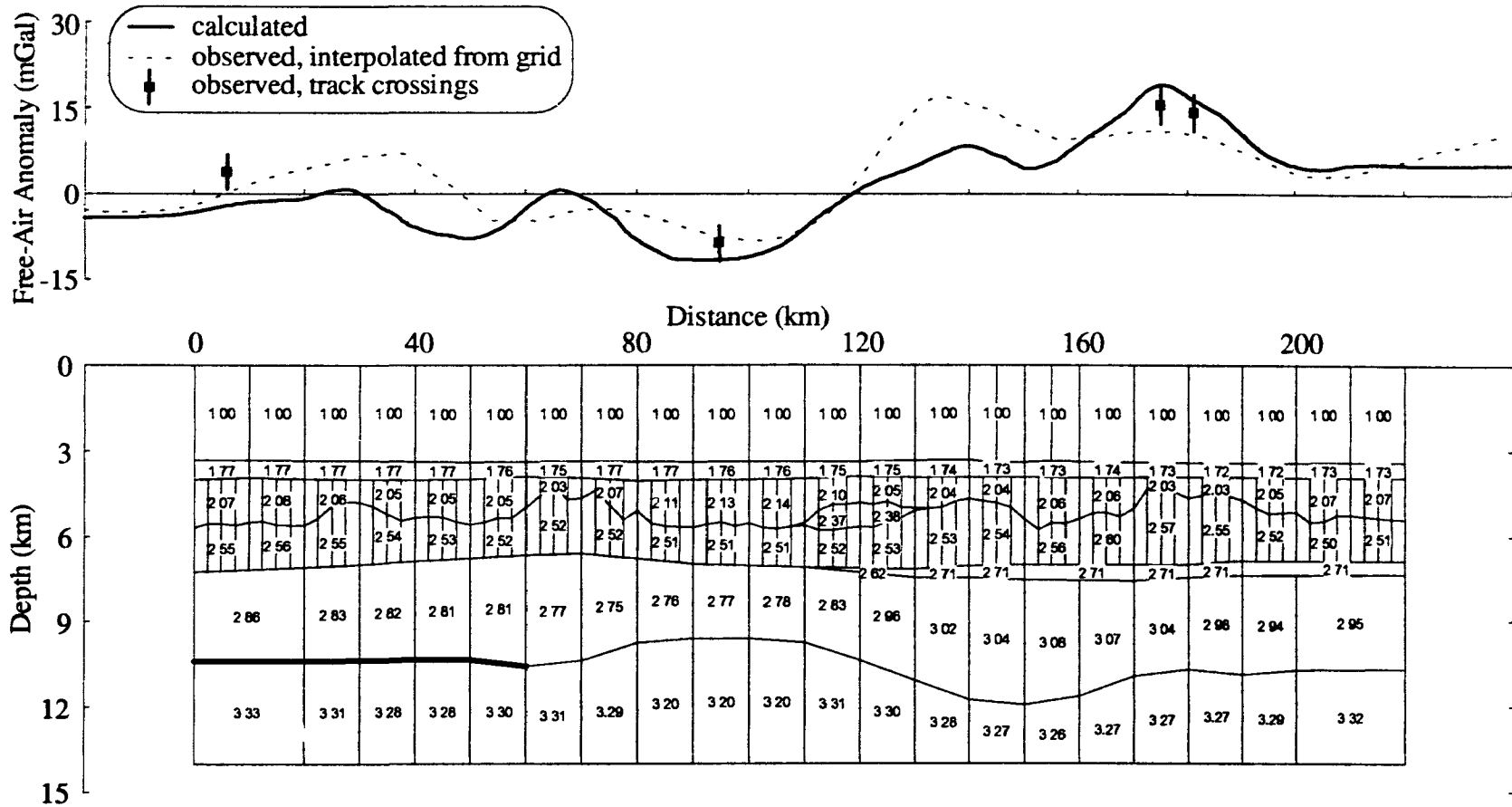


**Figure 5.9:** The density structure in Figure 5.7 has been modified by reducing the thickness of the lower crust trapezoids from 0 to 60 km (as indicated by the bold line) by 0.51 km. This is another means of reducing the regional asymmetry in the calculated free-air gravity anomaly between the flanks of the extinct spreading centre.

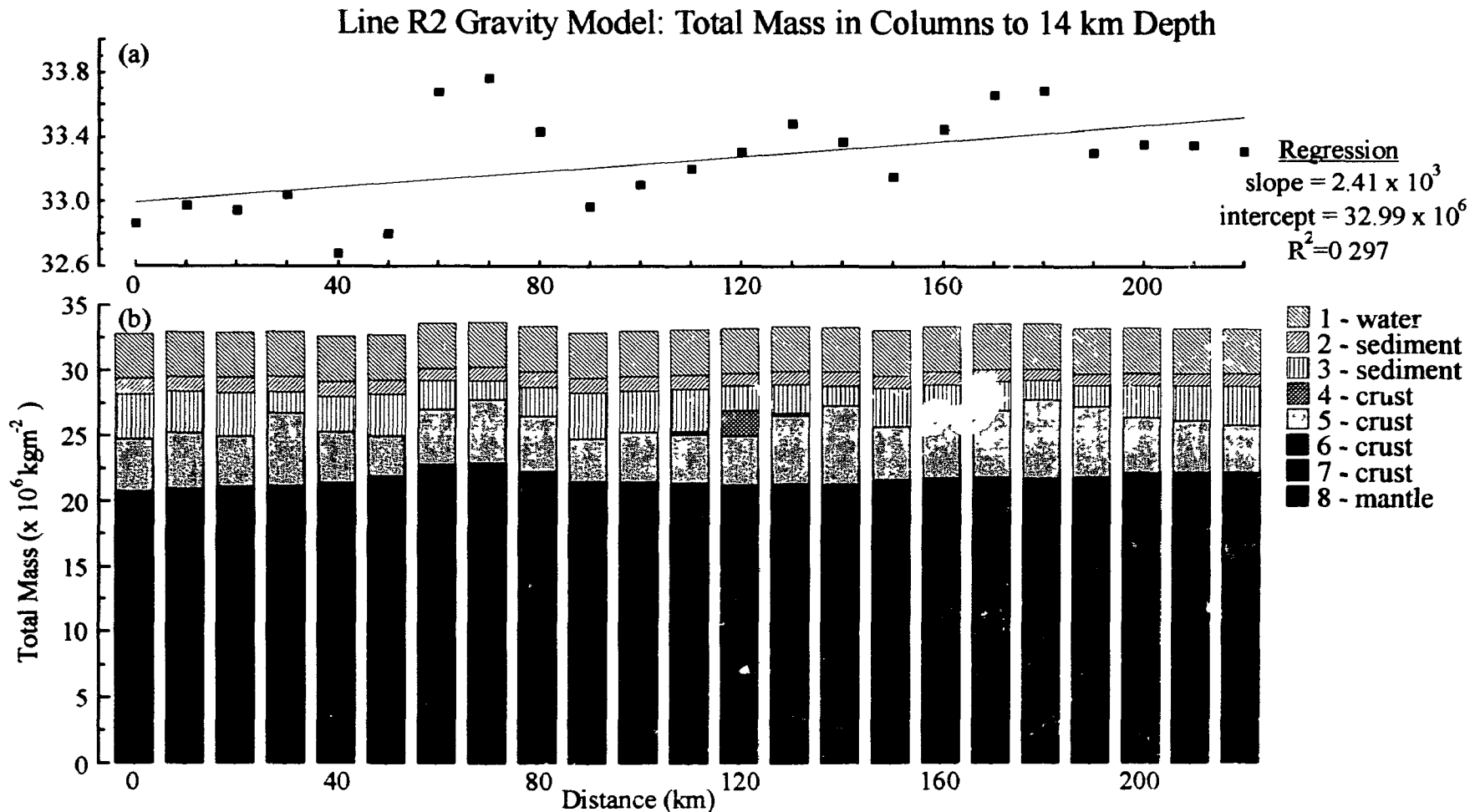


**Figure 5.10:** The total mass is calculated in vertical columns every 10 km across the final velocity-depth structure for seismic refraction line R2 (Fig. 4.2). (a) The total mass in columns to 14 km depth with a linear regression line to emphasize the asymmetry about the extinct spreading centre and (b) a stacked bar representation of the mass which each layer contributes to the total

to reduce this asymmetry. Two revisions, both involving modifications to the lower crust trapezoids from 0 to 60 km are presented in Figures 5.8 and 5.9. The models show the effects of increasing the density of these trapezoids by  $0.07 \text{ gcm}^{-3}$  or reducing their thickness by 0.51 km respectively. Through either revision to the lower crust trapezoids from 0 to 60 km, the free-air gravity contribution of this flank is increased by approximately 10 mGals. This increase, in conjunction with that realized by reducing the density of the mantle beneath the extinct spreading centre (section 5.2.3), largely removes the asymmetry at the end points of the refraction line at 0 and 220 km (Figs. 5.8 and 5.9).

The plausibility of these two revisions may be assessed by considering how they would effect the quality of the travel time fits between calculated and observed arrivals in the 2-D seismic refraction modelling (Chapter 4). In the first case, density increases of  $0.07 \text{ gcm}^{-3}$  correspond to velocity increases of approximately 0.25 km/s. This is a substantive velocity increase which has a marked influence. For lower crustal arrivals,  $P_3$ , the average  $T_{\text{RMS}}$  (for arrivals at OBS Q shooting northeast, Sonobuoy 11 and Sonobuoy 12) increases from 0.064 s to 0.117 and the average  $\chi^2$  increases from 0.92 to 3.02. For  $P_n$ , the average  $T_{\text{RMS}}$  (for arrivals at OBS Q shooting northeast, OBS O shooting southwest, OBS E shooting southwest and OBS N shooting southwest) increases from 0.069 to 0.080 s.

The  $T_{\text{RMS}}$  values for  $P_n$  are calculated for all arrivals at a receiver and not restricted to those raypaths which travel through the 0 to 60 km region. A more revealing quantity is  $\Delta T_{\text{MAX}}$ , the maximum travel time difference between the calculated raypaths in the revised and original models. While  $T_{\text{RMS}}$  will tend to underestimate the degradation in

travel time fits due to a model revision,  $\Delta T_{\text{MAX}}$  provides a bound for the other extreme. For the revision which introduced higher densities in the lower crust, the average  $\Delta T_{\text{MAX}}$  for  $P_n$  at the receivers listed in the previous paragraph is -0.14 s.

The second possible revision was a thinning of the lower crust trapezoids from 0 to 60 km (Fig. 5.9). For lower crustal arrivals,  $P_3$ , the average  $T_{\text{RMS}}$  (for arrivals at OBS Q shooting northeast, Sonobuoy 11 and Sonobuoy 12) increases from 0.064 s to 0.068 s and the average  $\chi^2$  increases from 0.92 to 1.12. For  $P_n$ , the average  $T_{\text{RMS}}$  (for arrivals at OBS Q shooting northeast, OBS O shooting southwest, OBS E shooting southwest and OBS N shooting southwest) increases from 0.069 to 0.095 s and the average  $\Delta T_{\text{MAX}}$  is -0.123 s. The degradation in  $P_n$  travel time fits is comparable for the two revisions, while the degradation in  $P_3$  traveltimes fits is much worse for the revision in which the density of the lower crust trapezoids is increased. On this basis, the thinning of the lower crust trapezoids is preferred as the revision whereby the asymmetry in the calculated free-air gravity anomaly is reduced.

In either of these cases, the modifications to the velocity-depth structure which are required to reduce the isostatic imbalance are substantial. The question remains, therefore, whether the asymmetry is an artifact of the 2-D seismic modelling or actually present in the region. The profile of the observed gravity anomaly along line R2 (Fig. 5.4) and the gridded data sets (Figs. 5.1 to 5.3) do not show a marked asymmetry. However, the initial stages of an asymmetric trend may be seen at the ends of the refraction line (Figs. 5.5 to 5.9). The observed values and the calculated anomaly were extended 20 km beyond the ends of the density structure to emphasize the onset of this trend.

While the asymmetry is not prevalent in the study area of this thesis, there are observations on a larger scale of an asymmetry in the regional behaviour of the free-air gravity anomaly in the Labrador Sea [Srivastava, 1981]. North of the Minna and Cartwright fracture zones (Fig. 2.1), the gravity anomaly is largely positive northeast of the extinct spreading centre and negative southwest of the extinct spreading centre, with the degree of asymmetry increasing northward towards Davis Strait. The regional behaviour of the free-air gravity anomaly in the Labrador and Norwegian-Greenland Seas was studied by Vogt *et al.* [1982]. They note that the asymmetry is most pronounced for crust formed between magnetic anomalies 25 to 29. Line R2 samples crust which is predominantly younger than magnetic anomaly 24 (Figs. 2.2 and 4.2), where Vogt *et al.* [1982] find a weaker asymmetry of approximately of 5 mGals.

In trying to attribute the origin of the regional asymmetry to a crustal or upper lithospheric phenomena rather than a sub-lithospheric one, Vogt *et al.* [1982] write:

"If the asymmetry arises in the crust and mantle lithosphere, we can consider as possible causes east flank/west flank differences in (a) depth to the acoustic basement, (b) thickness of the overlying sediments, (c) density of the sediments, crust and/or upper mantle, (d) thickness of the crust or (e) some combination of this factors."

and in summarizing their basin wide gravity model where the asymmetry is introduced by a thickening of oceanic layer 2 at the expense of oceanic layer 3 to the southwest of the extinct spreading centre, Vogt *et al.* [1982] write:

"...we regard the crustal model as a geologically plausible

hypothesis that can be tested by future seismic refraction measurements."

If the asymmetry in the calculated gravity anomaly along line R2 (Figs. 5.5 to 5.9) is considered to be consistent with the observed gravity field in a regional sense, the 2-D seismic velocity-depth structure along line R2 (Chapter 4) suggests that Vogt *et al.* [1982] were correct in assigning the asymmetry as a crustal phenomena. The source of this asymmetry, however, could be the high velocity/density of the lower crust to the northeast of the extinct spreading centre. The presence of this material along line R2 is detailed in this thesis (Chapter 4) and its presence at other locations northeast of the extinct spreading centre is summarized in Table 4.2. If this material is ubiquitous northeast of the extinct spreading centre, it would be largely responsible for the basin wide asymmetry in the gravity field.

#### *5.2.5 Evidence for Crustal Thinning in the Extinct Spreading Centre*

Another gravity model was devised to test whether the crustal thinning in the extinct spreading centre, as defined by the 1-D and 2-D seismic refraction results, is consistent with the free-air gravity anomaly. The initial gravity model was modified to explore the influence of the crust-mantle boundary and mantle densities while leaving the density structure of the water, sediment, and crustal layers intact. Specifically, the topography of the crust-mantle boundary (layer 7 to layer 8 in Fig. 4.1) is made to parallel the topography of the sediment-crust boundary (layer 3 to layer 4 or 5 in Fig. 4.1), thereby specifying a crust of constant thickness which is underlain by a mantle of uniform density. Through this specification, the thickness of the crust and/or density of the uppermost mantle do not provide varying degrees of compensation for the density or



topography variations which are present in the overlying layers.

The calculated free-air anomaly and density structure are presented in Figure 5.11. The peak to peak amplitude of the calculated free-air anomaly is 46 mGals, exceeding the 24 mGal difference between the observed values at the track crossings at 95 and 175 km. The negative contribution to the calculated anomaly from the low density of the lower crust within the extinct spreading centre ( $2.77 \text{ gcm}^{-3}$ ) is too large and can be reduced by a thinning of the crust. Likewise, the basement highs northeast of the extinct spreading centre make a positive contribution to the calculated anomaly which is too large and can be reduced by a thickening of the crust. To the southwest of the extinct spreading centre, the problems of asymmetry discussed in section 5.2.4 persist and no insight is gained by this model. The exaggeration of the calculated anomaly in this gravity model reveals that the variations in crustal thickness in the initial gravity model (section 5.2.1) serve to reduce the magnitude of the calculated anomaly. The free-air gravity anomaly is therefore consistent with a model where the low densities of the crust and upper mantle within the extinct spreading centre (80 to 110 km) are partially compensated by a thinning of the crust in this region.

### **5.3 Gabbroic Root Model**

The gabbroic root model [Hall *et al.*, 1986] is a geometric model for the structure of the crust and upper mantle at mid-ocean ridges. It stems from a structural and petrological analysis of the Bay of Islands ophiolite complex in western Newfoundland [Elthon *et al.*, 1982; Casey and Karson, 1981; Casey *et al.*, 1983]. The basalt cumulates from this ophiolite complex and some experimental studies of the petrology of mid-ocean

ridge basalts (MORB) [*e.g.* Stopler, 1980] suggest that the parental melts have not been in equilibrium with the harzburgite residual mantle at pressures less than 8 to 10 kbar (up to 30 km depth). This is consistent with the dynamic models of mantle flow (Chapter 1) in which buoyancy driven circulation focuses mantle upwelling into a narrow zone beneath the spreading centre and partial melting begins at substantial depths [Scott and Stevenson, 1989]. However, the petrological evidence and its interpretation remains equivocal. In discussing the petrology of cumulate gabbros dredged at the Mathematician Ridge (MR), an extinct spreading centre in the Pacific Ocean, Batiza and Vanko [1985] write:

"... mafic minerals in MR gabbros do not have the high (primitive) *Mg*-numbers characteristic of presumed high pressure phases, such as those from the Bay of Islands ophiolite...In addition, we cannot envision complete crystallization of the gabbros at pressures corresponding to depths over 30 km below the MR, and simultaneously explain the gabbro's occurrence at the deep-sea floor today."

Hall *et al.* [1986] provided a schematic model of their gabbroic root structure at slow spreading centres and this figure has been reproduced in Figure 5.12. The root structure underlying the mid-ocean ridge is composed of cumulate gabbroic and ultramafic rocks which extend to appreciable depths into the mantle. The shape of the root structure varies in relation to the spreading rate, widening as spreading rate decreases. This variability is central to the model as it provides an explanation for the spreading rate dependent behaviour of the free-air gravity anomaly which is observed at active spreading

### Gabbroic Root Model Schematic of Petrological and Density Structure

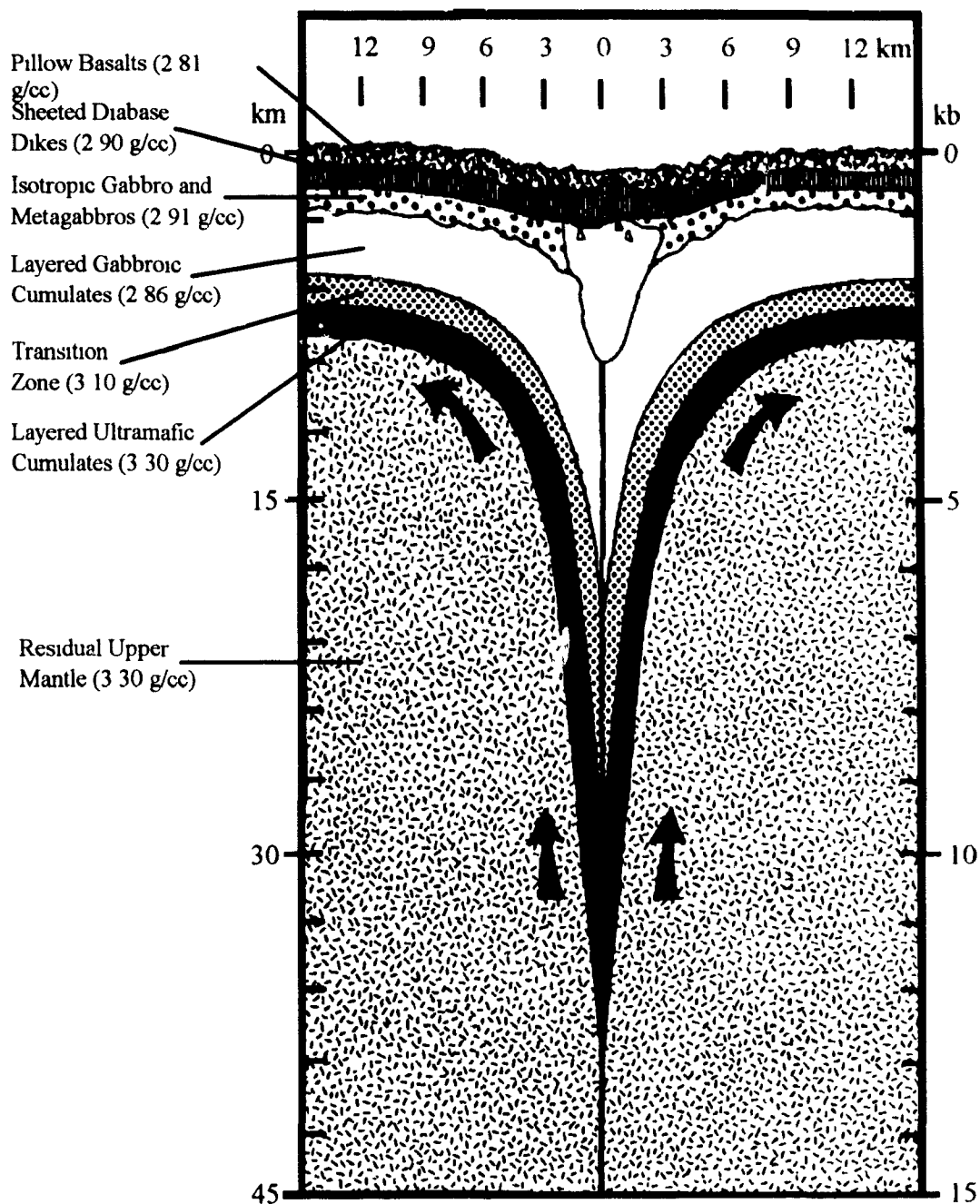


**Figure 5.12:** Schematic of the gabbroic root model [Fig. 1 in Hall *et al.*, 1986] proposed to underly active and extinct mid-ocean spreading centres. The partially gabbroic cumulate root extends vertically into the mantle beneath the ridge, providing a source for the free-air low observed at slow spreading centres. Densities are from Salisbury and Christensen [1978] at 25°C and 1 bar.

### Gabbroic Root Model: Residual Gravity Anomaly in the Labrador Sea

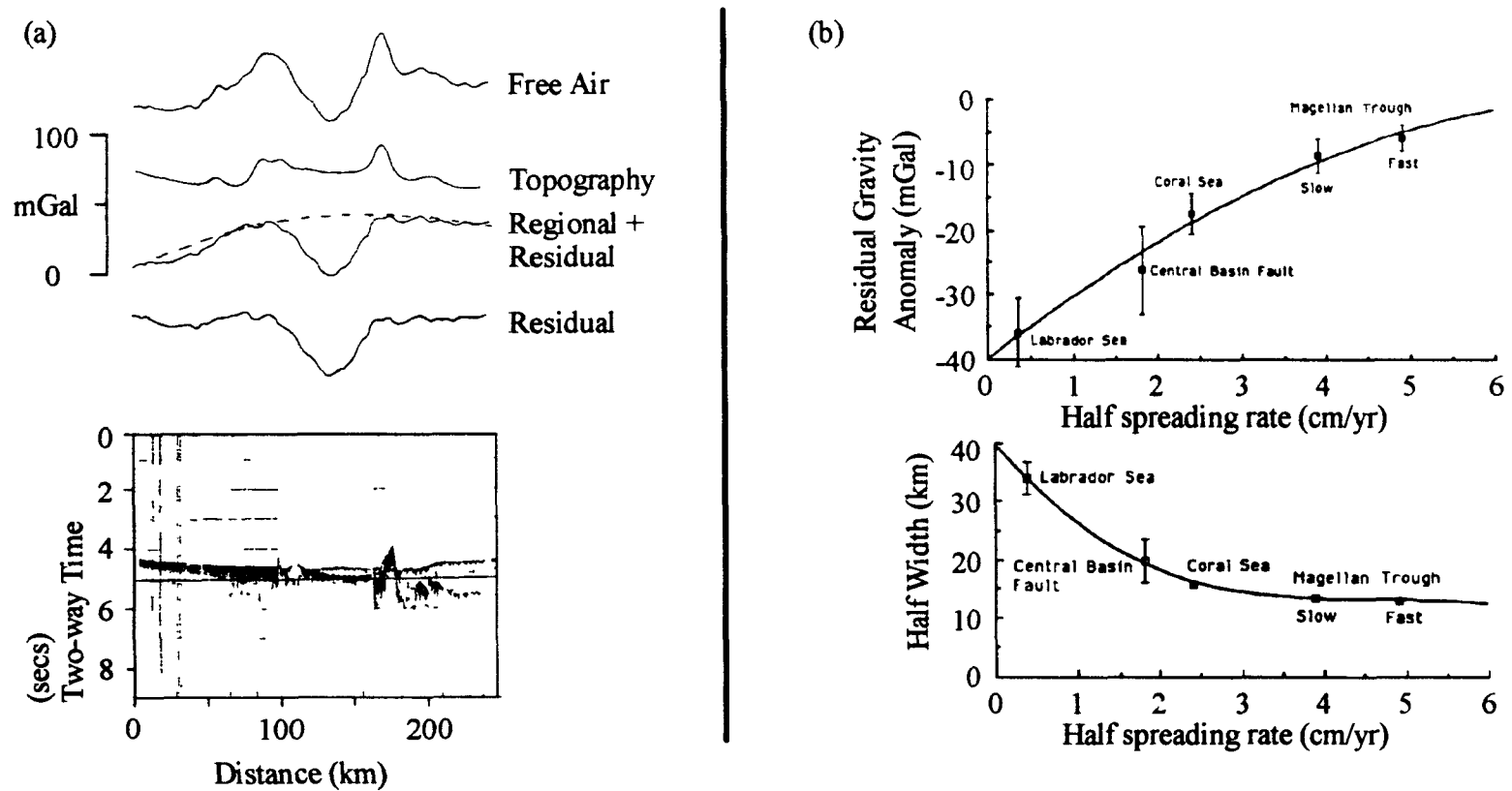


**Figure 5.13:** (a) Calculation of the residual gravity anomaly crossing the extinct spreading centre along Vema track 2911 in the southern Labrador Sea [Fig. 2a in Jonas *et al.*, 1991]. The basement topography (from reflection profile in lower panel) and regional trend are removed from the observed free-air anomaly leaving the residual anomaly. (b) Residual gravity anomaly and half width of several extinct spreading centres [Figs. 3a and 3b in Jonas *et al.*, 1991]

centres.

At slow half spreading rates ( $< 1$  cm/yr), free gravity fields with axial lows of  $60 \pm 10$  mGals and peak to peak distances of  $50 \pm 5$  km are typically observed [Cochran, 1979; Watts, 1982; Woodside, 1972]. As spreading rate increases, the amplitude of the free-air gravity low and its wavelength generally decrease. At fast half spreading rates ( $> 5$  cm/yr), the axial anomaly is positive ( $15 \pm 5$  mGal) and has a wavelength of approximately 35 km [Cochran, 1979; Lewis, 1982]. This systematic behaviour may not be explained solely by the basement topography [Watts, 1982] as a calculation of the residual gravity anomaly reveals (Fig. 5.13a). The residual gravity anomaly is the component of the gravity anomaly which remains following the subtraction of the gravitational attraction of the basement topography and a regional trend from the observed anomaly. It is a useful quantity as its source resides in the crust or upper mantle. Hall *et al.* [1986] calculate the contribution to the residual gravity anomaly from three sources: 1) mantle isotherms, density variations in the mantle due to its thermal structure; 2) a steady state axial magma chamber; and 3) their proposed gabbroic root structure. At slow spreading centres, these contribute -5.6, -0.9, and -29.8 mGals respectively [Table 3, Hall *et al.*, 1986]. At all spreading rates, the gabbroic root dominates the gravity field by at least an order of magnitude.

Hall *et al.* [1986] and Jonas *et al.* [1991] purport that the gabbroic root structure should be the only component remaining at an extinct spreading centre and be chiefly responsible for the axial low in the residual free-air gravity observed at these locations (Fig. 13b). At an extinct spreading centre, the contributions from the mantle isotherms and

magma chamber dissipate, but the gabbroic root structure is "frozen" in place at the time of extinction. The gravity field across the extinct spreading centre in the Labrador Sea is among those studied by Jonas *et al.* [1991]. They argue that the axial low in the residual gravity anomaly may be explained by a gabbroic root structure whose shape is determined by the pre-extinction spreading rates. Having conducted a seismic refraction study along a transect crossing the extinct spreading centre (Chapters 3 and 4) and gravity modelling (Chapter 5), it is appropriate to comment on the general viability of the gabbroic root model and its specific application to the extinct spreading centre in the Labrador Sea. To this end, the free-air gravity anomaly of the gabbroic root structure is calculated (section 5.3.1) and then coupled with the initial gravity model along line R2 (section 5.3.2).

#### *5.3.1 Free-Air Gravity Anomaly of the Root Structure*

The gravity model in Figure 5.14 is an attempt to replicate the Hall *et al.* [1986] calculation of the free-air gravity anomaly for the gabbroic root structure at an extinct spreading centre. Unfortunately, neither Hall *et al.* [1986] nor Jonas *et al.* [1991] provide the actual density structure which is used in their calculations or a numerical function which describes the shape of the root structure boundaries as a function of spreading rate. In the absence of this information, the schematic diagram (Fig. 5.12) for the root structure at slow spreading rates was used to develop the density structure in the lower panel of Figure 5.14. Following Hall *et al.* [1986], the low temperature density determination of rocks from the Bay of Islands ophiolite complex [Salisbury and Christensen, 1975] are used in the gravity model for the root structure at an extinct spreading centre. The axial magma chamber has been amalgamated into the crustal layer because its density at an

extinct spreading centre is the same as the surrounding crust.

The low density of the gabbroic root and thickening of the crust beneath the spreading centre, produce a calculated free-air gravity low with a peak value of -44 mGals (Fig. 5.14). This may be compared with the values of -36.3 and -35.8 mGals which Hall *et al.* [1986] calculate for (1) the generic root structure at slow spreading centres (Fig. 5.12) and (2) a half spreading rate of 0.35 cm/yr (the pre-extinction half spreading rate in the Labrador Sea [Kristofferson and Talwani, 1977]). It is presumed that the 8 mGal difference between the gravity model in Figure 5.14 and the published results of Hall *et al.* [1986] stems from using the schematic diagram to define the density structure. This difference, while troublesome, is considered when the results of coupling the initial gravity model to the root structure are discussed below.

### *5.3.2 Coupling of Root Structure to the Line R2 Gravity Model*

A density structure which couples the gabbroic root structure (Fig. 5.14) and the initial gravity model (Fig. 5.5) on line R2 is presented in the lower panel of Figure 5.15. This model retains all features of the initial gravity model which lie above the crust-mantle boundary. The gabbroic root structure, from the top of the transition zone downwards (Fig. 5.12), is then coupled to the base of the crust-mantle boundary. In this manner, the crustal level density variations within the initial gravity model and the region of low density material in the gabbroic root structure both contribute to the calculated anomaly.

The peak to peak amplitude of the free-air gravity anomaly calculated with this density structure is 54 mGals. This overestimates the actual peak to peak amplitude

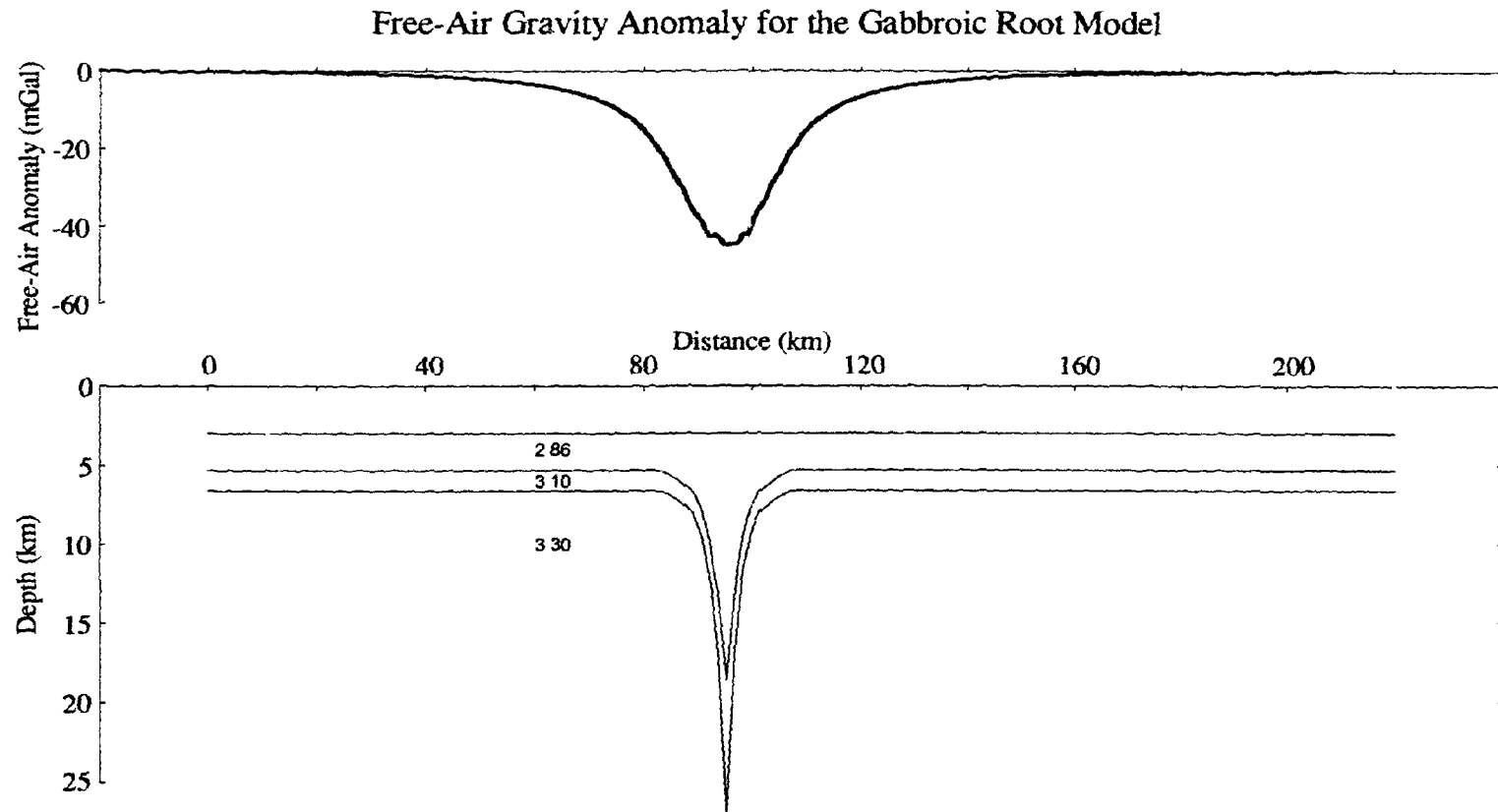


**Figure 5.14:** A gravity anomaly is calculated for the gabbroic root model at slow spreading centres (Fig. 5.12) of Hall *et al.* [1986]

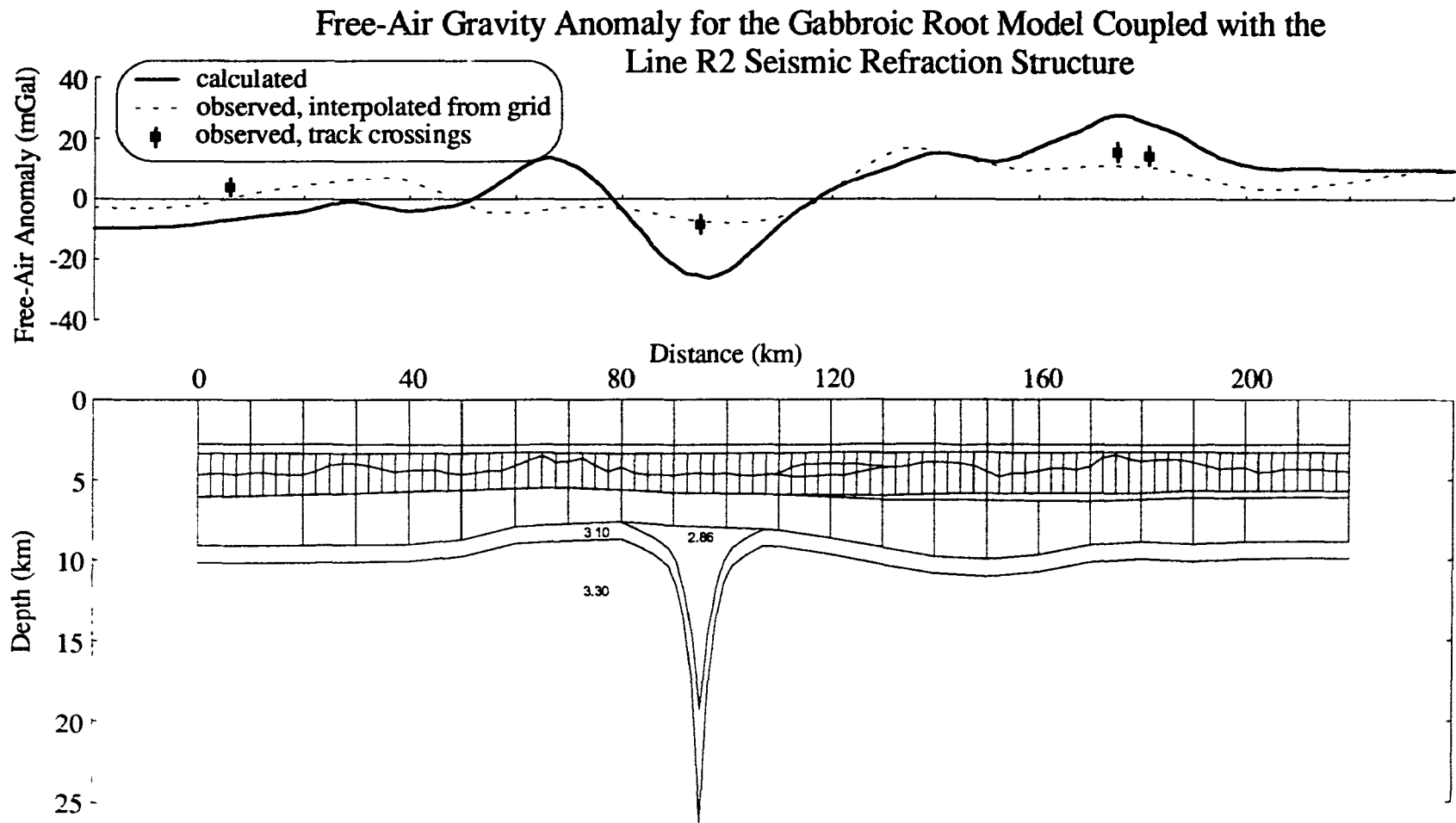


**Figure 5.15:** The gabbroic root model of Hall *et al.* [1986] is coupled with the initial gravity model for the seismic velocity-depth structure along line R2 (Fig. 5.5).

between the observed track crossings at 95 and 175 by 30 mGals. Recalling that the negative contribution of the root structure (Fig. 5.14) is 8 mGal too large, the difference may be reduced to 22 mGal. Nonetheless, the coupled model of the gabbroic root structure and the initial gravity model overestimates the actual free-air anomaly at the track crossings by a factor of 2, and an even greater amount when compared to the profile of observed values. Ideally, this comparison could be made to a residual gravity anomaly where the effects of the variable sediment thickness are removed to isolate the gravity anomaly which arises from the density structure of the crust and mantle. The computation of a meaningful residual gravity anomaly along line R2 would require observed values along track, or more track crossings at a very minimum. The present distribution of gravity stations in the vicinity of line R2 (Fig. 5.1) and variability in the profile of observed values according to the search area employed (Fig. 5.4) preclude the use of the profile of observed values in the calculation of a residual gravity anomaly.

Jonas *et al.* [1991] have calculated an average residual free-air gravity anomaly of  $-35.9 \pm 5.2$  mGals across the extinct spreading centre in the southern Labrador Sea from five ship track crossings (Vema cruises V2911A, V2911B, V2911C, V2911D, V2702E). Their uncertainty accounts for the extremal density values of 1.81 and 2.45  $\text{gcm}^{-3}$  for the sediment and 2.5 and 2.7  $\text{gcm}^{-3}$  for the basement used in calculating the gravitational attraction of the basement topography. The average residual gravity anomaly compares favourably with the value of -35.8 mGals predicted to underlie an extinct spreading centre with a pre-extinction half-spreading rate of 0.35 cm/yr [Hall *et al.*, 1986]. The agreement between these values in the Labrador Sea is taken to support the

gabbroic root model.

One aspect of their methodology in calculating the residual anomaly, namely the removal of the regional trend, serves to overestimate the actual value of this quantity. The regional trend is removed to supposedly isolate shallow sources in the crust and upper mantle from deeper sources in the mantle. The regional trend (Fig. 5.13a) which Jonas *et al.* [1991] specify has a broad convex form, peaking near the axial low. The removal of this trend maximizes the peak to peak amplitude between the flanks and the axial low. The mass balance calculations along refraction line R2 (Fig. 5.10) suggest that a linear trend would be more appropriate and this would decrease the peak to peak amplitude calculated.

#### **5.4 Summary**

The methodology and rigour of the gravity modelling along seismic refraction line R2 are limited foremost by the lack of coincident gravity measurements. A profile of the observed anomaly, interpolated from data separated from the refraction line by up to 17 km, must be relied upon for the assessment of gravity anomalies calculated for the density-depth structures presented. As such, the goal of the gravity modelling is not to match individual wiggles in the observed anomaly, but to address the general behaviour of the gravity field at the extinct spreading centre.

While the results are tempered by the lack of coincident gravity data, several important conclusions emerge in the gravity modelling. First, the observed free-air gravity anomaly is consistent with a thinning of the crust in the extinct spreading centre (80 to 110 km). The thinning helps to compensate the low densities of the crust and uppermost

mantle. Second, there is an asymmetry in the mass balance across the line R2 structure which gives rise to a broad asymmetry in the calculated anomaly. Revisions are introduced to the density-depth structure to eliminate this asymmetry as it is not prominent in the profile of observed values. If these revisions are carried back into the travel time modelling (Chapter 4), they degrade the quality of fit of computed arrival times to the limit of the uncertainty assigned to the observed travel time picks. While the asymmetry has only a weak expression in the observed anomaly at the ends of the refraction line R2, it is prominent on a regional scale across the basin. The gravity and seismic modelling along line R2 suggest that the high velocity/density of the lower crust to the northeast of the extinct spreading centre is primarily responsible for the asymmetry in the gravity field.

Third, it was hoped that gravity modelling along line R2 would unambiguously support or refute the hypothesis that mid-ocean spreading centres are underlain by deep gabbroic root structures. This degree of certainty cannot be achieved without coincident gravity data. However, the anomaly calculated when the gabbroic root structure is coupled with the initial gravity model for line R2, is strongly suggestive that the axial low in the free-air gravity anomaly (and residual gravity anomaly) does not require a gabbroic root zone for its generation. Lateral variations in the density of crust and uppermost mantle density, in conjunction with crust thickness variations, are the cause of this axial low at the extinct spreading centre in the Labrador Sea.

## **6. Discussion**

This thesis presents the results of the most comprehensive study of an extinct spreading centre which has been undertaken. Several outstanding issues concerning the processes at active spreading centres and of the evolution of the Labrador Sea may be addressed by integrating the seismic refraction results (Chapters 3 and 4) with modelling of the gravity field (Chapter 5) and the spreading rate history of the Labrador Sea (Section 6.1). This chapter considers several pertinent questions: How does mantle circulate beneath slow spreading centres and are the processes of crustal accretion dependent upon spreading rate? What is the source region for partial melt production? How does a dying mid-ocean ridge system behave? What is the nature of the crust within an extinct spreading centre and what processes of crustal accretion and/or alteration were responsible.

### **6.1 Spreading Rate History of the Labrador Sea Preceding Extinction**

In this section, magnetic anomalies are modelled to constrain the spreading rate behaviour of the spreading centre segment between the Snorri and Minna fracture zones (Fig. 2.1) in the Labrador Sea. The magnetic anomalies along selected ship tracks bearing northeast are presented in Figure 6.1 along with the position of the seismic refraction lines R1 and R2 (blue lines) and OBS and sonobuoy receivers (magenta crosses). The amplitude of the observed anomalies is represented by the excursion of the red dots perpendicular to their corresponding measurement locations on the ship tracks (red lines); positive anomalies are plotted to the north of a ship track and negative anomalies to the south. An interpretation of the pattern of magnetic anomalies, following Roest and

### Labrador Sea, Magnetic Anomaly along Track and Gridded Free-Air Gravity Anomaly

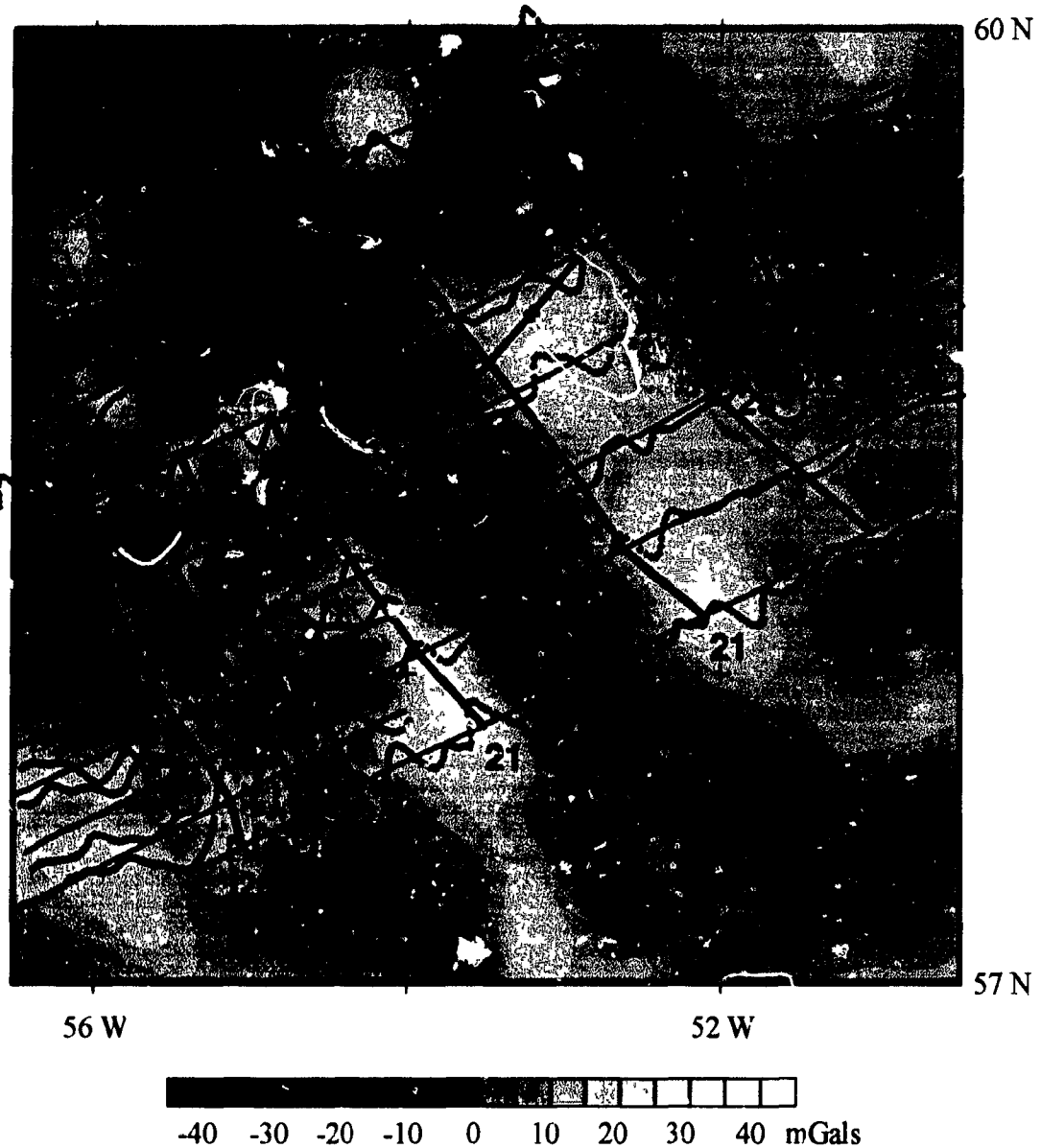


**Figure 6.1:** The magnetic anomaly along selected ship tracks (red lines) in the vicinity of refraction lines R1 and R2 (blue lines) in the Labrador Sea. Anomalies are plotted perpendicular to the ship track with positive values to the north. Receiver locations are marked in magenta. The gridded free-air gravity anomaly from Figure 5.1 is presented in gray scale. Identified magnetic lineations (green lines) follow the interpretation of Roest and Srivastava [1989b].

Srivastava [1989b], is delineated by the green lines and corresponding chronological identifiers. All of the aforementioned information is superimposed on a gray scale representation of the gridded free-air gravity anomaly (Fig. 5.1).

The magnetic anomalies through which lineations 25 and 26 are traced are readily discerned, whereas the amplitude of the magnetic anomalies from chron 24 to the extinct spreading centre are muted. Several processes, which are not mutually exclusive, could lead to the development of low amplitude magnetic anomalies in this region. The first relates to the separation between sections of the oceanic crust which are imparted with normal or reversed thermoremanent magnetization as they cool below the *Curie point* of magnetization. Denham and Schouten [1979] have quantified the probability of rocks with mixed geomagnetic polarities, and hence a muted magnetic anomaly, occurring in a vertical column. The probability depends primarily on two factors: the spreading rate and the width of the zone in which new material is accreted. Notably, the probability of mixed polarities increases as spreading rate decreases. A second explanation for the low amplitude magnetic anomalies is the period of oblique spreading in the Labrador Sea following the 45° change in spreading direction at chron 25 [Srivastava and Tapscott, 1986]. Roots and Srivastava [1984] suggest that spreading at an angle oblique to the ridge axis leads to greater segmentation of the ridge axis. The resulting plethora of normal and reverse polarity crustal blocks juxtaposed across the many small offset transform faults mutes the magnetic anomaly pattern. This hypothesis is supported by the correspondence between the geographical extent of rough basement topography and the axial magnetic quiet zone and an increasing intensity in the magnetic anomalies as the obliquity

decreases in the southern Labrador Sea. A third explanation is offered by Jackson and Reid [1983] who find that the intensity of observed magnetic anomalies is a function of spreading rate which they attribute to a corresponding relationship between crustal thickness and spreading rate [Reid and Jackson, 1981]. If a substantial portion of the crust is considered to have a magnetization, then the thinning of the crust within the extinct spreading centre would reduce the thickness of the source layer for the magnetic anomalies. Finally, there is the possibility that the intensity of magnetization may reflect variations in the petrology of the oceanic crust incurred as spreading ceased and/or more severe alteration by hydrothermal processes.

In general, having identified magnetic anomalies, the spreading rate history between successive magnetic anomalies may be calculated; there is a volume of crustal material required to span the distance between the anomalies and a time interval in which it must be generated. In the case of the Labrador Sea, this approach is complicated by at least three factors. 1) The exact time of cessation of spreading is unknown. Spreading must have ceased sometime between magnetic anomalies 21 and 13, chron 21 being the last distinguishable anomaly in the Labrador Sea basin and 13 being the first continuous anomaly parallel to the Mid Atlantic Ridge (Fig. 2.1). 2) The low amplitude magnetic anomalies from chrons 24 to 21 may not be unambiguously discerned. Consequently, spreading rate changes may not be resolved at each of the periods of normal polarity in this interval. 3) The change in spreading direction between chrons 24 and 25. This is partially avoided by focusing on spreading rate changes between chron 24 and the time of extinction, but the spreading at an angle oblique to the ridge axis remains.

Given that a detailed spreading history cannot be ascertained directly from the magnetic anomalies, synthetic magnetic anomaly profiles were developed for five plausible spreading rate scenarios and then compared with the observed profiles. Each of these models was required to generate 88 km of crust from chron 24 to the time chosen for the cessation of spreading. These spreading rate histories are presented in Figures 6.2a through 6.2e as a function of time (right panel) and as a function of distance from the spreading axis (left panel). The spreading rate histories which are modelled are: (a) spreading at a constant rate of 4.45 mm/yr from anomalies 24 to 13; (b) spreading at rates of 7.04 and 6.85 mm/yr from anomalies 24 to 21 and 21 to 20 respectively, followed by a sudden decrease in spreading rate to 1.64 mm/yr from anomalies 20 to 13; (c) a variant on (b) with spreading at a rate of 7.04 from anomaly 24 to 21 and spreading at a rate of 6.85 mm/yr extending from anomalies 21 to 18 when it is terminated instantaneously; (d) and (e), two models with a linear decrease in spreading rate from anomalies 21 to 13 and 24 to 13 respectively. The spreading rate history from Roest and Srivastava [1989a] at 60.56°N and 48°W for a section of the extinct spreading centre to the northwest of the Snorri fracture zone (Fig. 2.1) has also been replicated (Fig. 6.2f).

For each of these six potential spreading histories, the calculated magnetic anomalies are presented in Figures 6.3a through 6.3f, underlain by the respective sequences of normal polarity blocks used in the calculation and their chronological identifiers. The width of the blocks differs in accordance with the specified spreading rate and duration of that period of normal polarity, following the time scale for geomagnetic polarity in Table 1 of Kent and Gradstein [1986]. The blocks are 2 km thick and extend

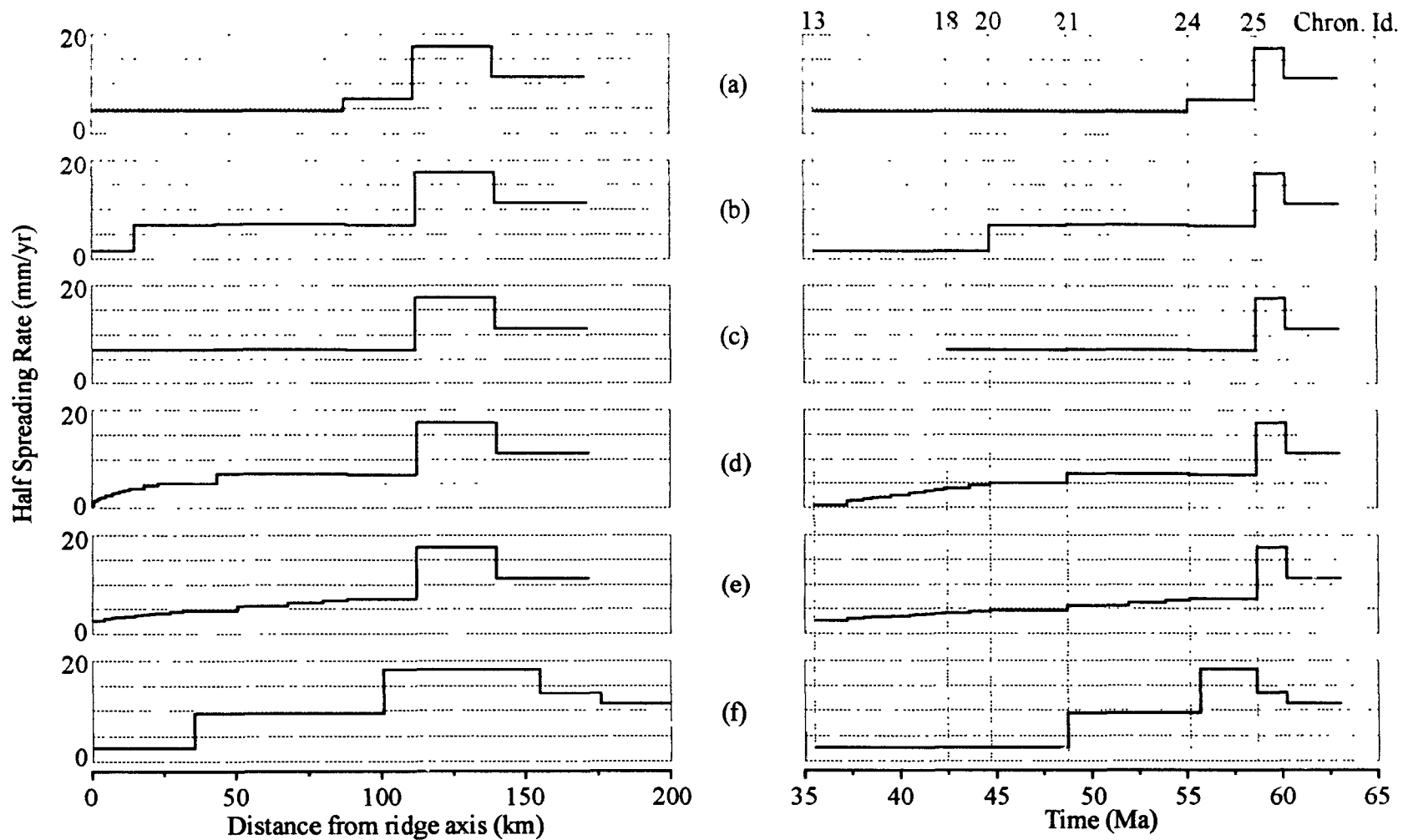


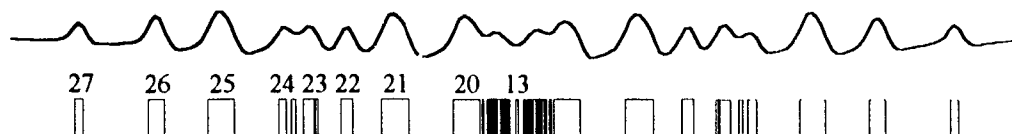
**Figure 6.2:** For each of the pre-extinction spreading rate scenarios in Figs. 6.2a through 6.2f, the half spreading rate behaviour used to generate the sequence of normal magnetic polarity blocks is plotted as a function of distance from the mid-ocean ridge axis (left panel) and as a function of time (right panel).

Calculated Magnetic Anomaly Patterns for Potential Pre-Extinction Spreading Rate Histories in the Labrador Sea

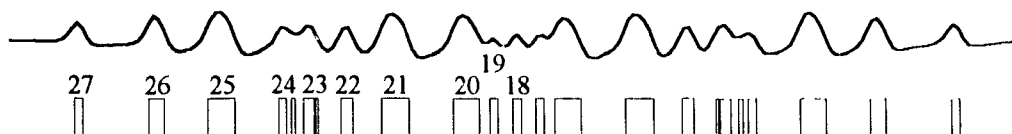
(a) Constant Spreading Rate from Chrons 24 to 13



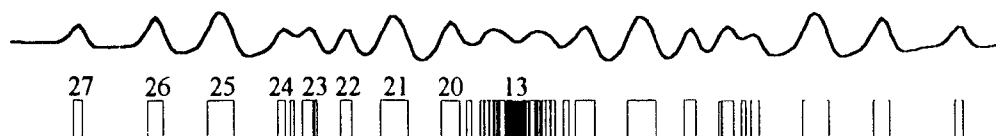
(b) Sudden Decrease in Spreading Rate at Chron 20



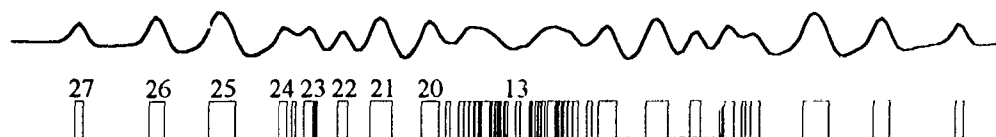
(c) Instantaneous Cessation of Spreading at Chron 18



(d) Linear Decrease in Spreading Rate from Chrons 21 to 13



(e) Linear Decrease in Spreading Rate from Chrons 24 to 13



(f) Spreading Rate History from Roest and Srivastava [1989a] at 60.56 N and 48 W

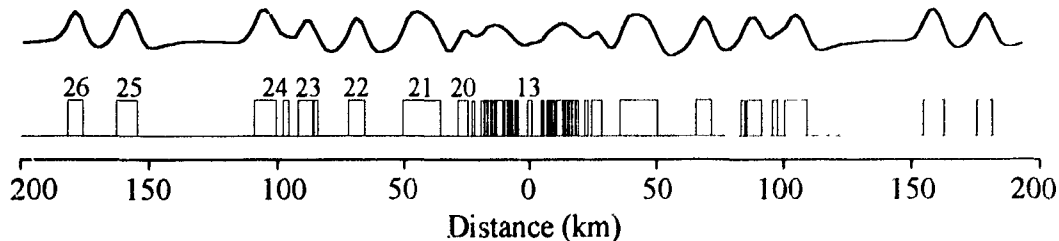


**Figure 6.3:** Magnetic anomaly patterns are calculated for a variety of pre-extinction spreading rate scenarios (a) to (f) in the Labrador Sea. Each anomaly pattern is underlain by the sequence of normal polarity blocks used to generate the anomaly and their respective chronological identifiers.

Observed and Calculated Magnetic Anomalies in the Vicinity of Seismic  
Refraction Lines R1 and R2 in the Labrador Sea

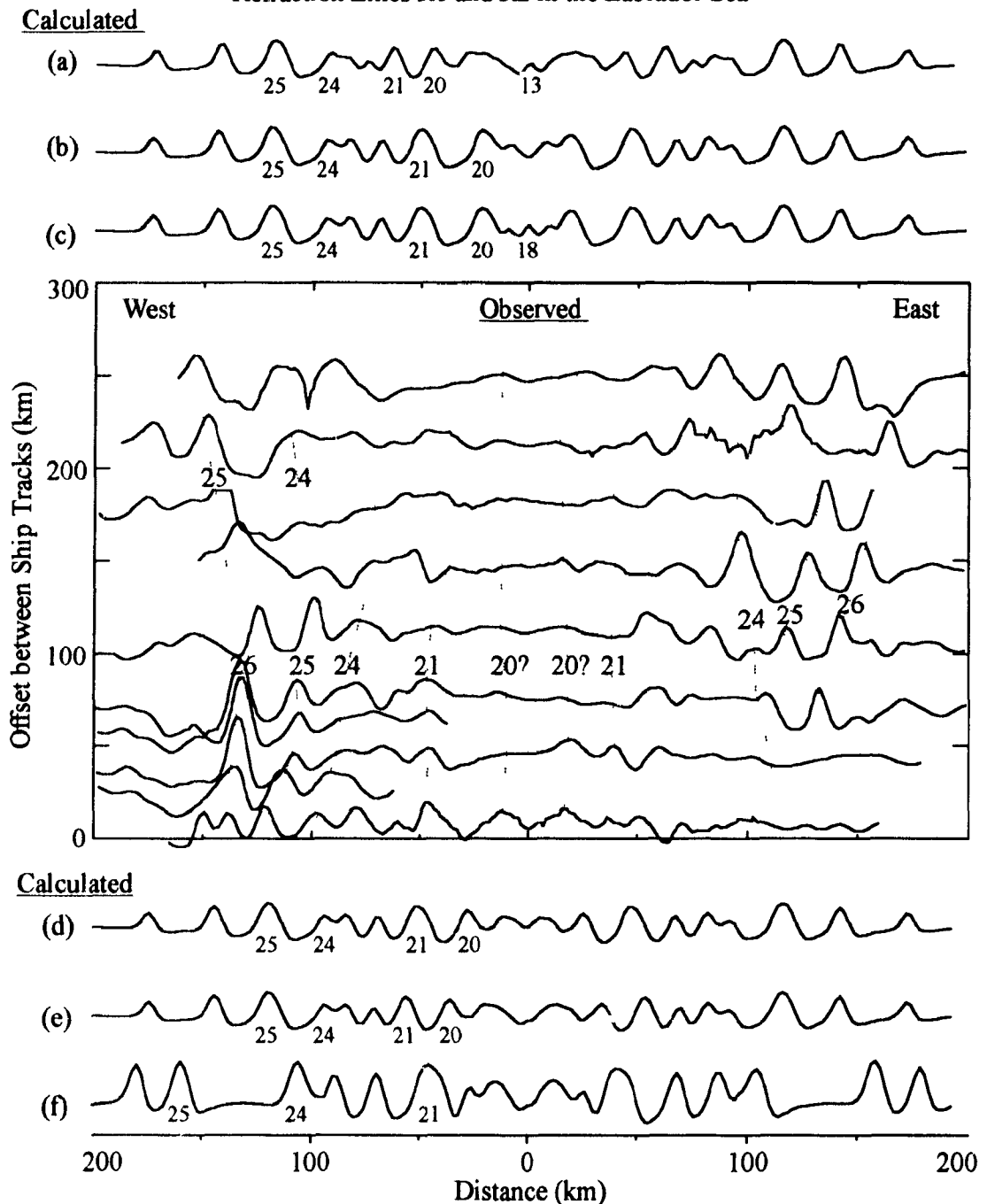


**Figure 6.4:** The calculated magnetic anomaly patterns for several pre-extinction spreading rate scenarios (Figs. 6.2a through 6.2f) are plotted with observed magnetic anomaly profiles in the vicinity of refraction lines R1 and R2 (Fig 6.1). Observed anomalies are plotted as a function of distance along a ship track relative to the point at which the profiles approach axial symmetry. The dashed lines delineate an interpretation of the magnetic anomalies following Roest and Srivastava [1989b].

from a depth of 4.5 to 6.5 km. The orientation of ridge axis is  $320^\circ$ , clockwise from north. Models are evaluated on their ability to replicate the spatial distribution and amplitude of the observed magnetic anomalies, in particular, the zone of low amplitude magnetic anomalies from chron 24 until the cessation of spreading. To this end, the synthetic profiles for the spreading rate scenarios (a) through (f), are plotted in Figure 6.4 along with the observed profiles from Figure 6.1. In this case, the observed profiles are plotted as a function of distance along their respective ship tracks relative to a point of symmetry at the extinct spreading centre.

Among these models, those with spreading at faster rates preceding an abrupt extinction ('b' and 'c' in Figs. 6.3 and 6.4) are the least appropriate. The amplitude of the anomalies from 24 to 20 are too high, anomaly 21 being a prominent example. The presence of discernable anomalies between 20 and the time of cessation (18 for 'c', 13 for 'b') is a further criteria upon which these models may be rejected. This is particularly true for the model where the cessation of spreading occurs at anomaly 18 (41.3 Ma) and is not prolonged by an additional 7 My as in the other models. Model 'a', with a constant spreading rate from anomaly 24 to 13 is also problematic. While it does effectively generate a broad zone of low amplitude anomalies, there is not enough crust separating anomaly 24 from anomaly 21 indicating that a higher spreading rate is required in this time interval. The remaining models, 'd' and 'e', involve linear decreases in spreading rate from anomalies 21 to 13 and 24 to 13 respectively. Model 'd' is selected as the most suitable because of its higher amplitude for anomaly 21 and separation between anomalies 21 west and 21 east.

In summary, some constraint may be placed on the pre-extinction spreading history of the Labrador Sea between chron 24 (55 Ma) and the time of cessation. It is likely that extinction occurred over a protracted period ending some time closer to anomaly 13 (35 Ma) than anomaly 20 (45 Ma). Further, the extinction was likely preceded by a period in which spreading rate was decreasing significantly by the time of anomaly 21 (49 Ma). The synthetic magnetic anomalies demonstrate that a linear decrease in spreading rate from 7.04 mm/yr to 0 mm/yr between anomalies 21 to 13 provides a plausible function describing the spreading rate decrease. Resolution of the spreading history is limited by the ability to identify the low amplitude anomalies about the extinct spreading centre and uncertainty as to the origin of these low amplitudes. If the low amplitudes arise in part from irregular polarities in the crust, then the inability to resolve a detailed spreading history is itself consistent with a decreasing spreading rate. In the magnetic modelling, the generation of lower amplitude anomalies is only partially realized. The algorithm is limited by its assumption that crust is accreted into laterally discrete units with normal and reversed geomagnetic polarities. The amplitudes of the observed anomalies are muted to a greater extent than those calculated because lower amplitudes in the modelling arise solely from the narrow breadth of the blocks and their proximity to blocks of opposite polarity.

## **6.2 Nature of the crust and uppermost mantle at the extinct spreading centre**

The 1-D and 2-D seismic refraction results (Chapters 3 and 4 respectively) along the strike of the extinct spreading centre and crossing it transversely find a prevalence of anomalously thin and low velocity crust in the extinct spreading centre which is underlain

by low velocities in the uppermost mantle. There are essentially two frameworks in which the crustal structure observed in the extinct spreading centre may be explained. These are a consideration of the crust as being igneous, emplaced through extrusive and plutonic processes, or a consideration of the seismically defined crust as altered upper mantle.

Oceanic crust, in the prevalent view is igneous rock which is solidified from partial melt which migrates to the accretionary axis. The details of this process remain equivocal, but following the analogies between ophiolite studies [*e.g.* Salisbury and Christensen, 1978] and marine seismic studies [*e.g.* Spudich and Orcutt, 1980], the general view of mature oceanic crust is one which is vertically structured. The upper crust (layer 2) is composed of extrusive volcanics (pillow basalts), underlain by a dense series of vertical dikes (sheeted diabase dikes) stemming from frequent episodes of injection from an underlying magma chamber. The lower crust (layer 3) is plutonically emplaced, solidifying from an axial magma chamber which is present at least episodically. Ultramafic cumulates precipitate from the magma chamber to form the base of the newly formed crust, while isotropic gabbros are formed by solidification to the sides of the axial chamber.

The low upper crustal velocities observed within the extinct spreading centre are comparable to those observed for young oceanic crust [Purdy, 1987]. Houtz and Ewing [1976] found that the velocity of the upper crust increases systematically with age; this increase has since been attributed to the filling of fractures and voids by chemical alteration and precipitation which reduce the anisotropy [Fryer *et al.*, 1989]. A plausible explanation for the low velocities of the upper crust within the extinct spreading centre

is that hydrothermal alteration did not operate with the vigour or for the periods required for significant alteration and precipitation in the fractures. This reasoning is not favoured, however, as it offers no explanation for the low velocities in the lower crust and evidence for increased hydrothermal alteration of the upper mantle.

Retaining the ophiolite based model of oceanic crust, another mechanism for generating the low velocities could be through a pervasive fracturing of the entire crust. This follows arguments that the spreading rate decreases preceding extinction are associated with a decrease in magmatism and an increasing requirement for tectonism to accommodate the divergence of the plates. Huang and Solomon [1988] present observations that the maximum centroid depth of active ridge-crest earthquakes increases from 2 to 3 km at full spreading rates of 40 to 45 mm/yr to 5 to 6 km at full spreading rates of 5 to 10 mm/yr. Meanwhile, Purdy *et al.* [1992] show, with a limited data set, that a systematic relationship exists between spreading rate and the depth to which a p-wave velocity inversion is observed at active spreading centres. Their preferred explanation is that the "major faults that extend to greater depths on slower-spreading ridges [Huang and Solomon, 1988] allow a more vigorous circulation of cooling sea water to reach greater depths, blocking the upward migration of large melt bodies". The maximum depth to which faulting extends is an indication of the thickness of the mechanically strong layer which is prone to brittle failure in response to the extensional stresses caused by the diverging plates.

A systematic relationship between spreading rate, faulting, hydrothermal circulation, and the depth below the spreading centre at which an appreciable partial melt

fraction is observed could be readily applied to the spreading centre in the Labrador Sea preceding its extinction. The zone in which crustal and upper mantle velocities are anomalously low is bounded within anomalies 21 west and 21 east (Fig. 6.5) where, based on the magnetic modelling (section 6.1), the slowest spreading rates could have been encountered. It is then within this zone that brittle failure of the crust should be most prevalent. Aside from explaining the low crustal velocities, this explanation is appealing as it provides a ready pathway for the hydrothermal alteration of the upper mantle which is observed (details later in this section).

A second view of the oceanic crust is one in which it is largely constituted of serpentinitized peridotite, upper mantle which has been cooled and altered hydrothermally [Hess, 1962; Dietz, 1963]. The Moho in this case does not represent a composition change between crust and mantle rocks but represents a hydration boundary, the depth to which upper mantle was altered. There is a linear relationship between the volume percentage of serpentinite and seismic p-wave velocity [Christensen, 1966] with velocities of approximately 5 km/s for 100% serpentinite increasing to 8.0 km/s for unaltered peridotites. Serpentinite has a  $V_p/V_s$  ratio which is much higher than other rocks likely to constitute the oceanic crust. It is on the basis of  $V_p/V_s$  studies [Christensen, 1972] that the serpentinite model of the oceanic crust has been largely rejected. However, it remains a viable alternative for the structure of the crust at oceanic fracture zones [Calvert and Potts, 1985; Loudon *et al.*, 1986] and has been applied as an alternative model for the East Pacific Rise based on gravity data and thermal models [Lewis, 1983].

Neither of these views of the oceanic crust is entirely satisfactory for explaining

the low crustal velocities which are observed in the region of the extinct spreading centre. If the serpentinite model is selected then the variable thickness of the crust within the extinct spreading centre (Fig. 3.8, line R1, 1-D travel time solutions), near linear velocity gradients (Fig 3.8, line R1, velocity-depth structures from  $\tau$ - $p$  inversions), and low velocity crust may be explained in terms of the regional variability in the depth to which hydrothermal circulation penetrated and altered the upper mantle. However, the presence of velocity gradients in the upper mantle beneath what has been resolved as the Moho by the seismic results would require a further complexity in the serpentinite model. Two stages of hydrothermal alteration would have to have been operative, one quite vigorous and short lived to establish the distinct boundary interpreted as the Moho and a second more protracted period of hydrothermal alteration to alter rocks below this boundary. While this mechanism is largely speculative, multiple stages of hydrothermal alteration are required to explain the petrology of gabbroic rocks dredged from the failed Mathematician Ridge [Stakes and Vanko, 1986]. An initial high temperature vapour phase is purported to be followed by a more pervasive lower temperature brine phase.

As the seismic refraction results favour a crustal layer which is discrete from the mantle and the ability to generate sharp hydration boundaries is worrisome, the preferred explanation for the low velocity crust builds upon the view of the crust as being igneous. At the present time, it is presumed that the velocity of the crust is lowered by pervasive fracturing owing to increased tectonism. The faults provide a pathway for fluids to penetrate into the uppermost crust and alter the peridotites. A pre-existing Moho is thus overprinted by one episode of hydrothermal alteration. Discernment between these

alternatives would require  $V_p/V_s$  ratios for the crustal level material. S-waves are observed on some OBSs, however, they are not well developed and only show arrivals for the mantle refraction,  $S_n$ .

Considering the nature of the upper mantle within the extinct spreading centre, low velocities are observed for the upper mantle in four of the seven refraction profiles shot on line R1 along the strike of the extinct spreading centre. The average upper mantle velocity is 7.74 km/s (Table 3.1) and is less than the velocities of 7.92, 7.82, and 7.94 km/s determined for the three upper mantle nodes within the extinct spreading centre in the 2-D modelling of the refraction data crossing the extinct spreading centre transversely (line R2 boundary and velocity nodes in Table C). This difference in velocity may be attributed to anisotropy in the mantle as a faster p-wave velocity is found in the direction of spreading due to the preferential alignment of crystals in the direction of spreading. Bibee and Shor [1976] show that a widespread anisotropy averaging 5% is observed for mantle velocities.

The low velocities themselves are interpreted as resulting from the hydrothermal alteration of upper mantle peridotites. No more than 10% of the peridotite must be serpentized to produce the observed velocities [Christensen, 1966]. There is widespread evidence for hydrothermal alteration and serpentization at oceanic fracture zones [*e.g.* Calvert and Potts, 1985; Christensen, 1972; Minshull *et al.*, 1991]. Calvert and Potts [1985] call upon this mechanism to explain the widespread occurrence of low upper mantle velocities in old Atlantic fracture zones and an apparent decrease in upper mantle velocity in fracture zones with increasing age. Given the similarity between the crustal

structures observed within the extinct spreading centre to those at oceanic fracture zones (section 3.4) and the likelihood of faults penetrating the entire crust at the slow spreading rates preceding extinction, it is reasonable that the extinct spreading centre is an environment in which upper mantle peridotites are prone to serpentinization.

Finally, it is worth noting that the observations of low crustal velocity within the extinct spreading centre in the Labrador Sea are consistent with the limited observations at other extinct spreading centres. In the Shikoku Basin in the North Phillipine Sea, low p-wave velocities are observed for seismic layers 2A and 2B [Nagumo *et al.*, 1980], there are no returns from deeper layers due to the small capacity of the air gun employed. In simple gravity models of the Aegir Ridge in the Norwegian-Greenland Sea, Uenzelmann-Neben *et al.* [1992] require an irregularly shaped low density body within the crust to fit the observed gravity field. The gravity modelling is performed along a multichannel reflection line crossing the ridge perpendicular to ridge strike. With this control of the basement topography in hand, they argue that the gravity field cannot be explained by sediment thickness alone. These observations are not a sufficient basis upon which the results presented in this thesis may be generalized to all extinct spreading centres, but the consistency in the results to date is encouraging.

### **6.3 Implications for 2-D Dynamic Models of Flow Beneath Mid-Ocean Ridges**

An objective of this thesis is an assessment of dynamic models for mantle circulation beneath mid-ocean ridges and their associated processes of crustal accretion. As reviewed in Chapter 1, these models are characterized by two end members in which mantle circulation is dominated by (1) the passive flow induced by the separation of the

overlying plates [Reid and Jackson, 1981] or (2) buoyancy forces localized beneath the spreading centre [Phipps Morgan, 1987; Scott and Stevenson, 1989]. The source region from which partial melt is extracted, its transport to the accretionary axis, and the production of crust as a function of spreading rate differs markedly in these two end member models.

Buoyancy dominated circulation predicts that mantle flow should occur rapidly in a narrow zone beneath the spreading centre with partial melting beginning at great depths ( $> 60$  km). For values of mantle viscosity appropriate for mid-ocean spreading centres ( $10^{19}$  Pa s, Craig and MacKenzie, [1986]), the production of crust is nearly independent of spreading rate [Sotin and Parmentier, 1989]. Circulation of this nature provides a theoretical framework for the petrological and geometric "gabbroic root" model of Hall *et al.* [1986] which was extensively reviewed in section 5.3. Circulation dominated by passive upwelling, by contrast, predicts that partial melt is extracted from a wide region [*e.g.* Spiegelman and MacKenzie, 1987], experiencing considerable lateral transport, and that crustal thickness becomes a discernable function of spreading rate when half spreading rates are less than 20 mm/yr [Reid and Jackson, 1981].

The extinct spreading centre in the Labrador Sea is among the finest examples of a spreading centre where the accretion of oceanic crust ceased due to a major re-orientation of lithospheric plates. It provides a tectonic setting in which the predictions of the end member dynamic models of mantle flow may be evaluated. Ideally, this assessment could be accomplished by directly comparing the observed variations in crustal thickness to changes in spreading rate preceding the extinction. This goal, as

postulated, is not tenable since the low amplitude of the magnetic anomalies is an inherent feature of the extinct spreading centre and limits the resolution of the seafloor spreading history (section 6.1).

However, the seismic velocity-depth structure, free-air gravity anomalies and magnetic anomalies in the study area of the extinct spreading centre in the Labrador Sea are self-consistent and congruous with a spreading centre where the availability of partial melt was restricted as spreading rate decreased preceding extinction. In support of this view, a summary of the research in this thesis is presented in Figure 6.5. The four figures presented are: (a) The preferred model for the spreading rate history (model 'd' in Fig. 6.2). The half spreading rate is plotted as a function of range from the spreading axis, placed at a distance of 95 km along R2. (b) The profile of observed free-air gravity anomaly which was extracted from the data gridded using a search area of 3 times a gaussian half-width of 15 km (Fig. 5.4). (c) The total crustal thickness along line R2, defined as the difference in depth between the sediment-crust and crust-mantle boundary nodes at distances where nodes exist on both boundaries (Fig. 4.1). And (d), the isovelocity contour representation of the 2-D seismic velocity-depth structure along line R2 (Fig. 4.2). The location of chrons 21, 20, and 13 in the preferred magnetic model are plotted to span across all four of the Figures 6.5a through 6.5d.

The most significant variations in these parameters begins at the time of chron 21 (49 Ma) and continues until the cessation of spreading. In the 90 km wide zone from anomaly 21 west to 21 east, there is a substantive thinning of the crust (maximum difference is 3.3 km between nodes at 90 and 140 km), a decrease in the seismic p-wave

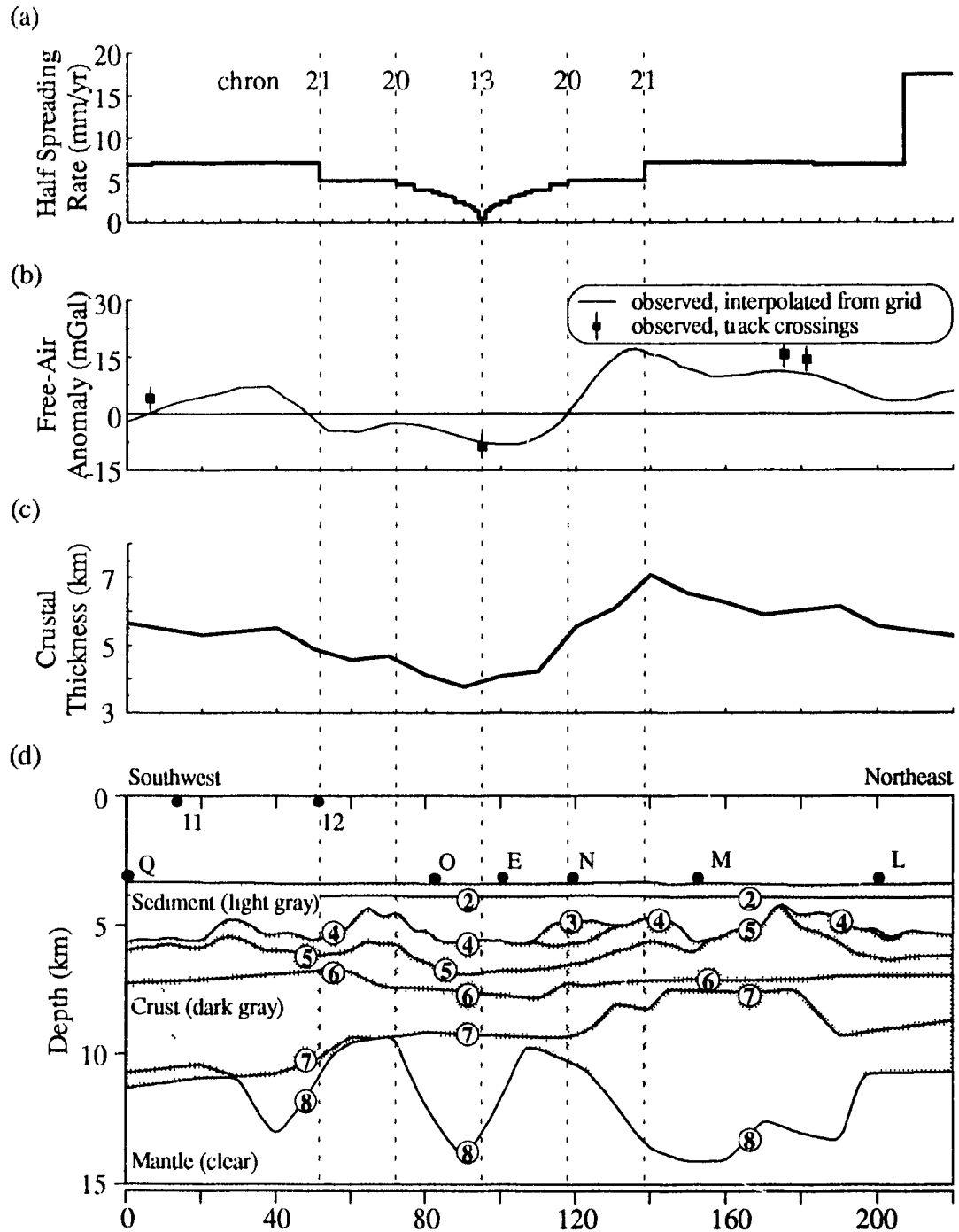


**Figure 6.5:** Summary of geophysical information along line R2 transversely crossing the extinct spreading centre in the Labrador Sea. (a) A linearly decreasing rate spreading rate from chron 21 to 13 (Fig. 6.3a). (b) Profile of the observed free-air gravity anomaly (Fig. 5.4). (c) Crustal thickness at each mantle boundary node in the 2-D seismic modelling (d) The isovelocity contour representation of the 2-D seismic velocity versus depth structure (Fig. 4.2).

velocity of the crust, and a low in the free-air gravity anomaly. Anomaly 21, as noted in section 6.1, is the last clearly discernable anomaly in the vicinity of the refraction lines. While spreading rate changes cannot be defined precisely by the magnetic modelling, the most substantive variations in the velocity-depth structure, gravity field, and magnetic field are consistent with a region in which the spreading rate could have been substantially reduced. On this basis, the presence of crustal thinning between anomalies 21 west and 21 east is seemingly consistent with the passive models of dynamic flow in which crustal thickness is a function of spreading rate (Fig. 1.1b).

To explore this initial conclusion, crustal thickness has been calculated for the six potential spreading rate histories using two of the crustal thickness versus spreading rate relationships of Reid and Jackson [1981]. The calculated crustal thicknesses are plotted in Figure 6.6 as a function of distance along refraction line R2, crossing the extinct spreading centre transversely, along with the observed crustal thickness from the 2-D modelling of the seismic refraction data (Fig. 6.5c). Thermal models I and II (left and right plot panels in Fig. 6.6 respectively) use the spreading rate versus crustal thickness relationship from curves 3 and 4 respectively (Fig. 1.1) of Reid and Jackson [1981]. Thermal model II is most appropriate for modelling the crustal thickness at oceanic hot spots while thermal model I is Reid and Jackson's [1981] preferred model to fit their compilation of seismic refraction measurements of crustal thickness. The spreading rates in the potential spreading rate histories in the Labrador Sea (Fig. 6.3) are all below 20 mm/yr, the region where crustal thickness is strongly dependent on the spreading rate.

For thermal model I, the calculated crustal thicknesses are consistently very much

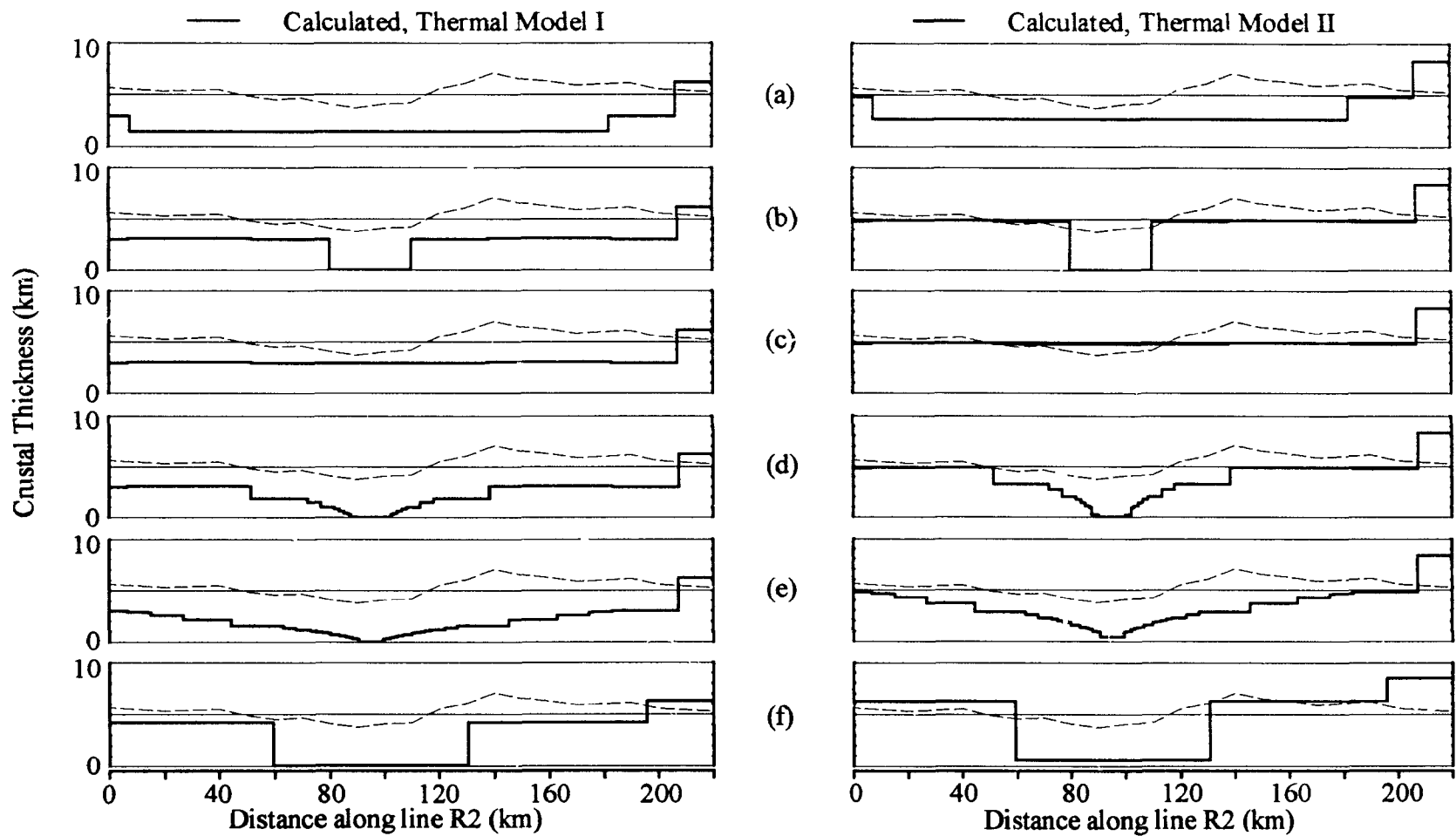


**Figure 6.6:** Using the pre-extinction spreading rate scenarios (Figs. 6.2a to 6.2f), the observed crustal thickness (broken line) along line R2 is compared with predicted values of crustal thickness (solid lines) following the thermal model of Reid and Jackson [1981]. Thermal model I, curve 3 in Figure 1.1 ( $T_{240}=1490^{\circ}\text{C}$  and  $f_0=5\%$ ). Thermal model II, curve 4 in Figure 1.1 ( $T_{240}=1490^{\circ}\text{C}$  and  $f_0=2\%$ ). The spreading axis is placed at 95 km.

less than the observed crustal thickness. The models with a linear decrease in spreading rate ('d' and 'e', left panel Fig. 6.6) are best able to replicate the rate at which the crust thins into the extinct spreading centre, but have a crustal thickness which is 3.5 km too thin. The best area of agreement between the calculated and observed crustal thicknesses is found at distances of 200 km and beyond along line R2 where higher spreading rates are encountered for the crust formed after the time of anomaly 24. Thermal model II produces a thicker crust (right panel, Fig. 6.6), nominally 5 km, for the crust formed between anomalies 21 and 24, outside of the region of rapid crustal thinning from 60 to 130 km. However, it is more sensitive to spreading rate changes and predicts a more rapid thinning of the crust as spreading rate decreases. The crustal thickness predictions for the linear decrease in spreading rate from anomaly 21 to 13 (model 'd' in Fig. 6.6) illustrates the more rapid thinning which is predicted by thermal model II in comparison with the thermal model I. For crust formed at higher spreading rates, thermal model II is also problematic. Crust which is 3 km too thick is produced at distances of 200 km and beyond along line R2.

Overall, the observed crustal thickness cannot be reconciled with the predictions of the Reid and Jackson [1981] thermal model. The discrepancy does not arise from inadequacies in the seafloor spreading rate history. The six potential spreading rate histories presented span the range of plausible scenarios from a rapid cessation of spreading to a more prolonged and gradual decrease. As none of these models provides an adequate fit to the observed crustal thickness, alternate explanations must be sought. Three such explanations are pursued in the remainder of this section.

The first interpretation is that some component of buoyant upwelling may indeed be an important factor in driving mantle circulation. In these flow models, crustal thickness is not predicted to vary as severely as a function of spreading rate relative to that predicted by models where flow is driven by passive upwelling. An obvious manner by which this explanation may be tested is a calculation of the crustal thickness predicted by buoyancy driven upwelling (Fig. 1.2b) using the six potential spreading rate histories. However, this is not possible because these models cannot achieve a steady state at lower spreading rates (less than approximately 5 mm/yr). Scott and Stevenson [1989] write "The behaviour we find is episodic with bursts of rapid upwelling and melting interspersed by periods of slow flow with little or no melting". Sotin and Parmentier [1989] observe a similar interplay between opposing thermal and compositional buoyancy force, at slow spreading rates and speculate that "... these crustal thickness oscillations may explain important aspects of seafloor structure". The interesting behaviour of these 2-D models should be recalled when the interplay between magmatism and volcanism at slow spreading rates is discussed in section 6.4.1.

The second explanation for the discrepancy between the observed and calculated crustal thicknesses is that the thickness of the igneous crust, resulting from the solidification of partial melt, has been misrepresented in the interpretation of the seismic refraction data. The oceanic crust within the extinct spreading centre could actually be much thinner, in agreement with the predictions of thermal models I and II, if the thickness of material presently interpreted as crust is largely comprised of partially serpentinized peridotites. Hydrothermal alteration of the upper mantle peridotites to

produce serpentized peridotites is capable of producing the low velocities which are observed in the extinct spreading centre. As discussed in section 6.2, this view of the oceanic crust is not favoured because of the seismic evidence for a discrete crustal layer and the requirement for a sharp Moho to be generated by hydrothermal alteration, but this view cannot be dismissed outright.

The third interpretation of the discrepancy between the observed and calculated crustal thicknesses is perhaps the most interesting, but also the most speculative. It concerns several anomalous characteristics of the Labrador Sea basin and its evolution. The Labrador Sea has been noted as being too shallow for its age [Hyndman, 1973; Srivastava and Arthur, 1989]. Relative to the standard thermal subsidence predicted by Parsons and Sclater [1977] with an initial ridge crest depth of 2.5 km and temperature of 1350°C at the base of the lithosphere, the sediment corrected depth of the basement in the Labrador Sea should be approximately 1 km deeper than observed. Heat flow measurements on the Labrador continental margin are normal for its age [Lévesque, 1992] and models for its thermal subsidence are fit by a standard temperature of 1350°C at the base of the lithosphere [Royden and Keen, 1980; Issler, 1988]. Meanwhile, in the Labrador Sea ocean basin, heat flow values are more than 25% higher than predicted by standard thermal models [Louden *et al.*, 1989]. This requires higher temperatures of 1750°C at the base of the lithosphere [Lévesque, 1992] or a 28 My delay in the onset of cooling of the oceanic crust [Louden *et al.*, 1989; Lévesque, 1992] which is attributed to a lateral flux of heat from a hot spot present under Davis Strait. The timing and existence of the hot spot activity [Hyndman, 1973; Srivastava *et al.*, 1989] is placed between 56

and 59 Ma (chrons 24 and 25), to coincide with: 1) the re-orientation of spreading in the Labrador Sea [Roest and Srivastava, 1989a]; 2) the onset of seafloor spreading between Greenland and Rockall plateau and 3) the emplacement of high temperature picritic basalts on the western margin of Greenland and on Baffin Island [Clarke and Upton, 1971].

To satisfy the observations of anomalously shallow basement depth and high heat flow, Lévesque [1992] demonstrates that at an elevated temperature for the mantle at the base of the lithosphere is required. However, the associated degree of partial melting of this anomalously hot mantle as it ascends (following White and Mackenzie, [1989]) would generate a crust which is approximately 30 km thick. Other predictions of crustal thickness may be obtained by considering the depth of the ridge crest during active spreading. Based on the subsidence history of the Labrador Sea, Keen *et al.* [a] and Srivastava and Arthur [1989] calculate an initial crestal depth of 1.6 km. For this crestal depth, the thermal model of adiabatically ascending mantle presented by Klein and Langmuir [1987] to satisfy the global correlation between basalt geochemistry, axial depth and crustal thickness predicts that a crustal thickness of approximately 14 km should be found in the Labrador Sea. Alternatively, if one follows the Keen *et al.* [1990b] empirical relationship between crustal thickness (using high quality seismic refraction measurements in the Atlantic and Pacific Oceans) and their respective ridge crest depths at age zero, a crustal thickness of approximately 7.5 km should be observed in the Labrador Sea. Keen *et al.* [1990b] attribute the difference between their empirical relationship and the theoretical relationship of Klein and Langmuir [1987] to the likelihood that not all melt

which is generated is segregated to form ocean crust.

The lack of anomalously thick crust in the Labrador Sea could be explained by the discrepancy between the observed crustal thickness and the crustal thickness predicted by a thermal model in which mantle circulation is driven by passive upwelling. At the slow spreading rates preceding extinction, the thermal models I and II (Fig. 6.6) from Reid and Jackson [1981] both suggest the crust should be severely thinned, to a degree which is not at all observed. The predicted thinning may only be partially realized because the time interval in which the slow spreading rates are encountered, chron 24 until the cessation of spreading, is the time interval in which the Labrador Sea is thought to have been influenced by hot spot activity and should have been creating thicker crust at the spreading centre. Partial melt supply would then be controlled by two counteracting effects: a reduction due to deeper penetration of conductive cooling at slow spreading rates and an enhancement due to higher mantle temperatures at the base of the lithosphere. Through this balance, normal crustal thicknesses are maintained between anomalies 24 and 21. From anomalies 21 until the cessation of spreading, spreading rate decreases are more severe and partial melt supply is sufficiently restricted as to produce the observed crustal thinning.

#### **6.4 Relationship to Observations at Slow Spreading Centres and Fracture Zones**

In this section, recent geophysical observations at the slow spreading Mid-Atlantic Ridge are first reviewed and then used to explore relationships between crustal structure at the extinct spreading centre in the Labrador Sea, the slow spreading Mid-Atlantic Ridge and oceanic fracture zones. At the Mid-Atlantic Ridge, recent studies suggest that within

a ridge segment there is considerable along axis variation in the thermal and mechanical properties of the lithosphere. The studies include along axis seismic refraction [Purdy and Detrick, 1986], high resolution multibeam bathymetry mapping [Sempere *et al.*, 1990; Lin *et al.*, 1990], multichannel seismic reflection [Detrick *et al.*, 1990], 3-D gravity studies [Prince and Forsyth, 1988; Kuo and Forsyth, 1988; Lin *et al.*, 1990], microearthquake source locations and delay time tomography [Toomey *et al.*, 1988; Kong *et al.* 1992] and geochemical studies [White *et al.*, 1992].

The seismic refraction results have found a 10-15 km wide zone of anomalously low velocities beneath a ridge segment axial high. Bathymetry data note an along axis transition from a broader deeper axial valley at ridge segment ends to a shallower, narrower axial valley at the ridge segment high. The multichannel seismic reflection data failed to find any shallow intracrustal reflector indicative of an axial magma chamber as is routinely found on segments of the fast spreading East Pacific Rise [Detrick *et al.*, 1987]. The gravity data have been used to compute a mantle Bouguer anomaly by removing the attraction of predictable components of the gravity field: a water layer, a sediment layer, and a constant crustal thickness layer. The mantle Bouguer anomaly shows distinct (approximately 20 to 50 mGal) lows at the position of axial bathymetric highs. These are interpreted as zones of crustal thickening and/or low density upper mantle. The inversion of teleseismic P and S waveforms suggests that the largest earthquakes occur near the ends of morphological segments and that the maximum centroid depth increases as spreading rate decreases. The lithosphere is interpreted as being thicker near the ends of tectonic segments and with tectonic stretching more

important than volcanism in these areas. Rare earth element inversions of some dredged and drilled gabbroic rocks show evidence for variable crustal thinning beneath fracture zones, while other basalts are indistinguishable from those generated on the ridge segments. The basalt geochemistry is interpreted in terms of a mantle level redistribution of melt to intrusive centres whence it may flow laterally along the axis at crustal or surface levels.

To harmonize these observations at slow spreading centres, crustal accretion must be focused at the centre of the ridge segment [Ballard and Francheteau, 1983; Solomon and Toomey, 1992; White *et al.* 1984]. This view of a 3-D flow pattern, with lateral migration of melt along the ridge axis, is supported by recent dynamical models for mantle circulation at active spreading centres which demonstrate that there is a transition from a 2-D to a 3-D mantle flow pattern as spreading rate decreases [Parmentier and Phipps Morgan, 1990]. Given these observations and their interpretation in terms of 3-D flow patterns, three questions are addressed in the following sections: 1) Can the along axis variability in the extent of magmatism and volcanism be related to the crustal structure at the extinct spreading centre in the Labrador Sea? 2) Does the extinct spreading centre in the Labrador Sea, or any other spreading centre, provide a location where 2-D models of flow at slow spreading rates may legitimately be assessed? 3) What may be learnt about processes leading to crustal thinning at oceanic fracture zones from a study of the extinct spreading centre in the Labrador Sea.

#### *6.4.1 Interplay between Magmatism and Volcanism*

An important consensus emerging from studies at slow spreading centres is that

crustal accretion is an episodic and not a steady state process. As there is no seismic evidence supporting the presence of steady state axial magma chambers at slow spreading centres [Detrick *et al.*, 1990], magmatism at the crustal level is considered to be an intermittent process. Consequently, plate divergence at slow spreading centres is partially accommodated through lithospheric stretching. This is unlike fast spreading centres where plate divergence can be accommodated by crustal accretion. Through an examination of the throw on normal faults at slow spreading centres, McDonald and Luyendyk, [1977] suggest that up to 20% of the plate divergence is accommodated in this manner. Along axis, ridge segment ends appear to be experiencing more tectonism than the axial high where crustal accretion is focused [Huang and Solomon, 1988; Lin and Bergman, 1990]. The ends of the ridge segments are cooler than any other portion of the ridge segment because of their proximity to the cold lithosphere against which they are juxtaposed. Consequently, they are mechanically stronger and more prone to brittle failure than other portions of the ridge crest. In addition, the ends of ridge segments are also areas where the production of partial melt supply and/or its transport is most severely limited [Phipps Morgan and Forsyth, 1988], requiring the tectonic extension to be accommodated by faulting.

Applying these observations to the extinct spreading centre in the Labrador Sea, the dissipation of thermal anomaly underlying the spreading centre could lead to a comparable scenario across the ridge axis. If spreading rate decreases are accompanied by an enhanced cooling of the crust by conduction, tectonism could be anticipated to increase. A fuller model for the extinct spreading centre preceding its extinction would

then have two components. First, partial melt would be partially restricted in accordance with a spreading rate dependence on its production. Second, this would be accompanied by an increased degree of tectonism as the crust became cooler by deeper penetration of conductive cooling at the slower spreading rates. There is also a feedback as the tectonism in turn introduces an enhanced cooling by providing pathways for advective cooling by hydrothermal circulation [Purdy et al., 1992]. The relevance of this interplay between magmatism and tectonism as spreading ceases to the generation of low seismic p-wave velocities within the crust at the extinct spreading centre was discussed in section 6.2.

#### *6.4.2 Applicability of 2-D Thermal Models*

The along axis variations at slow spreading centres require a 3-D pattern of mantle flow to explain present observations. At the slower spreading rates such as those encountered in the Labrador Sea preceding extinction, the applicability of the simpler 2-D models of mantle circulation may therefore be questioned. Their use, however, is justified on the basis of seismic observations of the structure of mature oceanic crust. The degree of inhomogeneity which is observed along axis at active spreading centres is simply not found in mature oceanic crust. In the most comprehensive of these studies, Purdy [1983] find that a 1-D velocity-depth structure is sufficient, and all that is warranted, to represent mature oceanic crust. This is based on the interpretation of numerous seismic refraction lines, both parallel and perpendicular to the Mid-Atlantic Ridge in 140 Ma crust in the Atlantic Ocean. Likewise, the refraction results along the axis of the extinct spreading centre in the Labrador Sea, line R1, while anomalous with regards to surrounding crust, do not show the degree of along axis variability which is associated with active slow

spreading centres. The only dominant feature in mature oceanic crust is the first order thinning into fracture zones.

If the focused crustal accretion observed at active spreading centres were a steady state feature, first order variations in crustal structure should be apparent in mature oceanic crust. Their absence suggests that the observations at active spreading centres are just an instantaneous view of these processes. On a longer time scale, the episodic nature of the crustal accretion processes leads to a homogenization of the crustal structure. Mature oceanic crust and that at the extinct spreading centre in the Labrador Sea may then be viewed as a composite of many episodic events of crustal accretion. In this sense, the 2-D dynamic models of flow remain valid as they represent a longer period average. The along axis component of the flow pattern must have a shorter period, whose effects are averaged out with time, except at the first order spatial discontinuity encountered at fracture zones.

#### *6.4.3 Cause of Thinning at Oceanic Fracture Zones*

Two elements lead to crustal thinning at oceanic fracture zone. Following Phipps Morgan and Forsyth [1988] and White *et al.* [1984], these are: 1) a reduced supply of partial melt to the accretionary axis due to the juxtaposition of cold and hot lithosphere decreasing melt production and 2) a truncation in the lateral pathways for melt migration owing to the large scale discontinuity which the fracture zone presents. In principle, the extinct spreading centre provides an environment which isolates the former of these components. It is free from the latter as line R1 was situated to sample the ridge segment away from the Minna and Snorri fracture zones (section 2.2). Any changes in crustal

thickness are then attributable to decreases in melt production as spreading rate decreases and the thermal anomaly beneath the spreading centre is dissipated. This allows the relative contribution of the thermal component at fracture zones to be assessed. On this basis, the degree of crustal thinning at the extinct spreading centre is comparable to that at oceanic fracture zones [Detrick *et al.*, in press; Loudon *et al.*, 1986] and one could attribute the thinning at fracture zones to a decrease in melt production.

This interpretation depends however upon the nature of the crust at oceanic fracture zones. At oceanic fracture zones, the affinity of this crust as being igneous or as being altered upper mantle remains equivocal. If the observed crustal thickness is emplaced by crustal accretion then the crustal structure at the extinct spreading centre would concur that crustal thickness at fracture zones is mediated by the thermal regime. If, however, the crust is actually altered upper mantle, then crustal thickness is restricted beyond that which can arise from a reduction of partial melt supply because of the thermal regime alone and must rely on a truncation of pathways for partial melt migration. The latter conclusion would be in keeping with crustal thickness observations at short offset fracture zones. For example, the Blake Spur fracture zone has a short offset and hence a relatively small thermal contrast between the ridge segment end and the colder lithosphere to which it is juxtaposed. Substantial crustal thinning and serpentinization are however observed by Minshull *et al.* [1991] in their interpretation of high quality expanding spread seismic refraction data. It should be noted that the extension of the observations at the extinct spreading centre to oceanic fracture zones presupposes that the viscosities of the mantle underlying the spreading centre in the

Labrador Sea preceding its extinction are comparable to those at active spreading centres. The thermal model Sotin and Parmentier [1989] illustrates the sensitivity of partial melt production and mantle circulation upon mantle viscosity (Fig. 1.2b).

## 7. Conclusions and Future Research

### 7.1 Conclusions

- (1) Crust within the extinct spreading centre is found to be thin and of anomalously low p-wave velocity when compared with mature oceanic crust. It is underlain by low upper mantle velocities which exhibit some anisotropy. This thinning is attributed to a decrease in partial melt supply to the accretionary axis as spreading ceased. The low velocities are attributed to an increase in the degree of tectonism preceding extinction which pervasively fractured the crust. This faulting also provides a pathway for hydrothermal alteration of the upper mantle peridotites and is the manner by which the low velocities in the uppermost mantle are produced. The lateral extent of the thinning and occurrence of low velocity crust are coincident with the time interval (chron 21 until the cessation of spreading) in which spreading rate decreased most rapidly.
- (2) The observed crustal thinning is consistent with a decreased supply of partial melt as spreading rate decreases. A 2-D model of passive flow predicts thinning which is far more severe than observed. This may be interpreted in three ways. First, a relatively low mantle viscosity ( $10^{19}$  Pa s) was present at the slow spreading rates preceding extinction in the Labrador Sea, allowing a component of active mantle flow to be operative and limit the degree of crustal thinning. Second, the predicted crustal thinning is offset by enhanced production of oceanic crust in response to the higher mantle temperatures from hot spot activity between chron 24 and the cessation of spreading. Third, the crust which has been identified as having an

igneous origin is actually hydrothermally altered upper mantle.

- (3) An analysis of the seismic refraction data and gravity modelling find no evidence or requirement for a gabbroic root structure [Hall *et al.*, 1986] to underlie the extinct spreading centre in the Labrador Sea. The gabbroic root model predicts that a zone of crustal thickening should underlie the extinct spreading centre while the opposite is in fact observed. The axial low in the free-air gravity field may be adequately explained in terms of lateral variations in the velocity/density of the crust and upper mantle with no requirement for a contribution from a low density relict of the source region extending deep into the mantle.

## 7.2 Future work

### 7.2.1. Gravity

The acquisition of gravity data along line R2 is recommended as a first priority for future data acquisition. The lack of coincident gravity measurements along seismic refraction line R2 limits the methodologies which can be employed in the gravity modelling and the confidence of the methods which are employed. An independent check of the 2-D seismic velocity-depth structure through a comparison of calculated and observed free-air gravity anomalies was undertaken. The discrepancy between these values southwest of the extinct spreading centre along refraction line R2 (Fig. 5.5), suggests that the velocity-depth structure in this area, where there is a paucity of shot-receiver raypaths, may require revision. However, the observed anomaly used in this comparison was interpolated from measurements on ship tracks which are separated from the refraction line by up to 17 km (Fig. 5.1) and does not constitute a suitable basis upon which

revisions to the velocity-depth structure should be based. Coincident gravity measurements would also allow the computation of a residual gravity anomaly through the subtraction of the predictable components from the observed field. This would isolate the gravity field owing to variations in crustal and upper mantle density and/or crustal thickness allowing a more direct assessment of the seismic velocity-depth structure and the predictions of Hall *et al.* [1986] and Jonas *et al.* [1991] that the extinct spreading centre in the Labrador Sea is underlain by a gabbroic root structure (section 5.3).

#### 7.2.2. Thermal Models

There are two modifications to 2-D or 3-D thermal models which would be beneficial in modelling the processes which occur as a spreading centre dies. First, these models all offer predictions of partial melt production and/or melt transport in steady state conditions (*ie.* at a constant spreading rate). This differs from the actual dynamics at the extinct spreading centre where plate spreading velocity surely decreased in some manner preceding the extinction. Further, models for active flow become unstable at the slow spreading rates thought to have preceded extinction and suggest a transition from a steady state to an episodic behaviour [Sotin and Parmentier, 1989]. Existing algorithms could be modified to accommodate a variable spreading rate behaviour [E.M. Parmentier, Personal Communication, 1990] thereby allowing predictions of crustal thickness for a variety of spreading rate histories to be evaluated. The second modification is an incorporation of variable viscosity into the thermal models. Viscosity has already been shown by Sotin and Parmentier [1989] to be an important parameter governing the degree to which localized buoyancy forces drive mantle circulation. Allowing viscosity to vary in accordance with

temperature, could have a significant impact on the upwelling and lateral movement of mantle in the dynamic models of mantle circulation and has only recently been considered [Shen and Forsyth, 1992]. Changes in viscosity are likely to precede the extinction of a spreading centre, as the thermal anomaly beneath the spreading centre dissipates.

### *7.2.3 Seismic Studies*

Resolving the source region in which partial melting occurs is a difficult task. In theory, the broad scale flow patterns of passive and buoyant upwelling should be distinguishable as the shear in these flows would likely impart an anisotropic fabric to the constituent mineral assemblages which could be detected seismically. In practice, this requires techniques and observations with a depth scale which is an order of magnitude greater than provided by conventional seismic refraction and reflection techniques which only sample the crust and uppermost mantle. Upon the advent of the requisite equipment and techniques, discernment between passive and active flow at spreading centres should be pursued by seismic methods.

## **Appendix A: Line R2 Refraction Profiles**

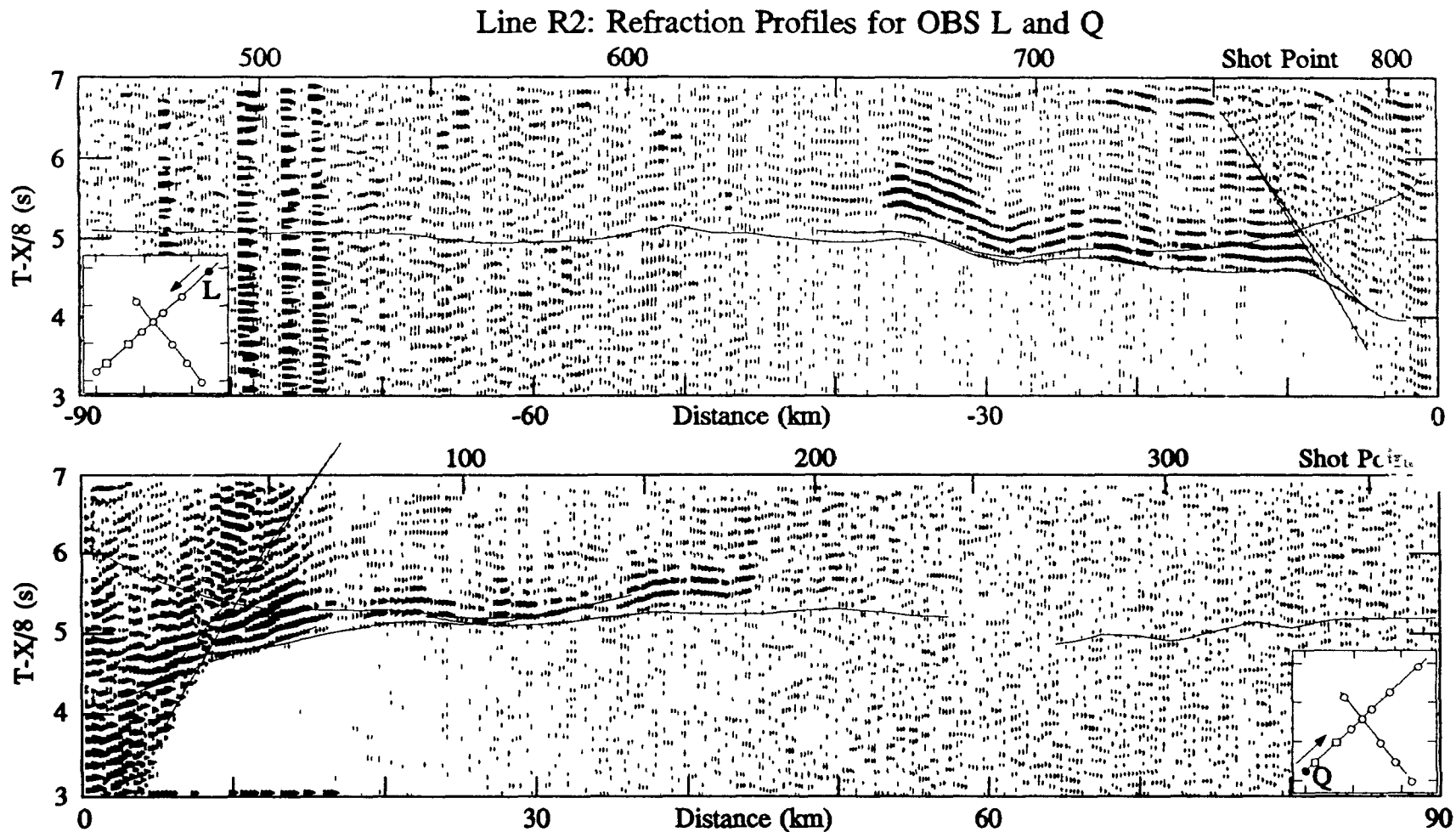


**Figure A.1:** Refraction profiles for (a) OBS L shooting southwest and (b) OBS Q shooting northeast. Traces are bandpass filtered from 4 to 12 Hz and a 3 trace mix has been applied. Gain has been applied as a function of distance. Travel time lines are from 2-D raytracing through the final velocity-depth structure in Fig. 4.2.

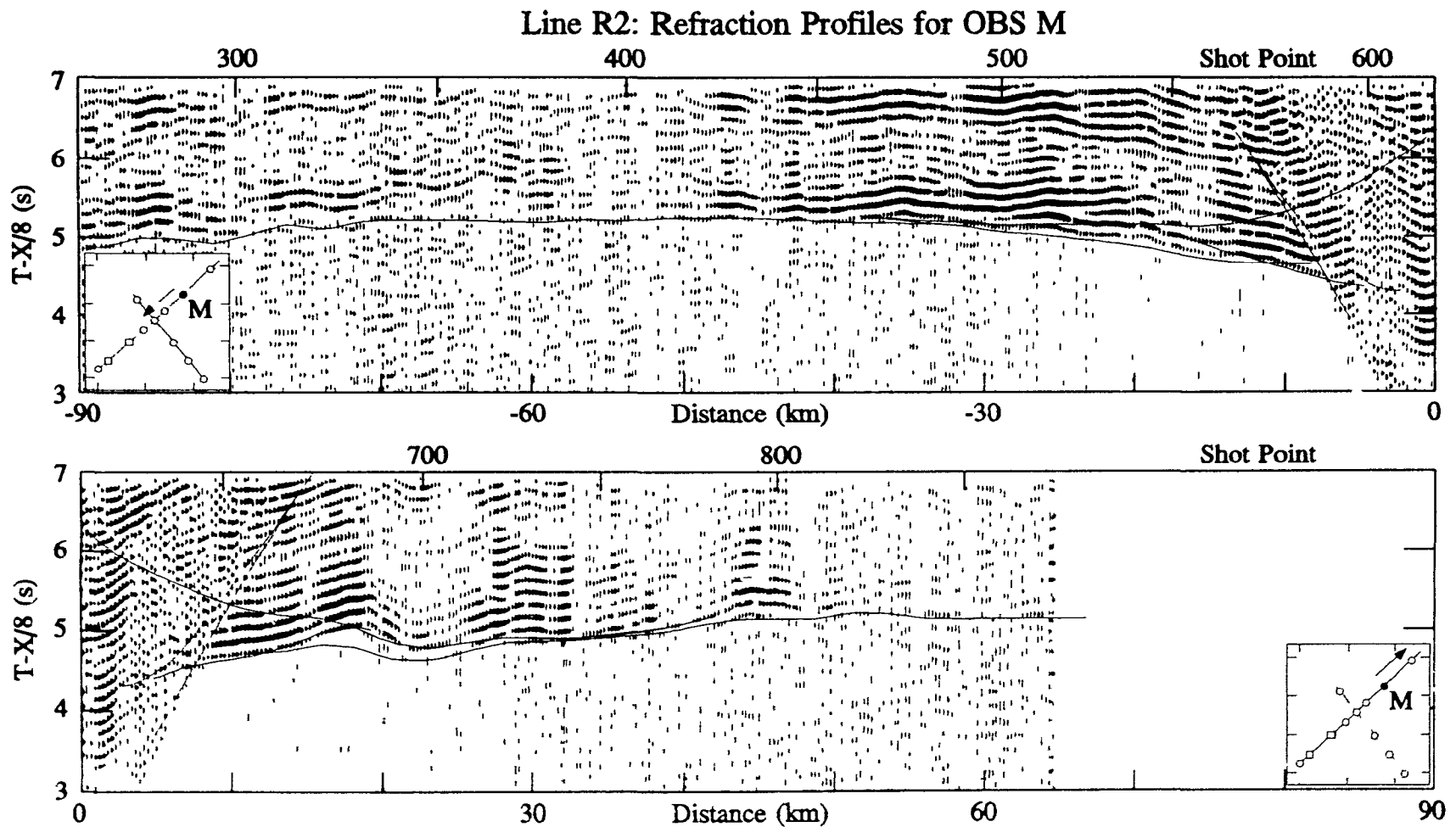


**Figure A.2:** Refraction profiles for (a) OBS M shooting southwest and (b) OBS M shooting northeast. Traces are bandpass filtered from 4 to 12 Hz, and a 3 trace mix has been applied. Gain has been applied as a function of range. Travel time lines are from 2-D raytracing through the final velocity-depth structure in Fig 4.2

### Line R2: Refraction Profiles for OBS N

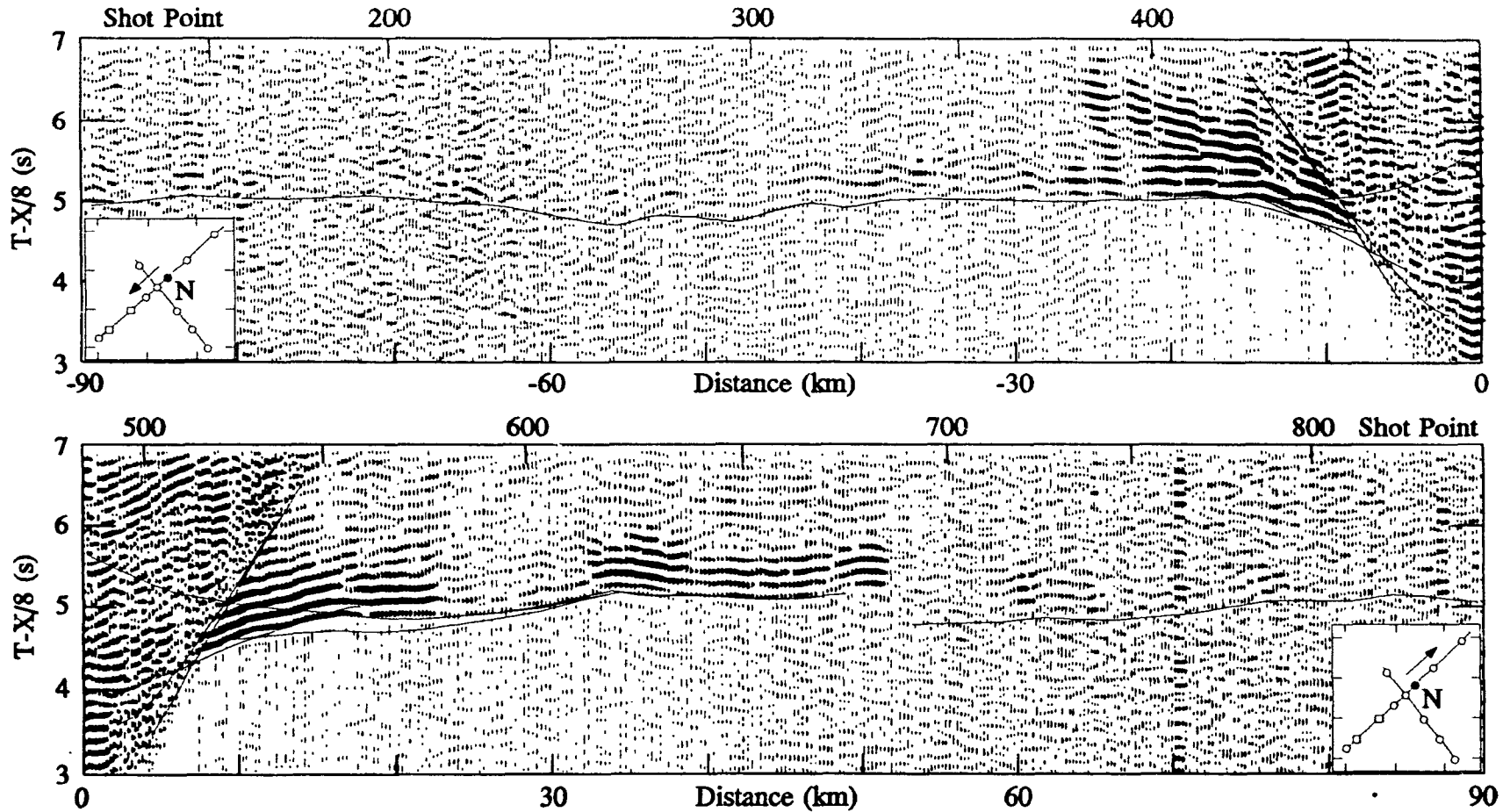


**Figure A.3:** Refraction profiles for (a) OBS N shooting southwest and (b) OBS N shooting northeast. Traces are bandpass filtered from 4 to 12 Hz, and a 3 trace mix has been applied. Gain has been applied as a function of range. Travel time lines are from 2-D raytracing through the final velocity-depth structure in Fig. 4.2.

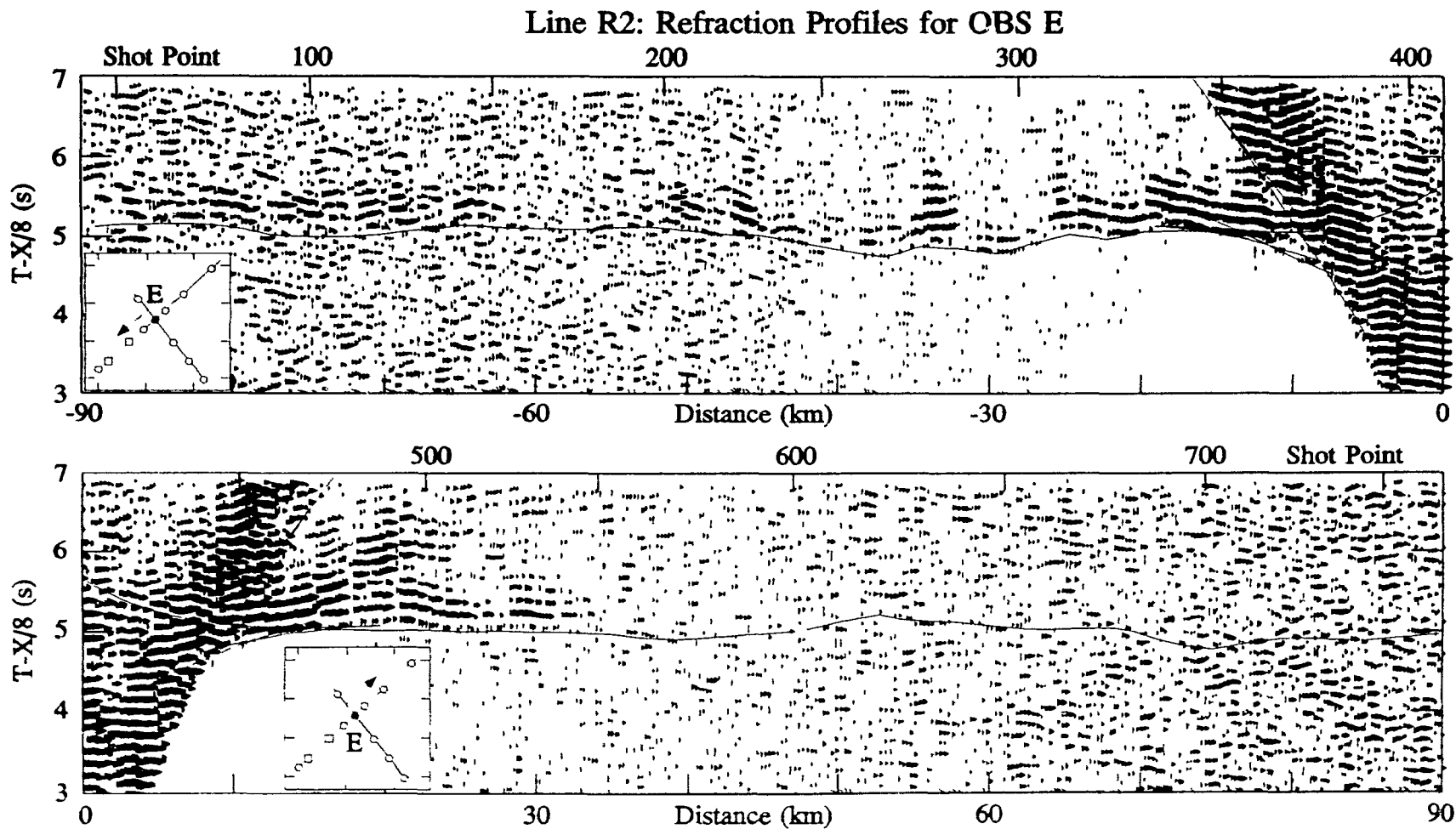


**Figure A.4:** Refraction profiles for (a) OBS E shooting southwest and (b) OBS E shooting northeast. Traces are bandpass filtered from 4 to 12 Hz, and a 3 trace mix has been applied. Gain has been applied as a function of range. Travel time lines are from 2-D raytracing through the final velocity-depth structure in Fig. 4.2.

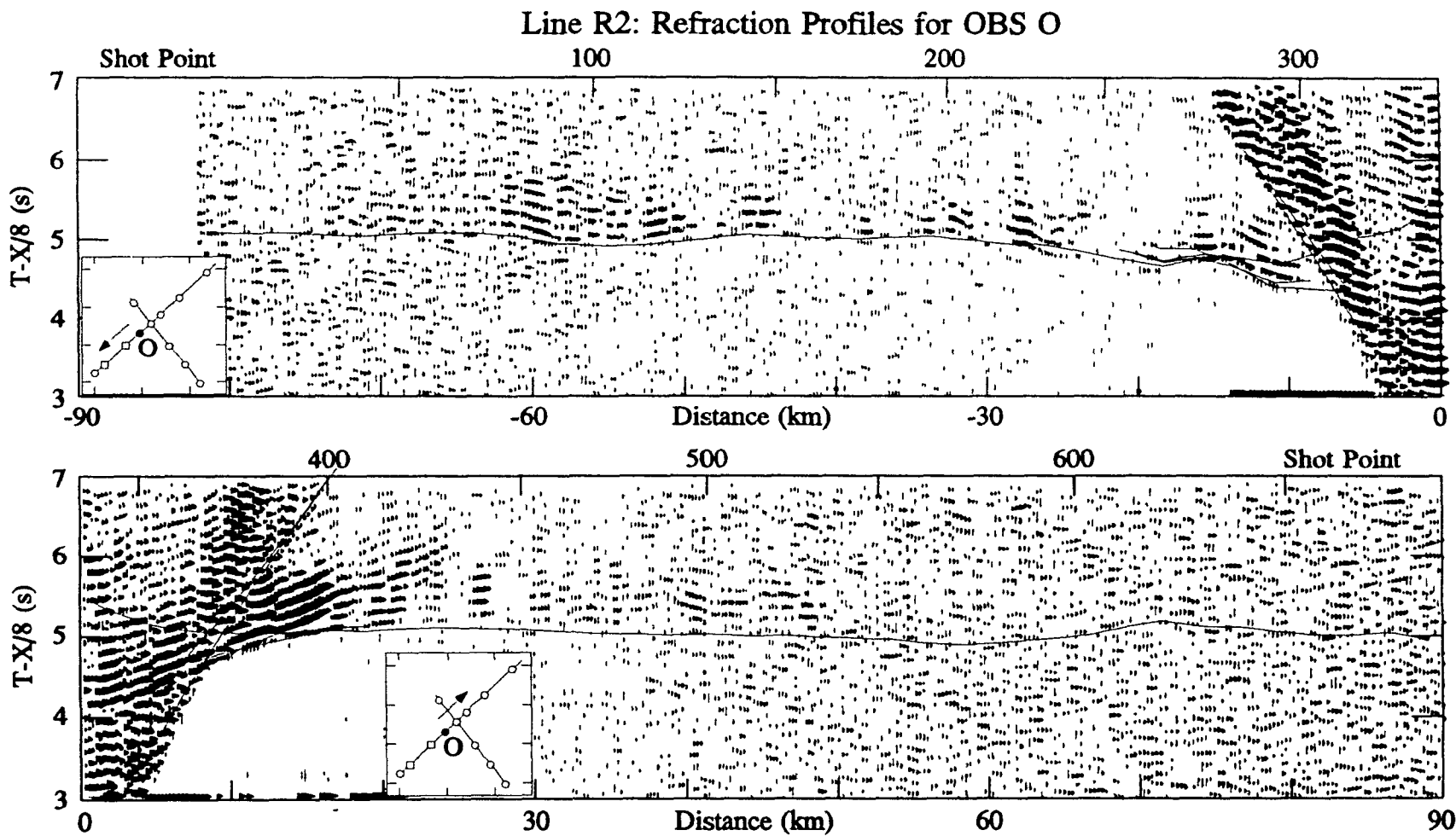


**Figure A.5:** Refraction profiles for (a) OBS O shooting southwest and (b) OBS O shooting northeast. Traces are bandpass filtered from 4 to 12 Hz and a 3 trace mix has been applied. Gain has been applied as a function of range. Travel time lines are from 2-D raytracing through the final velocity-depth structure in Fig. 4.2.

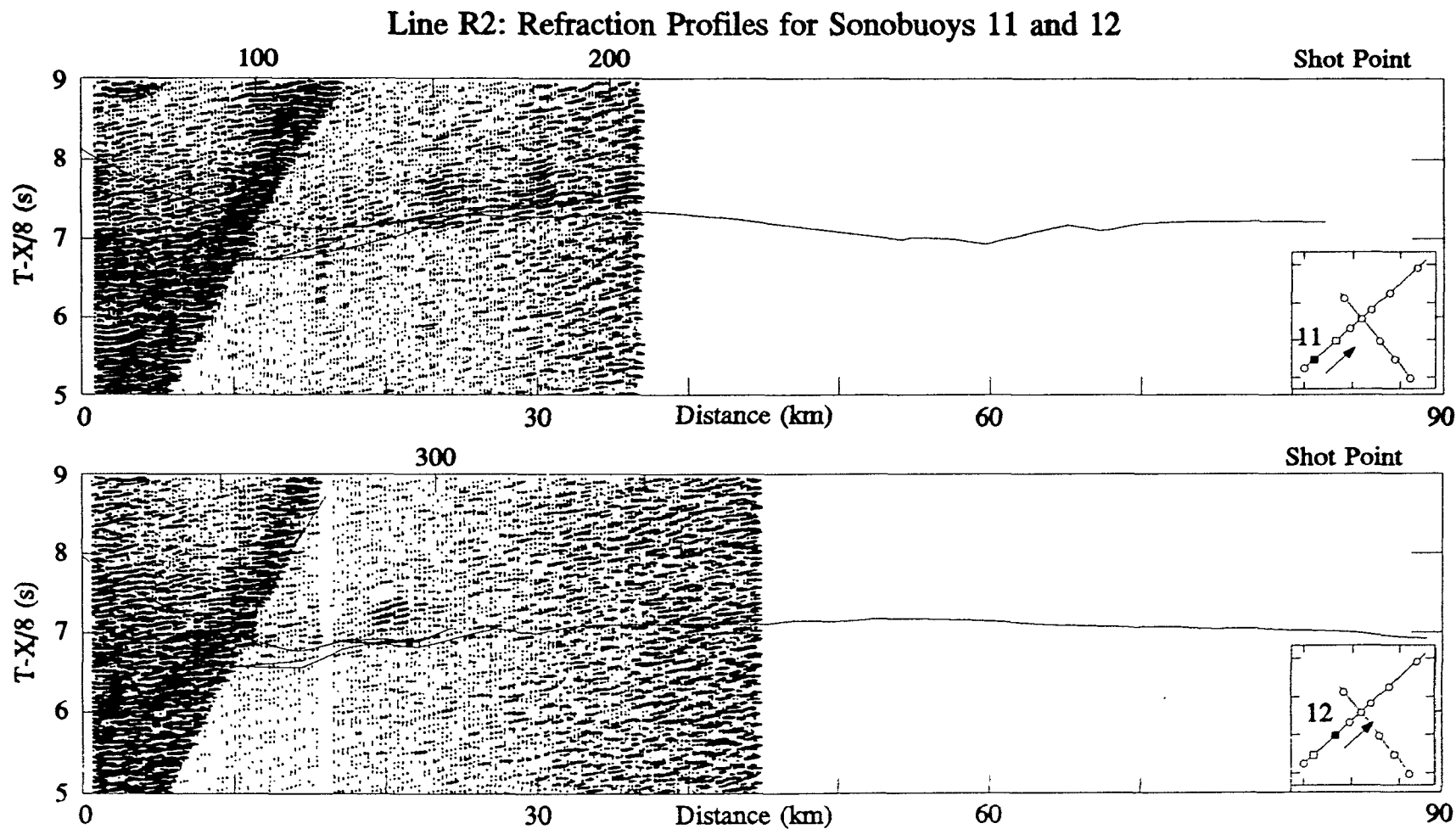


**Figure A.6:** Refraction profiles for (a) Sonobuoy 11 shooting northeast and (b) Sonobuoy 12 shooting northeast. Traces are bandpass filtered from 4 to 22 Hz, and a 3 trace mix has been applied. Gain has been applied as a function of range. Travel time lines are from the 2-D raytracing through the final velocity-depth structure in Fig. 4.2.

Line R2: Near Field Refraction Profiles for Sonobuoys 11 and 12

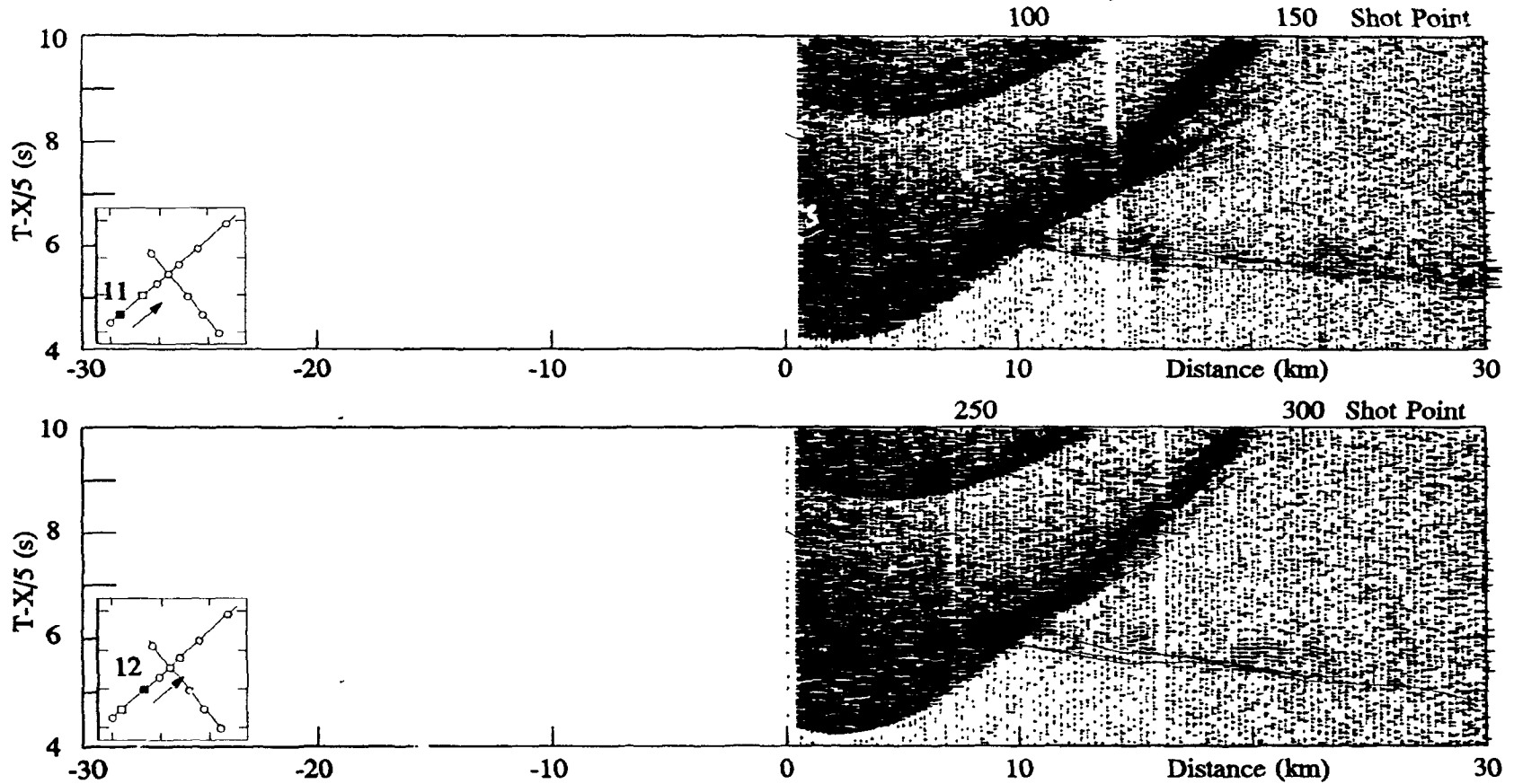


**Figure A.7:** Refraction profiles for (a) Sonobuoy 11 and (b) Sonobuoy 12. Traces are bandpass filtered from 4 to 22 Hz and gain has been applied as a function of range. Travel time lines are from the 2-D raytracing through the final velocity-depth structure in Fig. 4.2.

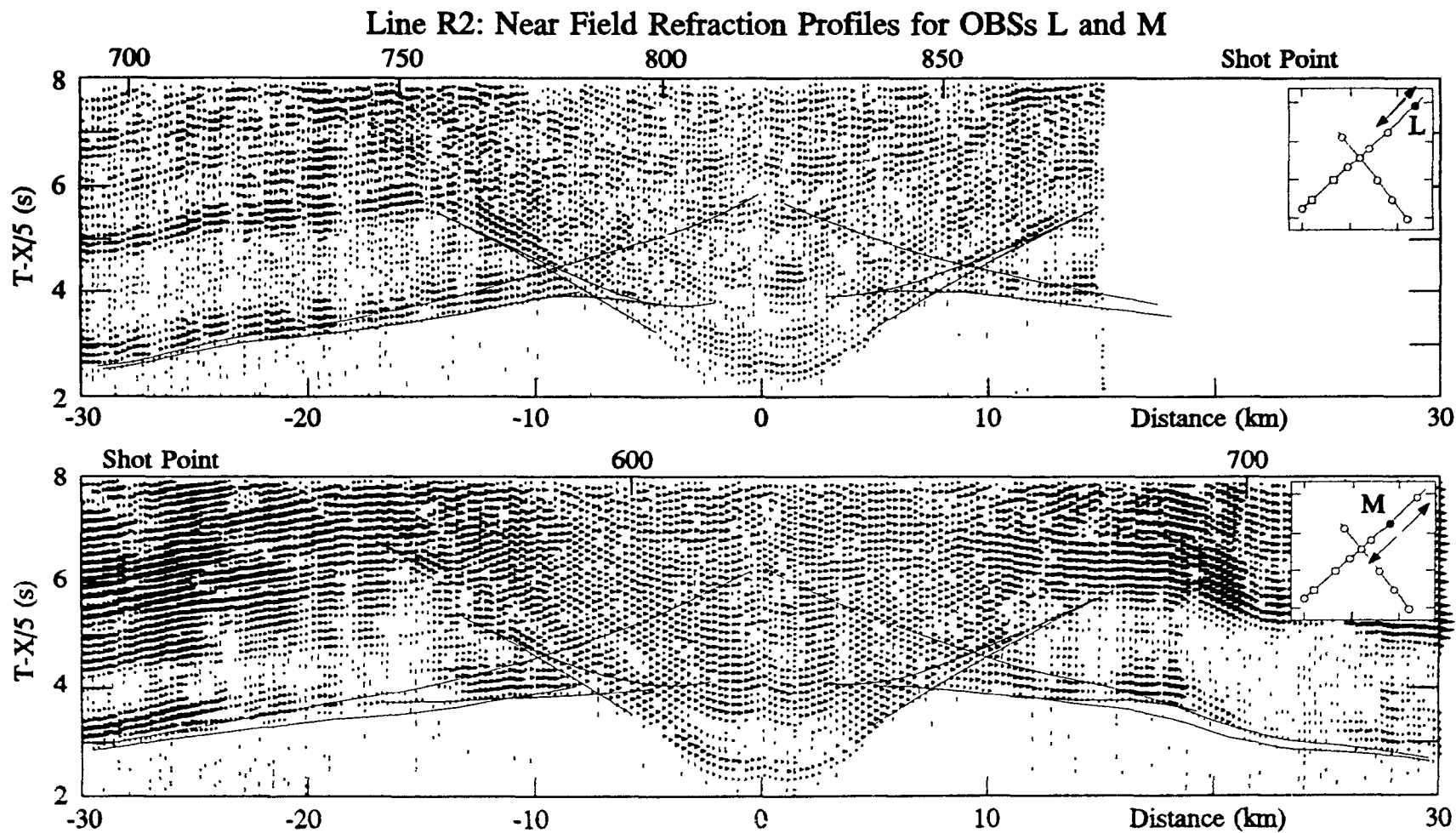


**Figure A.8:** Refraction profiles for (a) OBS L and (b) OBS M. Traces are bandpass filtered from 4 to 12 Hz and gain has been applied as a function of range. Travel time lines are from the 2-D raytracing through the final velocity-depth structure in Fig. 4.2.

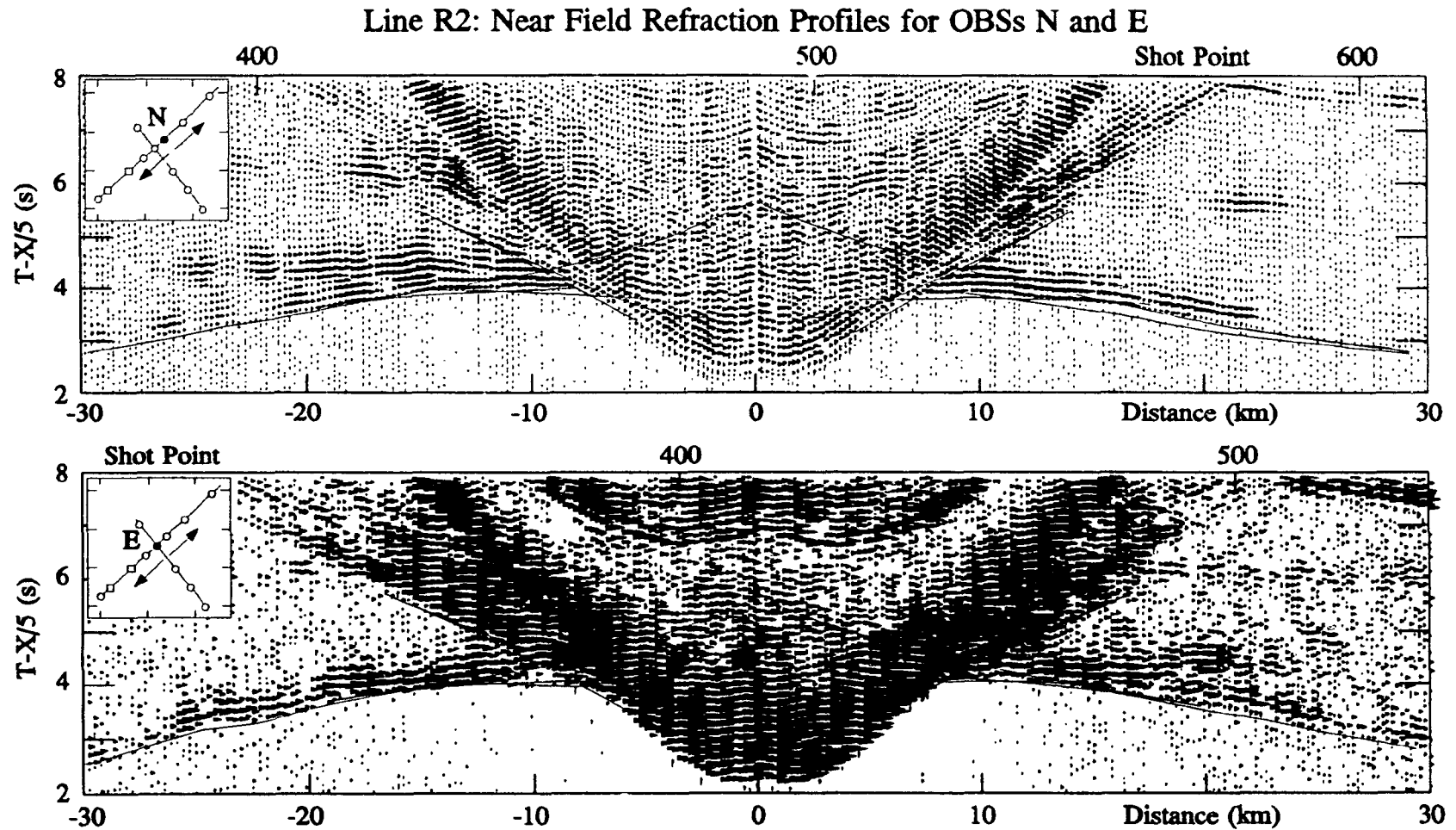


**Figure A.9:** Refraction profiles for (a) OBS N and (b) OBS E. Traces are bandpass filtered from 4 to 12 Hz and gain has been applied as a function of range. Travel time lines are from the 2-D raytracing through the final velocity-depth structure in Fig. 4.2.

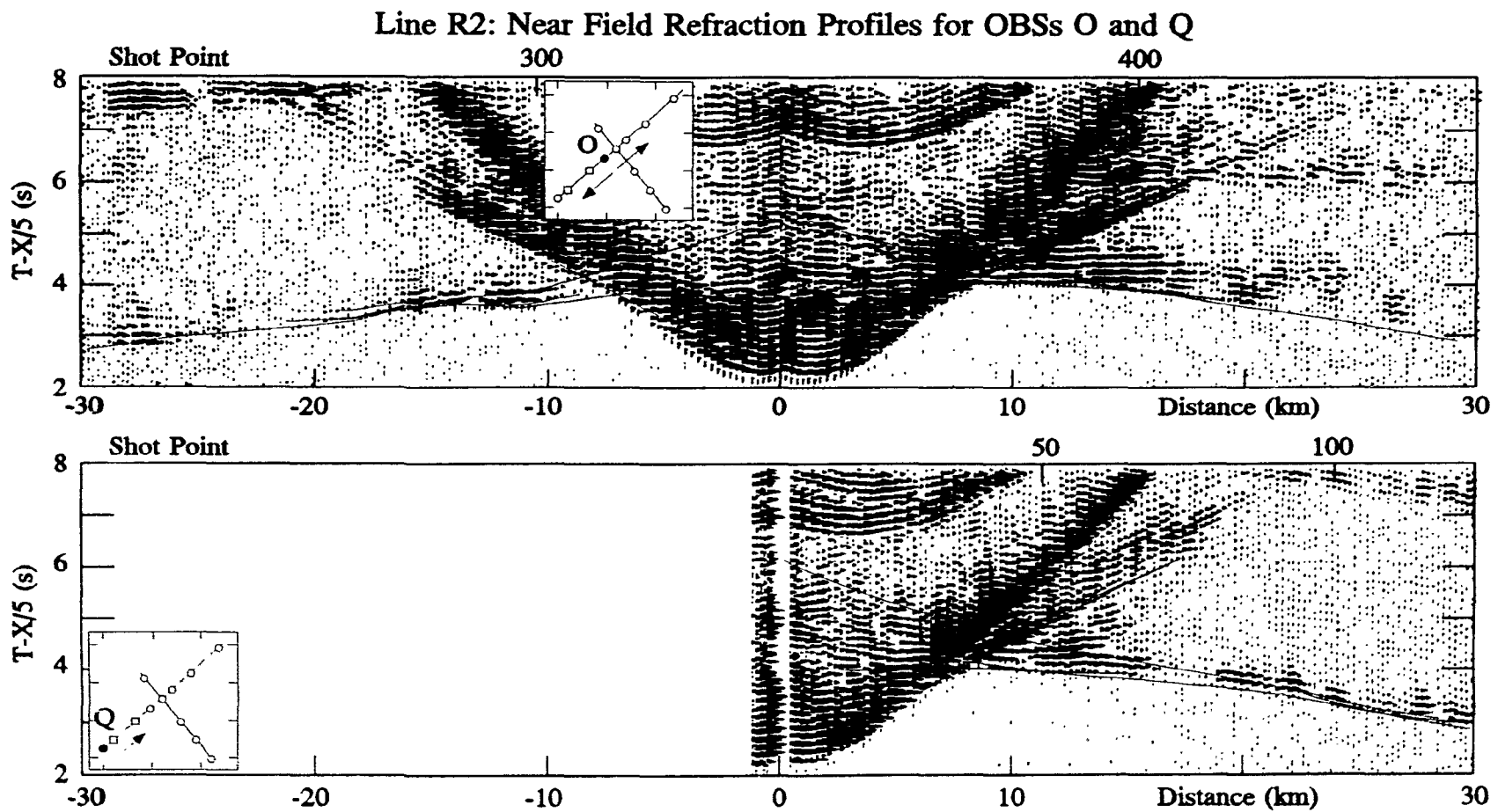


**Figure A.10:** Refraction profiles for (a) OBS O and (b) OBS Q. Traces are bandpass filtered from 4 to 12 Hz and gain has been applied as a function of range. Travel time lines are from the 2-D raytracing through the final velocity-depth structure in Fig. 4.2.

## **Appendix B: Line R1 Refraction Profiles**

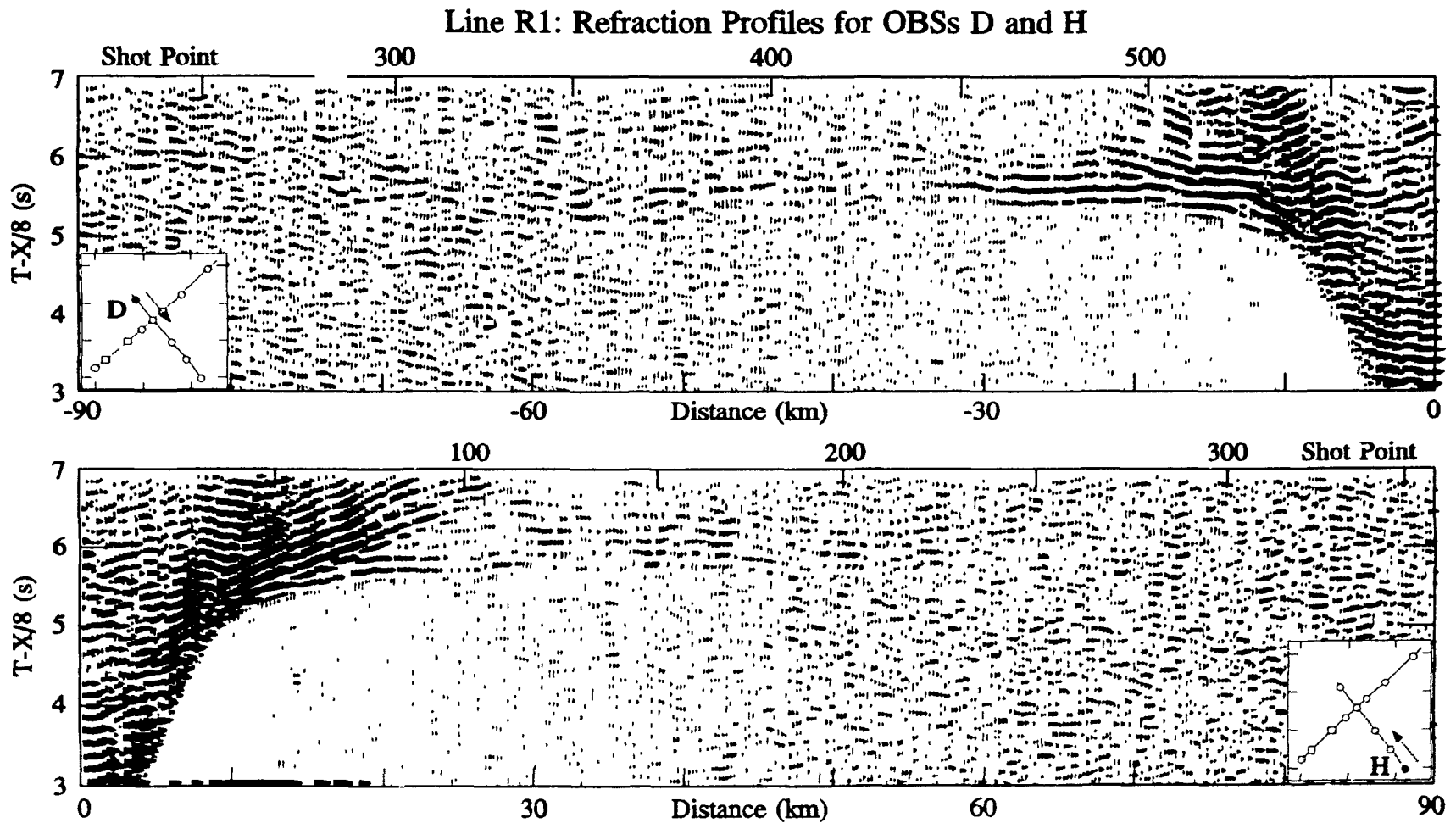


**Figure B.1:** Refraction profiles for (a) OBS D shooting southeast and (b) OBS H shooting northwest. Traces are bandpass filtered from 4 to 12 Hz, and a 3 trace mix has been applied. Gain has been applied as a function of range.

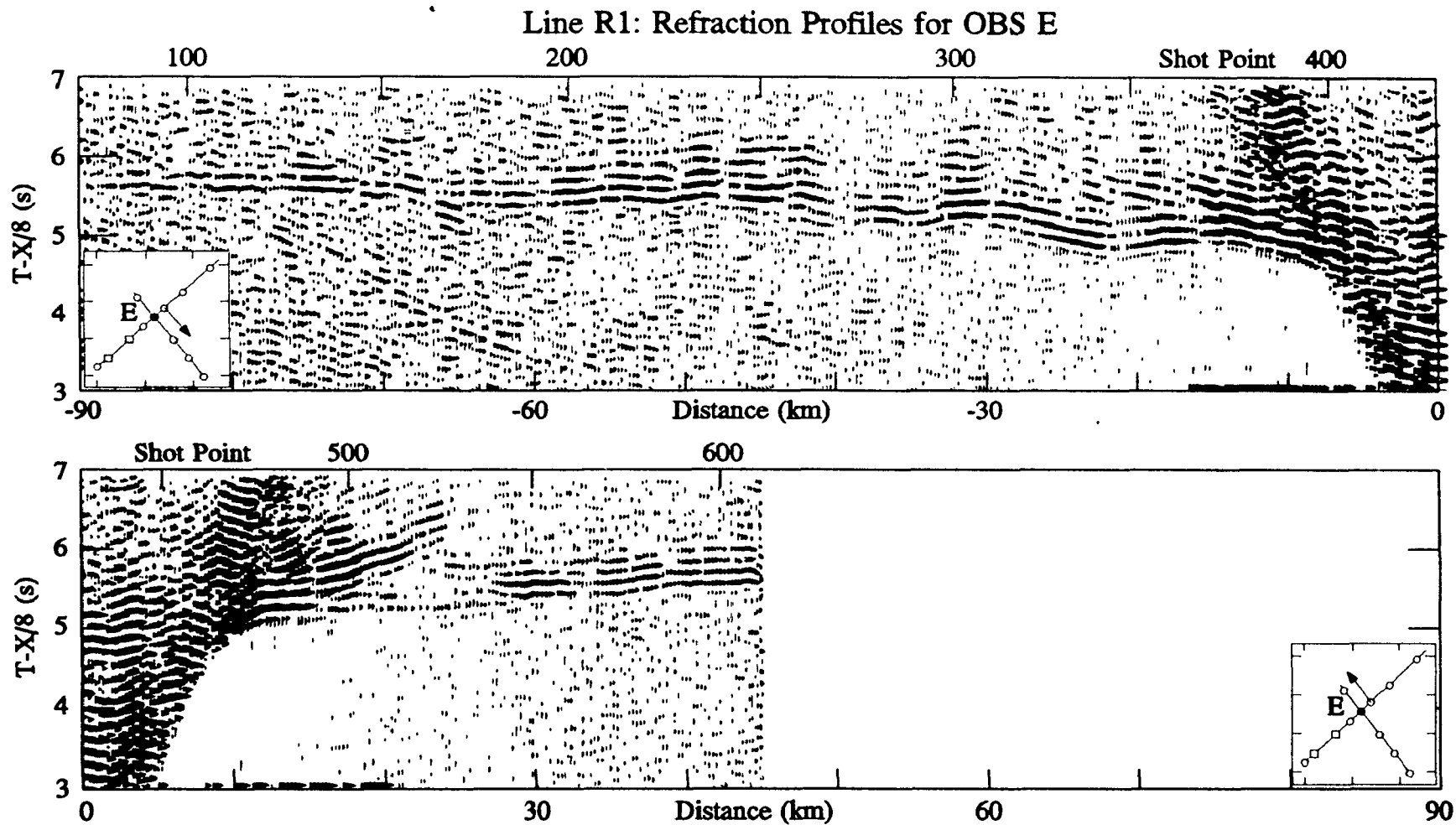


**Figure B.2:** Refraction profiles for (a) OBS E shooting southeast and (b) OBS E shooting northwest. Traces are bandpass filtered from 4 to 12 Hz, and a 3 trace mix has been applied. Gain has been applied as a function of range.

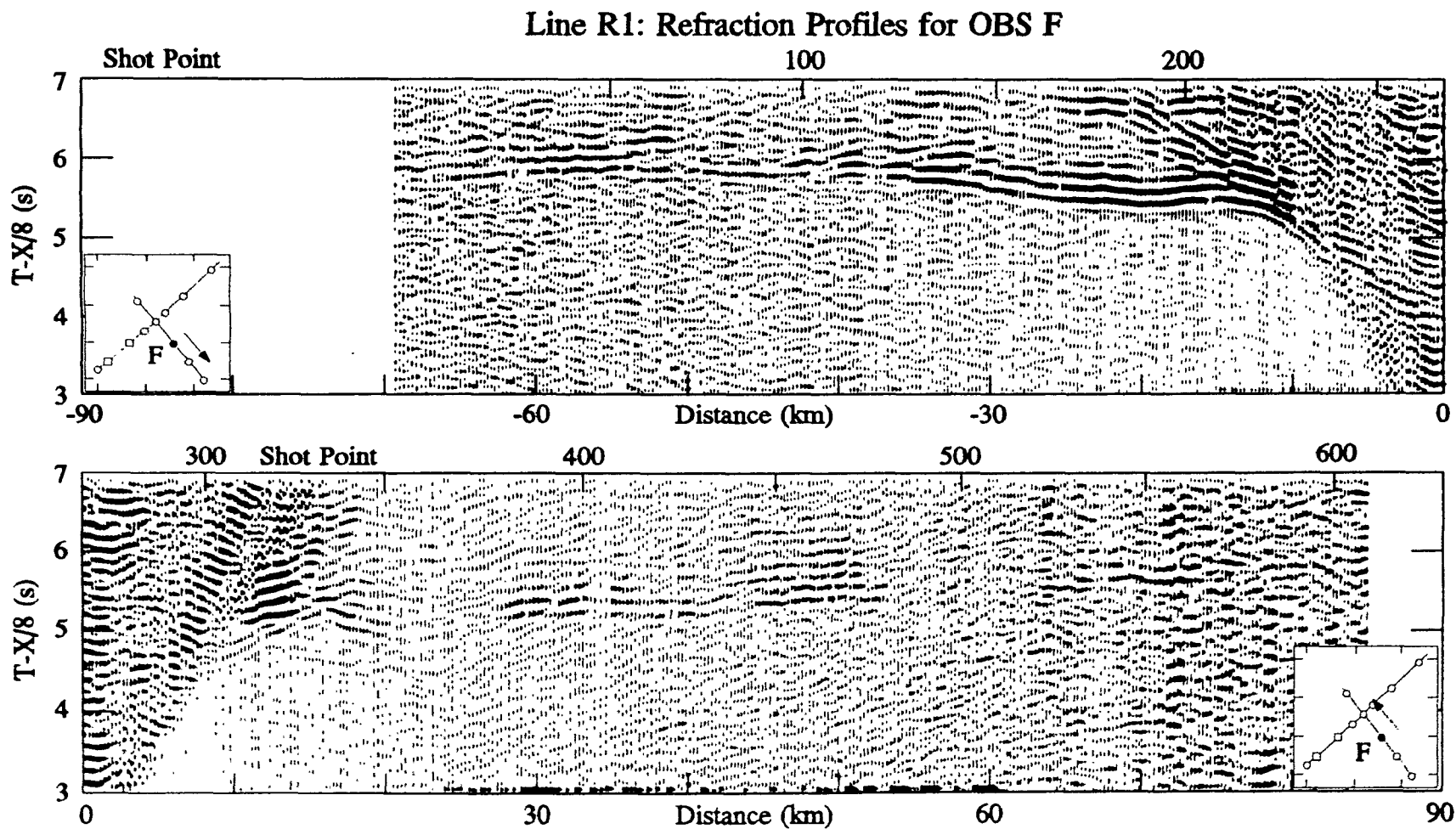


**Figure B.3:** Refraction profiles for (a) OBS F shooting southwest and (b) OBS F shooting northeast. Traces are bandpass filtered from 4 to 12 Hz, and a 3 trace mix has been applied. Gain has been applied as a function of range.

### Line R1: Refraction Profiles for OBS G

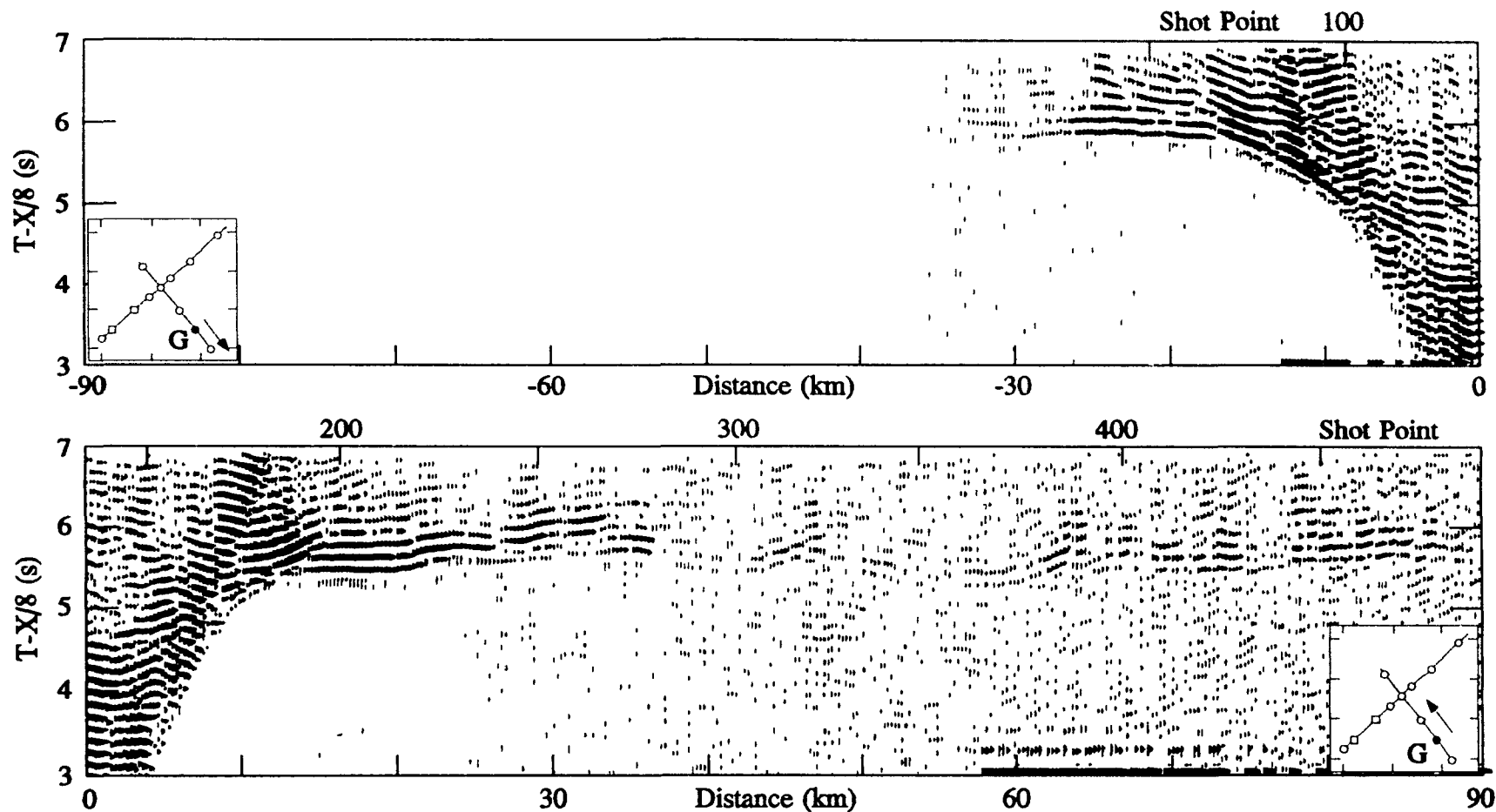


**Figure B.4:** Refraction profiles for (a) OBS G shooting southeast and (b) OBS G shooting northwest. Traces are bandpass filtered from 4 to 12 Hz, and a 3 trace mix has been applied. Gain has been applied as a function of range.

## **Appendix C: Tables of Boundary and Velocity Nodes**

**Table C:** Velocity nodes for 2-D velocity-depth structure on line R2

Layer 1: Water Upper Boundary			Layer 2: Sediment Upper Boundary			Layer 3: Sediment Upper Boundary			Layer 3: Sediment Lower Boundary		
Dist. (km)	Depth (km)	Vel. (km/s)	Dist. (km)	Depth (km)	Vel. (km/s)	Dist. (km)	Depth (km)	Vel. (km/s)	Dist. (km)	Depth (km)	Vel. (km/s)
220	sur- face	1.49	220	sea- floor	1.50	0	4.01	2.22	0	5.67	2.50
						10	3.94	2.23	10	5.49	2.48
						20	3.99	2.25	20	5.60	2.59
Layer 1: Water Lower Boundary			Layer 2: Sediment Lower Boundary			30	4.01	2.20	25	4.92	2.42
						50	4.02	2.20	30	4.80	2.38
220	sea- floor	1.49	0	4.01	2.16	60	3.91	2.22	35	5.20	2.45
						80	4.05	2.28	55	5.34	2.43
			10	3.94	2.10	90	4.02	2.40	60	4.97	2.45
			20	3.99	2.15	100	4.02	2.34	65	4.20	2.25
			30	4.01	2.15	110	3.99	2.38	70	4.66	2.36
			50	4.00	2.12	120	3.91	2.28	75	4.91	2.46
			60	3.91	2.07	130	3.94	2.20	80	5.10	2.55
			80	4.05	2.14	150	3.93	2.18	85	5.65	2.62
			90	4.02	2.12	160	3.95	2.21	90	5.68	2.69
			100	4.02	2.12	190	3.93	2.21	95	5.51	2.64
			110	3.99	2.10	200	3.95	2.21	100	5.53	2.62
			120	3.91	2.07	210	3.95	2.22	105	5.74	2.72
			130	3.94	2.07	220	3.95	2.20	110	5.52	2.66
			150	3.93	2.01				115	4.87	2.44
			160	3.95	2.05				125	4.79	2.38
			190	3.93	1.98				150	5.40	2.41
			200	3.95	2.02				155	5.52	2.49
			210	3.95	2.02				160	5.37	2.47
			220	3.95	2.04				170	5.02	2.45
									175	4.13	2.27
									180	4.65	2.35
									185	4.48	2.33
									190	4.71	2.38
									195	5.21	2.45
									200	5.14	2.50
									205	5.47	2.50
									210	5.25	2.48
									220	5.40	2.49





## References

- Ahern, J. L., and D. L. Turcotte, Magma migration beneath an ocean ridge. *Earth and Planetary Science Letters*, 45, 115-122, 1979.
- Anderson, R. N., and J. G. Sclater, Topography and evolution of the East Pacific Rise between 5°S and 20°S. *Earth and Planetary Science Letters*, 14, 433-441, 1972.
- Arthur, M. A., S. P. Srivastava, M. Kaminski, R. Jarrard, and J. Osler, Seismic stratigraphy and history of deep circulation and sediment drift development in Baffin Bay and the Labrador Sea, in *Proceedings of the Ocean Drilling Program, Scientific Results*, edited by S. P. Srivastava, M. A. Arthur, B. Clement et al., Vol. 105, pp. 957-988, 1989.
- Ballard, R. D., and J. Francheteau, Geologic processes of the mid-ocean ridge and their relation to sulfide deposition, in *Hydrothermal Processes at Seafloor Spreading Centers*, edited by P. A. Rona et al., pp. 141-168, Plenum, New York, 1983.
- Batiza, R., Failed rifts, in *The Geology of North America*, Vol. N: *The Eastern Pacific Ocean and Hawaii*, edited by E. L. Winterer, D. M. Hussong, and R. Decker, pp. 177-186, Geological Society of America, Boulder, Colorado, 1989.
- Batiza, R., and D. Vanko, Petrologic evolution of large failed rifts in the Eastern Pacific: Petrology of volcanic and plutonic rocks from the Mathematician Ridge area and Gaudalupe Trough. *Journal of Petrology*, 26, 564-602, 1985.
- Bibee, L. D., and G. G. J. Shor, Compressional wave anisotropy in the crust and upper mantle. *Geophysical Research Letters*, 3, 639-642, 1976.
- Bottinga, Y., and C. J. Allègre, Partial melting under spreading ridges. *Philosophical Transactions of the Royal Society of London*, 288, 501-525, 1978.
- Calvert, A. J., and C. G. Potts, Seismic evidence for hydrothermally altered mantle beneath the old crust of the Tydeman fracture zone. *Earth and Planetary Science Letters*, 75, 439-449, 1985.
- Casey, J. F., J. A. Karson, D. Elthon, E. Rosencrantz, and M. Titus, Reconstruction of the geometry of accretion during formation of the Bay of Islands ophiolite complex. *Tectonics*, 2, 509-528, 1983.
- Cerveny, V., I. Molotkov, and I. Psencik, *Ray Method in Seismology*, University of Karlova, Prague, Czechoslovakia, 1977.
- Chamot-Rooke, N., V. Renard, and X. LePichon, Magnetic anomalies in the Shikoku Basin: a new interpretation. *Earth and Planetary Science Letters*, 83, 214-228, 1987.
- Chapman, C. H., J. Chu, and D. G. Lyness, The WKBJ seismogram algorithm, in *Seismological Algorithms*, edited by D. J. Doornbos, pp. 47-74, Academic Press, 1988.
- Chen, Y. J., Oceanic crustal thickness versus spreading rate. *Geophysical Research Letters*, 19, 753-756, 1992.
- Christensen, N. J., Elasticity of ultrabasic rocks. *Journal of Geophysical Research*, 71, 5921-5931, 1966.
- Christensen, N. I., The abundance of serpentinites in the oceanic crust. *Journal of Geology*, 80, 709-719, 1972.

- Christensen, N. I., The magnitude, symmetry, and origin of upper mantle anisotropy based on fabric analyses of ultramafic tectonites. *Geophysical Journal of the Royal Astronomical Society*, 76, 89-111, 1984.
- Clarke, D. B., and B. G. J. Upton, Tertiary basalts of Baffin Island: field relations and tectonic setting. *Canadian Journal of Earth Sciences*, 8, 248-258, 1971.
- Cochran, J. R., Analysis of isostasy in the world's oceans, 2, mid-ocean ridge crests. *Journal of Geophysical Research*, 84, 4713-4729, 1979.
- Cormier, M., R. S. Detrick, and G. M. Purdy, Anomalously thin crust in oceanic fracture zones: new seismic constraints from the Kane Fracture Zone. *Journal of Geophysical Research*, 89, 10249-10266, 1984.
- Craig, C. H., and D. McKenzie, The existence of a thin low viscosity layer beneath the lithosphere. *Earth and Planetary Science Letters*, 78, 420-426, 1986.
- Daines, M. J., and F. M. Richter, An experimental method for directly determining the interconnectivity of melt in a partially molten system. *Geophysical Research Letters*, 15, 1459-1462, 1988.
- Denham, C. R., and H. Schouten, On the likelihood of mixed polarity in oceanic basement drill cores, in *Implications of Deep Drilling Results in the Atlantic Ocean: Ocean Crust, Proceedings of the Second Ewing Memorial Symposium*, 1979.
- Detrick, R. S., and G. M. Purdy, The crustal structure of the Kane fracture zone from seismic refraction studies. *Journal of Geophysical Research*, 85, 3759-3777, 1980.
- Detrick, R. S., M. H. Cormier, R. A. Price, D. W. Forsyth, and E. L. Ambos, Seismic constraints on the crustal structure within the Vema fracture zone. *Journal of Geophysical Research*, 87, 10599-10612, 1982.
- Detrick, R. S., P. Buhl, E. Vera, J. Mutter, J. Orcutt, J. Madsen, and T. Brocher, Multi-channel seismic imaging of a crustal magma chamber along the East Pacific Rise. *Nature*, 326, 35-41, 1987.
- Detrick, R. S., J. C. Mutter, P. Buhl, and I. Kim, No evidence from multichannel reflection data for a crustal magma chamber in the MARK area on the Mid-Atlantic Ridge, in *Nature*, 347, 61-64, 1990.
- Detrick, R. S., R. S. White, and G. M. Purdy, Chapter VI: Crustal structure of oceanic fracture zones. in *The Tectonics of Fracture Zones*, edited by P. J. Fox, Academic Press, in press.
- Dietz, R. S., Alpine serpentinites as oceanic rind fragments. *Bulletin of the Geological Society of America*, 74, 947-952, 1963.
- Drake, C. L., N. J. Campbell, G. Sander, and J. E. Nafe, A mid-Labrador Sea ridge. *Nature*, 200, 1085-1086, 1963.
- Elthon, D., J. F. Casey, and S. Komor, Mineral chemistry of ultramafic cumulates from the North Arm Massif of the Bay of Islands ophiolite: Implications for high pressure fractionation of oceanic basalts. *Journal of Geophysical Research*, 87, 11759-11777, 1982.
- Fox, P. J., E. Schreiber, H. Rowlett, and K. McCamy, The geology of the Oceanographer Fracture Zone - a model for fracture zones. *Journal of Geophysical Research*, 81, 4117-4128, 1976.

- Fryer, G. F., D. J. Miller, and P. A. Berge, Seismic anisotropy and age-dependent structure of the upper oceanic crust, in *Evolution of Mid-Ocean Ridges*, edited by J. Sinton, pp. 1-8, IUGG, 1989.
- Garmany, J., J. A. Orcutt, and R. L. Parker, Travel time inversion: a geometrical approach. *Journal of Geophysical Research*, 84, 3615-3622, 1979.
- Hall, S. A., J. F. Casey, and D. L. Elthon, A possible explanation of gravity anomalies over mid-ocean ridges. *Journal of Geophysical Research*, 91, 3724-3738, 1986.
- Heffler, D. E., and D. L. Barrett, OBS development at the Bedford Institute of Oceanography. *Marine Geophysical Researches*, 4, 227-245, 1979.
- Hess, H. H., History of ocean basins, in *Petrologic Studies: Buddington Volume*, pp. 599-620, Geological Society of America, Boulder, CO, 1962.
- Hinz, K., H. - Schlüter, A. C. Grant, S. P. Srivastava, D. Umpleby, and J. Woodside, Geophysical transects of the Labrador Sea: Labrador to southwest Greenland. *Tectonophysics*, 59, 151-183, 1979.
- Houtz, R., and J. Ewing, Upper crustal structure as a function of plate age. *Journal of Geophysical Research*, 81, 2490-2498, 1976.
- Huang, P. Y., and S. C. Solomon, Centroid depths of mid-ocean ridge earthquakes: Dependence on spreading rate. *Journal of Geophysical Research*, 93, 13445-13477, 1988.
- Hyndman, R. D., Evolution of the Labrador Sea. *Canadian Journal of Earth Sciences*, 10, 637-644, 1973.
- Issler, D. R., *The thermal and subsidence history of the Labrador margin*, Ph.D. Thesis, Dalhousie University, 1988.
- Jackson, H. R., and I. Reid, Oceanic magnetic anomaly amplitudes: variation with sea-floor spreading rate and possible implications. *Earth and Planetary Science Letters*, 63, 368-378, 1983.
- Jarrard, R. D., K. A. Dadey, and W. H. Busch, Velocity and density of sediments in the Eirik Ridge, Labrador Sea: Control by porosity and mineralogy, in *Proceedings of the Ocean Drilling Program, Scientific Results*, edited by S. P. Srivastava, M. A. Arthur, B. Clement et al., Vol. 105, pp. 811-835, 1989.
- Jonas, J., S. Hall, and J. F. Casey, Gravity anomalies over extinct spreading centers: A test of gravity models of active centers. *Journal of Geophysical Research*, 96, 11759-11777, 1991.
- Keen, M. J., E. M. Klein, and W. G. Melson, Ocean ridge basalt compositions correlate with paleobathymetry. *Nature*, 345, 423-426, 1990a.
- Keen, M. J., R. Courtney, J. McClain, and G. M. Purdy, Ocean-ridge crustal thickness correlated with paleobathymetry. *EOS*, 71, 1573 (Abstract), 1990b.
- Kennett, B. L. N., Towards a more detailed seismic picture of the oceanic crust and mantle. *Marine Geophysical Researches*, 3, 7-42, 1977.
- Kent, D. V., and F. M. Gradstein, A Jurassic to recent chronology, in *The Geology of North America*, Vol. M: *The Western North Atlantic Region*, edited by P. R. Vogt, and B. E. Tucholke, pp. 45-50, Geological Society of America, 1986.
- Kerr, J. W., A submerged continent remnant beneath the Labrador Sea. *Earth and Planetary Science Letters*, 2, 283-289, 1967.

- Klein, E. M., and C. H. Langmuir, Global correlations of ocean ridge basalt chemistry on axial depth and crustal thickness. *Journal of Geophysical Research*, 92, 8089-8115, 1987.
- Klitgord, K. D., and J. Mammerrickx, Northern East Pacific Rise: Magnetic anomaly and bathymetric framework. *Journal of Geophysical Research*, 87, 6725-6750, 1982.
- Kong, L. S. L., S. C. Solomon, and G. M. Purdy, Microearthquake characteristics of a mid-ocean ridge along-axis high. *Journal of Geophysical Research*, 97, 1659-1686, 1992.
- Kristoffersen, Y., and M. Talwani, Extinct triple junction south of Greenland and the Tertiary motion of Greenland relative to North America. *Bulletin of the Geological Society of America*, 88, 1037-1049, 1977.
- Kuo, B. -, and D. Forsyth, Gravity anomalies of the ridge-transform system in the South Atlantic between 31 and 34.5°S: Upwelling centers and variations in crustal thickness. *Marine Geophysical Researches*, 10, 205-232, 1988.
- Kuszniir, N. J., Thermal evolution of the oceanic crust: its dependence on spreading rate and effect on crustal structure. *Geophysical Journal of the Royal Astronomical Society*, 61, 167-181, 1980.
- Lévesque, S., *Heat flow across the Labrador Margin from shallow penetration measurements*, M. Sc. Thesis, Dalhousie University, 1992.
- Lewis, B. T. R., Constraints on the structure of the East Pacific Rise from gravity. *Journal of Geophysical Research*, 87, 8491-8500, 1982.
- Lewis, B. T. R., The East Pacific Rise and the thermal model. *Journal of Geophysical Research*, 88, 3348-3354, 1983.
- Lewis, S. D., and D. E. Hayes, The structure and tectonic evolution of the Central Basin Fault, West Phillipine Basin, in *The Geophysics of the Pacific Ocean Basin and Its Margin*, edited by G. H. Sutton, M. H. Manghanani, and R. Moberly, Geophysical Monographs, vol. 19, pp. 253-267, AGU, Washington, 1980.
- Lin, J., E. A. Bergman, Rift grabens, seismicity, and volcanic segmentation of the Mid-Atlantic Ridge: Kane to Atlantic fracture zones. *EOS*, 71, 1572 (Abstract), 1990.
- Lin, J., G. M. Purdy, H. Schouten, J. C. Sempere, and C. Zervas, Evidence from gravity data for focused magmatic accretion along the Mid-Atlantic Ridge. *Nature*, 344, 627-632, 1990.
- Loncarevic, B. D., Ocean bottom seismometry, in *CRC Handbook of Geophysical Exploration at Sea*, edited by R. A. Geyer, pp. 219-263, CRC Press, Boca Raton, Fla., 1983.
- Louden, K. E., R. S. White, C. G. Potts, and D. W. Forsyth, Structure and seismotectonics of the Vema fracture zone, Atlantic Ocean. *Journal of the Geological Society of London*, 143, 795-805, 1986.
- Louden, K. E., K. A. Dadey, and S. P. Srivastava, Heat flow measurements at hole 646A, in *Proceedings of the Ocean Drilling Program, Scientific Results*, edited by S. P. Srivastava, M. A. Arthur, B. Clement et al., Vol. 105, pp. 891-922, 1989.
- Ludwig, W. J., J. E. Nafe, and C. L. Drake, Seismic Refraction, in *The sea*, edited by A. E. Maxwell, pp. 53-84, Wiley-Interscience, New York, 1971.
- Ludwig, W. J., and P. D. Rabinowitz, Structure of the Vema fracture zone. *Marine*

- Geology*, 35, 99-110, 1980.
- Macdonald, K. C., and B. P. Luyendyk, Deep-tow studies of the structure of the Mid-Atlantic Ridge crest near lat 37°N. *Bulletin of the Geological Society of America*, 88, 621-636, 1977.
- Mammerickx, J., and D. Sandwell, Rifting of old oceanic lithosphere. *Journal of Geophysical Research*, 91, 1975-1988, 1986.
- Matthews, D. J., *Tables of the velocity of sound in pure water and seawater for use in echo-sounding and sound ranging*, His Majesty's Stationery Office, London, 1939.
- Meyerhoff, A. A., Origin of Arctic and North Atlantic Oceans, in *Arctic Geology*, edited by M. G. Pritchard, pp. 562-582, American Association of Petroleum Geologists, 1973.
- Minshull, T. A., R. S. White, J. C. Mutter, P. Buhl, R. S. Detrick, C. A. Williams, and E. Morris, Crustal structure at the Blake Spur Fracture Zone from expanding spread profiles. *Journal of Geophysical Research*, 96, 9955-9984, 1991.
- Nagumo, S., T. Ouchi, and S. Koresawa, Seismic velocity structure near the extinct spreading center in the Shikoku Basin, North Phillipine Sea. *Marine Geology*, 35, 135-146, 1980.
- Oakey, G. N., C. Currie, and P. Durling, A digital compilation of depth to basement of the east coast of Canada and adjacent areas, in *Open File #1964*, Geological Survey of Canada, 1988.
- Orcutt, J. A., Joint linear, extremal inversion of seismic kinematic data. *Journal of Geophysical Research*, 85, 2649-2660, 1980.
- Osler, J. C., and K. E. Loudon, Crustal structure of an extinct rift axis in the Labrador Sea: preliminary results from a seismic refraction survey. *Earth and Planetary Science Letters*, 108, 243-258, 1992.
- Parmentier, E. M., and J. Phipps Morgan, Spreading rate dependence of three-dimensional structure in oceanic spreading centres. *Nature*, 348, 325-328, 1990.
- Parsons, B., and J. G. Sclater, An analysis of the variations of ocean floor bathymetry and heat flow with age. *Journal of Geophysical Research*, 82, 803-827, 1977.
- Phipps Morgan, J., Melt migration beneath mid-ocean spreading centers. *Geophysical Research Letters*, 14, 1238-1241, 1987.
- Phipps Morgan, J., and D. Forsyth, Three-dimensional flow and temperature perturbations due to a transform offset: effects on oceanic crustal and upper mantle structure. *Journal of Geophysical Research*, 93, 2955-2966, 1988.
- Purdy, G. M., The correction for the travel time effects of seafloor topography in the interpretation of marine seismic data. *Journal of Geophysical Research*, 84, 8389-8396, 1982.
- Purdy, G. M. New observations of the shallow seismic structure of young oceanic crust. *Journal of Geophysical Research*, 92, 9351-9362, 1987.
- Purdy, G. M., The structure of 140 Myr old crust in the western central Atlantic Ocean. *Geophysical Journal of the Royal Astronomical Society*, 72, 115-138, 1983.
- Purdy, G. M., and R. S. Detrick, Crustal structure of the Mid-Atlantic Ridge at 23°N from seismic refraction studies. *Journal of Geophysical Research*, 91, 3739-3762, 1986.

- Purdy, G. M., L. S. L. Kong, G. L. Christeson, and S. C. Solomon, Relationship between spreading rate and the seismic structure of mid-ocean ridges. *Nature*, 355, 815-817, 1992.
- Reid, I., Crustal structure beneath the southern Grand Banks: seismic-refraction results and their implications. *Canadian Journal of Earth Sciences*, 25, 760-772, 1987.
- Reid, I., and H. R. Jackson, Ocean spreading rate and crustal thickness. *Marine Geophysical Researches*, 5, 165-172, 1981.
- Roest, W. R., and S. P. Srivastava, Sea-floor spreading in the Labrador Sea: A new reconstruction. *Geology*, 17, 1000-1003, 1989a.
- Roest, W. R., and S. P. Srivastava, Seafloor spreading history I: Magnetic anomalies along track, in *East coast basin atlas series: Labrador Sea*, edited by C. Hawkins, pp. 98, Minister of Supply and Services Canada, 1989b.
- Roots, W. D., and S. P. Srivastava, Origin of marine magnetic quiet zones in the Labrador and Greenland Seas. *Marine Geophysical Researches*, 6, 395-408, 1984.
- Royden, L., and C. E. Keen, Rifting process and thermal evolution of the continental margin of eastern Canada determined from subsidence curves. *Earth and Planetary Science Letters*, 51, 343-361, 1980.
- Salisbury, M. H., and N. I. Christensen, The seismic velocity structure of a traverse through the Bay of Islands ophiolite complex, Newfoundland, an exposure of oceanic crust and upper mantle. *Journal of Geophysical Research*, 83, 805-817, 1978.
- Scott, D. R., and D. J. Stevenson, A self-consistent model of melting, magma migration and buoyancy-driven circulation beneath mid-ocean ridges. *Journal of Geophysical Research*, 94, 2973-2988, 1989.
- Sempere, J. -, G. M. Purdy, and H. Schouten, Segmentation of the Mid-Atlantic Ridge between 24°N and 30°40'N. *Nature*, 344, 427-431, 1990.
- Shen, Y., and D. Forsyth, The effects of temperature- and pressure- dependent viscosity on three dimensional passive flow of the mantle beneath a ridge-transform system. *Journal of Geophysical Research*, 97, 19717-19728, 1992.
- Sinha, M. C., and K. E. Loudon, The Oceanographer Fracture Zone, I. Crustal structure from seismic refraction studies. *Geophysical Journal of the Royal Astronomical Society*, 75, 713-736, 1983.
- Solomon, S. C., and D. R. Toomey, The structure of mid-ocean ridges. *Annual Reviews of Earth and Planetary Science*, 20, 329-364, 1992.
- Sotin, C., and E. M. Parmentier, Dynamical consequences of compositional and thermal density stratification beneath spreading centres. *Geophysical Research Letters*, 16, 835-838, 1989.
- Sparks, D. W., and E. M. Parmentier, Melt extraction from the mantle beneath spreading centers. *Earth and Planetary Science Letters*, 105, 368-377, 1991.
- Spiggleman, M., and D. McKenzie, Simple 2-D models for melt extraction at mid-ocean ridges and island arcs. *Earth and Planetary Science Letters*, 83, 137-152, 1987.
- Spudich, P., and J. Orcutt, A new look at the seismic velocity structure of the oceanic crust. *Reviews of Geophysics and Space Physics*, 18, 627-645, 1980.
- Srivastava, S. P., Free air gravity map-814B (Paper 85-16), in *Geophysical maps and*

- geological sections of the Labrador Sea*, edited by S. P. Srivastava, Geological Survey of Canada, 1986.
- Srivastava, S. P., and C. R. Tapscott, Plate kinematics of the North Atlantic, in *The Geology of North America*, Vol. M: *The Western North Atlantic Region*, edited by P. R. Vogt, and B. E. Tucholke, pp. 379-404, Geological Society of America, 1986.
- Srivastava, S. P., R. K. H. Falconer, and B. MacLean, Labrador Sea, Davis Strait, Baffin Bay: geology and geophysics - A review (Memoir 7), pp. 333-398, Canadian Society of Petroleum Geologists, Calgary, 1981.
- Srivastava, S. P., B. MacLean, and P. Girouard, Depth to basement map (Paper 85-16), in *Geophysical Maps and Geological Sections of the Labrador Sea*, edited by S. P. Srivastava, Geological Survey of Canada, 1986.
- Srivastava, S. P., C. G. Powell, A. G. Nunns, L. C. Kovacs, D. G. Roberts, M. T. Jones, C. Uruski, and D. Voppel, Magnetic anomalies of total intensity, in *Geophysical Atlas of the North Atlantic between 50° to 70°N and 0° to 65°W*, edited by S. P. Srivastava, D. Voppel, and B. Tucholke, pp. 3-4, Dtsch. Hydrogr. Inst., Hamburg, 1988.
- Srivastava, S. P., and M. A. Arthur, Tectonic evolution of the Labrador Sea and Baffin Bay: constraints imposed by regional geophysics and drilling results from leg 105, in *Proceedings of the Ocean Drilling Program, Scientific Results*, edited by S. P. Srivastava, M. A. Arthur, B. Clement et al., Vol. 105, pp. 989-1009, 1989.
- Srivastava, S. P., K. E. Louden, S. Chough, D. Mosher, B. D. Loncarevic, P. Mudie, A. de Vernal, and B. MacLean, Results of detailed geological and geophysical measurements at ODP sites 645 in Baffin Bay and 646 and 647 in the Labrador Sea, in *Proceedings of the Ocean Drilling Program, Scientific Results*, edited by S. P. Srivastava, M. A. Arthur, B. Clement et al., Vol. 105, pp. 891-922, 1989.
- Stakes, D., and D. A. Vanko, Multistage hydrothermal alteration of gabbroic rocks from the failed Mathematician Ridge. *Earth and Planetary Science Letters*, 79, 75-92, 1986.
- Stergiopoulos, A. B., *Geophysical crustal studies off the SW Greenland margin*, M. Sc. Thesis, Dalhousie University, 1984.
- Stoffa, P. L., P. Buhl, J. B. Diebold, and F. Wenzel, Direct mapping of seismic data to the domain of intercept time and ray parameter: A plan wave decomposition. *Geophysics*, 46, 225-267, 1981.
- Stöpler, E., A phase diagram from mid-ocean ridge basalts: Preliminary results and implications for petrogenesis. *Contributions to Mineralogy and Petrology*, 74, 13-27, 1980.
- Talwani, M., and O. Eldholm, Evolution of the Norwegian-Greenland Sea. *Bulletin of the Geological Society of America*, 88, 969-999, 1977.
- Talwani, M., J. Worzel, and M. Landisman, Rapid gravity computations for two dimensional bodies with application to the Mendocino submarine fracture zone. *Journal of Geophysical Research*, 64, 49-59, 1959.
- Tomoda, Y., K. Kobayashi, J. Segawa, M. Nomura, and K. Kimura, Linear magnetic anomalies in the Shikoku Basin, northeastern Phillipine Sea. *Journal of*

- Geomagnetism and Geoelectricity*, 28, 47-56, 1975.
- Toomey, D. R., S. C. Solomon, and G. M. Purdy, Microearthquakes beneath the median valley of the Mid-Atlantic Ridge near 23N: Tomography and tectonics. *Journal of Geophysical Research*, 93, 9093-9112, 1988.
- Uenzelmann-Neben, G., W. Jokat, H. Miller, and S. Steinmetz, The Aegir Ridge: structure of an extinct spreading axis. *Journal of Geophysical Research*, 97, 9203-9218, 1992.
- Van der Linden, W. J., Crustal attenuation and seafloor spreading in the Labrador Sea. *Earth and Planetary Science Letters*, 27, 409-423, 1975.
- Vogt, P. R., L. C. Kovacs, C. Bernero, and S. P. Srivastava, Asymmetric geophysical signatures in the Greenland-Norwegian and southern Labrador Sea and the Eurasia basin. *Tectonophysics*, 89, 95-160, 1982.
- Vogt, P. R., L. C. Kovacs, C. Bernero, and S. P. Srivastava, Asymmetric geophysical signatures in the Greenland-Norwegian and southern Labrador Seas and the Eurasia basin. *Tectonophysics*, 89, 95-160, 1982.
- Watts, A. B., Gravity anomalies over oceanic rifts, in *Continental and oceanic rifts*, edited by G. Palmeson, pp. 99-105, American Geophysical Union, Washington, 1982.
- Weissel, J. K., and D. E. Hays, Evolution of the Tasman Sea reappraised. *Earth and Planetary Science Letters*, 36, 77-84, 1977.
- Weissel, J. K., and A. B. Watts, Tectonic evolution of the Coral Sea Basin. *Journal of Geophysical Research*, 84, 4572-4582, 1979.
- White, R. S., and D. McKenzie, Magmatism at rift zones: the generation of volcanic continental margins and flood basalts. *Journal of Geophysical Research*, 94, 7685-7729, 1989.
- White, R. S., R. S. Detrick, M. C. Sinha, and M. H. Cormier, Anomalous seismic crustal structure of oceanic fracture zones. *Geophysical Journal of the Royal Astronomical Society*, 79, 779-798, 1984.
- White, R. S., D. P. McKenzie, and R. K. O'Nions, Ocean crustal thickness from seismic measurements and rare earth element inversions. *Journal of Geophysical Research*, 97, 19683-19716, 1992.
- Whitmarsh, R. B., Axial intrusion beneath the median valley of the Mid-Atlantic Ridge at 37°N detected by explosion seismology. *Geophysical Journal of the Royal Astronomical Society*, 42, 189-215, 1975.
- Woodside, J. M., The Mid-Atlantic Ridge near 45°N, the gravity field. *Canadian Journal of Earth Sciences*, 9, 942-959, 1972.
- Zelt, C. A., and R. B. Smith, Seismic travelttime inversion for 2-D crustal velocity structure. *Geophysical Journal International*, 108, 16-34, 1992.